

INFRARED CONSTRAINTS ON ULTRAVIOLET THEORIES

A Dissertation

Presented to the Faculty of the Graduate School

of Cornell University

in Partial Fulfillment of the Requirements for the Degree of

Doctor of Philosophy

by

Yuhsin Tsai

August 2012

© 2012 Yuhsin Tsai
ALL RIGHTS RESERVED

INFRARED CONSTRAINTS ON ULTRAVIOLET THEORIES

Yuhsin Tsai, Ph.D.

Cornell University 2012

While our current paradigm of particle physics, the Standard Model (SM), has been extremely successful at explaining experiments, it is theoretically incomplete and must be embedded into a larger framework. In this thesis, we review the main motivations for theories beyond the SM (BSM) and the ways such theories can be constrained using low energy physics.

The hierarchy problem, neutrino mass and the existence of dark matter (DM) are the main reasons why the SM is incomplete. Two of the most plausible theories that may solve the hierarchy problem are the Randall-Sundrum (RS) models and supersymmetry (SUSY). RS models usually suffer from strong flavor constraints, while SUSY models produce extra degrees of freedom that need to be hidden from current experiments. To show the importance of infrared (IR) physics constraints, we discuss the flavor bounds on the anarchic RS model in both the lepton and quark sectors. For SUSY models, we discuss the difficulties in obtaining a phenomenologically allowed gaugino mass, its relation to R -symmetry breaking, and how to build a model that avoids this problem.

For the neutrino mass problem, we discuss the idea of generating small neutrino masses using compositeness. By requiring successful leptogenesis and the existence of warm dark matter (WDM), we can set various constraints on the hidden composite sector. Finally, to give an example of model independent bounds from collider experiments, we show how to constrain the DM–SM particle interactions using collider results with an effective coupling description.

BIOGRAPHICAL SKETCH

Yuhsin Tsai was born in Hsinchuang, Taiwan, on May 30 1982 as the first child of Lang-Fu Tsai and Yu-Chun Chang. At the age of four, his family moved to Chudong where his brother, Yu-Haw Tsai, was born. Six years later, the family moved to Hsinchu — the Silicon Valley in Taiwan — where Yuhsin lived and studied before coming to Cornell for his Ph.D.

By the age of fourteen, Yuhsin had decided he wanted to be a physicist, even though it was still not clear to him if he had the talent for it. As a child, he had fallen down the stairs several times, but never thought about its relation to gravity. He also tried to think of what would happen when traveling at the speed of light, but soon gave up. However, seduced by the joy of understanding nature, he enrolled at National Tsing-Hua University to study physics in 2000.

It was here that Yuhsin met a high energy theorist, Professor Darwin Chang, who played a key role in leading him to the world of particle physics. One day, during Yuhsin's second year at Tsing-Hua, he bumped into Darwin and asked, "I heard you know group theory. Could you teach me that?". They began a weekly meeting for group theory. Soon, the meetings increased to several times a week, and the topics were extended to many aspects in physics. This was the time Yuhsin began to understand how high energy physicists think and wanted to join them. Unfortunately, Darwin was diagnosed with gastric cancer in 2004, the same year as Yuhsin graduated from Tsing-Hua and joined the army. They continued to meet frequently after that, sharing ideas about life and physics until Darwin passed away in Dec 2005. Seeing the last stage of a physicist's life, Yuhsin was moved by how one's enthusiasm in understanding things can overcome physical pain. This strengthened his decision of becoming a high energy physicist, and he went to Cornell to pursue his goal.

In 2008, Yuhsin was accepted into the research group of Professor Yuval Grossman. Working with Yuval, Professor Csaba Csáki and many other talented collaborators, he learned many exciting things about beyond the SM physics. In 2010, Yuhsin was awarded a Fermilab Fellowship for Theoretical Physics, which gave him the chance to move to Fermilab for a year and work with Professor Roni Harnik on dark matter and collider physics. After receiving his degree, he will join the research group at UC Davis as a postdoctoral research associate.

This document is dedicated to Chao-Yi and my family

ACKNOWLEDGEMENTS

I thank my father Lang-Fu, mother Yu-Chun, and brother Yu-Haw for always being there for me. It is not easy for people in our culture to appreciate the price paid for understanding nature, but they did it well and are always proud of me.

Thank you Yuval for believing in me and giving me a lot of freedom in doing research. Besides the instruction in physics, I also thank you for giving me the chance to work with many good physicists. This broaden my thinking and made me more independent.

Thank you Csaba for working with me and teaching me physics. I learned a lot not just by talking to you, but also by preparing to talk to you. This helped me examine my thought process more carefully. Thank you Peter for always making time to talk to me and providing a valuable window into the experimental world. Thank you Maxim, Liam, Tung-Mow and everybody in the theory group for creating such a wonderful atmosphere for everyone to work and thrive together.

Thank you Roni for being my advisor at Fermilab. I have been so lucky to have someone to whom I can ask random physics questions and get inspiring answers. Also thanks Paddy, Joachim, Bogdan, Graham, Adam and everyone in the Fermilab theory group for teaching me collider and dark matter physics.

Thank you David and Flip for being excellent collaborators and wonderful friends. You are always my instructors on physics and many other things. Also thank Bibhushan, Monika, Dean and Ricky as being esteemed collaborators. Thank you Sohang, David, Josh, Itay, Yang, Dan, Gang, Johannes, Mathieu, Ben, Jack, Nick, Thomas, Mike, Mario for making the group like a home, and thank Yi-Ting, Yan-Juin, Jun-Hao, Chen-Chien, Yen-Chi, Hsin-Wei for all the wonderful low-energy (condensed matter) conversations.

Thank you Amanda and Darwin for helping me to come to Cornell here to pursue my dream. Thank you all my friends in Taiwan, you always give me a reason to keep going. Finally, dear Chao-Yi, my whole PhD life is a story with you.

TABLE OF CONTENTS

Biographical Sketch	iii
Dedication	v
Acknowledgements	vi
Table of Contents	vii
List of Tables	xii
List of Figures	xiii
1 Introduction	1
1.1 Hierarchy problem in the SM	2
1.1.1 SUSY and its breaking	2
1.1.2 The Randall-Sundrum model	5
1.2 Experimental motivation for BSM theories	7
1.2.1 Neutrino oscillations	7
1.2.2 Matter-antimatter asymmetry	8
1.2.3 Dark matter	9
1.3 IR constraints on BSM theories	10
1.3.1 Flavor constraints on the anarchic RS model	11
1.3.2 SUSY breaking, gaugino mass and R -symmetry	13
1.3.3 Dirac leptogenesis, WDM and composite neutrinos	15
1.3.4 Collider constraints on DM	17
2 Lepton Flavor Violation in RS Model	20
2.1 Introduction	21
2.2 Review of anarchic Randall-Sundrum models	24
2.3 Tree-level constraints from $\mu \rightarrow 3e$ and $\mu \rightarrow e$ conversion	26
2.3.1 Minimal RS model	28
2.3.2 Custodially protected model	29
2.4 Operator analysis of $\mu \rightarrow e\gamma$	31
2.5 Calculation of $\mu \rightarrow e\gamma$ in a warped extra dimension	35
2.5.1 Calculation of a	38
2.5.2 Calculation of b	39
2.5.3 Modifications in custodial modes	41
2.5.4 Constraints and tension	43
2.6 Power counting and finiteness	45
2.6.1 4D and 5D theories of bulk fields	46
2.6.2 Bulk fields in the 5D formalism	47
2.6.3 Bulk fields in the KK formalism	51
2.6.4 Brane fields in the 5D formalism	52
2.6.5 Brane fields in the KK formalism	55
2.6.6 Matching KK and loop cutoffs	59
2.6.7 Two-loop structure	62
2.7 Outlook and Conclusion	64

3	$b \rightarrow s\gamma$ Penguin in RS Model	67
3.1	Introduction	68
3.2	Flavor in Randall-Sundrum models	71
3.3	Calculation of the $b \rightarrow q\gamma$ Penguin in RS	74
3.3.1	Effective Hamiltonian for $b \rightarrow q\gamma$ transitions	74
3.3.2	Structure of the amplitude	75
3.3.3	Calculation of $\Delta C_7^{(\prime)}$	78
3.3.4	Calculation of $\Delta C_8^{(\prime)}$	80
3.3.5	Modifications from custodial symmetry	82
3.4	Radiative B decays	84
3.4.1	The $B \rightarrow X_{s,d}\gamma$ decay	85
3.4.2	Master formula for $\text{Br}(B \rightarrow X_s\gamma)$	86
3.4.3	Master formula for $\langle \text{Br}(B \rightarrow X_d\gamma) \rangle$	87
3.4.4	Analytic estimate of constraints	87
3.4.5	CP asymmetry in $B \rightarrow K^*\gamma$	88
3.5	Semileptonic B decays	90
3.5.1	Effective Hamiltonian for $b \rightarrow s\mu^+\mu^-$ transitions	90
3.5.2	Benchmark observables	94
3.6	Numerical analysis	100
3.6.1	Strategy	100
3.6.2	General pattern of RS contributions	101
3.6.3	Effects on benchmark observables	107
3.7	Conclusions	111
4	Spontaneous R-symmetry Breaking with Multiple Pseudomoduli	115
4.1	Introduction	116
4.2	Model Definition	118
4.3	Pseudomoduli Masses at 1-Loop	120
4.4	Vanishing 1-Loop Masses	122
5	Avoiding Light Gaugino Mass Problem with An Uplifted Model	126
5.1	Introduction	127
5.2	Overview of the SSMGM Model	130
5.3	Reviewing the ISS Framework	136
5.3.1	The necessity of metastable SUSY-breaking	136
5.3.2	The ISS Model	138
5.3.3	Uplifting the ISS Model	142
5.4	The Adjoint Instability	145
5.4.1	The messenger contribution to $V_{\text{eff}}(Z)$	145
5.4.2	Model Building Requirements for Stabilizing Z	147
5.5	Vacuum Structure & Spectrum	148
5.5.1	The Uplifted Vacuum ($k = 0$)	148
5.5.2	The ISS Vacuum ($k = 1$)	154

5.6	Direct Gauge Mediation	155
5.7	Stabilizing the Uplifted Vacuum	157
5.7.1	Organizing the Spectrum & Contributions to V_{CW}	158
5.7.2	Conditions for local minimum	159
5.7.3	Validity of 1-loop calculation	163
5.7.4	Lifetime Constraints on Uplifted Vacuum Stabilization	164
5.8	Conclusions	165
6	Leptogenesis in The Composite Neutrino Model	167
6.1	INTRODUCTION	168
6.2	COMPOSITE RIGHT-HANDED NEUTRINO	169
6.3	THE UV COMPLETE THEORY	171
6.3.1	Particle Content	172
6.3.2	Interactions	174
6.3.3	Experimental Bounds	177
6.4	LEPTOGENESIS	180
6.4.1	Standard leptogenesis	180
6.4.2	Dirac-type leptogenesis	182
6.5	DISCUSSIONS AND CONCLUSIONS	186
7	Warm Dark Matter in The Composite Neutrino Model	187
7.1	Introduction	188
7.2	The Composite Dirac Neutrino Model	189
7.2.1	Setup	189
7.2.2	Spectrum	193
7.2.3	Dirac vs Majorana	195
7.2.4	Decoupling	196
7.3	Warm Dark Matter	197
7.3.1	Non-Thermal WDM	197
7.3.2	Thermal WDM	198
7.3.3	Supercooled Confinement	199
7.3.4	Entropy Production Estimate	200
7.4	Conclusions	202
8	LEP Constraints on Dark Matter Interactions	203
8.1	Introduction	204
8.2	The Interaction of Dark matter with Leptons	206
8.3	LEP Limits on the effective Dark Matter–electron coupling	207
8.4	Limits on the Dark Matter–nucleon scattering cross section	212
8.5	Limits on the Dark Matter annihilation cross section	217
8.6	Constraints on theories with light mediators	221
8.7	Conclusions	226

9	LHC Constraints on Dark Matter Interactions	233
9.1	Introduction	234
9.2	An Effective Theory for dark matter interactions	235
9.3	Mono-jets at the LHC	238
9.3.1	Comparing Various Mono-Jet Analyses	238
9.3.2	Mono-Jet Bounds Compared to Direct Dark Matter Searches	246
9.3.3	Limits on Dark Matter Annihilation	248
9.4	Light mediators	251
9.5	Mono-photons at the LHC	256
9.6	Dark Matter Coupling through Higgs Exchange	258
9.6.1	The Invisible Higgs Analysis as a Dark Matter Search	259
9.6.2	A Lower Bound on Dark Matter–Nucleon Scattering from Current Higgs Limits	263
9.7	Conclusions	265
A	Details for $\mu \rightarrow e\gamma$ Calculation	269
A.1	Matching 5D amplitudes to 4D EFTs	270
A.2	Estimating the size of each diagram	271
A.2.1	Relative sizes of couplings	272
A.2.2	Suppression mechanisms in diagrams	272
A.2.3	Dimensionless integrals	274
A.2.4	Robustness against equationment	274
A.3	Analytic expressions	275
A.3.1	Dominant diagrams	276
A.3.2	Subdominant a coefficient diagrams	277
A.3.3	Subdominant b coefficient diagrams	282
A.3.4	Custodial Models	283
A.4	Position, momentum, and position/momentum space	284
A.5	Bulk Feynman Rules	289
A.6	Derivation of fermion propagators	291
A.6.1	Flat 5D fermion propagator	291
A.6.2	Warped 5D fermion propagator	295
A.6.3	Euclidean warped 5D fermion propagator	298
A.7	Finiteness of the brane-localized neutral Higgs diagram	299
A.7.1	Momentum space	300
A.7.2	Position/momentum space	302
B	Details for $b \rightarrow s\gamma$ Calculation	305
B.1	Dimensionless Integrals for Leading Diagrams	306
B.1.1	Propagator functions	306
B.1.2	C_7 integrals	307
B.1.3	C_8 integrals	309
B.2	Estimating the size of the misalignment contribution	310

B.2.1	Misalignment from f_{b_L}	312
B.2.2	Misalignment from f_{b_R}	313
B.2.3	Size of misalignment coefficients	314
B.3	Comments on 5D dipole theory uncertainties	314
B.3.1	KK decomposition	315
B.3.2	5D cutoff	316
C	Useful Lemma for R-symmetry Breaking	318
D	Derivation of The Average Dark Matter Velocity in A Dwarf Galaxy	321
E	Some Remarks for Leptogenesis with Composite Neutrinos	323
E.1	Matching the UV theory to the effective theory	324
E.2	Calculation of $\mu \rightarrow e\gamma$	326
E.3	Coherent muon-electron conversion	328
	Bibliography	331

LIST OF TABLES

6.1	The fermions and scalars of the $SU(6)_C$ model. We divide the particles into four groups. From top to bottom: the SM fields, the messenger, the preons and the optional lepton number violating Majorana fermion.	172
6.2	Parameter counting. We divide the couplings into three groups: For the L-conserving model, we only have the couplings in the first group. For the L-violating model, if N is a 189, we have the couplings in both the first and the second group. When N is a singlet, we have all the three groups. For each coupling we list the number of parameter as well as the number of parameter in our “physical” basis choice. We list separately the number of real and imaginary parameters.	177
7.1	$U(1)_F$ charges assignments to the massless bound states n_R and the SM fields $q = \{\phi, Q, U, D, L, E\}$, which also have the usual SM charges (not shown). The n_R are SM sterile by construction.	191
7.2	Confinement scale Λ and ϵ for $(n, n-1)$ theories. Such theories with $n > 7$ have $\epsilon \not\ll 1$, and are not considered further.	194
9.1	The expected and observed number of events at ATLAS and CMS, the error is a combination of a) Monte Carlo statistical uncertainties, and b) control sample statistical uncertainties and other systematic uncertainties. For the case of ATLAS we have combined a) and b) in quadrature.	240
A.1	Flat case coefficients in (A.6.78) upon solving with the boundary conditions (A.6.80–A.6.83). We have used the notation $c_p x = \cos \chi_p x$ and $s_p x = \sin \chi_p x$	294
A.2	Left-handed RS fermion propagator coefficients: the $z > z'$ coefficients are obtained by swapping $R \leftrightarrow R'$ in the arguments of the functions, leaving the $\alpha_{L,R}$ constant.	297

LIST OF FIGURES

2.1	A contribution to $\mu \rightarrow e\gamma$ from a brane-localized Higgs. The dashed line represents the Higgs while the cross represents a Yukawa coupling with a Higgs vev.	23
2.2	Neutral boson diagrams contributing to the a coefficient defined in (2.4.29). Fermion arrows denote the zero mode chirality, i.e. the SU(2) representation. External legs whose arrows do not point outward have an implicit external mass insertion. Dotted lines represent the fifth component of a bulk gauge field. Analytic forms for these diagrams are given in Appendix A.3.	36
2.3	Charged boson diagrams contributing to the a coefficient following the conventions in Fig. 2.2. Analytic forms for these diagrams are given in Appendix A.3.	37
2.4	Diagrams contributing to the b coefficient following the conventions in Fig. 2.2. Not shown: zero mass-insertion Z^5 diagram. Analytic forms for these diagrams are given in Appendix A.3.	38
2.5	The leading diagrams contributing to the a and b coefficients following the same conventions as Fig. 2.2.	40
2.6	Bounds on the anarchic Yukawa and KK scales in the minimal (a) and custodial (b) models from tree- and loop-level constraints, (2.3.19), (2.3.26), and (2.4.39). Each curve rules out the region to its left. The solid hyperbola is the appropriate tree-level bound. The thick solid straight line is the $b = 0$ loop-level bound. The red dashed (blue dotted) curve is the loop-level bounds in the case where b has the same (opposite) sign as a and takes its 1σ magnitude $ b = b _{1\sigma} = 0.03$	43
2.7	One-mass-insertion neutral scalar diagrams. The leading order k -dependence of each diagram cancels when the two are summed together. .	53
2.8	The fermion line in the mass basis for diagrams with an internal KK mode ($J > 3$). For simplicity we do not show the internal photon insertion. . . .	57
2.9	Yin-Yang and double rainbow topologies of two-loop diagrams. The dotted line represents either a gauge or Higgs boson. We have omitted the photon emission and an odd number of mass insertions.	63
3.1	Leading contributions to the anarchic (a) and misalignment (b) terms of the C_7 Wilson coefficient. Arrows indicate SU(2) _L representation; this is equivalent to labeling the chirality of the zero mode for SM fields. Here Q , U and D denote the 5D chiral fermion fields containing the SM left-handed doublets and right-handed up and down singlets, respectively. H^- is the charged component of the Higgs doublet that serves as the Goldstone boson of W^- after electroweak symmetry breaking, and G is the 5D gluon field. Additional diagrams related by exchanging the order of the mass insertion and photon emission are left implicit.	79

3.2	Leading contributions to the a and b terms of the C_8 Wilson coefficient following the notation of Fig. 3.1. G_μ refers to only the gluon four-vector.	81
3.3	Additional custodial diagrams contributing to the C_7 and C_8 coefficients.	83
3.4	RS contributions to the $b \rightarrow s$ Wilson coefficients $C_7(M_{KK})$ (upper left), $C'_7(M_{KK})$ (upper right), $C_8(M_{KK})$ (lower left) and $C'_8(M_{KK})$ (lower right) in the minimal (red) and custodial (blue) models, and from the misalignment contribution alone (yellow).	102
3.5	RS contributions to the $b \rightarrow s\gamma$ Wilson coefficients C_7 (left) and C'_7 (right), evaluated at the scale $\mu_b = 2.5 \text{ GeV}$. The minimal model distribution is shown in red, and the custodial one in blue.	103
3.6	Relative sizes of anarchic contributions to the Wilson coefficients $C_7(\mu_b)$ (left) and $C'_7(\mu_b)$ (right) from the RG evolution and operator mixing of $\Delta C_8^{(\prime)}$ from M_{KK} to μ_b , normalized to the Higgs penguin contribution to $\Delta C_7^{(\prime)}(M_{KK})$, with relevant RG evolution factors included. The yellow bin shows the ratio of the Higgs penguin contribution to $\Delta C_8^{(\prime)}(M_{KK})$. The red and blue distributions show the ratio of the gluon penguin to $\Delta C_8^{(\prime)}(M_{KK})$ for the minimal and custodial model respectively.	104
3.7	RS contributions to the $b \rightarrow d$ Wilson coefficients $C_7(M_{KK})$ (upper left), $C'_7(M_{KK})$ (upper right), $C_8(M_{KK})$ (lower left) and $C'_8(M_{KK})$ (lower right) in the minimal model (red), the custodial model (blue), and from the misalignment contribution alone (yellow).	106
3.8	RS contribution to $\text{Br}(B \rightarrow X_s \gamma)$ (left) and $\langle \text{Br}(B \rightarrow X_d \gamma) \rangle$ in the minimal (red) and custodial (blue) model. The experimental constraints according to (3.4.21) and (3.4.22) are displayed as grey bands.	106
3.9	CP asymmetry $S_{K^* \gamma}$ as a function of $\text{Br}(B \rightarrow X_s \gamma)$. The black dot indicates the central SM prediction, while the dashed lines show the experimental central values. The grey bands display the experimental 1σ and 2σ ranges for $S_{K^* \gamma}$	108
3.10	Correlation between $\text{Br}(B \rightarrow X_s \gamma)$ and $\text{Br}(B \rightarrow X_s \mu^+ \mu^-)$ for $q^2 \in [1, 6] \text{ GeV}^2$. The black dot indicates the central SM prediction, while the dashed lines show the experimental central values.	108
3.11	Transverse asymmetry $A_T^{(2)}$ as a function of q^2 . The SM prediction is indicated by the black line, while each blue line corresponds to an RS parameter point.	109
3.12	Correlation between $S_{K^* \gamma}$ and $A_T^{(2)}(q^2 = 1 \text{ GeV}^2)$. The black dot indicates the central SM prediction, while the dashed line shows the experimental central value. The grey bands display the experimental 1σ and 2σ ranges for $S_{K^* \gamma}$	110

5.1	(a) The tree-level potential without the instanton term as a function of $ M_{sing} $ and S , where we have enforced tree-level VEVs $ \bar{S} = S $ and $Z = \bar{Z} = -d\sqrt{N_f}M_{sing}S/m'$. The valley marked with a green band is perfectly flat in the $ M_{sing} $ direction and shows that the potential has a SUSY-breaking minimum for $S^2 = \frac{hf^2}{d} - \frac{m'^2}{d^2N_f}$. Note that the messengers are tachyonic for $ M_{sing} < m'/\sqrt{dh}$. (b) The same potential with the instanton term added. The minimum along the S -direction is approximately unchanged close to the origin but is significantly shifted as we move outwards along the $ M_{sing} $ direction. As we walk along the valley in the $ M_{sing} $ direction (which now tilts slightly away from the origin) we eventually reach the SUSY-minimum at $ M_{sing} \sim \sqrt{\Lambda}f$ and $S, Z = 0$. (c) We compute quantum corrections to the potential along the pseudomodulus direction, i.e. the green band in (b), by setting all fields to their VEVs in terms of $ M_{sing} $. The vacuum is stabilized at $ M_{sing} \sim \sqrt{h/d}f \rightarrow Z, \bar{Z} \sim \sqrt{h/d}f^2/m'$. The parameters used for these plots in units of m' were $N_f = 5$, $\Lambda = 3.8 \times 10^9$, $f = 63$ and $(g, d, h) = (0.02513, 0.02, 1)$	152
5.2	(a) For $ F/X = 100$ TeV and $d = 0.04$ in Scenario 1, V_{eff} has a local minimum in area of the r - t plane enclosed by the green curve. For Scenario 2 this area shrinks down to the shaded region due to the increased effect of the instanton term. (b) Areas of the r - t plane where V_{eff} has a local minimum for $d = 0.04, 0.02, 0.01$ (green/light, blue/medium, red/dark) in Scenario 1. $r_{max} \propto d^{5/6}$, so decreasing d from 0.04 to 0.01 decreases the area where there is a minimum. These areas do not depend significantly on h	161
5.3	Estimate of $\log_{10} r_{max}$ for different values of $d \sim \Lambda/\Lambda_{UV}$. The upper and lower regions are excluded to satisfy $\Lambda \ll \Lambda_{UV}$ and $r > 1$	162
6.1	The diagrams that generate the effective couplings of the model. (a) generates the Yukawa coupling of eq. (6.2.1) and (b) the L-violating term of eq. (6.2.5).	176
6.2	The Ω decay process that gives the L-asymmetry.	183
7.1	Mixing angle $\sin^2(2\theta_d)$ up to $\mathcal{O}(1)$ uncertainty (light gray) as a function of m_d , for $(n, n-1)$ theories. Also shown: The thermal production Lyman- α exclusion (hatched region, see e.g. [107]); the x-ray flux exclusion for ν^d energy fraction $\Omega_d = \Omega_{DM}$ (heavy black line, see e.g. [109, 105]); non-resonant production contours (dashed lines), labelled by the ratio of energy fractions Ω_d/Ω_{DM} [54, 110, 284]; resonant total DM production contours (dash-dotted lines) for lepton asymmetries $Y_{\Delta L} = 8, 12, 16, 25 \times 10^{-6}$ (resp. top to bottom), and their corresponding Lyman- α lower bounds on the WDM mass (black dots) [110].	195

7.2	A sketch of the thermal history. Species freeze-out (<i>a-b</i>) along the S_i adiabat (lower dashed), is followed by the CPT (<i>b-c</i>), which is a first-order g_{*s} phase transition in ζ . The CPT is followed by thermalization (<i>c-d</i>) along the S_f adiabat (upper dashed) until $g_{*s} = g_{*s}^f$ at which $T = T_f$. Once $T = T_\chi$, the CHS and SM decouple.	201
8.1	Distribution of normalized photon energy in single-photon events at DELPHI. The agreement between the data (black dots with error bars) and both the full DELPHI Monte Carlo (solid yellow/light gray shaded histogram) as well as our CompHEP simulation (dotted histogram) is excellent. The blue shaded histogram shows what a hypothetical Dark Matter signal from $e^+e^- \rightarrow \gamma\bar{\chi}\chi$ would look like. We have assumed vector-type contact interactions between electrons and dark matter, $m_\chi = 10$ GeV, and $\Lambda = 300$ GeV, see eq. (8.2.1). The peak at $x_\gamma \sim 0.8$ corresponds to the process $e^+e^- \rightarrow \gamma Z^0 \rightarrow \gamma\nu\bar{\nu}$, with an on-shell Z^0	208
8.2	DELPHI lower limits on the cutoff scale Λ of the dark matter effective theory for the four operators eqs. (8.2.1)–(8.2.4) as a function of the dark matter mass. The wiggles in the plot are due to limited Monte Carlo statistics.	211
8.3	DELPHI upper limits (thick lines) on the cross section for dark matter–nucleon scattering compared to results from direct detection experiments (thin lines and shaded regions). The left-hand plot is for spin-independent scattering, as would come from operators \mathcal{O}_S , \mathcal{O}_V , \mathcal{O}_t , and the right is for spin-dependent scattering through operator \mathcal{O}_A . The spin-independent limits of CDMS and XENON-100 are taken from Refs. [30] and [43], respectively. The spin-dependent limits of DAMA, XENON-10, PICASSO, COUPP and SIMPLE are taken from Refs. [86], [38], [71], [76] and [224], respectively. The DAMA and CoGeNT-allowed regions are based on our own fit [279] to the data from Refs. [86] and [3]. Following [247], we have conservatively assumed large systematic uncertainties on the DAMA quenching factors: $q_{\text{Na}} = 0.3 \pm 0.1$ for sodium and $q_{\text{I}} = 0.09 \pm 0.03$ for iodine. All limits are computed at the 90% confidence level, while the DAMA and CoGeNT allowed regions are shown at the 90% and 3σ confidence levels.	213
8.4	Diagram for vector-type dark matter–proton scattering at the one-loop level.	215
8.5	DELPHI upper limits on the cross section for spin-independent dark matter–nucleon scattering for the case of dark matter with tree level couplings only to electrons, but loop level couplings also to quarks, compared to results from the direct detection experiments DAMA [86], CoGeNT [3], CDMS [30], and XENON-100 [43]. The DAMA and CoGeNT allowed regions are based on our own fit [279] to the data from refs. [86, 3]. We conservatively assume $q_{\text{Na}} = 0.3 \pm 0.1$ and $q_{\text{I}} = 0.09 \pm 0.03$ for the DAMA quenching factors. All limits are computed at the 90% confidence level, while the DAMA and CoGeNT allowed regions are shown at the 90% and 3σ confidence levels.	217

8.6	LEP upper limits on the dark matter annihilation cross section $eV\sigma v$, assuming that dark matter production at LEP and dark matter annihilation as probed by astrophysical and cosmological observations can be described by contact operators. In the upper left panel, we show limits on the process $\bar{\chi}\chi \rightarrow e^+e^-$ (the only one that can be constrained model-independently by LEP), while in the other panels we have made the assumption that dark matter couples equally to all charged leptons. For the average dark matter velocity eVv^2 we have assumed the value at freeze-out in the top panels, while the bottom left panel is for the Draco dwarf galaxy which has very small eVv^2 . In the bottom right panel we compare the LEP limit on the v -independent interactions, \mathcal{O}_V and \mathcal{O}_t , to limits from a variety of astrophysical observations [11, 233, 248].	229
8.7	DELPHI lower limits on the cutoff scale $\Lambda = M/\sqrt{g_e g_\chi}$ of the dark matter effective theory. Dashed lines have been computed under the assumption that the effective theory is valid up to LEP energies, whereas the dotted and solid lines are for cases where the mediator mass M is so small that the effective theory breaks down. Once the mediator can be produced on-shell, its width Γ becomes relevant, as demonstrated by the shaded regions. Γ_{\min} is the minimum allowed width of the mediator, where $g_e \approx g_\chi = M/\Lambda$, and $\Gamma_{\min} \gtrsim 10^{-4}$ GeV.	230
8.8	DELPHI lower limits on the cross section for dark matter-nucleon scattering for different dark matter interaction models. As in Figure 8.7, from which the limits are derived, dashed lines correspond to a contact operator interaction between dark matter and electrons at LEP, while the solid and dotted lines are for interactions mediated by light particles. In the background, we show the constraints from the direct detection experiments XENON-100, CDMS, DAMA, and CoGeNT (upper left, upper right and lower right panels) and from DAMA, PICASSO, XENON-10, COUPP and SIMPLE (lower left panel), see fig. 8.3 for details.	231
8.9	LEP upper limits on the dark matter annihilation cross section $eV\sigma v$ for different assumptions on the mass of the particle that mediates dark matter production and annihilation. We show limits only for the annihilation channel $\bar{\chi}\chi \rightarrow e^+e^-$, which is the only one that can be probed model-independently at LEP. If dark matter has several annihilation channels, these limits can be straightforwardly (but in a model-dependent way) translated into limits on the total annihilation cross section, as done in the upper right and bottom panels of Figure 9.6. As in Figure 8.7, from which the limits are derived, dashed lines correspond to a contact operator interaction between dark matter and electrons at LEP, while the solid and dotted lines are for interactions mediated by light particles.	232
9.1	Dark matter production in association with a single jet in a hadron collider.	238

9.2	Measured missing energy spectra of $j + \cancel{E}_T$ for the three ATLAS analyses and the CMS analysis discussed in the text (black data points with error bars) compared to the collaborations' background predictions (yellow shaded histograms) and to our Monte Carlo prediction with (blue histograms) and without (black dotted lines) a dark matter signal. In all cases the DM signal comes from the vector operator, \mathcal{O}_V , and $m_\chi = 10$ GeV, $\Lambda = 400$ GeV. Our simulations are rescaled to match the overall normalization of the collaborations' background predictions.	242
9.3	Limits on the suppression scale Λ for the vector operator, \mathcal{O}_V , where only the coupling to up quarks is considered, for the three ATLAS analyses and the analysis of CMS. In all cases the observed (expected) bound is represented by a solid (dashed) line.	243
9.4	Limits on the suppression scale Λ for various operators, where only the coupling to one quark flavor at a time is considered, for the veryHighPT ATLAS analysis. In all cases the observed (expected) bounds are shown as solid (dashed) lines.	246
9.5	ATLAS limits on (a) spin-independent and (b) spin-dependent dark matter–nucleon scattering, compared to limits from the direct detection experiments. In particular, we show constraints on spin-independent scattering from CDMS [30], XENON-10 [39], XENON-100 [44], DAMA [86], CoGeNT [4, 208] and CRESST [40], and constraints on spin-dependent scattering from DAMA [86], PICASSO [71], XENON-10 [38], COUPP [76] and SIMPLE [224]. DAMA and CoGeNT allowed regions are based on our own fits [279, 206, 208] to the experimental data. Following [247], we have conservatively assumed large systematic uncertainties on the DAMA quenching factors: $q_{\text{Na}} = 0.3 \pm 0.1$ for sodium and $q_{\text{I}} = 0.09 \pm 0.03$ for iodine, which leads to an enlargement of the DAMA allowed regions. All limits are shown at 90% confidence level, whereas for DAMA and CoGeNT we show 90% and 3σ contours. For CRESST, the contours are 1σ and 2σ as in [40].	248
9.6	ATLAS constraints on dark matter annihilation for flavor-universal vector or axial vector couplings of dark matter to quarks. (If dark matter can annihilate also to leptons, the bounds are weakened by a factor $1/\text{BR}(\bar{\chi}\chi \rightarrow \bar{q}q)$.) We consider an environment with $\langle v_{\text{rel}}^2 \rangle = 0.24$, corresponding to the epoch at which thermal relic dark matter freezes out in the early universe. $\langle v_{\text{rel}}^2 \rangle$ is much smaller in present-day environments such as galaxies, which leads to improved collider bounds on the annihilation rate in those systems. The value of $\langle \sigma v_{\text{rel}} \rangle$ required for dark matter to be a thermal relic is indicated by the horizontal black line.	250

9.7	ATLAS limit on $\Lambda \equiv M/\sqrt{g_\chi g_q}$ as a function of the mass M of the particle mediating dark matter–quark interactions. We have assumed s -channel vector-type interactions, and we have considered the values $m_\chi = 50$ GeV (red) and $m_\chi = 500$ GeV (blue) for the dark matter mass. We have varied the width Γ of the mediator between the values $M/3$ (lower boundary of colored bands) and $M/8\pi$ (upper boundary of colored bands). Dashed dark gray lines show contours of constant $\sqrt{g_\chi g_q}$	253
9.8	Limits from the CMS mono-photon analysis on the suppression scale Λ for the vector operator, \mathcal{O}_V , where only the coupling to one quark flavor at a time is considered. The expected bound is shown with a dashed line and the observed one with a solid line.	258
9.9	Limits from the CMS mono-photon analysis on spin-independent dark matter–nucleon scattering, compared to limits from direct detection experiments. In particular, we show constraints on spin-independent scattering from CDMS [30], XENON-10 [39], XENON-100 [44], DAMA [86], CoGeNT [4, 208] and CRESST [40]. DAMA and CoGeNT allowed regions are based on our own fits [279, 206, 208] to the experimental data. Following [247], we have conservatively assumed large systematic uncertainties on the DAMA quenching factors: $q_{\text{Na}} = 0.3 \pm 0.1$ for sodium and $q_{\text{I}} = 0.09 \pm 0.03$ for iodine, which leads to an enlargement of the DAMA allowed region. All limits are shown at 90% confidence level, whereas for DAMA and CoGeNT we show 90% and 3σ contours. For CRESST, the contours are 1σ and 2σ as in [40].	259
9.10	Left: Projected 95% C.L. upper bounds on dark matter–nucleon scattering mediated by a Higgs boson from future ATLAS searches for invisible Higgs decays. Limits are shown for the $Z + H$ and vector boson fusion (VBF) production modes, and for Higgs masses of 120 GeV and 250 GeV [320]. Right: <i>Lower</i> 95% C.L. bounds on dark matter–nucleon scattering mediated by a Higgs boson, derived from the CMS exclusion of a Standard Model Higgs boson in certain mass ranges [139], assuming that the Higgs was missed at the LHC due to its large invisible width. The direct detection limits we show for comparison are the same as in figures 9.5 and 9.9.	263
A.1	equationment of the external mass insertion diagrams with Standard Model gauge bosons. χ and ψ are left- and right-chiral Weyl spinors respectively. The gauge boson vertices don't change fermion chirality so that the internal fermion must be a chirality-flipping KK mode. We have neglected the contribution where the external mass insertion connects two zero mode fermions since this is suppressed by $m_\mu R'$	275

A.2	A simple loop diagram to demonstrate the power counting principles presented. The lines labeled p_i represent the net external momentum flowing into each vertex so that p_i^z corresponds to the KK mass of the i^{th} external particle.	286
B.1	A sketch of the 5D momentum space where the circle of radius Λ represents the boundary of a 5D Lorentz invariant loop momentum integration region. Marks on the k_z axis show the masses of KK states. Dashed lines demonstrate that the 4D loop cutoff which respects 5D Lorentz invariance depends on the particular KK mode.	316
B.2	Plot of the charged Higgs integrand as a function of the dimensionless loop momentum in the position/momentum space picture. The dashed line is a heuristic 5D cutoff Λ representing the strong coupling scale. The shaded region represents the error from taking the loop momentum to infinity rather than Λ ; the contribution of this shaded region is approximately 15% of the total integral.	317
E.1	In the upper part are the vertices we use in the calculation: (a) $-ie\gamma^\mu$ (b) $-ie(p + p')^\mu$ (c) iY^L . The lower part are the kinematics we use in the calculation. The case with the photon going out from e is not shown, since we can obtain the result directly from the first diagram.	327
E.2	$\mu - e$ conversion in nuclei emitted by photon and Z	329

CHAPTER 1

INTRODUCTION

Physics rules are approximations of nature. With the help of mathematical tools, they explain and predict experimental results when a self consistent framework. However, approximations have their limits. Current physics rules should only be considered as an effective description of the observed world. Due to experimental limits, a theory can only be examined at the reachable energy scale, and it is not surprising that the current understanding needs to be modified to accommodate results from higher energy experiments. Theories that are approximations of the low energy physics are called infrared (IR) theories, while more fundamental descriptions which are consistent up to a higher energy scale are called the ultraviolet (UV) theories. Progress in high energy physics is nothing but identifying the limit for the current scenario to break down, treating it as an IR theory and extending it to an UV description with the help of experiments.

The Standard Model (SM), which was built as a UV theory describing the strong and electroweak interactions is now understood to only be an IR theory only. How to move a step forward by building a consistent UV theory is the central issue in high energy physics today. With the three generations of quarks and leptons, the SM has correctly predicted almost all the measured scattering cross sections, decay rates and various asymmetries mediated by the strong and the electroweak forces. Furthermore, the Higgs mechanism gives a concise tool to unify and break the electroweak symmetry while satisfying various electroweak precision measurement (EWPM) constraints.

However, even with all the success in predicting the experimental results, it is still difficult to think of the SM as the true UV theory of nature for two reasons. First, the theory requires fine tuning, and there is no way to explain the necessary energy cutoffs and

the mass hierarchy within the model. Moreover, current progress in our understanding in dark matter (DM), dark energy, neutrino oscillations, matter-antimatter asymmetry, strong-CP problem, flavor physics, and cosmology strongly suggest the existence of extra particles and interactions. These reasons motivate us to look for theories that lie beyond the SM (BSM). Let us, therefore, begin with a review of some of these motivations.

1.1 Hierarchy problem in the SM

The most important fine-tuning problem in the SM relates to the cutoff dependence of the Higgs mass correction. When adding radiative corrections to the Higgs mass, the one-loop contribution from the SM particles are quadratically divergent. If the Plank scale — the scale where the quantum effects of gravity become strong ($\sim 10^{19}$ GeV) — is the fundamental scale of nature, then the bare Higgs mass needs to be at the same order but adjusted very precisely to cancel the quadratic divergence to obtain an electroweak scale mass. The unnatural adjustment has to be one in 10^{17} , and the gigantic difference between the two scales grants the issue a famous name — the hierarchy problem.

1.1.1 SUSY and its breaking

There are two possible ways to make the Higgs mass natural — either by having an additional symmetry that forbids the quadratic divergence, or separating the two scales by embedding them in a non-trivial geometry. The most popular scenarios for the two different approaches are supersymmetry (SUSY) and the Randall-Sundrum (RS) model respectively. Supersymmetry is the only way to combine an internal symmetry with space-time symmetry. The operators of the internal symmetry relate elementary particles of one spin

to other particles that differ by half a spin. The new particles obtained by shifting the spin of the SM particles are called superpartners. They give additional loop corrections to the Higgs mass. For the fermion and gauge boson loops attached to the Higgs propagator, there are diagrams with sfermions (the scalar partners of the fermion) and gauginos (the fermionic partners of the gauge boson) loops that cancel the quadratic divergence. The one-loop Higgs mass correction then becomes logarithmically divergent, which allows a much higher cutoff scale given by the nature scale. Another nice feature of having superpartners is that they make gauge coupling unification exact. Around 10^{16} GeV, the renormalization group (RG) running in the minimal SUSY model makes the couplings of the three gauge interactions coincide. This does not happen in the SM.

Although the existence of superpartners solves the hierarchy problem and leads to unification, the new particles need to be hidden from existing collider searches. More precisely, SUSY needs to be broken, and most of the superpartners need to be heavier than the electroweak scale. How to break SUSY and produce a phenomenologically allowed spectrum is then an important question. Ideally, SUSY breaking occurs generically, which means that there is no tuning between the parameters and no need for extra gauge symmetries to be put in by hand. This philosophy leads to several constraints when trying to build a plausible model.

First, in order to preserve the symmetric protection against quadratic divergent to the Higgs mass correction, SUSY needs to be broken spontaneously. The SUSY algebra requires SUSY breaking vacua to be positive. This is not an easy task for a generic model: if the number of equations for solving the VEVs is the same as the number of variables, then making all the scalar VEVs zero would be a solution that preserves SUSY. However, having additional symmetries places extra constraints that may forbid the trivial solution. A natural candidate is R -symmetry, which is a $U(1)$ symmetry that exists in the

SUSY algebra with both the SUSY generators and the anti-commuting coordinates θ, θ^\dagger carry an R -charge. A theorem from Nelson and Seiberg [313] shows that R -symmetry is a necessary condition for a generic SUSY breaking. We then want to preserve it in the UV theory. Although R -symmetry is important for SUSY breaking, we still have to break it spontaneously above the TeV scale. This is because gauginos are Majorana fermions in most of SUSY models (except models with Dirac gauginos[210, 281]), and R -symmetry needs to be broken to generate TeV scale masses. Again, this is not an easy task because of various SUSY constraints, and we discuss the issue in Sec. 1.3.2.

Superpartners get masses from SUSY breaking. If the masses are generated at tree-level with renormalizable couplings, there is a sum rule for the fermion and boson masses that forces some superpartners to be lighter than the SM particles. To avoid experimental constraints, superpartners in the visible sector need to get mass through non-renormalizable couplings. This means the breaking needs to be transmitted to the visible sector through mediators that suppress the generated masses from the SUSY breaking scale and violate the sum rule in the visible sector. The most studied mediating mechanisms are non-renormalizable gravitational interactions or the loop-induced SM gauge interactions. Gravity is a natural candidate for the mediation; when combined with SUSY, the supergravity (SUGRA) model automatically provides the necessary non-renormalizable interactions. However, since the mediation occurs at the Plank scale, flavor symmetry is broken at a high energy scale and can be mediated through the gravitational interactions and generate an order one flavor changing couplings at the TeV scale which are forbidden by flavor changing neutral currents (FCNCs) constraints. By comparison, SUSY breaking in gauge mediation models is transmitted by light messengers which carry charges both in the SUSY breaking and the visible sectors. The visible sector couplings are the SM gauge interactions, which are flavor blind and generate no flavor-

changing couplings. We therefore focus on this type of model when discussing gaugino masses and R -symmetry breaking in Sec. 1.3.2.

1.1.2 The Randall-Sundrum model

Randall-Sundrum (RS) models imagine that the universe is a five-dimensional anti de Sitter space, and the elementary particles are either localized on a four-dimensional brane or propagate in the bulk. Unlike the large extra dimension (ADD) model, which uses additional sub-millimeter sized flat dimensions to suppress gravity, the RS model has a warped geometry, and the size of the extra dimension is only the inverse of the Plank scale. There are two popular models: RS1 has a finite size for the extra dimension bounded by two branes, while RS2 is similar but with one brane placed infinitely far away so there is only one brane left in the model. For the purpose of generating a hierarchical mass spectrum, it is easier to consider RS1.

In RS1, the warping of the extra dimension is analogous to the warping of the space-time in the vicinity of a massive object. This generates a large ratio of energy scales so that the natural energy scale at one end of the extra dimension is much larger than at the other end. To solve the hierarchy problem between the electroweak and the Plank scales, the natural scale of one brane is set to be the Plank scale (UV brane) and the scale of the other brane to be the TeV scale (IR brane). With the warped geometry, the Higgs localized on the IR-brane with a TeV scale cutoff can be connected with Plank scale physics. The quadratic divergence in the Higgs mass correction then should only be cut around the TeV scale and is absorbed by the bare mass at a similar scale.

Another consequence of the warped geometry is the generation of a hierarchical mass

spectrum. If a SM fermion lives in the bulk, the wave function corresponding to the lowest energy solution carries a warp suppression on one of the branes. This makes the Yukawa coupling between UV-localized fermions and an IR-localized Higgs exponentially suppressed. Since the coefficient in the exponential suppression determines the 5D localization of a fermion, a small change of the localization generates a big mass difference. We are then able to reproduce the hierarchical SM mass spectrum using anarchic and order one Yukawa matrices.

The overlap between wave functions in the bulk, however, causes flavor problems. Besides Yukawa couplings, the bulk mass of the 5D fermions gives an additional source of flavor violation. There then exist non-SM FCNC diagrams depending on both the Yukawa and the fermion localization. Fortunately, most of the flavor-violating processes are given by the difference between the bulk masses and the so-called RS-GIM mechanism saves the model from many flavor constraints. However, flavor experiments still provide important bounds on the anarchic RS model which we discuss them in Sec. 1.3.1.

Another important feature of RS models is their relation to the AdS/CFT correspondence, which makes them dual to technicolor models (for a review, see [?]). By the AdS/CFT correspondence, the RS model is dual to a strongly coupled conformal field theory (CFT). A dictionary can be built between the two descriptions, where every 5D bulk field is associated with a CFT operator, and the boundary value of the bulk field acts as a source field for the CFT operator. Using this, the n -point functions in the strongly-coupled CFT can be computed by knowing the 5D on-shell bulk action.

Compactifying the AdS_5 space as in the RS1 model breaks conformal symmetry, and the position in the extra dimension is related to the 4D CFT energy scale between the UV and the IR cutoffs. The UV-brane breaks conformal invariance explicitly. Since low-

ering the energy scale (moving towards the IR-brane) restores the conformal symmetry, the breaking must come from irrelevant operators. This makes the source field localized on the UV-brane capable of obtaining a kinetic term and become dynamical. The UV-localized field in the 5D theory is then mainly composed of this elementary source field in the CFT language. On the other hand, the IR-brane breaks the conformal invariance spontaneously, which generates a pseudo-Nambu-Goldstone boson that gets a mass when brane stabilizing terms are included. Since the breaking at the IR-scale is dynamically generated, an IR-localized field in the 5D picture then is mainly composed of composite fields in the strongly coupled theory, which gets a mass scale and breaks the symmetry. To summarize, the CFT dual of RS models, UV localized fields such as leptons are closer to elementary fields, while the IR localized fields such as the tops are more composite. For neutrinos, generating a small Yukawa mass from the overlap integral between UV- and IR-localized neutrinos is dual to models obtaining small neutrino masses using composite right-handed neutrinos. We discuss the idea and applications of composite neutrinos in Sec. 1.3.3.

1.2 Experimental motivation for BSM theories

1.2.1 Neutrino oscillations

Another motivation for physics beyond the SM is the necessity of new degrees of freedom to explain various experimental anomalies. For example, through the study of neutrino oscillations, it has been confirmed that neutrinos have small but non-zero masses, and that the mass matrix carries large mixing angles. This means we have to include an additional mass matrix in the Lagrangian, which only contains left-handed neutrinos in the

SM case. Once we add the mass matrix, a natural question to ask is why the neutrino masses (around eV scale) are much smaller than the electroweak scale. In analogy with the hierarchy problem between the Planck/electroweak scales, the gap between fermion masses also has a hierarchical structure that needs to be explained. There are many plausible ideas to produce light neutrinos. One of them is to assume that neutrinos, like any other SM particle, only gets mass from coupling to the Higgs, and the coupling is suppressed due to the compositeness of the RH neutrinos. The idea is realized in the composite neutrino and the RS models. We discuss these models in Sec. 1.3.3.

1.2.2 Matter-antimatter asymmetry

From the cosmological point of view, the SM itself does not provide enough tools to generate the universe we see today, in particular the observed matter–antimatter asymmetry. The number of baryons in the universe is not equal to the number of antibaryons. In fact, all the structures that we observe in the universe — stars, galaxies, and clusters — consist of matter, and there is no antimatter in any appreciable quantity. Since it is natural to assume that the universe started from a state with an equal number of baryons and antibaryons, the observed baryon asymmetry must have been generated dynamically. This scenario is called baryogenesis. There are several baryogenesis models, and all of which require BSM physics. For models producing net baryon number around the electroweak scale, a strong first order phase transition is necessary to preserve the generated asymmetry from being washed out by the sphaleron effect. A sphaleron is a non-perturbative solution in the finite temperature Higgs vacuum that shifts a vacuum carrying one baryon number to another. The average effect diminishes the sum of the baryon and lepton numbers ($B + L$) but preserves the difference ($B - L$). When the net lepton number is zero,

sphalerons wash out the baryon asymmetry, and this is why a strong first order phase transition is required to get the baryon production out of equilibrium. In the minimal supersymmetric standard model (MSSM), a strong first order phase transition can be realized with the help of light stops, since they can thermally produce a large enough cubic term in the Higgs potential that makes the phase transition first order.

Another way of getting the asymmetry without a strong first order phase transition is to generate a net lepton number and let sphalerons to convert it to a baryon asymmetry, since $B + L$ is not conserved and $B - L$ is preserved. This type of scenario is called leptogenesis. The popular leptogenesis models not only generate the required baryon asymmetry but also explain the hierarchy between the neutrino mass and the electroweak scale. In this thesis, we give an example of a leptogenesis model within the framework of composite neutrinos in Sec. 1.3.3.

1.2.3 Dark matter

Besides neutrinos and matter-antimatter asymmetry, observations from the dynamics of the stars also indicate the existence of new particles. These particles should be massive like the SM fermions but have no or very weak interaction with photons, which gives them a vivid name: dark matter (DM). The discrepancy between the predicted and observed dynamics of galaxies reveals the existence of DM. When estimating the gravitational force necessary for the observed orbit velocities of stars in the Milky Way and other galaxies, the calculated mass is much larger than what is accounted for by visible matter. Many other observations also indicate the presence of DM, including the flat radius dependence in the rotational speed of galaxies, the gravitational lensing of background objects by clusters (such as the Bullet Cluster), and the temperature distribution of hot gas

in galaxies. Current estimates show that DM constitutes 83% of the matter in the universe and 23% of the mass-energy density. How they can be included in an extension of the SM is a central issue in building a BSM theory. Previously, the most exciting DM candidate was the lightest supersymmetric particle (LSP). It can be long-lived, electrically neutral, have an electroweak scale mass and annihilation cross section producing the right relic abundance. However, due to increasingly strong bounds from collider and direct detection experiments, the parameter space for the LSP mass and interactions in the minimal model has been seriously squeezed. This means that there is no uniquely preferred DM model, and it is an urgent task to constrain the parameter space from various experimental results. However, it is non-trivial to combine these results and to determine the useful experimental signatures. In Sec. 1.3.4, we give an example of how one may constrain DM interactions using the mono-jet and mono-photon searches at colliders. We also give an example of a warm dark matter (WDM) candidate in the composite neutrino model in Sec. 1.3.3.

1.3 IR constraints on BSM theories

We briefly discuss some IR physics constraints on the BSM scenarios mentioned above, including flavor constraints on the anarchic RS model, gaugino mass constraints on a dynamical SUSY breaking scenario, and the requirements for having leptogenesis and WDM in the composite neutrino model. As we will see, there are constraints from both the theoretical and experimental points of view. To give an explicit example of how to set experimental constraints to UV theories, we also discuss DM constraints from colliders using the effective coupling description. We will get into details of the analysis in the following chapters.

1.3.1 Flavor constraints on the anarchic RS model

As we discussed, the bulk masses of fermions in RS introduce new sources of flavor violation. It is important to know how strong the flavor constraints are in the model. There are two kinds of flavor constraints — one from tree-level processes and the one from loop-induced processes. At tree-level, FCNCs are induced by the non-universality of the gauge boson wave functions in the bulk. Taking $\mu \rightarrow e$ conversion as an example, the SM like Z -boson wave function is not flat near the IR-brane because it gets a mass from the brane-localized Higgs. Its overlap integral to fermions then is flavor non-universal, which generates flavor mixings in the mass basis. To reduce the effect, one can pull the fermion wave functions away from the IR-brane. However, in order to maintain the fermion masses, the size of the anarchic Yukawa needs to be increased simultaneously. This means the tree-level flavor violation is inversely proportional to the size of the anarchic Yukawa.

In contrast, the loop-induced flavor mixing is proportional to the size of the Yukawa. In the basis where all the flavor mixings exist in the Yukawa, the loop induced FCNC has to change the flavor from the Higgs mass insertion. The size of the loop is then proportional to some powers of the anarchic Yukawa. Combining this with the tree-level constraints, we can set both an upper and a lower bound on the anarchic Yukawa for a given size of the bulk. Since the size of the bulk should be around $1/\text{TeV}$ for colliders to produce the excited states, this sets direct bounds on the anarchic RS model.

There are FCNC constraints from both the lepton and the quark sectors. For leptons, the most stringent tree-level constraints come from the $\mu \rightarrow e$ conversion and the $\mu \rightarrow 3e$ decay, while the most important loop-induced constraint is from the $\mu \rightarrow e\gamma$ penguin. In the SM, one-loop penguin contributions are UV-convergent. This is because the SM is

a renormalizable theory so the leading order diagram has to be finite. However, the RS model is a non-renormalizable theory, which can be seen by the fact that all the couplings beside the bulk mass carry negative energy dimensions. An infinite number of counterterms then is necessary to regulate all the higher order operators, and there is no guarantee that the leading order diagram has to be finite. Because of this, all the previous attempts in estimating the size of the one-loop $\mu \rightarrow e\gamma$ were based on a naive dimensional analysis (NDA). It was believed that the diagram with a brane-Higgs running in the loop has to be logarithmic-divergent, and there is no way to calculate the Yuakwa bound precisely.

However, the old belief is wrong, and the one-loop $\mu \rightarrow e\gamma$ is actually finite and calculable. In Chapter 2, we calculate the leading order diagrams explicitly and explain the reason for the finiteness. Instead of the Kaluza-Klein (KK) decomposition approach, we derive Feynman rules from the 5D Lagrangian directly and use them to perform a full 5D calculation. By doing this, the only cutoff that shows up in the calculation is the 4D momentum, which makes the finiteness more obvious than in the KK calculation, in which various cutoffs from summing the KK modes need to be included. Besides this, there is a non-trivial matching between the 4D momentum and the KK sum cutoffs in the KK calculation. As we show in Chapter 2, a wrong matching gives an incorrect result, and the prescription for doing a correct 4D calculation is still an open question. Nevertheless, the issue is only present when doing the KK calculation, which gives further contribution for doing the calculation in 5D. The result of our $\mu \rightarrow e\gamma$ calculation sets a complementary bound to the tree-level constraints and the allowed KK scale needs to be above 6 TeV.

Flavor bounds in the quark sector also provide stringent constraints. The tree-level exchange of KK gluons and neutral electroweak gauge bosons contribute to meson-anti meson mixing and induces left-right operators that do not exist in the SM. The effects receive significant enhancement due to the QCD running. In the kaon system they are also

chirally enhanced by the ratio between the KK and strange masses. This leads to new CP violating effects in the well-measured observable, ϵ_K , which pushes the KK gluon mass up to 10 – 20 TeV generically. In Chapter 3, we examine the phenomenological observables of the loop-induced process $b \rightarrow q\gamma$ ($q = s, d$) with a brane-localized Higgs using the full 5D calculation. In comparison to $\mu \rightarrow e\gamma$, the theoretical predictions are more involved due to the RG evaluation from the KK scale to the B meson scale and below. The large range of energy scales introduces mixing between different operators, so for the low energy observables the effect of the gluon loops should also be included. We calculate the branching ratio $\text{Br}(B \rightarrow X_s \gamma)$ and the CP averaged branching ratio $\langle \text{Br}(B \rightarrow X_d \gamma) \rangle$. Using these and the tree-level constraints, we perform parameter scans and make predictions of the RS contribution to $\text{Br}(B \rightarrow X_s \mu^+ \mu^-)$, forward backward asymmetry A_{FB} in $B \rightarrow K^* \mu^+ \mu^-$, the time-dependent CP asymmetry $S_{K^* \gamma}$ and the transverse asymmetry $A_T^{(2)}$ in $B \rightarrow K^* \mu^+ \mu^-$. As we will see, many of the observables get distinct RS contributions and may be seen in near future experiments.

1.3.2 SUSY breaking, gaugino mass and R -symmetry

Naively, SUSY breaking happens at a high energy scale and should suffer stringent constraints from electroweak scale physics. If we require the theory to be natural — i.e. that there is no tuning of the parameters, no extra flavor violation in the IR theory and no SUSY vacua — then the IR physics can set direct constraints on the SUSY breaking scenario. Among various constraints from the IR physics, obtaining a phenomenologically allowed gaugino mass plays a very important role.

As discuss in Sec. 1.1.1, spontaneous SUSY breaking generically requires the existence of an R -symmetry [313]. Nevertheless, the R -symmetry needs to be spontaneously bro-

ken in a lower energy scale in order for gauginos to obtain Majorana masses. In general one can envision either tree-level spontaneous R -breaking or radiatively induced breaking. Models with tree-level R -breaking exist, but they are rather cumbersome and have not yet been found naturally in dynamical SUSY breaking models. We thus focus on the case with R -breaking generated by loop-induced potentials.

A SUSY breaking vacuum is necessarily accompanied by a flat direction called a pseudomodulus (PM). It carries R -charge 2 and serves as the SUSY breaking spurion. For a loop-induced R -breaking, the PM gets negative mass from the Coleman-Weinberg potential and breaks the symmetry spontaneously. The generic breaking mechanism is constrained: it is shown in [341] that for a generalized O’Raifeartaigh model with a single PM, there can be no radiatively induced R -symmetry breaking at the one loop level if all the fields carry R -charge 0 or 2. Since the simplest charge assignment in the superpotential is to have the PM carrying an R charge 2 and all the other fields carry a zero R -charge, the proof explains the tiny gaugino masses in many well-known models. When having a single PM, the PM must couple to SUSY breaking. It is then interesting to ask if the same R -charge constraint applies for models with multiple pseudomoduli, in which case only one of the PM relates to SUSY breaking while the others can be responsible for the R -breaking. A few attempts have been made to build such kind of models, but none of them get the expected breaking through explicit calculations. In 4, we give a general proof for this surprising result.

Even for models with a leading order R -breaking, the gaugino mass is much smaller than the scalar masses. This is a problem since a gluino lighter than stops forces the stops to be heavy and causes a “little hierarchy” problem. It has been found in [274] that the anomalously small gaugino mass is closely related to the global properties of the vacua of the theory. If SUSY is broken in the lowest energy state of the vacua, then the

leading order gaugino mass vanishes. The reason for this is as follows. The leading order gaugino mass is proportional to the derivative with respect to the PM on the fermion masses. If the result is not zero, the fermion masses depend on the PM, and there is always a PM VEV corresponding to zero fermion masses. However, the fermion masses show up in the diagonal blocks of the scalar mass matrix. The vanishing diagonal blocks generate tachyons, and the SUSY breaking vacuum then is not a global minimum. If SUSY breaking does occur in the global minimum, then the fermion mass is independent of the PM, and the leading order gaugino mass vanishes.

One way to avoid the constraint is to have SUSY breaking in a meta-stable vacuum. Models like this usually require tuning and contain Landau poles as a result of stabilizing the vacuum. To build a phenomenologically preferred model, we propose a simple Intriligator, Seiberg and Shih (ISS) - type scenario [262] with a minimal flavor content. Expanding the theory around a meta-stable SUSY breaking vacuum and stabilizing it with a singlet sector, we obtain large gaugino masses without Landau poles. We discuss this in Chapter 5.

1.3.3 Dirac leptogenesis, WDM and composite neutrinos

Composite neutrinos are an interesting way to generate small neutrino masses. The basic idea is that there exists a hidden sector with strong dynamics at a scale Λ . Confinement in this sector leaves some chiral symmetries exact and produces massless composite fermions. If these fermions serve as RH neutrinos, their couplings to the active neutrinos go through effective couplings. Assuming the only interaction between the hidden and the SM sectors is through a heavy mediator at a mass scale M , the effective Yukawa coupling for the neutrinos carries a suppression $(\Lambda/M)^3$. We then only need $(\Lambda/M) < 10^{-4}$

to explain the hierarchically smaller neutrino masses.

How to produce the observed mixing angles within the framework is still an open question. No matter how the mixing angle is generated, the mechanism should put stringent constraints to the model. In fact, even before specifying a complete flavor structure, incorporating leptogenesis and WDM into neutrino models makes predictions that are experimentally constrained. Here we briefly introduce the ideas and leave the detailed discussion for Chapter 6 and 7.

As discussed in Sec. 1.2.2, leptogenesis is a plausible idea to generate matter–anti-matter asymmetry. In the most studied neutrino model, the see-saw mechanism, leptogenesis is realized by the decay of heavy Majorana neutrinos. A Majorana mass term breaks lepton number, and the CP violating decay of the Majorana neutrinos produces net lepton number, which is then transformed into the SM baryon number through sphaleron effects. However, leptogenesis does not necessarily come with lepton number violation. Even for pure Dirac neutrinos, if the scattering process separates the positive and negative lepton numbers into the SM and hidden sectors, the sphaleron relates only to the SM lepton number and can still produce the baryon number. The leptogenesis scenario that conserves lepton number is called Dirac leptogenesis.

In Chapter 6, we explore the possibilities of the standard or Dirac leptogenesis in the composite neutrino model. We first give a minimal UV completion of the model, and then identify the decay process that generates the asymmetry. A successful model needs to satisfy several constraints: the correct active neutrino masses, the right amount of baryon asymmetry, the out-of-equilibrium condition of the decay process, the separation of the lepton number between the two sectors, bounds on the light degrees of freedom around the big-bang nucleosynthesis (BBN), and the potential FCNC given by the mediators.

We give a model that satisfies all of these constraints while keeping the energy scale for the decay as low as 10 TeV. This low-energy leptogenesis avoids the gravitino problem, believed by some people to be a problem in the standard leptogenesis, by allowing a low reheating temperature.

Besides leptogenesis, neutrinos are also closely related to DM. Sterile neutrinos with masses at the keV scale are a popular WDM candidate. WDM refers to particles with free-streaming length comparable to the size of a region which can subsequently evolve into a dwarf galaxy. This leads to predictions that are very similar to cold dark matter (CDM) on large scales, including the cosmic microwave background (CMB), galaxy clustering, and large galaxy rotation curves. Unlike CDM, however, WDM predicts less small-scale density perturbations. This reduces the predicted abundance of dwarf galaxies and may lead to a lower density of DM in the central parts of large galaxies, which may be a better fit to observations.

In the composite neutrino framework, the compensators used to cancel anomalies in the hidden sector can serve as WDM particles. They can either be thermally produced or generated through oscillation from the active neutrinos. While the overproduced WDM is diluted by an out-of-equilibrium decay in the usual case, the required entropy dilution in this case can be generated by the confinement of the composite neutrino sector. We discuss the mechanism and various astrophysical bounds in Chapter 7.

1.3.4 Collider constraints on DM

At the end of this thesis, we give an example of how one may set model independent bounds on UV-theories using experimental results at an IR-scale. The theories we want

to constrain are DM-models with various DM-SM interactions, and the experiments we use are the mono-jet and mono-photon searches at Large Electron-Positron Collider (LEP) and Large Hadron Collider (LHC).

Compared to colliders, direct detection experiments are better designed for constraining DM interactions with electroweak scale DM masses. The idea of the experiments is simple — bury sensitive detectors underground and wait for DM particles to bump into them. However, there are several problems for these type of experiments. First, to extract the interaction strength from the raw data, one must make several astrophysical and experimental assumptions. Moreover, all current generation detectors lose sensitivity when DM particles are lighter than 10 GeV, which is the interesting region where the experiments DAMA, CoGeNT and CRESS claimed DM observations. Finally, the bounds become weak if the DM interaction is spin-dependent since the scattering is not coherent through the nucleons.

Colliders do a better job on all of the above issues. They produce DM particles directly, and there is no need to know the astrophysical properties of DM in the universe. The bounds are better for light DM particles since the lighter they are, the easier they are to produce. Also, there is no coherent scattering of DM particles in colliders and the spin-dependent interactions are not suppressed relative to spin-independent one. Thus, colliders provide valuable constraints which are complementary to direct detection results. For a model independent study, we assume that mediators that generate DM–SM interactions are heavy enough that the effective coupling description is valid. For example, if DM particles are Dirac fermions (χ), the vector coupling to quarks (q) can be written as

$$\frac{(\bar{\chi} \gamma^\mu \chi)(\bar{q} \gamma_\mu q)}{\Lambda^2}. \quad (1.3.1)$$

Collider experiments set a lower bound on Λ based on the absence of DM signals in the final results. Since the same coupling is responsible for signals in direct detection, we can calculate an upper bound on the scattering cross section and compare it to the direct detection results. In this thesis, we use the mono-jet and mono-photon searches at LEP and LHC for this project. As we will see, the current constraints can already exclude some of the DM parameter space. Besides direct detection, the collider bounds can also be used to calculate bounds for the annihilation cross section of DM particles. In addition, utilizing current Higgs searches, we can also set interesting bounds for scenarios where DM couple to the SM particles through a Higgs portal. We discuss this in Chapter 9.

CHAPTER 2

LEPTON FLAVOR VIOLATION IN RS MODEL

Based on the 2010 article “Warped Penguins”, written in collaboration with Csaba Csáki, Yuval Grossman, Philip Tanedo and published in Phys.Rev. D83 (2011) 073002.

2.1 Introduction

The Randall-Sundrum (RS) set up for a warped extra dimension is a novel framework for models of electroweak symmetry breaking [330]. When fermion and gauge fields are allowed to propagate in the bulk, these models can also explain the fermion mass spectrum through the split fermion proposal [52, 236, 221]. In these anarchic flavor models each element of the Yukawa matrices can take natural $\mathcal{O}(1)$ values because the hierarchy of the fermion masses is generated by the exponential localization of the fermion wave functions away from the Higgs field [26, 28].

The same small wavefunction overlap that yields the fermion mass spectrum also gives hierarchical mixing angles [26, 250, 270, 307] and suppresses tree-level flavor-changing neutral currents (FCNCs) by the RS-GIM mechanism [26, 28]. This built-in protection, however, may not always be sufficient to completely protect against the most dangerous types of experimental FCNC constraints. In the quark sector, for example, the exchange of Kaluza-Klein (KK) gluons induces left-right operators that contribute to CP violation in kaons and result in generic bounds of $\mathcal{O}(10 - 20 \text{ TeV})$ for the KK gluon mass [150, 93, 124, 113, 31, 95]. To reduce this bound one must either introduce additional structure (such as horizontal symmetries [334, 152] or flavor equationment [203, 158]) or alternately gain several $\mathcal{O}(1)$ factors [18] by promoting the Higgs to a bulk field, inducing loop-level QCD matching, etc. This latter approach is limited by tension with loop-induced flavor-violating effects [214].

The leptonic sector of the anarchic model is similarly bounded by FCNCs. Agashe, Blechman and Petriello recently studied the two dominant constraints in the lepton sector: the loop-induced $\mu \rightarrow e\gamma$ photon penguin from Higgs exchange and the tree-level contribution to $\mu \rightarrow 3e$ and $\mu \rightarrow e$ conversion from the exchange of the Z boson KK

tower [20]. These processes set complementary bounds due to their complementary dependence on the overall magnitude of the anarchic Yukawa coupling, Y_* . While $\mu \rightarrow e\gamma$ is proportional to Y_*^3 due to two Yukawa couplings and a chirality-flipping mass insertion, the dominant contribution to $\mu \rightarrow 3e$ and $\mu \rightarrow e$ conversion comes from the nonuniversality of the Z boson near the IR brane. In order to maintain the observed mass spectrum, increasing the Yukawa coupling pushes the bulk fermion profiles away from the IR brane and hence away from the flavor-changing part of the Z . This reduces the effective four-dimensional (4D) FCNC coupling so that these processes are proportional to Y_*^{-1} . For a given KK gauge boson mass, these processes then set an upper and lower bound on the Yukawa coupling which are usually mutually exclusive.

A key feature of the lepton sector is that one expects large mixing angles rather than the hierarchical angles in the Cabibbo-Kobayashi-Maskawa (CKM) matrix. One way to obtain this is by using a global flavor symmetry for the lepton sector [148] (see also [321, 129]). Including these additional global symmetries can relax the tension between the two bounds. For example, imposing an A_4 symmetry on the leptonic sector completely removes the tree-level constraints [148]. Another interesting possibility for obtaining large lepton mixing angles is to have the wavefunction overlap for the neutrino Yukawa peak near the UV brane [25]. For generic models with anarchic fermions, however, [20] found that the tension between $\mu \rightarrow e\gamma$ and tree-level processes ($\mu \rightarrow 3e$ and $\mu \rightarrow e$ conversion) push the gauge boson KK scale to be on the order of 5–10 TeV.

The main goal of this paper is to present a detailed one-loop calculation of the $\mu \rightarrow e\gamma$ penguin in the RS model with a brane-localized Higgs and to show that this amplitude is finite.

To perform the calculation and obtain a numerical result we choose to work in the

five-dimensional (5D) mixed position/momentum space formalism [325, 121]. This setup is natural for calculating processes on an interval with brane-localized terms, as shown in Fig. 2.1. In particular, there are no sums over KK modes, the chiral boundary conditions are fully incorporated in the 5D propagators, and the UV behavior is clear upon Wick rotation where the basis of Bessel functions becomes exponentials in the 4D loop momentum. The physical result is, of course, independent of whether the calculation was done in 5D or in 4D via a KK decomposition. We show explicit one-loop finiteness in the KK decomposed theory and remark upon the importance of taking into account the correct number of KK modes relative to the momentum cutoff when calculating finite 5D loops.

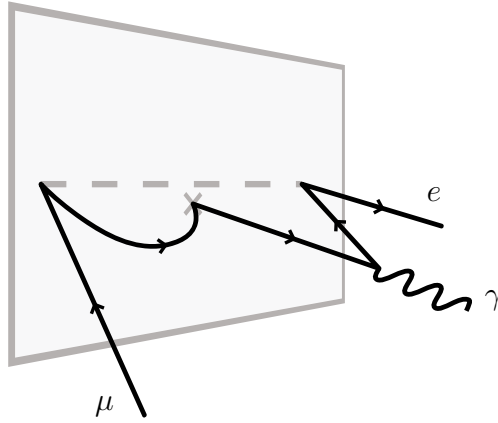


Figure 2.1: A contribution to $\mu \rightarrow e\gamma$ from a brane-localized Higgs. The dashed line represents the Higgs while the cross represents a Yukawa coupling with a Higgs vev.

The paper is organized as follows: We begin in Sections 2.2 and 2.3 by reviewing the flavor structure of anarchic Randall-Sundrum models and summarizing tree-level constraints on the anarchic Yukawa scale. We then proceed the analysis of $\mu \rightarrow e\gamma$. The dipole operators involved in this process are discussed in Section 2.4 and the relevant coefficient is calculated using 5D methods in Section 2.5. In Section 2.6 we discuss the origin of finiteness in these operators in both the 5D and 4D frameworks. We remark on subtleties in counting the superficial degree of divergence, the matching of the number of KK modes with any effective 4D momentum cutoff, and remark on the expected

two-loop degree of divergence. We conclude with an outlook for further directions in Section 8.7. In Appendix A.1 we highlight the matching of local 4D effective operators to *nonlocal* 5D amplitudes. Next in Appendices A.2 and A.3 we give estimates for the size of each diagram and analytic expressions for the (next-to)leading $\mu \rightarrow e\gamma$ diagrams. Appendices A.4, A.5, and A.6 focus on the formalism of quantum field theory in mixed position/momentum space, respectively focusing on a discussion of power counting, a summary of RS Feynman rules, and details on the derivation of the bulk fermion propagators. Finally, in Appendix A.7 we explicitly demonstrate a subtle cancellation in the single-mass insertion neutral Higgs diagram that is referenced in Section 2.6.

2.2 Review of anarchic Randall-Sundrum models

We now summarize the main results for anarchic RS models. For a review see, e.g. Refs [157]. We consider a 5D warped interval $z \in [R, R']$ with a UV brane at $z = R$ and an IR brane at $z = R'$. The metric is

$$ds^2 = \left(\frac{R}{z}\right)^2 (dx_\mu dx_\nu \eta^{\mu\nu} - dz^2), \quad (2.2.1)$$

where we see that R is also the AdS curvature scale so that $R/R' \sim \text{TeV}/M_{\text{Pl}}$. These conformal coordinates are natural in the context of the AdS/CFT correspondence but differ from the classical RS conventions $z = R \exp(ky)$ and $k = 1/R$. The relevant scales have magnitudes $R^{-1} \sim M_{\text{Pl}}$ and $R'^{-1} \sim \text{TeV}$. Fermions are bulk Dirac fields which propagate in the full 5D space and can be decomposed into left- and right-handed Weyl spinors χ and $\bar{\psi}$ via

$$\Psi(x, z) = \begin{pmatrix} \chi(x, z) \\ \bar{\psi}(x, z) \end{pmatrix}. \quad (2.2.2)$$

In order to obtain a chiral zero mode spectrum, these fields are subject to the chiral (orbifold) boundary conditions

$$\psi_L(x^\mu, R) = \psi_L(x^\mu, R') = 0 \quad \chi_R(x^\mu, R) = \chi_R(x^\mu, R') = 0, \quad (2.2.3)$$

where the subscripts L and R denote the $SU(2)_L$ doublet (L) and singlet (R) representations, i.e. the chirality of the zero mode. The fermion bulk masses are given by c/R where c is a dimensionless parameter controlling the localization of the normalized 5D zero mode profiles,

$$\chi_c^{(0)}(x, z) = \frac{1}{\sqrt{R'}} \left(\frac{z}{R}\right)^2 \left(\frac{z}{R'}\right)^{-c} f_c \chi_c^{(0)}(x) \quad \text{and} \quad \psi_c^{(0)}(x, z) = \chi_{-c}^{(0)}(x, z) \quad (2.2.4)$$

where we have defined the usual RS flavor function

$$f_c = \sqrt{\frac{1-2c}{1-(R/R')^{1-2c}}}. \quad (2.2.5)$$

We assume that the Higgs is localized on the IR brane. The Yukawa coupling is

$$S_{\text{Yuk}} = \int d^4x \left(\frac{R}{R'}\right)^4 \bar{E}_i (R Y_{ij}) L_j \cdot H + \text{h.c.} \quad (2.2.6)$$

where Y_{ij} is a dimensionless 3×3 matrix such that $(Y_5)_{ij} = R Y_{ij}$ is the dimensionful parameter appearing in the 5D Lagrangian. In the anarchic approach Y is assumed to be a random matrix with average elements of order Y_* . After including all warp factors and rescaling to canonical fields the effective 4D Yukawa and mass matrices for the zero modes are

$$y_{ij}^{\text{SM}} = f_{c_{L_i}} Y_{ij} f_{-c_{R_j}} \quad m_{ij} = \frac{v}{\sqrt{2}} y_{ij}^{\text{SM}}, \quad (2.2.7)$$

so that the fermion mass hierarchy is set by the $f_1 \ll f_2 \ll f_3$ structure for both left- and right-handed zero modes. In other words, the choice of c for each fermion family introduces additional flavor structure into the theory which generates the zero mode spectrum while allowing the fundamental Yukawa parameters to be anarchic.

In the Standard Model the diagonalization of the fermion masses transmits the flavor structure of the Yukawa sector to the kinetic terms via the CKM matrix where it is manifested in the flavor-changing charged current through the W^\pm boson. We shall use the analogous mass basis in Section 2.3 for our calculation of the Yukawa constraints from $\mu \rightarrow 3e$ and $\mu \rightarrow e$ conversion operators. The key point is that in the gauge basis the interaction of the neutral gauge bosons is flavor diagonal but not flavor universal. The different fermion wave functions cause the overlap integrals to depend on the bulk mass parameters. Once we rotate into the mass eigenbasis we obtain flavor changing couplings for the neutral KK gauge bosons.

In the lepton sector this does not occur for the zero mode photon since its wave-function remains flat after electroweak symmetry breaking and hence $\mu \rightarrow e\gamma$ remains a loop-level process. Thus for the primary analysis of this paper we choose a basis where the 5D fields are diagonal with respect to the bulk masses while the Yukawas are completely general. In this basis all of the relevant flavor-changing effects occur due to the Yukawa structure of the theory with no contributions from W loops. In the Standard Model, this corresponds to the basis before diagonalizing the fermion masses so that all flavor-changing effects occur through off-diagonal elements in the Yukawa matrix manifested as mass insertions or Higgs interactions. This basis is particularly helpful in the 5D mixed position/momentum space framework since the Higgs is attached to the IR brane, which simplifies loop integrals.

2.3 Tree-level constraints from $\mu \rightarrow 3e$ and $\mu \rightarrow e$ conversion

For a fixed KK gauge boson mass M_{KK} , limits on $\mu \rightarrow 3e$ and $\mu \rightarrow e$ conversion in nuclei provide the strongest *lower* bounds on the anarchic Yukawa scale Y_* . These tree-level

processes are parameterized by Fermi operators generated by Z and Z' exchange, where the prime indicates the KK mode in the mass basis. The effective Lagrangian for these lepton flavor-violating Fermi operators are traditionally parameterized as [127]

$$\begin{aligned} \mathcal{L} = & \frac{4G_F}{\sqrt{2}} [g_3(\bar{e}_R\gamma^\mu\mu_R)(\bar{e}_R\gamma_\mu e_R) + g_4(\bar{e}_L\gamma^\mu\mu_L)(\bar{e}_L\gamma^\mu e_L) + g_5(\bar{e}_R\gamma^\mu\mu_R)(\bar{e}_L\gamma_\mu e_L) \\ & + g_6(\bar{e}_L\gamma^\mu\mu_L)(\bar{e}_R\gamma_\mu e_R)] + \frac{G_F}{\sqrt{2}} \bar{e}\gamma^\mu(v - a\gamma_5)\mu \sum_q \bar{q}\gamma_\mu(v^q - a^q\gamma_5)q, \end{aligned} \quad (2.3.8)$$

where we have only introduced the terms that are non-vanishing in the RS set up, and use the normalization where $v^q = T_3^q - 2Q^q \sin^2 \theta$. The axial coupling to quarks, a^q , vanishes in the dominant contribution coming from coherent scattering off the nucleus. The $g_{3,4,5,6}$ are responsible for $\mu \rightarrow 3e$ decay, while the v, a are responsible for $\mu \rightarrow e$ conversion in nuclei. The rates are given by (with the conversion rate normalized to the muon capture rate):

$$\text{Br}(\mu \rightarrow 3e) = 2(g_3^2 + g_4^2) + g_5^2 + g_6^2, \quad (2.3.9)$$

$$\text{Br}(\mu \rightarrow e) = \frac{p_e E_e G_F^2 F_p^2 m_\mu^3 \alpha^3 Z_{eff}^4}{\pi^2 Z \Gamma_{\text{capt}}} Q_N^2 (v^2 + a^2), \quad (2.3.10)$$

where the parameters for the conversion depend on the nucleus and are calculated in the Feinberg-Weinberg approximation [199] and we write the charge for a nucleus with atomic number Z and neutron number N as

$$Q_N = v^u(2Z + N) + v^d(2N + Z). \quad (2.3.11)$$

. The most sensitive experimental constraint comes from muon conversion in $^{48}_{22}\text{Ti}$, for which

$$E_e \sim p_e \sim m_\mu, \quad F_p \sim 0.55, \quad Z_{\text{eff}} \sim 17.61, \quad \Gamma_{\text{capt}} \sim 2.6 \cdot \frac{10^6}{\text{s}} \quad (2.3.12)$$

We now consider these constraints for a minimal model (where $f_{e_L} = f_{e_R}$, $f_{\mu_L} = f_{\mu_R}$) and for a model with custodial protection.

2.3.1 Minimal RS model

In order to calculate the coefficients in the effective Lagrangian (2.3.8), we need to estimate the flavor-violating couplings of the neutral gauge bosons in the theory. In the basis of physical KK states all lepton flavor-violating couplings are the consequence of the non-uniformity of the gauge boson wave functions. Let us first consider the effect of the ordinary Z boson, whose wave function is approximately (we use the approximation (2.19) of [149] with a prefactor for canonical normalization)

$$h^{(0)}(z) = \frac{1}{\sqrt{R \log \frac{R'}{R}}} \left[1 + \frac{M_Z^2}{4} z^2 \left(1 - 2 \log \frac{z}{R} \right) \right]. \quad (2.3.13)$$

The coupling of the Z to fermions can be calculated by performing the overlap integral with the fermion profiles in (3.2.4) and is found to be

$$g^{Zff} = g_{\text{SM}}^Z \left(1 + \frac{(M_Z R')^2 \log \frac{R'}{R}}{2(3 - 2c)} f_c^2 \right). \quad (2.3.14)$$

After rotating the fields to the mass eigenbasis we find that the off-diagonal coupling of the Z boson to charged leptons is given by the nonuniversal term and is approximately

$$g_{L,R}^{Ze\mu} \approx (g_{\text{SM}}^Z)^{L,R} \Delta_{e\mu}^{(0)} \equiv (g_{\text{SM}}^Z)^{L,R} \frac{(M_Z R')^2 \log \frac{R'}{R}}{2(3 - 2c)} f_{eL,R} f_{\mu L,R}. \quad (2.3.15)$$

Using these couplings one can estimate the coefficients of the 4-Fermi operators in (2.3.8),

$$g_{3,4} = 2g_{L,R}^2 \Delta_{e\mu}^{(0)} \quad g_{5,6} = 2g_L g_R \Delta_{e\mu}^{(0)} \quad (v \pm a) = 2g_{L,R} \Delta_{e\mu}^{(0)} \quad (2.3.16)$$

where the $g_{L,R}$ are proportional to the left- and right-handed charged lepton couplings to the Z in the Standard Model, $g_L = -\frac{1}{2} + s_W^2$ and $g_R = s_W^2$. The Z' exchange contribution to $\mu \rightarrow 3e$ ($\mu \rightarrow e$) is a 15% (5%) correction and the γ' exchange diagram is an additional 5% (1%) correction; we shall ignore both here. We make the simplifying assumption that

$f_{e_L} = f_{e_R}$ and $f_{\mu_L} = f_{\mu_R}$ and then express these in terms of the Standard Model Yukawa couplings as $f = \sqrt{\lambda/Y_*}$. The expressions for the lepton flavor-violating processes are then

$$\text{Br}(\mu \rightarrow 3e) = 10^{-13} \left(\frac{3 \text{ TeV}}{M_{\text{KK}}} \right)^4 \left(\frac{2}{Y_*} \right)^2 \quad (2.3.17)$$

$$\text{Br}(\mu \rightarrow e)_{\text{Ti}} = 2 \cdot 10^{-12} \left(\frac{3 \text{ TeV}}{M_{\text{KK}}} \right)^4 \left(\frac{2}{Y_*} \right)^2. \quad (2.3.18)$$

The current experimental bounds are $\text{Br}(\mu \rightarrow 3e) < 10^{-12}$ [78] and $\text{Br}(\mu \rightarrow e)_{\text{Ti}} < 6.1 \cdot 10^{-13}$ [354] so that $\mu \rightarrow e$ conversion provides the most stringent constraint,

$$\left(\frac{3 \text{ TeV}}{M_{\text{KK}}} \right)^2 \left(\frac{2}{Y_*} \right) < 0.5. \quad (2.3.19)$$

For a 3 TeV Z' , the anarchic Yukawa scale must satisfy $Y_* \gtrsim 3.7$, which agrees with [20].

2.3.2 Custodially protected model

Since the bound in (2.3.19) is model dependent, one might consider weakening this constraint by having the leptons transform under the custodial group

$$\text{SU}(2)_L \times \text{SU}(2)_R \times \text{U}(1)_X \times \text{P}_{LR}, \quad (2.3.20)$$

where P_{LR} is a discrete $L \leftrightarrow R$ exchange symmetry. Such a custodial protection was introduced in [22] to eliminate large corrections to the $Zb\bar{b}$ vertex in the quark sector. It was later found that this symmetry also eliminates some of the FCNCs in the Z sector [31] so that one might also expect it to alleviate the lepton flavor violation bounds. We shall now estimate the extent to which custodial symmetry can relax the bound on Y_* . Further discussion including neutrino mixing can be found in [17].

To custodially protect the charged leptons one chooses the $(L, R)_X$ representation $(2, 2)_0$ for the left-handed leptons, $(3, 1)_0 \oplus (1, 3)_0$ for the charged right-handed leptons, and $(1, 1)_0$ for the right-handed neutrinos. There are two neutral zero mode gauge bosons, the Standard Model Z and γ , and three neutral KK excitations, γ', Z' and Z_H , where the latter two are linear combinations of the Z and Z_X boson modes. The coupling of the left handed leptons to the ordinary Z and the Z' are protected since those couplings are exactly flavor universal in the limit where P_{LR} is exact. The breaking of P_{LR} on the UV brane leads to small residual contributions which we neglect. The remaining flavor-violating couplings for the left-handed leptons come from the exchange of Z_H and the γ' , while the right-handed leptons are unprotected.

Since $(v - a)$ couples to right-handed leptons its coupling is unprotected and is the same as in (2.3.16). For $(v + a)$, on the other hand, the leading-order effect comes from the $Z^{(1)}$ component of the Z_H , whose composition in terms of gauge KK states is [31]

$$Z_H = \cos \xi Z^{(1)} + \sin \xi Z_X^{(1)} + \beta Z^{(0)}, \quad (2.3.21)$$

where $Z^{(0)}$ is the flat zero mode Z -boson which does not contribute to FCNCs, $\cos \xi \approx \sqrt{\frac{1}{2} - s_W^2}/c_W$, and β is a small correction of order $\mathcal{O}(v^2/M_{\text{KK}}^2)$. The flavor-changing coupling of the KK gauge bosons is analogous to that of KK gluons in [150],

$$g_{L,R}^{Z^{(1)}e\mu} \approx (g_{\text{SM}}^Z)^{L,R} \Delta_{e\mu}^{L,R(1)} \equiv (g_{\text{SM}}^Z)^{L,R} \sqrt{\log \frac{R'}{R}} \gamma_c f_{e_{L,R}} f_{\mu_{L,R}}, \quad (2.3.22)$$

where

$$\gamma_c = \frac{\sqrt{2}}{J_1(x_1)} \int_0^1 dx x^{1-2c} J_1(x_1 x) \approx \frac{\sqrt{2}}{J_1(x_1)} \frac{0.7x_1}{2(3-2c)} \quad (2.3.23)$$

and $x_1 = M_{\text{KK}} R'$ is the first zero of $J_0(x)$. The analogous $\gamma^{(1)}$ coupling is given by $g_{\text{SM}}^Z \rightarrow e$. Taking into account the Z_H and $\gamma^{(1)}$, the $(v + a)$ effective coupling to left-handed leptons is

$$(v + a) = 2g_L g_{\text{KK}} \frac{M_Z^2}{M_{\text{KK}}^2} \left(\cos^2 \xi + \frac{Q_N^{Z_X}}{Q_N} \cos \xi \sin \xi \right) \Delta_{e\mu}^{L(1)} + 2s_W^2 c_W^2 g_{\text{KK}} \frac{M_Z^2}{M_{\text{KK}}^2} \frac{Q_N^\gamma}{Q_N} \Delta_{e\mu}^{L(1)} \quad (2.3.24)$$

The $\cos \xi \sin \xi$ term in the parenthesis represents the $Z_X^{(1)}$ component of the Z_H which couples to the quarks in the nucleus via

$$Q_N^{Z_X} = -\frac{1}{\sqrt{2}} c_W \cos \xi (5Z + 7N) - \frac{2\sqrt{2}}{\cos \xi} s_W \frac{g'}{g} (Z + N), \quad g_{\text{KK}} = \frac{1}{\sqrt{\log R'/R}} \quad (2.3.25)$$

The g_{KK} factor gives the universal (flavor-conserving) coupling of KK gauge bosons to zero mode fermions. Q_N^γ is the electric charge of the nucleus normalized according to (2.3.10), $Q_N^\gamma = 2Z$.

Minimizing over the flavor factors $f_{e_{L,R}}$ and $f_{\mu_{L,R}}$ subject to the zero mode fermion mass spectrum and comparing to the experimental bound listed above (2.3.19), we find that the conversion rate must satisfy

$$\left(\frac{3 \text{ TeV}}{M_{\text{KK}}} \right)^2 \left(\frac{2}{Y_*} \right) < 1.6. \quad (2.3.26)$$

lowering the bound to $Y_* \gtrsim 1$ for a 3 TeV KK gauge boson scale.

2.4 Operator analysis of $\mu \rightarrow e\gamma$

We work in 't Hooft–Feynman gauge ($\xi = 1$) and a flavor basis where all bulk masses c_i are diagonal. The 5D amplitude for $\mu \rightarrow e\gamma$ takes the form

$$CH \cdot \bar{L}_i \sigma^{MN} E_j F_{MN}, \quad (2.4.27)$$

where it is understood that the 5D fields should be replaced by the appropriate external states which each carry an independent z position in the mixed position/momentum space formalism. These positions must be separately integrated over when matching to an effective 4D operator so that (2.4.27) can be thought of as a dimension-8 5D scattering amplitude whose prefactor C is a function of the external state positions, as explained in

Appendix A.1. When calculating this amplitude in the mixed position/momentum space formalism, the physical external state fields have definite KK number, which we take to be zero modes. The external field profiles and internal propagators depend on 4D momenta and z -positions so that vertex z -positions are integrated from $z = R$ to $z = R'$ while loop momenta are integrated as usual.

After plugging in the wave functions for the fermion and photon zero modes, including all warp factors, matching the gauge coupling, and expanding in Higgs-induced mass insertions, the leading order 4D operator and coefficients for $\mu \rightarrow e\gamma$ are

$$R'^2 \frac{e}{16\pi^2} \frac{v}{\sqrt{2}} f_{L_i} \left(a_{k\ell} Y_{ik} Y_{k\ell}^\dagger Y_{\ell j} + b_{ij} Y_{ij} \right) f_{-E_j} \bar{L}_i^{(0)} \sigma^{\mu\nu} E_j^{(0)} F_{\mu\nu}^{(0)} + \text{h.c.} \quad (2.4.28)$$

The term proportional to three Yukawa matrices comes from the diagrams shown in Figs. 2.2 and 2.3, while the single-Yukawa term comes from those in Fig. 2.4. In the limit where the bulk masses are universal, we may treat the Yukawas as spurions of the $U(3)^3$ lepton flavor symmetry and note that these are the products of Yukawas required for a chirality-flipping, flavor-changing operator.

In anarchic flavor models, however, the bulk masses for each fermion species is independent and introduce an additional flavor structure into the theory so that the $U(3)^3$ lepton flavor symmetry is not restored even in the limit $Y \rightarrow 0$. The indices on the dimensionless $a_{k\ell}$ and b_{ij} coefficients encode this flavor structure as carried by the internal fermions of each diagram. Because the lepton hierarchy does not require very different bulk masses, both $a_{k\ell}$ and b_{ij} are nearly universal.

Next note that the zero-mode mass matrix (3.2.7) introduces a preferred direction in flavor space which defines the mass basis. In fact, up to the non-universality of b_{ij} , the single-Yukawa term in (2.4.28) is proportional to—or equationed—with (3.2.7). Hence upon rotation to the mass basis, the off-diagonal elements of this term are typically much

smaller than its value in the flavor basis [21, 65] and would be identically zero if the bulk masses were universal. Given a set of bulk mass parameters, the extent to which a specific off-diagonal element of the b_{ij} term is suppressed depends on the particular structure of the anarchic 5D Yukawa matrix. This is a novel feature since the structure of the underlying anarchic Yukawa is usually washed out in observables by the hierarchies in the f_c flavor functions.

On the other hand, a product of anarchic matrices typically indicates a very different direction in flavor space from the original matrix so that the a_{ij} term is not equationed and we may simplify the product to

$$\sum_{k,\ell} a_{k\ell} Y_{ik} Y_{k\ell}^\dagger Y_{\ell j} = a Y_*^3 \quad (2.4.29)$$

for each i and j . Here we have *defined* the prefactor a ; different definitions can include an overall $\mathcal{O}(1)$ factor from the sum over anarchic matrix elements. We have used the anarchic limit and the assumption that neither $a_{k\ell}$ nor b_{ij} vary greatly over realistic bulk mass values. This assumption is justified in Section 2.5 where we explicitly calculate these coefficients to leading order. Further, we have assumed that the scales of the anarchic electron and neutrino Yukawa matrices are the same so that $(Y_E)_{ij} \sim (Y_N)_{ij} \sim Y_*$.

To determine the physical $\mu \rightarrow e\gamma$ amplitude from this expression we must go to the standard 4D mass eigenbasis by performing a bi-unitary transformation to diagonalize the Standard Model Yukawa,

$$\lambda^{\text{SM}} = U_L \lambda^{(\text{diag})} U_R^\dagger, \quad (2.4.30)$$

where the magnitudes of the elements of the unitary matrices $U_{L,R}$ are set, in the anarchic scenario, by the hierarchies in the flavor constants

$$(U_L)_{ij} \sim \frac{f_{L_i}}{f_{L_j}} \text{ for } f_{L_i} < f_{L_j}. \quad (2.4.31)$$

For future simplicity, let us define the relevant part of the $b_{ij}Y_{ij}$ matrix after this rotation,

$$bY_* = \sum_{k,\ell} (U_L)_{2k} b_{k\ell} Y_{k\ell} (U_R^\dagger)_{\ell 1}. \quad (2.4.32)$$

The traditional parameterization for the $\mu \rightarrow e\gamma$ amplitude is written as [20]

$$\frac{-iC_{L,R}}{2m_\mu} \bar{u}_{L,R} \sigma^{\mu\nu} u_{R,L} F_{\mu\nu}, \quad (2.4.33)$$

where $u_{L,R}$ are the left- and right-handed Dirac spinors for the leptons. Comparing (2.4.28) with (8.6.11) and using the magnitudes of the off-diagonal terms in the U_L rotation matrix in (2.4.31), we find that in the mass eigenbasis the coefficients are given by

$$C_L = (aY_*^3 + bY_*) R'^2 \frac{e}{16\pi^2} \frac{v}{\sqrt{2}} 2m_\mu f_{L_2} f_{-E_1}, \quad (2.4.34)$$

$$C_R = (aY_*^3 + bY_*) R'^2 \frac{e}{16\pi^2} \frac{v}{\sqrt{2}} 2m_\mu f_{L_1} f_{-E_2}. \quad (2.4.35)$$

The $\mu \rightarrow e\gamma$ branching fraction and its experimental bound are given by

$$\text{Br}(\mu \rightarrow e\gamma)_{\text{thy}} = \frac{12\pi^2}{(G_F m_\mu^2)^2} (|C_L|^2 + |C_R|^2), \quad (2.4.36)$$

$$\text{Br}(\mu \rightarrow e\gamma)_{\text{exp}} < 1.2 \cdot 10^{-11}. \quad (2.4.37)$$

While the generic expression for $\text{Br}(\mu \rightarrow e\gamma)$ depends on the individual wave functions $f_{L,-E}$, the product $C_L C_R$ is fixed by the physical lepton masses and the relation $C_L^2 + C_R^2 \geq 2C_L C_R$ so that one can put a lower bound on the branching ratio

$$\text{Br}(\mu \rightarrow e\gamma) \geq 6 |aY_*^2 + b|^2 \frac{\alpha}{4\pi} \left(\frac{R'^2}{G_F} \right)^2 \frac{m_e}{m_\mu} \approx 5.1 \cdot 10^{-8} |aY_*^2 + b|^2 \left(\frac{3 \text{ TeV}}{M_{\text{KK}}} \right)^4. \quad (2.4.38)$$

Thus for a 3 TeV KK gauge boson scale we obtain an upper bound on Y_*

$$|aY_*^2 + b| \left(\frac{3 \text{ TeV}}{M_{\text{KK}}} \right)^2 \leq 0.015. \quad (2.4.39)$$

Note that the b coefficient is independent of Y_* so that sufficiently large b can rule out the assumption that the 5D Yukawa matrix can be completely anarchic—i.e. with no assumed

underlying flavor structure—at a given KK scale no matter how small one picks Y_* . This is a new type of constraint on anarchic flavor models in a warped extra dimension. Conversely, if b is of the same order as a and has the opposite sign, then the bounds on the anarchic scale Y_* are alleviated. We will show below that b is typically suppressed relative to a but can, in principle, take a range of values between $b = -0.5$ and 0.5 . For simplicity we may use the case $b = 0$ as a representative and plausible example, in which case the bound on the anarchic Yukawa scale is

$$Y_* \leq 0.12 |a|^{-\frac{1}{2}}. \quad (2.4.40)$$

In Section 2.5.4 we quantify the extent to which the b term may affect this bound. Combined with the lower bounds on Y_* from tree-level processes in Section 2.3, this bound typically introduces a tension in the preferred value of Y_* depending on the value of a . In other words, it can force one to either increase the KK scale or introduce additional symmetry structure into the 5D Yukawa matrices which can reduce a in (2.4.29) or force a cancellation in (2.4.39).

2.5 Calculation of $\mu \rightarrow e\gamma$ in a warped extra dimension

In principle, there are a large number of diagrams contributing to the a and b coefficients even when only considering the leading terms in a mass insertion expansion. These are depicted in Figs. 2.2–2.4. Fortunately, many of these diagrams are naturally suppressed and the dominant contribution to each coefficient is given by the two diagrams shown in Fig. 2.5. Analytic expressions for the leading and next-to-leading diagrams are given in Appendix A.3 along with an estimate of the size of each contribution.

The flavor structure of the diagrams contributing to the b coefficient is equationed with

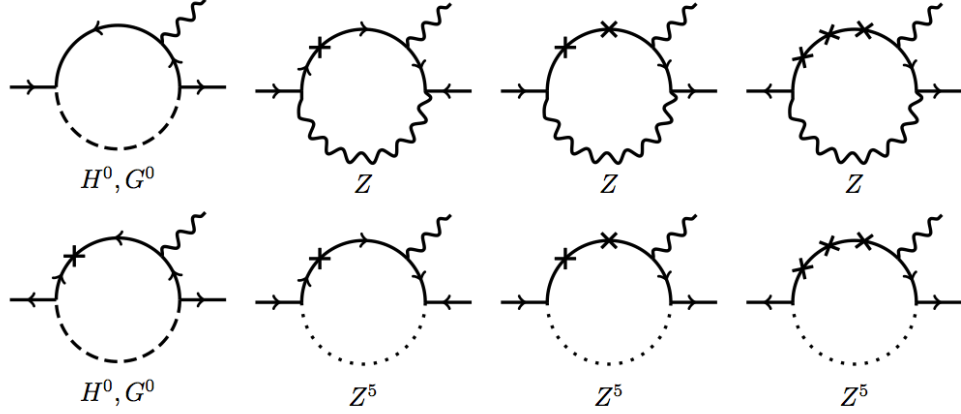


Figure 2.2: Neutral boson diagrams contributing to the a coefficient defined in (2.4.29). Fermion arrows denote the zero mode chirality, i.e. the $SU(2)$ representation. External legs whose arrows do not point outward have an implicit external mass insertion. Dotted lines represent the fifth component of a bulk gauge field. Analytic forms for these diagrams are given in Appendix A.3.

the fermion zero-mode mass matrix [28, 20, 18]. The rotation of the external states to mass eigenstates thus suppresses these diagrams up to the bulk mass (c) dependence of internal propagators which point in a different direction in flavor space and are not equationed. Since KK modes do not carry very strong bulk mass dependence, the diagrams which typically give the largest contribution after equationment are those which permit zero mode fermions in the loop. We provide a precise definition of the term “typically” in Section 2.5.2.

The Ward identity requires that the physical amplitude for a muon of momentum p to decay into a photon of polarization ϵ and an electron of momentum p' takes the form

$$\mathcal{M} = \epsilon_\mu \mathcal{M}^\mu \sim \epsilon_\mu \bar{u}_{p'} [(p + p')^\mu - (m_\mu + m_e)\gamma^\mu] u_p. \quad (2.5.41)$$

This is the combination of masses and momenta that gives the correct chirality-flipping tensor amplitude in (8.6.11). This simplifies the calculation of this process since one only has to identify the coefficient of the $\bar{u}_{p'}(p + p')^\mu u$ term to determine the entire amplitude; all other terms are redundant by gauge invariance [287]. The general strategy is to use

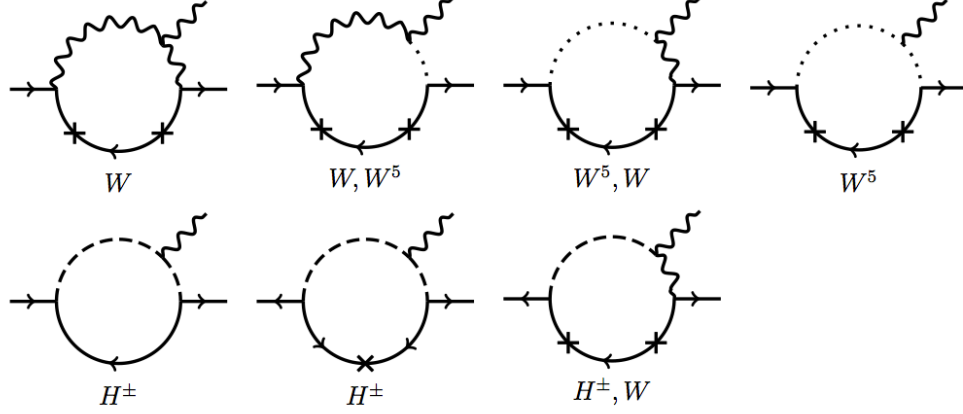


Figure 2.3: Charged boson diagrams contributing to the a coefficient following the conventions in Fig. 2.2. Analytic forms for these diagrams are given in Appendix A.3.

the Clifford algebra and the equations of motion for the external spinors to determine this coefficient. This allows us to directly write the finite physical contribution to the amplitude without worrying about the regularization of potentially divergent terms which are not gauge invariant. In Section 2.6.1 we will further use this observation to explain the finiteness of this amplitude in 5D.

In addition to the diagrams in Figs. 2.2–2.4, there are higher-order diagrams with an even number of additional mass insertions and brane-to-brane propagators. Following the Feynman rules in Appendix A.5, each higher-order pair of mass insertions is suppressed by an additional factor of

$$\left(\frac{\not{k}}{k} \frac{R'^4}{R^4} \cdot (-i) \frac{R^3}{R'^3} R Y_* \frac{v}{\sqrt{2}} \right)^2 \sim \frac{1}{2} (Y_* R' v)^2 \sim \mathcal{O}(10^{-2}), \quad (2.5.42)$$

since we assume anarchic Yukawa matrices, $Y_* \sim 2$. We are thus justified in considering only the leading-order terms in the mass insertion approximation.

We now present the leading contributions to the a and b coefficients. Other diagrams give a correction on the order of 10% of these results. We provide explicit formulas and numerical estimates for the next-to-leading order corrections in Appendix A.3.

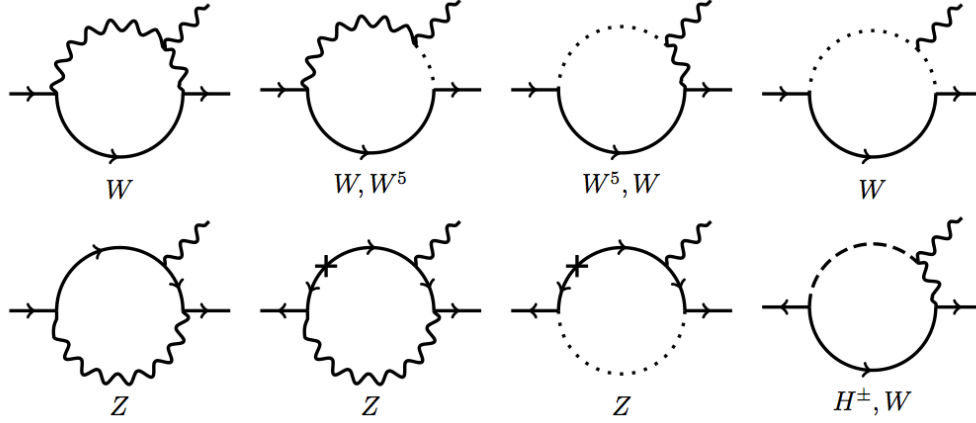


Figure 2.4: Diagrams contributing to the b coefficient following the conventions in Fig. 2.2. Not shown: zero mass-insertion Z^5 diagram. Analytic forms for these diagrams are given in Appendix A.3.

2.5.1 Calculation of a

We now calculate the leading-order contribution to the amplitude to determine the a coefficient in (2.4.29). As discussed above, it is sufficient to compute the coefficient of the $(p + p')^\mu$ term in the amplitude. The dominant contribution to a comes from the W boson diagrams in Fig. 2.5a. This is because diagrams with 5D gauge bosons are enhanced relative to the Higgs diagrams by a factor of $\ln R'/R \sim 37$. Further, the W diagrams are enhanced over the Z diagrams due to the size of their respective Standard Model couplings to leptons. Additional suppression factors can arise from the structure of each diagram and are discussed in Appendix A.2. Explicit calculation confirms that the W loop with two internal mass insertions indeed gives the leading contribution to a .

The charged and neutral boson diagrams have independent flavor structures, $(Y_E Y_N^\dagger Y_N)_{\mu e}$ and $(Y_E Y_E^\dagger Y_E)_{\mu e}$ respectively. The anarchic Yukawa assumption implies that both of these terms should be of the same order, Y_*^3 . However one must remember that there may be a relative sign between these contributions depending on the specific an-

archic Y_N and Y_E matrices. In other words, $a = a_{\text{charged}} \pm a_{\text{neutral}}$ where the sign cannot be specified generically. However, because $a_{\text{neutral}} \ll a_{\text{charged}}$, we ignore the neutral boson loops, though these neutral boson diagrams may become appreciable if one allows a hierarchy between the overall scales of the Y_N and Y_E matrices.

The W loop in Fig. 2.5a contains an implicit mass insertion on the external muon leg. As explained in Appendix A.2, the 5D fermion propagator between this mass insertion and the loop vertex is dominated by the KK mode which changes fermion chirality. This is because the chirality-preserving piece of the propagator goes like \not{p} . Invoking the muon equation of motion gives a factor of $f_\mu^{(0)}(vR')f_\mu^{(0)} \sim (m_\mu R')$ for the external leg. This is much smaller than the $f_\mu^{(0)}(vR')f_\mu^{(\text{KK})}$ factor from the chirality-flipping part of the propagator. Compared to the mass insertion connecting the zero mode external muon to a KK intermediate state, the mass insertion connecting two zero mode fermions is smaller by a factor of the exponentially suppressed zero mode profile¹.

Using the Feynman rules in Appendix A.5, the amplitude this diagram is

$$\mathcal{M}^\mu|_{(p+p')} = \frac{i}{16\pi^2} (R')^2 f_{c_{L\mu}} Y_*^3 f_{-c_{Ee}} \frac{ev}{\sqrt{2}} \left(\frac{g^2}{2} \ln \frac{R'}{R} \right) \left(\frac{R'v}{\sqrt{2}} \right)^2 I_{2\text{MIW}} \bar{u}_{p'}(p+p')^\mu u_p \quad (2.5.43)$$

where $I_{2\text{MIW}} = -0.31$ is a dimensionless loop integral. Taking $R'v/\sqrt{2} = .17$ and $g^2/2 \ln(R'/R) = 7.3$, the a coefficient in (2.4.29) is

$$a = -0.065. \quad (2.5.44)$$

2.5.2 Calculation of b

As discussed above, the diagrams contributing to b are sensitive to the structure of the anarchic Yukawa matrix relative to that of the non-universal internal bulk fermion masses.

¹We thank Martin Beneke, Paramita Dey, and Jürgen Rohrwild for pointing this out.

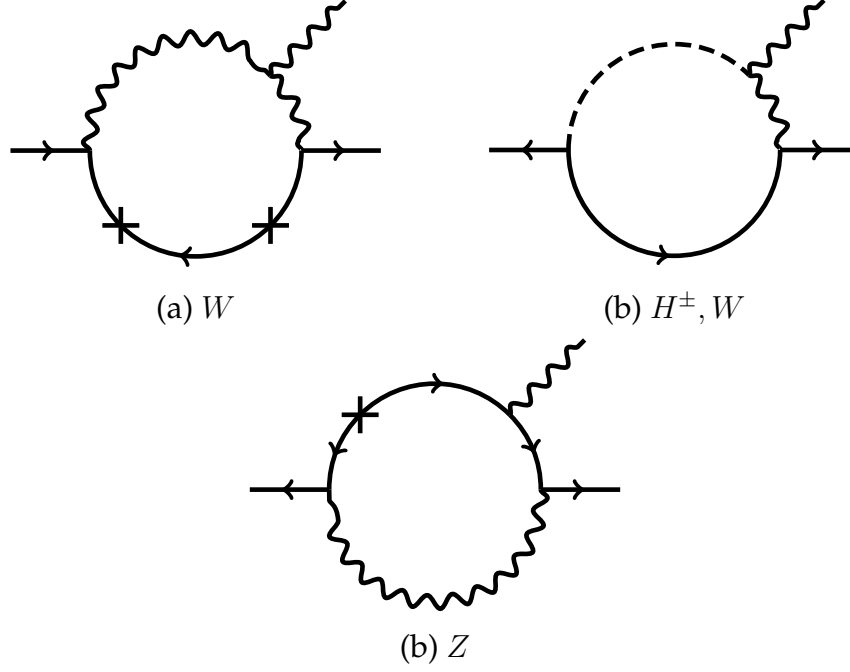


Figure 2.5: The leading diagrams contributing to the a and b coefficients following the same conventions as Fig. 2.2.

For example, if the bulk mass parameters were universal, then the b coefficient operator would be equationed and the off-diagonal element would vanish. The sign of this off-diagonal term is a function of the initial anarchic matrix so that the b term may interfere constructively or destructively with the a term calculated above. We numerically generate anarchic matrices whose elements have random sign and random values between 0.5 and 2 to determine the distribution of probable Yukawa structures. Such a distribution is peaked about zero so that the choice $b = 0$ is a reasonable simplifying assumption. For a more detailed description of the range of bounds accessible by the anarchic RS scenario, one may use the 1σ value of $|b|$ as characteristic measure of how large an effect one should expect from generic anarchic Yukawas.

The dominant contributions to the b coefficient are shown in Fig. 2.5b. These are the diagram with a charged Goldstone and a W in the loop and the diagram with a Z and

a single mass insertion in the loop. Following the analysis in Appendix A.2.4, these diagrams can have zero mode fermions propagating in the loop and hence are sensitive to the bulk mass parameters of the internal fermions being summed in the loop. This, in turn, implies that the diagrams are more robust against equationment upon rotating to the zero mode mass basis.

The amplitudes associated with this diagram are

$$\mathcal{M}(1\text{MIZ})|_{(p+p')^\mu} = \frac{i}{16\pi^2} (R')^2 f_{c_L} Y_E f_{-c_E} \frac{ev}{\sqrt{2}} \left(g_{Z_L} g_{Z_R} \ln \frac{R'}{R} \right) \times I_{1\text{MIZ}}, \quad (2.5.45)$$

$$\mathcal{M}(0\text{MIHW})|_{(p+p')^\mu} = \frac{i}{16\pi^2} (R')^2 f_{c_L} Y_E f_{-c_E} \frac{ev}{\sqrt{2}} \left(\frac{g^2}{2} \ln \frac{R'}{R} \right) \times I_{0\text{MIHW}}, \quad (2.5.46)$$

where $g_{Z_{L,R}}$ is the Standard Model coupling of the Z to left- and right-handed leptons respectively. The values for the dimensionless integrals are given in (A.3.12) and (A.3.13).

After scanning over anarchic matrices as defined above, the 1σ value for the b coefficient is

$$|b^{1\sigma}| = 0.03. \quad (2.5.47)$$

Here we take the 1σ value of the b coefficient assuming the bulk masses of the minimal model $c_L = c_R$ as a representative benchmark for a plausible general estimate of the generically allowed range of b .

2.5.3 Modifications in custodial modes

In Section 2.3.2 it was shown that custodial symmetry weakens the bounds from tree-level FCNCs. Since we would like to assess the tension between tree- and loop-level bounds, we should also examine the effect of the additional custodial modes on $\mu \rightarrow e\gamma$. These

additional diagrams are described by the same topologies as those in Figs. 2.2–2.4 but differ by replacing internal lines with custodial bosons and fermions. The expression for the amplitude differs by coupling constants and the use of propagators with different boundary conditions, but not in the overall structure of each amplitude and so are straightforward to extract from the minimal model expressions. The leading topologies are unchanged so that it is sufficient to consider the custodial versions of the diagrams in Fig. 2.5.

For the two-mass-insertion W diagram, there are two additional diagrams with custodial fermions: one with a W_L and the other with a W_R in the loop. The P_{LR} symmetry enforces that the couplings are identical while the different boundary conditions modify the definitions of the internal propagators so that the only difference comes from the value of the dimensionless integral in (2.5.43). The each diagram contributes a dimensionless integral $I = -0.2$, so that the a coefficient is modified to

$$a_{\text{cust.}} = -0.15. \quad (2.5.48)$$

Custodial diagrams do not contribute to the b coefficient at leading order. For example, one might consider the diagram with a Z loop where the Z is replaced by a Z_X , the orthogonal mixture of the custodial X and W_R^3 bosons. However, leptons carry no X charge so that the effective coupling is only to right chiral modes. For $\mu_R \rightarrow e_L \gamma$, such a diagram would not be allowed. The leading custodial b coefficient diagrams are an order of magnitude smaller than the minimal model diagrams and we shall ignore them in this paper.

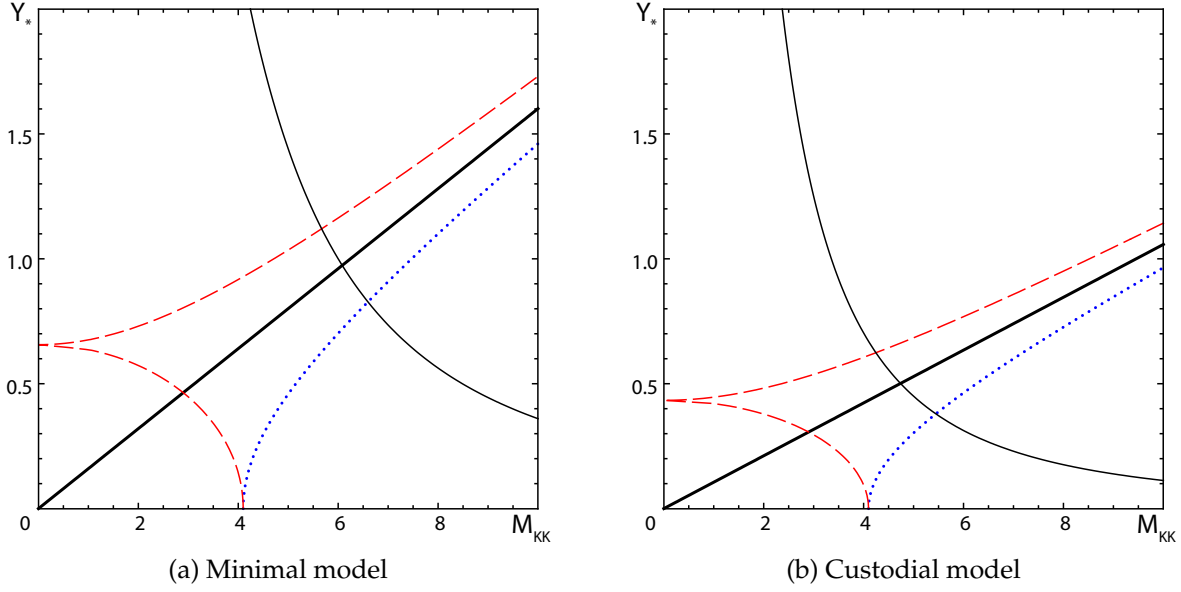


Figure 2.6: Bounds on the anarchic Yukawa and KK scales in the minimal (a) and custodial (b) models from tree- and loop-level constraints, (2.3.19), (2.3.26), and (2.4.39). Each curve rules out the region to its left. The solid hyperbola is the appropriate tree-level bound. The thick solid straight line is the $b = 0$ loop-level bound. The red dashed (blue dotted) curve is the loop-level bounds in the case where b has the same (opposite) sign as a and takes its 1σ magnitude $|b| = |b|_{1\sigma} = 0.03$.

2.5.4 Constraints and tension

We can now estimate the upper bound on the anarchic Yukawa scale Y_* in (2.4.39),

$$|aY_*^2 + b| \left(\frac{3 \text{ TeV}}{M_{\text{KK}}} \right)^2 \leq 0.015. \quad (2.5.49)$$

First let us consider the scenario where the b coefficient takes its statistical mean value, $b = 0$, and $M_{\text{KK}} = 3\text{TeV}$. In this case the minimal model suffers a $\mathcal{O}(10)$ tension between the tree-level lower bound on Y_* and the loop-level upper bound,

$$Y_* > 4 \qquad Y_* < 0.5. \quad (2.5.50)$$

The custodial model slightly alleviates this tension,

$$Y_* > 1.25 \qquad Y_* < 0.3. \quad (2.5.51)$$

These discrepancies should be interpreted as an assessment on the extent to which the 5D Yukawa matrices may be generically anarchic. The tension in the bounds above imply that for $M_{\text{KK}} = 3\text{TeV}$, one must accept some mild tuning in the relative sizes of the 5D Yukawa matrix. This is shown by the hyperbola and solid line in Fig. 2.6.

Alternately, one may ask that assuming totally anarchic Yukawas, what is the minimum value of M_{KK} for which the tension is alleviated? In the minimal model the tree- and loop-level bounds allow mutually consistent Yukawa scales for $M_{\text{KK}} > 6$ starting at $Y = 1$. Similarly, for the custodial model the tree- and loop-level bounds allow consistent values for $M_{\text{KK}} > 4.75$ starting at $Y = 0.5$.

Next one may consider the effect of the b coefficient which is sensitive to the particular flavor structure of the anarchic 5D Yukawa matrix relative to the choice of fermion bulk mass parameters. The 1σ range of b values for randomly generated anarchic matrices is $b \in (-0.03, 0.03)$. Because this term is independent of Y_* , the value of b can directly constraint the KK scale. For the 1σ value this sets $M_{\text{KK}} \gtrsim 4 \text{ TeV}$, as can be seen from the intersection of the red dashed lines and blue dotted lines with the horizontal axes in Fig. 2.6.

The most interesting range for b , however, is the regime where it can cancel the a term in term in (2.4.39). In such a regime the loop level bounds can deviate significantly from the prediction with only the a coefficient, allowing one to relax the constraints on Y_* and M_{KK} . However, because the 1σ value of b is an order of magnitude smaller than a in the lepton sector, this region is disfavored by tree-level bounds. For broad model-building purposes, the key point is that the effect of the b coefficient lines in Fig. 2.6 represent the freedom to reduce (or enhance) the loop-level constraints through the mis-equationment of the anarchic Yukawas relative to the bulk masses. This mis-equationment comes from

the choice of two independent spurions in flavor space and is not a tuning in the hierarchies of the Yukawa matrices.

In Fig. 2.6 the red dashed line shows the bound when b takes its 1σ magnitude and has an opposite sign from a ; the cusp at $M_{KK} = 0$ represents the case where the a and b terms cancel. The blue dotted line shows the case where b takes its 1σ magnitude and has the same sign as a . What is important to note is that as one takes $|b|$ less than $|b|_{1\sigma}$, these lines continuously converge upon the straight line corresponding to $b = 0$ so that any combination of Y_* and M_{KK} between the upper red dashed line and the blue dotted line can be plausibly achieved within the anarchic paradigm. Let us make the caveat that the above values are estimates at $\mathcal{O}(10\%)$ accuracy. Specific results depend on model-dependent factors such as the extent to which the matrices are anarchic, the relative scale of the charged lepton and neutrino anarchic values, or extreme values for bulk masses. For completeness we provide analytic formulas for the leading and next-to-leading order diagrams in Appendix A.3.

2.6 Power counting and finiteness

We now develop an intuitive understanding of the finiteness of this 5D process, highlight some subtleties associated with the KK versus 5D calculation of the loop diagrams², and estimate the degree of divergence of the two-loop result. Our primary tool is naïve dimensional analysis, from which we may determine the superficial degree of divergence for a given 5D diagram. Special care is given to the treatment of brane-localized fields and the translation between the manifestly 5D and KK descriptions.

²The finiteness of dipole operators has been investigated in gauge-higgs unified models where a higher-dimensional gauge invariance can render these terms finite [14]. Here we do not assume the presence of such additional symmetries.

2.6.1 4D and 5D theories of bulk fields

It is instructive to review key properties of $\mu \rightarrow e\gamma$ in the Standard Model. This amplitude was calculated by several authors [287, 131, 322, 297, 288]. Two key features are relevant for finiteness:

1. **Gauge invariance** cancels the leading order divergences. The Ward identity requires $q_\mu \mathcal{M}^\mu = 0$, where \mathcal{M}^μ is the amplitude with the photon polarization peeled off and q_μ is the photon momentum. This imposes a nontrivial q -dependence on \mathcal{M} and reduces the superficial degree of divergence by one.
2. **Lorentz invariance** prohibits divergences which are odd in the loop momentum, k . In other words, $\int d^4k \not{k}/k^{2n} = 0$. After accounting for the Ward identity, the leading contribution to the dipole operator is odd in k and thus must vanish. Specifically, one of the \not{k} terms in a fermion propagator must be replaced by the fermion mass m .

Recall that the **chiral structure** of this magnetic operator requires an explicit internal mass insertion. In the Standard Model this is related to both gauge and Lorentz invariance so that it does not give an additional reduction in the superficial degree of divergence. Before accounting for these two features, naïve power counting in the loop integrals appears to suggest that the Standard Model amplitude is logarithmically divergent from diagrams with two internal fermions and a single internal boson. Instead, one finds that these protection mechanisms force the amplitude to go as M^{-2} where M is the characteristic loop momentum scale.

We can now extrapolate to the case of a 5D theory. First suppose that the theory is modified to include a *noncompact* fifth dimension: then we could trivially carry our results

from 4D momentum space to 5D except that there is an additional loop integral. By the previous analysis, this would give us an amplitude that goes as M^{-1} and is thus finite. Such a theory is not phenomenologically feasible but accurately reproduces the UV behavior of a bulk process in a compact extra dimension so long as we consider the UV limit where the loop momentum is much larger than the compactification and curvature scales. This is because the UV limit of the loop probes very small length scales that are insensitive to the compactification and any warping. This confirms the observation that $\mu \rightarrow e\gamma$ in Randall-Sundrum models with all fields (including the Higgs) in the bulk is UV-finite [20]. In the case where there are brane-localized fields, this heuristic picture is complicated since the $\mu \rightarrow e\gamma$ loop is intrinsically localized near the brane and is sensitive to its physics; we address this issue below.

2.6.2 Bulk fields in the 5D formalism

We may formalize this power counting in the mixed position/momentum space formalism. This also generalizes the above argument to theories on a compact interval. Each loop carries an integral d^4k and so contributes +4 to the superficial degree of divergence. We can now consider how various features of particular diagrams can render this finite.

1. **Gauge invariance** ($p + p'$). As argued above and shown explicitly in (2.5.41), the Ward identity identifies the gauge invariant contribution to this process to be proportional to $(p + p')^\mu$, which reduces the overall degree of divergence by one.
2. **Bulk Propagators.** The bulk fermion propagators in the mixed position/momentum space formalism have a momentum dependence of the form $\not{k}/k \sim 1$ while the bulk boson propagators go like $1/k$. This matches the power counting

from summing a tower of KK modes. Note that this depends on $k = \sqrt{k^2}$ so that the Lorentz invariance in Section 2.6.1 for a noncompact extra dimension is no longer valid.

3. **Bulk vertices (dz), overall z -momentum conservation.** Each bulk vertex carries an integral over the vertex position which brings down an inverse power of the momentum flowing through it. This can be seen from the form of the bulk propagators, which depend on z in the dimensionless combination kz up to overall warp factors. In the Wick-rotated UV limit, the integrands reduce to exponentials so that their integrals go like $1/k$. In momentum space this suppression is manifested as the momentum-conserving δ function in the far UV limit where the loop momentum is much greater than the curvature scale.

An alternate and practical way to see the $1/k$ scaling of an individual dz integral comes from the Jacobian as one shifts to dimensionless integration variables,

$$y = k_E R' \qquad x = k_E z \qquad (2.6.52)$$

so that $y \in [0, \infty]$ plays the role of the loop integrand and $x \in [yR/R', y]$ plays the role of the integral over the interval extra dimension. These are the natural objects that appear as arguments in the Bessel functions contained in the bulk field propagators, as demonstrated in Appendix A.6.3. In these variables each dx brings down a factor of $1/y$ from the Jacobian of the integration measure. These variables are natural choices because they relate distance intervals in the extra dimension to the scales that are being probed by the loop process. The *physically* relevant distance scales are precisely these ratios.

4. **Overall z -momentum conservation.** We must make one correction to the bulk vertex suppression due to overall z -momentum conservation. This is most easily seen

in momentum space where one δ -function from the bulk vertices conserves overall external momentum in the extra dimension and hence does not affect the loop momentum. In mixed position/momentum space this is manifested as one dz integral bringing down an inverse power of only external momenta without any dependence on the loop momentum. We review this in Appendix A.4, where we discuss the passage between position and momentum space. The overall z -momentum conserving δ -function thus adds one unit to the superficial degree of divergence to account for the previous overcounting of $dz \sim 1/k$ suppressions.

5. **Derivative coupling.** The photon couples to charged bosons through a derivative coupling which is proportional to the momentum flowing through the vertex. This gives a contribution that is linear in the loop momentum, k^μ .
6. **Chirality: mass insertion, equation of motion.** To obtain the correct chiral structure for a dipole operator, each diagram must either have an explicit fermion mass insertion or must make use of the external fermion equation of motion (EOM). For a bulk Higgs field, each fermion mass insertion carries a dz integral which goes like $1/k$. As described in Section 2.5, the use of the EOM corresponds to an explicit external mass insertion. Thus fermion chirality reduces the degree of divergence by one unit.

We may now straightforwardly count the powers of the loop momentum to determine the superficial degree of divergence for the case where the photon is emitted from a fermion (one boson and two fermions in the loop) or a boson (two bosons and one fermion in the loop). The latter case differs from the former in the number of boson propagators and the factor of k^μ in the photon Feynman rule.

	Neutral	Charged
	Boson	Boson
Loop integral (d^4k)	+4	+4
Gauge invariance ($p + p'$)	-1	-1
Bulk fermion propagators	0	0
Bulk boson propagator	-1	-2
Bulk vertices (dz)	-3	-3
Overall z -momentum	+1	+1
Derivative coupling	0	+1
Mass insertion/EOM	-1	-1
<hr/>		
<i>Total degree of divergence</i>	-1	-1

The WH^\pm diagram in Fig. 2.4 is a special case since it has neither a derivative coupling nor an additional chirality flip, but these combine to make no net change to the superficial degree of divergence. We confirm our counting in Section 2.6.1 that the superficial degree of divergence for universal extra dimension where all fields propagate in the bulk is -1 so that the flavor-changing penguin is manifestly finite.

Before moving on to the case of a brane-localized boson, let us remark that this bulk counting may straightforwardly be generalized to the case of a bulk boson with brane-localized mass insertions. To do this, we note that the brane-localized mass insertion breaks momentum conservation in the z direction and this no longer contributes $+1$ to the degree of divergence. On the other hand, each mass insertion no longer contributes -1 from the dz integral so that the changes in the “overall z -momentum” and “mass

insertion/EOM" counting cancel out. We find that diagrams with a bulk gauge boson and brane-localized mass insertions have the same superficial degree of divergence as the lowest order diagrams in a *bulk* mass insertion expansion.

2.6.3 Bulk fields in the KK formalism

All of the power counting from the 5D position/momentum space formalism carries over directly to the KK formalism with powers of m_{KK} treated as powers of k . The position/momentum space propagators already carry the information about the entire KK tower as well as the profiles of each KK mode. Explicitly converting from a 5D propagator to a KK reduction,

$$\Delta_{5D}(k, z, z') = \sum_n f^{(n)}(z) \Delta_{\text{KK}}^{(n)}(k) f^{(n)}(z'), \quad (2.6.53)$$

where $f^{(n)}$ is the profile of the n^{th} KK mode. The sum over KK modes is already accounted for in the 5D propagator; for example, for a boson $\Delta_{\text{KK}}^{(n)} \sim 1/k^2$ while $\Delta_{5D} \sim 1/k$. The vertices between KK modes are given by the dz integral over each profile, which reproduces the same counting since each profile depends on z as a function of $m_{\text{KK}}^{(n)} z$. Conservation of z -momentum is replaced by conservation of KK number in the UV limit of large KK number.

Indeed, it is almost tautological that the KK and position/momentum space formalisms should match for bulk fields since the process of KK reducing a 5D theory implicitly passes through the position/momentum space construction. This will become slightly more nontrivial in the case of brane-localized fields. We shall postpone a discussion of mixing between KK states until Section 2.6.5.

2.6.4 Brane fields in the 5D formalism

The power counting above appears to fail for loops containing a brane-localized Higgs field. The brane-localized Higgs propagator goes like $1/k^2$ rather than $1/k$ for the bulk propagator, but this comes at the cost of two vertices that must also be brane-localized, thus negating the suppression from the dz integrals. The charged Higgs has two brane-localized Higgs propagators, but loses a third dz integral from the brane-localized photon emission. Finally, there are no additional contributions from the brane-localized fermion mass insertions nor are there any corrections from the conservation of overall z -momentum since it is manifestly violated by the brane-localized vertices (see Appendix A.4 for a detailed discussion). In the absence of any additional brane effects, both types of loops would be logarithmically divergent, as discussed in [20].

Fortunately, two such brane effects appear. First consider the two neutral Higgs diagrams in Fig. 2.2. The diagram with no mass insertion requires the use of an external fermion equation of motion which still reduces the superficial degree of divergence by one so that it is finite. The diagram with a single mass insertion is finite in the Standard Model due to a cancellation between the Higgs and neutral Goldstone diagrams, as discussed in Section 2.5. More generally, even for a single type of brane-localized field, there is a cancellation between diagrams in Fig. 2.7 where the photon is emitted before and after the mass insertion. This can be seen by writing down the Dirac structure coming from the fermion propagators to leading order in the loop momentum,

$$\mathcal{M}_a \sim \not{k}\gamma^\mu\not{k}\not{k} - k\gamma^\mu k\not{k} = k^2(\not{k}\gamma^\mu - \gamma^\mu\not{k}) \quad (2.6.54)$$

$$\mathcal{M}_b \sim \not{k}\not{k}\gamma^\mu\not{k} - \not{k}k\gamma^\mu k = k^2(\gamma^\mu\not{k} - \not{k}\gamma^\mu) \quad (2.6.55)$$

The terms with three factors of \not{k} are contributions where “correct-chirality” fermions propagate into the bulk, while the terms with only one \not{k} are contributions where “wrong-

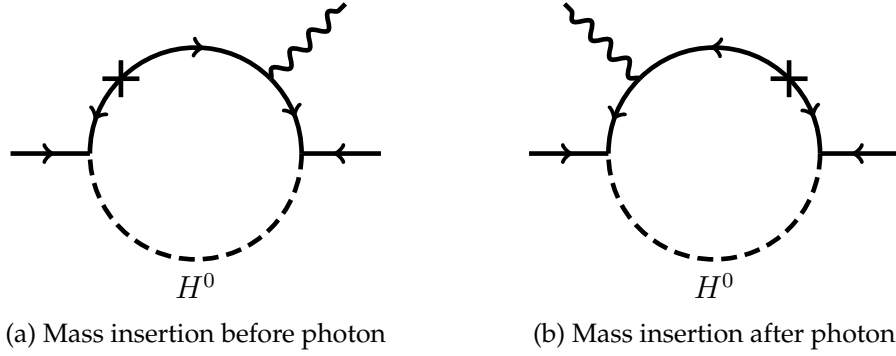


Figure 2.7: One-mass-insertion neutral scalar diagrams. The leading order k -dependence of each diagram cancels when the two are summed together.

chirality" fermions propagate into the bulk. The structure of the latter terms comes from the $\gamma^5 \partial_z$ term in the Dirac operator. The structures above multiply scalar functions which, to leading order in k , are identical for each term. From the Clifford algebra it is clear that (2.6.54) and (2.6.55) cancel so that the contribution that is nonvanishing in the UV must be next-to-leading order in the loop momentum. In Appendix A.7 this cancellation is connected to the chiral boundary conditions on the brane and is demonstrated with explicit flat-space fermion propagators. We thus find that the brane-localized neutral Higgs diagrams have an additional -1 contribution to the superficial degree of divergence.

Next we consider the charged Goldstone diagrams. These diagrams have an additional momentum suppression coming from a positive power of the charged Goldstone mass M_W^2 appearing in the numerator due to a cancellation within each diagram. In fact, we have already seen in Section 2.5.1 how such a cancellation appears. For the single-mass-insertion charged Goldstone diagram in Fig. 2.3, we saw in (A.2.6) that the form of the 4D scalar propagators and the photon-scalar vertex cancels the leading-order loop momentum term multiplying the required $(p + p')^\mu$. The cancellation introduces an additional factor of $M_W^2/(k^2 - M_W^2)$ so that the superficial degree of divergence is reduced by two. Note that the position/momentum space propagators for a *bulk* Higgs have a

different form than that of the 4D brane-localized Higgs and do not display the same cancellation. In the KK picture this is the observation that the cancellation in (A.2.6) takes the form $M_{\text{KK}}^2/(k^2 - M_{\text{KK}}^2)$, which does not provide any suppression for heavy KK Higgs modes.

Finally, the diagrams where the photon emission vertex mixes the W and brane-localized charged Goldstone are special cases. The photon vertex carries neither a dz integral nor a k^μ Feynman rule and hence makes no net contribution to the degree of divergence. A straightforward counting including the brane-localized Goldstone, bulk W , and the single bulk vertex thus gives a degree of divergence of -1 .

We summarize the power counting for a brane-localized Higgs as follows:

	Neutral	Charged	$W-H^\pm$
	boson	boson	mixing
Loop integral (d^4k)	+4	+4	+4
Gauge invariance ($p + p'$)	-1	-1	-1
Brane boson propagators	-2	-4	-2
Bulk boson propagator	0	0	-1
Bulk vertices (dz)	-1	0	-1
Photon Feynman rule	0	+1	0
Brane chiral cancellation	-1	0	0
Brane M_W^2 cancellation	0	-2	0
<i>Total degree of divergence</i>	-1	-2	-1

It may seem odd that the brane-localized charged Higgs loop has a different superficial degree of divergence than the other 5D cases, which heretofore have all been -1 . This, however, should not be surprising since the case of a brane-localized Higgs is manifestly different from the universal extra dimension scenario. It is useful to think of the brane-localized Higgs as a limiting form of a KK reduction where the zero mode profile is sharply peaked on the IR brane. The difference between the bulk and brane-localized scenarios corresponds to whether or not one includes the rest of the KK tower.

2.6.5 Brane fields in the KK formalism

Let us now see how the above power counting for the brane-localized Higgs manifests itself in the Kaluza-Klein picture [20]. Observe that this power counting for both the $W-H^\pm$ and the charged boson loops are trivially identical to the 5D case due to the arguments in Section 2.6.3. For example, the M_W^2 cancellation is independent of how one treats the bulk fields. The neutral Higgs loop, however, is somewhat subtle since the “chiral cancellation” is not immediately obvious in the KK picture.

We work in the mass basis where the fermion line only carries a single KK sum (not independent sums for each mass insertion) and the zero mode photon coupling preserves KK number due to the flat $A^{(0)}$ profile. In this basis the internal fermion line carries one KK sum and it is sufficient to show that for a single arbitrarily large KK mode the process scales like $1/M_{\text{KK}}^2$. The four-dimensional power counting in Section 2.6.1 appears to give precisely this, except that Lorentz invariance no longer removes a degree of divergence. This is because this suppression came from the replacement of a loop momentum \not{k} by the fermion mass m . For an arbitrarily large KK mode, the fermion mass itself is the loop momentum scale and so does not reduce the degree of divergence. In the absence of

any additional suppression coming from the mixing of KK modes, it would appear that the KK power counting only goes like $1/M_{\text{KK}}$ so that the sum over KK modes should be logarithmically divergent, in contradiction with the power counting for the same process in the 5D formalism.

We shall now show that the pair of Yukawa couplings for the neutral Higgs also carries the expected $1/k$ factor that renders these diagrams finite and allows the superficial degrees of divergence to match between the KK and 5D counting. It is instructive to begin by defining a basis for the zero and first KK modes in the weak (chiral) basis. We denote left (right) chiral fields of KK number a by $\chi_{L,R}^{(a)}$ ($\psi_{L,R}^{(a)}$) where the L, R refers to $\text{SU}(2)_L$ doublets and singlets respectively. We can arrange these into vectors

$$\chi = \left(\chi_{L_i}^{(0)}, \chi_{R_i}^{(1)}, \chi_{L_i}^{(1)} \right) \quad \psi = \left(\psi_{R_i}^{(0)}, \psi_{R_i}^{(1)}, \psi_{L_i}^{(1)} \right), \quad (2.6.56)$$

where i runs over flavors. It is helpful to introduce a single index $J = 3a + i$ where $i = 1, 2, 3$ according to flavor and $a = 0, 1, 2$ according to KK mode (writing $a = 2$ to mean the *first* KK mode with opposite chirality as the zero mode). Thus the external muon and electron are χ_2 and ψ_1 respectively, while an internal KK mode takes the form χ_J or ψ_J with $J > 3$. This convention in (2.6.56) differs from that typically used in the literature (e.g. [20]) in the order of the last two elements of ψ . This basis is useful because the KK terms are already diagonal in the mass matrix ($\psi M \chi + \text{h.c.}$),

$$M = \begin{pmatrix} m^{11} & 0 & m^{13} \\ m^{21} & M_{\text{KK},1} & m^{23} \\ 0 & 0 & M_{\text{KK},2} \end{pmatrix} \quad (2.6.57)$$

where each element is a 3×3 block in flavor space and we have written

$$m = \frac{v}{\sqrt{2}} f_{R_i}^{(a)} Y_* f_{L_j}^{(b)} \ll M_{\text{KK}}, \quad (2.6.58)$$

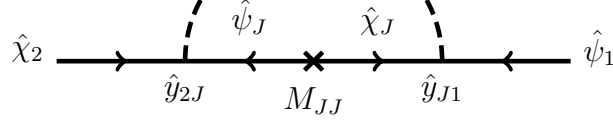


Figure 2.8: The fermion line in the mass basis for diagrams with an internal KK mode ($J > 3$). For simplicity we do not show the internal photon insertion.

with indices as appropriate and M_{KK} diagonal. Let us define $\epsilon = v/M_{\text{KK}}$ to parameterize the hierarchies in the mass matrix. For a bulk Higgs, these terms are replaced by overlap integrals and the M_{32} block is nonzero, though this does not affect our argument. Note that $M_{\text{KK},1}$ and $M_{\text{KK},2}$ are typically not degenerate due to $\mathcal{O}(m)$ differences in the doublet and singlet bulk masses. In the gauge eigenbasis the Yukawa matrix is given by

$$y = \frac{\sqrt{2}}{v} M \Big|_{M_{\text{KK}}=0} \sim \begin{pmatrix} 1 & 0 & 1 \\ 1 & 0 & 1 \\ 0 & 0 & 0 \end{pmatrix}, \quad (2.6.59)$$

where we have assumed $f_L, f_R, Y_* \sim \mathcal{O}(1)$ for simplicity since the hierarchies in the $f^{(0)}$ s do not affect our argument. The 1 elements thus refer to blocks of the same order of magnitude that are *not* generically diagonal. The 0 blocks must vanish by gauge invariance and chirality.

We now rotate the fields in (2.6.56) to diagonalize the mass matrix (2.6.57); we indicate this by a caret, e.g. $\hat{\chi}$. In this basis the Yukawa matrix is also rotated $y \rightarrow \hat{y}$. The fermion line for this process is shown in Fig. 2.8; the Yukawa dependence of the amplitude is

$$\mathcal{M} \sim \hat{y}_{1J} \hat{y}_{J2}. \quad (2.6.60)$$

First let us note that in the unrealistic case where $\hat{y} = y$, one of the Yukawa factors in (2.6.60) is identically zero for all internal KK modes, $J > 3$. One might then expect that the mass rotation would induce a mixing of the zero modes with the KK modes that

induces $\mathcal{O}(\epsilon)$ blocks into the Yukawa matrix,

$$\hat{y} \stackrel{?}{\sim} \begin{pmatrix} 1 & \epsilon & 1 \\ 1 & \dots & \dots \\ \epsilon & \dots & \dots \end{pmatrix}. \quad (2.6.61)$$

If this were the case then the product $\hat{y}_{1J}\hat{y}_{J2}$ would not vanish, but would be proportional to $\epsilon \sim 1/M_{\text{KK}}$, which is precisely the KK dependence that we wanted to show. While this intuition is correct and captures the correct physics, the actual Yukawa matrix in the mass basis has the structure (c.f. (67) in [20])

$$\hat{y} \sim \begin{pmatrix} 1 & 1 + \epsilon & -1 + \epsilon \\ 1 + \epsilon & \dots & \dots \\ 1 - \epsilon & \dots & \dots \end{pmatrix}. \quad (2.6.62)$$

The new $\mathcal{O}(1)$ elements come from the large rotations induced by the m^{21} and m^{13} blocks. These factors cancel out so that we still have the desired $\hat{y}_{1J}\hat{y}_{J2} \sim \epsilon$ relation. Physically this is because these $\mathcal{O}(1)$ factors come from the “large” rotation from chiral zero modes to light Dirac SM fermions. Thus they represent the “wrong-chirality” coupling of the external states induced by the usual mixing of Weyl states from a Dirac mass. This does *not* include the mixing with the heavy KK modes, which indeed carries the above ϵ factors so that the final result is

$$\hat{y}_{1J}\hat{y}_{J2} \sim \epsilon \sim \frac{1}{M_{\text{KK}}}, \quad (2.6.63)$$

giving the correct -1 contribution to the superficial degree of divergence for the neutral Higgs diagrams to render them manifestly finite.

A few remarks are in order. First let us emphasize again that promoting the Higgs to a bulk field makes the 3–2 block of the y matrix nonzero. This does not affect the

above argument so that the KK decomposition confirms the observation that the amplitude with a bulk Higgs is also finite [20]. Of course, for a bulk Higgs the power counting in Section 2.6.2 gives a more direct check of finiteness. Next, note that without arguing the nature of the zeros in the gauge basis Yukawa matrix or the physical nature of the ϵ mixing with KK modes, it may appear that the $1/M_{\text{KK}}$ dependence of $\hat{y}_{1J}\hat{y}_{J2}$ requires a “miraculous” fine tuning between the matrix elements of (2.6.62). Our discussion highlights the physical nature of this cancellation as the mixing with heavy states that is unaffected by the $\mathcal{O}(1)$ mixing of light chiral states.

Finally, let us point out that the above arguments are valid for the neutral Higgs diagram where $y = y_E$, the charged lepton Yukawa matrix. The analogous charged Higgs diagram contains neutrino Yukawa matrices y_N so that there is no additional $1/k$ from mixing.

2.6.6 Matching KK and loop cutoffs

There is one particularly delicate point in the single-mass-insertion neutral Higgs loop in the KK reduction that is worth pointing out because it highlights the relation between the KK scales $M_{\text{KK}}^{(n)}$ and the 5D loop momentum. To go from the 5D to the 4D formalism we replace our position/momentum space propagators with a sum of Kaluza-Klein propagators,

$$\Delta_{5\text{D}}(k, z, z') = \sum_{n=0}^N f^{(n)}(z) \frac{k + M_n}{k^2 - M_n^2} f^{(n)}(z'). \quad (2.6.64)$$

The full 5D propagator is exactly reproduced by summing the infinite tower of states, $N \rightarrow \infty$. More practically, the 5D propagator with characteristic momentum scale k is well-approximated by at least summing up to modes with mass $M_n \approx k$. Modes that are

much heavier than this decouple and do not give an appreciable contribution. Thus, when calculating low-energy, tree-level observables in 5D theories, it is sufficient to consider only the effect of the first few KK modes. On the other hand, this means that one must be careful in loop diagrams where internal lines probe the UV structure of the theory. In particular, significant contributions from internal propagators near the threshold $M_n \approx k$ would be missed if one sums only to a finite KK number while taking the loop integral to infinity. This is again a concrete manifestation of the remarks below (2.6.52) that the length scales probed by a process depend on the characteristic momentum scale of the process.

Indeed, a Kaluza-Klein decomposition for a single neutral Higgs yields

$$|\mathcal{M}|_{(p+p')^\mu} = \frac{gv}{16\pi^2} f_\mu f_{-e} \bar{u}_e (p+p')^\mu u_\mu \times \frac{1}{M^2} \left[c_0 + c_1 \left(\frac{v}{M} \right)^2 + \mathcal{O} \left(\frac{v}{M} \right)^3 \right] \quad (2.6.65)$$

for some characteristic KK scale $M \approx M_{\text{KK}}$ and dimensionless coefficients c_i that include a loop integral and KK sums. In order to match the 5D calculation detailed above, we shall work in the mass insertion approximation so that there are now two KK sums in each coefficient. The leading c_0 term is especially sensitive to the internal loop momentum cutoff Λ relative to the internal KK masses,

$$c_0 = - \sum_{n=1}^N \sum_{m=1}^N \frac{\lambda^2}{2(n^2 + \lambda^2)(m^2 + \lambda^2)} \equiv - \frac{1}{\lambda^2} \sum_{n=1}^N \sum_{m=1}^N \hat{c}_0(n, m), \quad (2.6.66)$$

where we have written mass scales in terms of dimensionless numbers with respect to the mass of the first KK mode: $M_n \sim nM_{\text{KK}}$ and $\Lambda \sim \lambda M_{\text{KK}}$. It is instructive to consider the limiting behavior of each term $\hat{c}_0(n, m)$ for different ratios of the KK scale (assume $n = m$) to the cutoff scale λ :

$$\hat{c}_0(n, n) \longrightarrow \left(\frac{n}{\lambda} \right)^2 \quad \text{for } n \ll \lambda \quad (2.6.67)$$

$$\hat{c}_0(n, n) \longrightarrow \left(\frac{n}{\lambda} \right)^0 \quad \text{for } n \approx \lambda \quad (2.6.68)$$

$$\hat{c}_0(n, n) \longrightarrow \left(\frac{\lambda}{n} \right)^4 \quad \text{for } n \gg \lambda. \quad (2.6.69)$$

We see that the dominant contribution comes from modes whose KK scale is near the loop momentum cutoff while the other modes are suppressed by powers of the ratio of scales. In particular, if one calculates the loop for any internal mode of *finite* KK number while taking the loop cutoff to infinity, then the c_0 contribution vanishes because the $n \approx \lambda$ contributions are dropped. From this one would incorrectly conclude that the leading order term is c_1 and that the amplitude is orders of magnitude smaller than our 5D calculation. Thus one cannot consistently take the 4D momentum to infinity without simultaneously taking the 5D momentum (i.e. KK number) to infinity. Or, in other words, one must always be careful to include the nonzero contribution from modes with $n \approx \lambda$. One can see from power counting on the right-hand side of (2.6.66) that so long as the highest KK number N and the dimensionless loop cutoff λ are matched, c_0 gives a nonzero contribution even in the $\lambda \rightarrow \infty$ limit.

This might seem to suggest UV sensitivity or a nondecoupling effect³. However, we have already shown that $\mu \rightarrow e\gamma$ is UV-finite in 5D. Indeed, our previous arguments about UV finiteness tell us that the overall contribution to the amplitude from large loop momenta (and hence high KK numbers) must become negligible; we see this explicitly in the UV limit of (2.6.66). The key statement is that the KK scale and the UV cutoff of the loop integral must be *matched*, $N \gtrsim \lambda$. This can be understood as maintaining momentum-space rotational invariance in the microscopic limit of the effective theory (much smaller than the curvature scale). Further, the prescription that one must match our KK and loop cutoffs $N \gtrsim \lambda$ is simply the statement that we must include all the available modes of our effective theory. It does *not* mean that one must sum a large number of modes in an effective KK theory. In particular, one is free to perform the loop integrals with a low cutoff $\Lambda \sim M_{\text{KK}}$ so that only a single KK mode runs in the loop. This result gives a nonzero value for c_0 which matches the order of magnitude of the full 5D calculation and

³Further discussion of these points can be found in the appendix of [97].

hence confirms the decoupling of heavy modes.

2.6.7 Two-loop structure

As with any 5D effective theory, the RS framework is not UV complete. This nonrenormalizability means that it is possible for processes to be cutoff-sensitive. Since an effective $\mu \rightarrow e\gamma$ operator (in the sense of Appendix A.1) cannot be written at tree level, there can be no tree-level counter term and so we expect the process to be finite at one-loop order, as we have indeed confirmed above. In principle, however, higher loops need not be finite.

The one-loop analysis presented thus far assumes that we may work in a regime where the relevant couplings are perturbative. In other words, we have assumed that higher-loop diagrams are negligible due to an additional $g^2/16\pi^2$ suppression, where g is a generic internal coupling. This naturally depends on the divergence structure of the higher-loop diagrams. If such diagrams are power-law divergent then it is possible to lose this window of perturbativity even for relatively low UV cutoff $\Lambda \sim M_{\text{KK}}$. We have shown that even though naïve dimensional analysis suggests that the $\mu \rightarrow e\gamma$ amplitude should be linearly divergent in 5D, the one-loop amplitudes are manifestly finite.

Here we argue that the two-loop diagrams should be no more than logarithmically divergent for bulk bosons so that there is an appreciable region of parameter space where the process is indeed perturbative and the one-loop analysis can be trusted. This case is also addressed in [20]. The relevant topologies are shown in Fig. 2.9. In this case, the power counting arguments that we have developed in this section carry over directly to the two-loop diagrams:

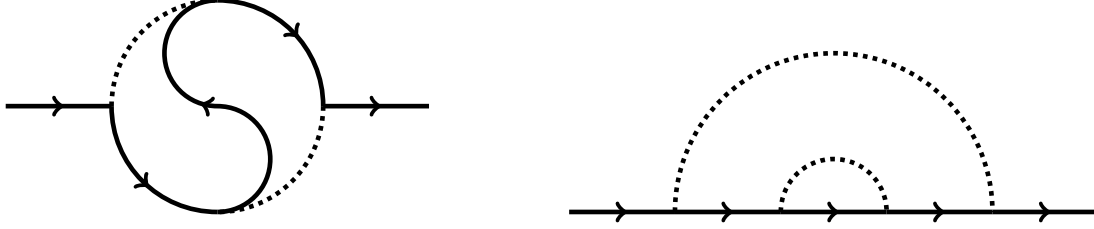


Figure 2.9: Yin-Yang and double rainbow topologies of two-loop diagrams. The dotted line represents either a gauge or Higgs boson. We have omitted the photon emission and an odd number of mass insertions.

Loop integrals (d^4k)	+8
Gauge invariance ($p + p'$)	-1
Bulk boson propagators	-2
Bulk vertices (dz)	-5
<hr/>	
<i>Total degree of divergence</i>	0

We find that the superficial degree of divergence is zero so that the process is, at worst, logarithmically divergent.

The power counting for the brane-localized fields is more subtle, as we saw above. Naïve power counting suggests that the two-loop, brane-localized diagrams are no more than quadratically divergent. However, just as additional cancellations manifested themselves in the one-loop, brane-localized case, it may not be unreasonable to expect that those cancellations might carry over to the two-loop diagrams. Checking the existence of such cancellations requires much more work we leave this to a full two-loop calculation.

2.7 Outlook and Conclusion

We have presented a detailed calculation of the $\mu \rightarrow e\gamma$ amplitude in a warped RS model using the mixed position/momentum representation of 5D propagators and the mass insertion approximation, where we have assumed that the localized Higgs VEV is much smaller than the KK masses in the theory. Our calculation reveals potential sensitivity to the specific flavor structure of the anarchic Yukawa matrices since this affects the relative signs of coefficients that may interfere constructively or destructively. We thus find that while generic flavor bounds can be placed on the lepton sector of RS models, one can systematically adjust the structure of the Y_E and Y_N matrices to alleviate the bounds while simultaneously maintaining anarchy. In other words, there are regions of parameter space which can improve agreement with experimental constraints without fine tuning. Conversely, one may generate anarchic flavor structures which—for a given KK scale—cannot satisfy the $\mu \rightarrow e\gamma$ constraints for *any* value of the anarchic scale Y_* . Over a range of randomly generated anarchic matrices, the parameter controlling this Y_* -independent structure has a mean value of zero and a 1σ value which can push the KK scale to 4 TeV.

It is interesting to consider the case where $M_{\text{KK}} = 3$ TeV where KK excitations are accessible to the LHC. When the b coefficient takes its statistical mean value, $b = 0$, the minimal model suffers a $\mathcal{O}(10)$ tension between the tree-level lower bound on Y_* and the loop-level upper bound,

$$Y_* > 4 \qquad Y_* < 0.5. \qquad (2.7.70)$$

This tension is slightly alleviated in the custodial model,

$$Y_* > 1.25 \qquad Y_* < 0.3. \qquad (2.7.71)$$

Thus for $M_{\text{KK}} = 3$ TeV one must accept some mild tuning in the relative sizes

of the 5D Yukawa matrix. Fig. 2.5.4 summarizes the bounds including the effect of the b coefficient.

On the other hand, we know that anarchic models generically lead to small mixing angles (see however [25]). These fit the observed quark mixing angles well but are in stark contrast with the lepton sector where neutrino mixing angles are large, $\mathcal{O}(1)$, and point to additional flavor structure in the lepton sector. For example in [148] a bulk A_4 non-Abelian discrete symmetry is imposed on the lepton sector. This leads to a successful explanation of both the lepton mass hierarchy and the neutrino mixing angles (see also [172]) while all tree-level lepton number-violating couplings are absent, so the only bound comes from the $\mu \rightarrow e\gamma$ amplitude.

We have also provided different arguments for the one-loop finiteness of this amplitude which we verified explicitly through calculations. We have illuminated how to correctly perform the power counting to determine the degree of divergence from both the 5D and 4D formalisms. The transition between these two pictures is instructive and we have demonstrated the importance of matching the number of KK modes in a 4D EFT to any 4D momentum cutoff in loop diagrams. The power-counting analysis can be particularly subtle for the case of brane-localized fields and we have shown how one-loop finiteness can be made manifest. Finally, we have addressed the existence of a perturbative regime in which these one-loop results give the leading result by arguing that the bulk field two-loop diagrams should be at most logarithmically divergent and that it is at least feasible that the brane-localized two-loop diagrams may follow this power counting.

In addition to $\mu \rightarrow e\gamma$, there is an analogous flavor-changing dipole-mediated process in the quark sector, $b \rightarrow s\gamma$ with additional gluon diagrams with the same topology as the Z diagrams described here. Because of operator mixing, connecting the $b \rightarrow s\gamma$ amplitude

to QCD observables requires the Wilson coefficients for both the photon penguin $C_{7\gamma}$ and the gluon penguin C_{8g} . A discussion can be found in [28], though there it was expected that these penguins would be logarithmically divergent. Further, it would be interesting to note whether the experimental bounds on this process admits the small- Y_* region of parameter space where the b term may be of the same order as the a term. We leave the explicit evaluation of the $b \rightarrow s\gamma$ amplitude in warped space to future work [97].

CHAPTER 3

$B \rightarrow S\gamma$ PENGUIN IN RS MODEL

Based on the 2012 article “Warped Penguins”, written in collaboration with Monika Blanke, Bibhushan Shakya and Philip Tanedo arXiv:1203.6650.

3.1 Introduction

The Randall-Sundrum (RS) scenario of a warped extra dimension provides an elegant solution to the hierarchy problem [330, 323, 222, 165, 237, 126] and a way to understand strongly coupled dynamics through the AdS/CFT correspondence [293, 51, 331]. For reviews see [147, 157, 220, 346]. One of the promising phenomenological features to come out of this framework is an explanation of the Standard Model (SM) flavor structure through the split-fermion scenario [222, 237, 53, 238]. In these models the Yukawa matrices are anarchic and the spectrum of fermion masses is generated by the exponential suppression of zero mode wavefunctions with a brane-localized Higgs [28]. This also automatically generates hierarchical mixing angles [28, 251, 270] and suppresses many tree-level flavor-changing neutral currents (FCNCs) through the RS-GIM mechanism [28]. In order to protect against large contributions to the T parameter coming from bulk gauge fields, one may introduce a gauged custodial symmetry [24] that is broken on the boundaries; a straightforward discrete extension of such a symmetry also protects against corrections to the $Zb\bar{b}$ vertex [22, 142] and flavor changing couplings of the Z boson to left-handed down-type quarks [95, 31].

These flavor protection mechanisms are not always sufficient to completely protect RS models from stringent experimental flavor constraints. In the quark sector, the tree-level exchange of Kaluza-Klein (KK) gluons and neutral electroweak gauge bosons contributes to meson-antimeson mixing and induces left-right operators. These operators are not present in the SM and receive a significant enhancement through QCD effects due to their large anomalous dimension. In the kaon system they are also chirally enhanced by a factor of m_K^2/m_s^2 . These contributions lead to new CP violating effects in the kaon system, namely the well-measured observable ε_K , and result in generic bounds of $\mathcal{O}(10 -$

20 TeV) for the KK gluon mass [31, 151, 94, 113, 189, 73, 125]. To reduce this bound, one must introduce additional structure such as horizontal symmetries [335, 153], flavor alignment [204, 159], or an extended strong sector [74]. Alternately, one may promote the Higgs to a bulk field [19] to localize the fermion zero modes closer to the UV brane.

Additional constraints on the RS flavor sector come from loop-induced dipole operators through penguin diagrams. The first estimates for these operators were performed in [28, 251, 27, 20] assuming UV sensitivity at all loops within the 5D effective theory and a calculation within the two-site approach was performed in [19]. In [28] the bound $M_{\text{KK}} > \mathcal{O}(10 \text{ TeV})$ was derived from the constraint on the neutron electric dipole moment. The RS dipole contributions lead to dangerously large effects in direct CP violation in the $K \rightarrow \pi\pi$ decays measured by the ratio ε'/ε [214]. Combining the bound from the latter ratio with the ε_K constraint leads to a lower bound on the KK scale independent of the strength of the 5D Yukawa. More recently it was shown that even for the brane Higgs scenario the one-loop induced magnetic penguin diagrams are finite in RS and can be calculated effectively in a manifestly 5D formalism [156]. The lepton flavor violating penguin $\mu \rightarrow e\gamma$ sets bounds on the KK and anarchic Yukawa scales that are complementary to tree-level processes, so the tension between these bounds quantifies the degree of tuning required in the 5D Yukawa matrix [20].

In this paper we examine the calculation and phenomenological observables of the quark sector processes $b \rightarrow q\gamma$ ($q = s, d$) in the RS framework with a brane-localized Higgs field using the mixed position–momentum space formalism. These processes differ from their leptonic analogs for various reasons beyond the spectrum and diagrams involved. Firstly, while the branching ratio of $\mu \rightarrow e\gamma$ is only bounded from above, the branching ratios for $B \rightarrow X_s\gamma$ and, to a lesser extent, $B \rightarrow X_d\gamma$ are well-measured and in good agreement with the SM. Secondly, theoretical predictions are more involved due

to the renormalization group (RG) evolution from the KK scale to the B meson scale and hadronic effects at the latter scale. The RG running over this large range of energy scales introduces a sizable mixing between the various effective operators, so that one must also include the effects of the magnetic gluon penguin $C_8^{(\prime)}$ in addition to the magnetic photon penguin $C_7^{(\prime)}$.

After reviewing the flavor structure of RS models in Section 3.2, we calculate the $C_7^{(\prime)}$ and $C_8^{(\prime)}$ Wilson coefficients of the quark dipole operators in Section 3.3. We provide explicit formulae for the dominant RS contributions to the Wilson coefficients at the KK scale in both the minimal and custodial models and analyze the size of these contributions. In Sections 3.4 and 3.5, we subsequently perform the RG evolution down to the B meson scale and obtain predictions for the branching ratios $\text{Br}(B \rightarrow X_{s,d}\gamma)$.

Finally, in Section 3.6, we investigate the phenomenological implications on a number of benchmark observables related to the photon and gluon penguin operators. We first show that these operators give non-negligible constraints for both minimal and custodial models. We then restrict our attention to realistic models with a bulk custodial symmetry $SU(2)_L \times SU(2)_R \times U(1)_X \times P_{LR}$ and consider the effect of benchmark observables on points in parameter space that pass tree-level constraints as evaluated in [94]. Rather than performing a detailed analysis of all observables provided by the $B \rightarrow X_s\gamma$, $B \rightarrow K^*\gamma$, $B \rightarrow X_s\mu^+\mu^-$ and $B \rightarrow K^*\mu^+\mu^-$ decay modes, we focus on a number of benchmark observables in order to illustrate the pattern of effects and leave a more detailed analysis for future work. Specifically we study:

- The branching ratio $\text{Br}(B \rightarrow X_s\gamma)$ and the CP averaged branching ratio $\langle \text{Br}(B \rightarrow X_d\gamma) \rangle$ which we impose as constraints on our parameter scan.
- The branching ratio $\text{Br}(B \rightarrow X_s\mu^+\mu^-)$ and the forward backward asymmetry A_{FB} in

$B \rightarrow K^* \mu^+ \mu^-$. Stringent data that are in good agreement with the SM exist for both observables, placing strong bounds on various new physics (NP) scenarios. The custodial RS model naturally predicts small effects in these observables since they are rather insensitive to NP contributions to the primed magnetic Wilson coefficients.

- The time-dependent CP asymmetry $S_{K^* \gamma}$ in $B \rightarrow K^* \gamma$ and the transverse asymmetry $A_T^{(2)}$ in $B \rightarrow K^* \mu^+ \mu^-$, evaluated in the region of low dimuon invariant mass $1 \text{ GeV}^2 < q^2 < 6 \text{ GeV}^2$.

Since the RS contributions generally exhibit the hierarchy $\Delta C'_7 \gg \Delta C_7$ [28, 27] the latter observables are particularly suited to look for RS contributions. CP asymmetries in radiative B decays were already suggested in [28, 27] as good probes to look for RS effects. We quantify the possible size of effects and study the possible RS contributions to the various observables in a correlated manner. We also included the transverse asymmetry $A_T^{(2)}$, which has not been considered in the context of RS models before.

3.2 Flavor in Randall-Sundrum models

We summarize here the relevant aspects of flavor physics and the RS scenario. For a review of the general framework see e.g. [157, 220, 346, 73, 31]. We consider a 5D warped interval $z \in [R, R']$ with an infrared (IR) brane at $z = R' \sim (\text{TeV})^{-1}$ and an ultraviolet (UV) brane at $z = R \sim M_{\text{Pl}}$, the AdS curvature scale. In conformal coordinates the metric is

$$ds^2 = \left(\frac{R}{z}\right)^2 (dx_\mu dx_\nu \eta^{\mu\nu} - dz^2). \quad (3.2.1)$$

One may recover the classic RS conventions with the identifications $z = R \exp(ky)$ and $k = 1/R$, $k \exp(-kL) = 1/R'$. Fermions are Dirac fields that propagate in the bulk and

can be written in terms of left- and right-handed Weyl spinors χ and $\bar{\psi}$ via

$$\Psi(x, z) = \begin{pmatrix} \chi(x, z) \\ \bar{\psi}(x, z) \end{pmatrix}. \quad (3.2.2)$$

In order to obtain a spectrum with chiral zero modes, fermions must have chiral (orbifold) boundary conditions,

$$\psi_L(x^\mu, R) = \psi_L(x^\mu, R') = 0 \quad \text{and} \quad \chi_R(x^\mu, R) = \chi_R(x^\mu, R') = 0, \quad (3.2.3)$$

where the subscripts L and R denote the $SU(2)_L$ doublet (L) and singlet (R) representations, i.e. the chirality of the zero mode (SM fermion). The localization of the normalized zero mode profile is controlled by the dimensionless parameter c ,

$$\chi_c^{(0)}(x, z) = \frac{1}{\sqrt{R'}} \left(\frac{z}{R}\right)^2 \left(\frac{z}{R'}\right)^{-c} f_c \chi_c^{(0)}(x) \quad \text{and} \quad \psi_c^{(0)}(x, z) = \chi_{-c}^{(0)}(x, z), \quad (3.2.4)$$

where c/R is the fermion bulk mass. Here we have defined the RS flavor function characterizing the fermion profile on the IR brane,

$$f_c = \sqrt{\frac{1 - 2c}{1 - (R/R')^{1-2c}}}. \quad (3.2.5)$$

We assume that the Higgs is localized on the IR brane. The Yukawa coupling is

$$S_{\text{Yuk}} = \int d^4x \left(\frac{R}{R'}\right)^4 \left[-\frac{1}{\sqrt{2}} \left(\bar{Q}_i \cdot \tilde{H} R Y_{u,ij} U_j + \bar{Q}_i \cdot H R Y_{d,ij} D_j + \text{h.c.} \right) \right] \quad (3.2.6)$$

where Y_{ij} are dimensionless 3×3 matrices such that $(Y_5)_{ij} = R Y_{ij}$ is the dimensionful parameter appearing in the 5D Lagrangian with Y assumed to be a random ‘anarchic’ matrix with average elements of order Y_* . After including warp factors and canonically normalizing fields, the effective 4D Yukawa and zero mode mass matrices are

$$y_{ij}^{\text{SM}} = f_{c_{L_i}} Y_{ij} f_{-c_{R_j}} \quad m_{ij} = \frac{v}{\sqrt{2}} y_{ij}^{\text{SM}}, \quad (3.2.7)$$

so that the fermion mass hierarchy is set by the $f_1 \ll f_2 \ll f_3$ structure for both left- and right-handed zero modes. At the same time, the hierarchical pattern of the CKM matrix is also generated naturally. In other words, the choice of c for each fermion family introduces additional flavor structure into the theory that generates the zero mode spectrum while allowing the fundamental Yukawa parameters to be anarchic.

In this document we work in the gauge basis where the bulk mass matrices and the interactions of the neutral gauge bosons are flavor diagonal but not flavor universal. The Yukawa couplings are non-diagonal in this basis and cause the resulting fermion mass matrices to be non-diagonal. Since these off-diagonal entries are governed by the small parameter vR' , we will treat them as a perturbative correction in the mass insertion approximation.

Realistic RS models typically require a mechanism to suppress generically large contributions to the Peskin-Takeuchi T parameter and the $Zb\bar{b}$ coupling; a common technique is to extend the bulk gauge symmetry to [24, 155, 23, 22, 142, 122, 118]

$$SU(3)_c \times SU(2)_L \times SU(2)_R \times U(1)_X \times P_{LR}. \quad (3.2.8)$$

Here P_{LR} is a discrete symmetry exchanging the $SU(2)_L$ and $SU(2)_R$ factors; in order to protect the left-handed $Zb\bar{b}$ coupling from anomalously large corrections, the left-handed down type quarks have to be eigenstates under P_{LR} . This in turn requires enlarged fermion representations with respect to the minimal model. As we will see later, while the additional gauge bosons present in the custodial model do not have a significant impact on the $b \rightarrow q\gamma$ and $b \rightarrow qg$ ($q = d, s$) amplitudes, the additional fermion modes contribute and generally enhance the effect.

3.3 Calculation of the $b \rightarrow q\gamma$ Penguin in RS

We now calculate the RS contributions to the $b \rightarrow q\gamma$ and $b \rightarrow qg$ ($q = d, s$) decays. These contributions are calculated at the KK scale $M_{\text{KK}} \sim 1/R'$; in subsequent sections we will relate these to renormalization group (RG) evolved coefficients and observables at the low scale $\sim m_b$.

We only evaluate the dominant diagrams, working in Feynman gauge and the mass insertion approximation, where the expansion parameter is $vR'/\sqrt{2} \sim \mathcal{O}(0.1)$. We have checked explicitly that the diagrams presented here dominate those that were neglected by at least an order of magnitude; a more detailed calculation is beyond the scope of this work and, in our opinion, premature before the discovery of RS KK modes. We refer to [156] for details of the 5D calculation, Feynman rules, and guidelines for estimating the dominant diagrams. For additional notation and conventions, especially with respect to the custodially protected model, see [31]. See Appendix B.3 for comments on theory uncertainties.

3.3.1 Effective Hamiltonian for $b \rightarrow q\gamma$ transitions

The $b \rightarrow q\gamma$ ($q = d, s$) transitions are most conveniently described by an effective Hamiltonian in the operator product expansion, see e. g. [111] for a review. The dipole terms most sensitive to new physics are

$$\mathcal{H}_{\text{eff}} = -\frac{G_F}{\sqrt{2}} V_{tq}^* V_{tb} \left[C_7(\mu) Q_7(\mu) + C_7'(\mu) Q_7'(\mu) + C_8(\mu) Q_8(\mu) + C_8'(\mu) Q_8'(\mu) \right] + \text{h.c.}, \quad (3.3.9)$$

where we neglect terms proportional to $V_{uq}^* V_{ub}$. The effective operators are

$$Q_7 = \frac{e}{4\pi^2} m_b (\bar{q} \sigma_{\mu\nu} P_R b) F^{\mu\nu} \quad Q'_7 = \frac{e}{4\pi^2} m_b (\bar{q} \sigma_{\mu\nu} P_L b) F^{\mu\nu} \quad (3.3.10)$$

$$Q_8 = \frac{g_s}{4\pi^2} m_b (\bar{q} \sigma_{\mu\nu} T^a P_R b) G^{\mu\nu,a} \quad Q'_8 = \frac{g_s}{4\pi^2} m_b (\bar{q} \sigma_{\mu\nu} T^a P_L b) G^{\mu\nu,a}, \quad (3.3.11)$$

where $P_{L,R} = (1 \mp \gamma^5)/2$. In this document we will focus on new contributions from the RS model to these operators. There are also contributions from non-dipole operators $Q_{1,\dots,6}$ and their chirality-flipped (primed) counterparts, but these are far less sensitive to NP and can be assumed to be equal to their SM contributions¹.

At leading order in the SM, the primed Wilson coefficients $C'_{7,8}$ are suppressed by m_s/m_b and therefore negligible, so the relevant Wilson coefficients at the scale M_W are

$$C_7^{\text{SM}}(M_W) = -\frac{1}{2} D'_0(x_t), \quad C_8^{\text{SM}}(M_W) = -\frac{1}{2} E'_0(x_t), \quad (3.3.12)$$

where $x_t = m_t^2/M_W^2$, and $D'_0(x_t) \approx 0.37$ and $E'_0(x_t) \approx 0.19$ are loop functions given explicitly in (3.15–3.16) of [112]. In what follows we refer to the RS contributions to these operators as $\Delta C_{7,8}^{(\prime)}$.

3.3.2 Structure of the amplitude

In order to calculate the $b \rightarrow (s, d)\gamma$ and $b \rightarrow (s, d)g$ penguins, we work in a manifestly 5D framework. Unlike the 4D KK reduction, this procedure automatically incorporates the entire KK tower² at the cost of an expansion with respect to the Higgs-induced mass term ($\sim vR'$).

¹The impact of flavor changing neutral gauge bosons on the operators $Q_{1,\dots,6}$ has recently been studied in [115]. Since the relevant contributions in RS are suppressed both by the KK scale and the RS GIM mechanism, the contributions are expected to be small and will be neglected in this paper.

² An alternate method of including the entire KK tower based on residue theorems was presented in [201], though it obfuscates the physical intuition presented below.

Using the on-shell condition for the photon, the general form of the left-to-right chirality $f_i^L(p) \rightarrow f_j^R(p')\gamma$ amplitude, C_7 , in a 5D theory can be written as [156, 287]

$$\mathcal{M}_{L^i \rightarrow R^j} = \frac{ie}{16\pi^2} \frac{vR'^2}{\sqrt{2}} \sum_{k,\ell} \left(a_{k\ell} Y_{ik}^\dagger Y_{k\ell} Y_{\ell j}^\dagger + b_{ij} Y_{ij}^\dagger \right) f_{Q_i} f_{D_j} \bar{u}_{p'}^R [(p+p')^\mu - (m_b + m_q)\gamma^\mu] u_p^L \epsilon_\mu \quad (3.3.13)$$

where ϵ is the photon polarization. The chirality flipped amplitude is given by the conjugate of this result, $\mathcal{M}_{R^i \rightarrow L^j} = (\mathcal{M}_{L^j \rightarrow R^i})^\dagger$. The expression for the gluon penguin is analogous with the appropriate substitutions. Using the fermion equations of motion, the term in the square brackets gives the required dipole structure $\sigma^{\mu\nu} F_{\mu\nu}$, so a simple way to identify the gauge-invariant contribution to the amplitude is to determine the coefficient of the $(p+p')^\mu$ term [287]. In [156] this observation was used to show the manifest one-loop finiteness of these dipole transitions in 5D theories. Matching (3.3.13) to the effective Hamiltonian (3.3.9) yields expressions for the RS contributions to the Wilson coefficients, ΔC .

We refer to the coefficients $a_{k\ell}$ and b_{ij} in (3.3.13) as the *anarchic* and the *misalignment* contributions, respectively. They are products of couplings and dimensionless integrals whose flavor indices reflect the bulk mass dependence of internal propagators. Upon diagonalizing the SM fermion mass matrix, the anarchic term a is not diagonalized and generally remains anarchic. On the other hand, in the limit where the bulk masses are degenerate, the flavor structure of the b term is aligned with the SM Yukawa matrices and thus contains no flavor-changing transitions in the mass basis [28, 19, 20]. This alignment is pronounced for the first and second generation fermions because their bulk masses are nearly degenerate, but special care is required for the third generation quarks since these are localized towards the IR brane. The physical contribution of the b coefficient comes from the robustness of off-diagonal elements of $b_{ij} Y_{ij} f_{Q_i} f_{D_j}$ after passing to the basis in which $Y_{ij} f_{Q_i} f_{D_j}$ is diagonalized. Contrary to the usual assumption of Yukawa anarchy,

the overall size of the b term depends on the misalignment of the specific anarchic Yukawa matrix relative to the set of bulk masses as flavor spurions. One measure of this effect is the 1σ standard deviation from $b = 0$ in a scan over random anarchic matrices [156]; we use this to identify the dominant contributions to this misalignment term.

By assumption, the anarchic contribution is independent of the SM flavor sector, so there is no analogous alignment suppression to the a coefficient. However, depending on the internal modes in the loop, each diagram contributing to this term carries one of two possible independent flavor spurions that can be built out of the Yukawa matrices that may enter this product: $Y_u^\dagger Y_u Y_d^\dagger$ and $Y_d^\dagger Y_d Y_u^\dagger$. These matrices may have arbitrary relative phase, so the two terms may add either constructively or destructively. The misalignment contribution is a third independent flavor spurion, which also carries a relative phase dependent on the particular choice of parameters.

We express the anarchic (a) and misalignment (b) coefficients in terms of dimensionless integrals, which are defined in Appendix B.1. The C_8 diagrams where a gluon is emitted from an internal gluon have integral results that are typically $\mathcal{O}(1)$ while the integrals for the other diagrams are typically $\mathcal{O}(10^{-1})$ in magnitude. Note that the contribution to a from each diagram matches what is expected from a naive dimensional analysis. This is in contrast to the analogous calculation for $\mu \rightarrow e\gamma$, where the leading diagrams are smaller than the naive estimated size. There are thus no problems with the two-loop contribution yielding a larger contribution than expected from the perturbative expansion.

Below we present the calculation for the right-to-left chirality (unprimed) Wilson coefficients $\Delta C_{7,8}$ for $b \rightarrow q$; the left-to-right chirality (primed) Wilson coefficients are obtained by Hermitian conjugation of the $q \rightarrow b$ amplitude. The anarchic contribution to the left-to-right chirality coefficients are enhanced over the right-to-left coefficients by a

factor of f_{b_L}/f_{b_R} , while the misalignment contribution is of the same order of magnitude. This behavior is explained qualitatively in Appendix B.2 and demonstrated numerically in Section 3.6.

3.3.3 Calculation of $\Delta C_7^{(\prime)}$

Fig. 3.1 shows the dominant contributions to the C_7 photon penguin operator. The RS contribution to the $b \rightarrow q\gamma$ Wilson coefficient is

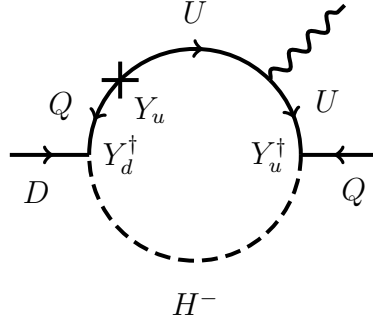
$$\Delta C_7 = \frac{-vR'^2}{8m_b G_F} (V_{tq}^* V_{tb})^{-1} \sum_{ijk\ell} (U_{qi}^{D_L})^\dagger f_{Q_i^d} f_{D_j} \left[\sum_{k,\ell} a_{k\ell} Y_{ik}^{u\dagger} Y_{k\ell}^u Y_{\ell j}^{d\dagger} + b_{ij} Y_{ij}^{d\dagger} \right] U_{jb}^{D_R}. \quad (3.3.14)$$

$U^{D_{L,R}}$ are the rotation matrices between the 5D gauge and the light down quark mass bases.

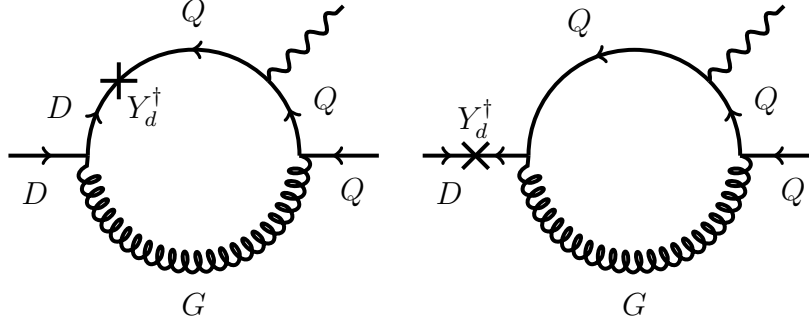
Note that throughout our analysis we use the tree level matching condition for the 5D gauge couplings and neglect possible brane kinetic terms that may alter this matching. While this affects the misalignment contribution to $C_7^{(\prime)}$ and the calculation for $C_8^{(\prime)}$, the anarchic contribution to $C_7^{(\prime)}$, containing only one gauge coupling vertex instead of three, remains relatively unaffected. Since the latter gives the dominant contribution to the observables discussed in section 3.6, we do not expect this assumption to have a significant impact on our predictions.

ΔC_7 : anarchic contribution

The dominant anarchic contribution is the diagram with one mass insertion and a charged Higgs (Goldstone) in the loop, Fig. 3.1a. Note that this diagram is not present in the



(a) Charged Goldstone loop



(b) Gluon (G_μ or G_5) loops with a single mass insertion

Figure 3.1: Leading contributions to the anarchic (a) and misalignment (b) terms of the C_7 Wilson coefficient. Arrows indicate $SU(2)_L$ representation; this is equivalent to labeling the chirality of the zero mode for SM fields. Here Q , U and D denote the 5D chiral fermion fields containing the SM left-handed doublets and right-handed up and down singlets, respectively. H^- is the charged component of the Higgs doublet that serves as the Goldstone boson of W^- after electroweak symmetry breaking, and G is the 5D gluon field. Additional diagrams related by exchanging the order of the mass insertion and photon emission are left implicit.

analogous leptonic penguin, which has a neutrino in the loop. The next-to-leading diagrams contributing to this coefficient are gluon loops with three mass insertions. These diagrams carry an independent flavor structure ($Y_d^\dagger Y_d Y_d^\dagger$) and can interfere either constructively or destructively with Fig. 3.1a. However, they are only 5% corrections because they have a different topology, carry two more mass insertions, and are proportional to $Q_d = -1/3$; these factors more than compensate for the gauge coupling enhancement of $g_s^2 \ln R'/R \approx 36$. The value for the a coefficient in (3.3.14) coming from the penguin in

Fig. 3.1a is a dimensionless integral whose explicit form is given in (B.1.11),

$$a = Q_u I_{C_{7a}}, \quad (3.3.15)$$

where $Q_u = 2/3$ is the charge of the internal up-type quark.

ΔC_7 : misalignment contribution

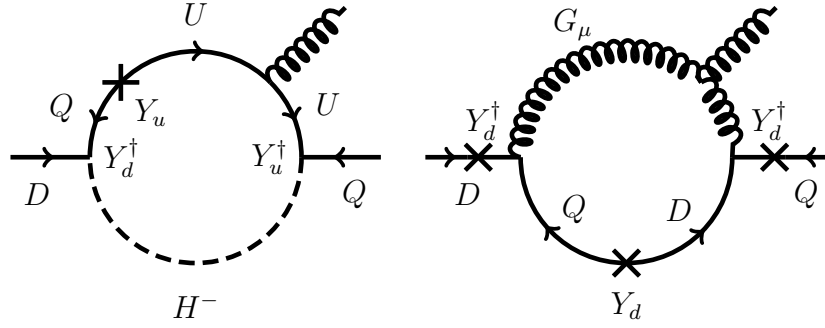
The dominant misalignment contributions come from gluon diagrams with a single mass insertion. As shown in Fig. 3.1b, this insertion can either be on an internal or external fermion line. The final misalignment contribution in (3.3.14) is

$$b = Q_d \frac{4}{3} \left(g_s^2 \ln \frac{R'}{R} \right) I_{C_{7b}}. \quad (3.3.16)$$

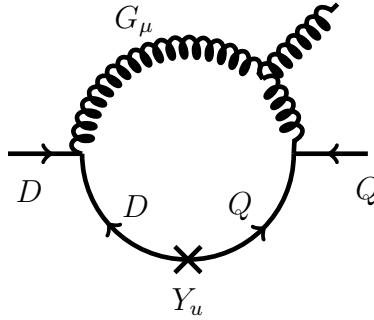
Here Q_d is the charge of the internal down-type quark, $4/3$ is a color factor, $\ln R'/R$ is a warp factor associated with bulk gauge couplings, and $I_{C_{7b}}$ is a dimensionless integral defined in (B.1.12).

3.3.4 Calculation of $\Delta C_8^{(\prime)}$

The gluon penguin operators C_8 and C'_8 differ from their photon counterparts due to additional QCD vertices available and the magnitude of the QCD coupling, $g_{5D}^2/R = g_s^2 \ln R'/R \approx 36$. Because of this, the dominant diagrams contributing to $b \rightarrow qg$ cannot be obtained from $b \rightarrow q\gamma$ by simply replacing the photon with a gluon in the leading diagrams for $C_7^{(\prime)}$. The general expression for ΔC_8 is the same as that for ΔC_7 in (3.3.14), with coefficients a and b coming from the diagrams shown in Fig. 3.2.



(a) Charged Goldstone and three mass insertion gluon loops. Not shown: gluon loop with two and three internal line mass insertions.



(b) One mass insertion gluon loop

Figure 3.2: Leading contributions to the a and b terms of the C_8 Wilson coefficient following the notation of Fig. 3.1. G_μ refers to only the gluon four-vector.

ΔC_8 : anarchic contribution

There are two classes of dominant contributions to the anarchic (a) coefficient in $C_8^{(\prime)}$. In addition to the charged Higgs diagrams analogous to Fig. 3.1a, there are gluon diagrams with three mass insertions on the fermion lines, which are now sizable due to the size of the strong coupling constant and the three-point gauge boson vertex. Of the latter class, one only needs to consider diagrams with at most one mass insertion on each external leg since sequential insertions on an external leg are suppressed by factors of $m_q R'$. Note that these two sets of diagrams contribute with different products of Yukawa matrices; while the Higgs diagrams are proportional to $Y_u^\dagger Y_u Y_d^\dagger$, the gluon diagrams are proportional to

$Y_d^\dagger Y_d Y_d^\dagger$. Thus these two terms may add either constructively or destructively and may even add with different relative sizes if there is a hierarchy between the overall scale of the up- and down-type 5D anarchic Yukawas. The a coefficient is

$$a = I_{C_{7a}} \oplus \frac{3}{2} \left(g_s^2 \ln \frac{R'}{R} \right)^2 \left(\frac{R'v}{\sqrt{2}} \right)^2 I_{C_{8a}}^G, \quad (3.3.17)$$

where we have written \oplus to indicate that the two terms carry independent flavor spurions. Here $I_{C_{7a}}$ is the same dimensionless integral appearing in (3.3.15). The second term includes color factors, warped bulk gauge couplings, and explicit mass insertions in addition to the dimensionless integral $I_{C_{8a}}$ defined in (B.1.15).

ΔC_8 : misalignment contribution

The single mass insertion gluon emission diagram in Fig. 3.2b gives the dominant misalignment term. Additional diagrams with the gluon emission from the quark line are suppressed by a relative color factor of $1/6$ versus $3/2$ and can be neglected. The expression for this diagram is

$$b = \frac{3}{2} \left(g_s^2 \ln \frac{R'}{R} \right) I_{C_{8b}}. \quad (3.3.18)$$

with $I_{C_{8b}}$ defined in (B.1.19). We have again pulled out an explicit color factor and the warped bulk gauge coupling.

3.3.5 Modifications from custodial symmetry

In models with a gauged bulk custodial symmetry, the additional matter content may also contribute to the $b \rightarrow q\gamma(g)$ transitions. Since custodial symmetry enlarges the electroweak sector, the only way to connect these custodial modes to the external SM states

that gives contributions comparable to those in Fig. 3.1 and Fig. 3.2 is through Higgs interactions, as contributions from W and Z loops and their custodial siblings are suppressed due to the relative size of the electroweak gauge couplings compared to the Yukawa and strong couplings. The leading custodial contributions are shown in Fig. 3.3; these are the same diagrams that contribute to the anarchic (a) terms of the C_7 and C_8 Wilson coefficients and now appear with additional custodial fermions, denoted by U', U'' , and D' . Observe that each of these custodial contributions is proportional to $Y_d^\dagger Y_d Y_d^\dagger$. In partic-

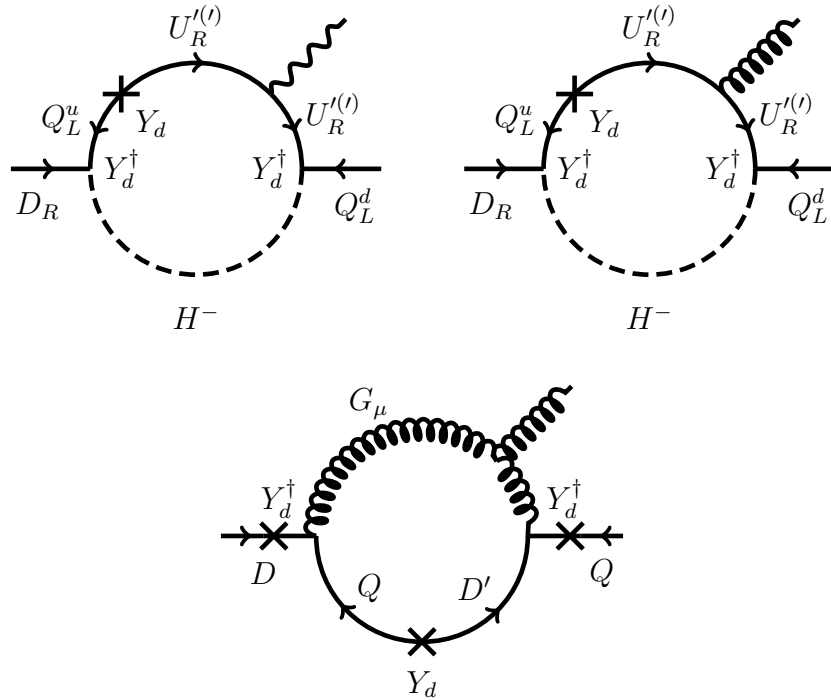


Figure 3.3: Additional custodial diagrams contributing to the C_7 and C_8 coefficients.

ular, the custodial Higgs diagrams carry a flavor structure that is independent of that of their minimal model counterparts.

By construction, boundary conditions for custodial fermions are chosen such that they have no zero modes. In particular, the U' , U'' , and D' have the same IR boundary condition as their SM counterparts but the opposite UV boundary condition. Since the lo-

calization of the Higgs pulls the loop towards the IR brane, the contribution of these custodial fermions is well-approximated by the contributions of their SM counterparts. In other words, the custodial fermions only have KK modes, but since the minimal model diagrams are dominated by the KK fermion contribution, the custodial modes contribute approximately equally to the process. From this point of view, it is also clear that custodial diagrams do not make appreciable contributions to the b coefficient from misalignment because they do not carry internal zero modes, which are sensitive to the bulk mass spectrum.

Note that the U' and U'' couplings to the charged Higgs come with a factor of $1/\sqrt{2}$ while the D' coupling to the Higgs does not [94]. Thus the additional custodial diagrams contribute an analytic structure that is nearly identical to the minimal model diagrams except for the Yukawa matrices, which now come with the product $Y_d^\dagger Y_d Y_d^\dagger$. Since this is independent of the $Y_d^\dagger Y_u Y_u^\dagger$ flavor spurion in the minimal model diagrams, the addition of the custodial diagrams generically enhances the penguin amplitude by less than the factor of two that one would obtain in the limit $Y_d = Y_u$. This shows that while custodial symmetry can be used to suppress tree-level flavor changing effects in RS models, this comes at the cost of generically enhancing loop-level flavor processes.

3.4 Radiative B decays

We now examine the physical observables most directly related to the parton-level $b \rightarrow q(\gamma, g)$ operators derived above: B meson decays with an on-shell photon.

3.4.1 The $B \rightarrow X_{s,d}\gamma$ decay

The SM predictions for the inclusive decays $B \rightarrow X_{s,d}\gamma$ are [305, 146]

$$\text{Br}(B \rightarrow X_s\gamma)_{\text{SM}} = (3.15 \pm 0.23) \cdot 10^{-4}, \quad \langle \text{Br}(B \rightarrow X_d\gamma) \rangle_{\text{SM}} = (15.4_{-3.1}^{+2.6}) \cdot 10^{-6}. \quad (3.4.19)$$

These can be compared to the measured values [55]

$$\text{Br}(B \rightarrow X_s\gamma)_{\text{exp}} = (3.55 \pm 0.27) \cdot 10^{-4}, \quad \langle \text{Br}(B \rightarrow X_d\gamma) \rangle_{\text{exp}} = (14 \pm 5) \cdot 10^{-6}. \quad (3.4.20)$$

Here $\langle \text{Br}(B \rightarrow X_d\gamma) \rangle$ refers to the CP averaged branching ratio in which the hadronic uncertainties cancel to a large extent [84]. We have extrapolated the experimental value for $\langle \text{Br}(B \rightarrow X_d\gamma) \rangle$ to the photon energy cut $E_\gamma > 1.6 \text{ GeV}$ used for the theory prediction.

Rather than performing an extensive error analysis, we simply require the new RS contributions to fulfill the constraints

$$\Delta \text{Br}(B \rightarrow X_s\gamma) = \text{Br}(B \rightarrow X_s\gamma)_{\text{exp}} - \text{Br}(B \rightarrow X_s\gamma)_{\text{SM}} = (0.4 \pm 0.7) \cdot 10^{-4} \quad (3.4.21)$$

$$\Delta \text{Br}(B \rightarrow X_d\gamma) = \langle \text{Br}(B \rightarrow X_d\gamma) \rangle_{\text{exp}} - \langle \text{Br}(B \rightarrow X_d\gamma) \rangle_{\text{SM}} = -(1 \pm 11) \cdot 10^{-6} \quad (3.4.22)$$

Neglecting all uncertainties associated with NP contributions, these constraints represent the 2σ ranges when combining experimental and theoretical uncertainties in quadrature. Although the data and prediction for $B \rightarrow X_d\gamma$ are currently less precise than those for $B \rightarrow X_s\gamma$, an important and partly complementary constraint can be obtained from the former decay, as recently pointed out in [146]. Since the data for $B \rightarrow X_d\gamma$ lie slightly below the SM prediction, $\Delta \text{Br}(B \rightarrow X_d\gamma) < 0$ is somewhat favored, leaving little room for NP contributing to C'_7 . In contrast, a positive NP contribution to $\text{Br}(B \rightarrow X_s\gamma)$ is welcome to bring the theory prediction closer to the data. We note that if the tree level values for the CKM parameters are used instead of the SM best fit values, the predicted central value for $\langle \text{Br}(B \rightarrow X_d\gamma) \rangle_{\text{SM}}$ rises to about $19 \cdot 10^{-6}$, increasing the tension with the data.

3.4.2 Master formula for $\text{Br}(B \rightarrow X_s \gamma)$

Following the strategy of [115, 114, 96], which use the results of [306], the “master formula” for the inclusive $B \rightarrow X_s \gamma$ branching ratio in terms of the SM branching ratio, Br_{SM} , and NP contributions to the Wilson coefficients is

$$\text{Br}(B \rightarrow X_s \gamma) = \text{Br}_{\text{SM}} + 0.00247 \left[|\Delta C_7(\mu_b)|^2 + |\Delta C_7'(\mu_b)|^2 - 0.706 \text{Re}(\Delta C_7(\mu_b)) \right]. \quad (3.4.23)$$

The RS contributions to $\Delta C_7^{(\prime)}(\mu_b)$ are obtained from the RG evolution of $\Delta C_7^{(\prime)}$ and $\Delta C_8^{(\prime)}$, calculated in Section 3.3 at the high scale $M_{\text{KK}} = 2.5 \text{ TeV}$, down to the B scale, $\mu_b = 2.5 \text{ GeV}$,

$$\Delta C_7^{(\prime)}(\mu_b) = 0.429 \Delta C_7^{(\prime)}(M_{\text{KK}}) + 0.128 \Delta C_8^{(\prime)}(M_{\text{KK}}). \quad (3.4.24)$$

All known SM non-perturbative contributions have been taken into account while the RS contribution is included at leading order neglecting uncertainties. This approach is an approximation to studying the effects of RS physics on the decay in question; however, in view of the other uncertainties involved—such as the mass insertion approximation and taking into account only the leading diagrams—this approach gives sufficiently accurate results to estimate the size of RS contributions. A more accurate and detailed analysis is beyond the scope of our analysis and, in our view, premature before the discovery of RS KK modes.

3.4.3 Master formula for $\langle \text{Br}(B \rightarrow X_d \gamma) \rangle$

A master formula can be obtained in a similar manner for the CP-averaged $B \rightarrow X_d \gamma$ branching ratio. Using the expressions collected in [146, 96, 255] we find

$$\begin{aligned} \langle \text{Br}(B \rightarrow X_d \gamma) \rangle = \langle \text{Br}_{\text{SM}} \rangle + 10^{-5} & \left[1.69 (|\Delta C_7|^2 + |\Delta C_7'|^2) + 0.24 (|\Delta C_8|^2 + |\Delta C_8'|^2) \right. \\ & + 1.06 \text{Re} [\Delta C_7 \Delta C_8^* + \Delta C_7' \Delta C_8'^*] - 3.24 \text{Re}(\Delta C_7) \\ & \left. - 0.16 \text{Im}(\Delta C_7) - 1.03 \text{Re}(\Delta C_8) - 0.04 \text{Im}(\Delta C_8) \right] \end{aligned} \quad (3.4.25)$$

where all of the RS contributions to the $b \rightarrow d$ Wilson coefficients $\Delta C_{7,8}^{(\prime)}$ are evaluated at M_{KK} .

3.4.4 Analytic estimate of constraints

Assuming anarchic Yukawa couplings, one may estimate the size of the RS contributions to the Wilson coefficients in terms of the anarchic coefficients in Section 3.3.3,

$$|\Delta C_7(M_{\text{KK}})^{b \rightarrow s, d \gamma}| \sim \frac{1}{4\sqrt{2}G_F} a Y_*^2 R'^2 \sim 0.015 a Y_*^2 \left(\frac{R'}{1 \text{ TeV}^{-1}} \right)^2, \quad (3.4.26)$$

$$|\Delta C_7'(M_{\text{KK}})^{b \rightarrow s \gamma}| \sim \frac{1}{4\sqrt{2}G_F} a Y_*^2 R'^2 \frac{m_s}{m_b |V_{ts}|^2} \sim 0.18 a Y_*^2 \left(\frac{R'}{1 \text{ TeV}^{-1}} \right)^2, \quad (3.4.27)$$

$$|\Delta C_7'(M_{\text{KK}})^{b \rightarrow d \gamma}| \sim \frac{1}{4\sqrt{2}G_F} a Y_*^2 R'^2 \frac{m_d}{m_b |V_{td}|^2} \sim 0.20 a Y_*^2 \left(\frac{R'}{1 \text{ TeV}^{-1}} \right)^2, \quad (3.4.28)$$

where we neglect the misalignment contributions. Here Y_* is the average size of the anarchic Yukawa couplings Y_{ij} which we assume to be equal for Y_u and Y_d .

Generically the contribution to the chirality-flipped operator C_7' is larger than the one to C_7 by more than an order of magnitude. This is a direct consequence of the hierarchical pattern of quark masses and CKM angles: in order to fit the observed spectrum, the left-

handed b_L quark has to be localized close to the IR brane, and consequently its flavor violating interactions are far more pronounced than those of the right-handed b_R .

Neglecting the subdominant contributions from ΔC_7 and $\Delta C_8^{(\prime)}$, we can constrain the size of $\Delta C_7'$ by making use of the data on $\text{Br}(B \rightarrow X_s \gamma)$ and $\langle \text{Br}(B \rightarrow X_d \gamma) \rangle$. We obtain the following constraints from the master formulas and the experimental constraints quoted above:

$$|\Delta C_7'(M_{\text{KK}})^{b \rightarrow s \gamma}| < 0.47, \quad |\Delta C_7'(M_{\text{KK}})^{b \rightarrow d \gamma}| < 0.77. \quad (3.4.29)$$

Using (3.4.27–3.4.28) and $a \sim 0.33$ we can derive an upper bound on the size of the Yukawa couplings, Y_* ,

$$\frac{Y_* R'}{\text{TeV}^{-1}} < 2.8 \quad \text{from } B \rightarrow X_s \gamma, \quad (3.4.30)$$

$$\frac{Y_* R'}{\text{TeV}^{-1}} < 3.4 \quad \text{from } B \rightarrow X_d \gamma, \quad (3.4.31)$$

For $R' = 1 \text{ TeV}^{-1}$ these are of the same order as the perturbativity bound on the Yukawa coupling [151]. We see that the generic constraint from $B \rightarrow X_s \gamma$ is slightly stronger than that from $B \rightarrow X_d \gamma$ due to the larger uncertainties in the latter case. However, since they only differ by an $\mathcal{O}(1)$ factor, in specific cases the latter constraint may be more restrictive, so one must take both processes into account when constraining the RS parameter space.

3.4.5 CP asymmetry in $B \rightarrow K^* \gamma$

Like many extensions of the SM, RS generally induces large CP violating phases. It is thus of great interest to also study CP violation in $b \rightarrow s \gamma$ transitions. While the direct CP asymmetry in the inclusive $B \rightarrow X_s \gamma$ decay is in principle highly sensitive to NP contributions, in practice the SM contribution is dominated by long-distance physics and

therefore plagued by large non-perturbative uncertainties [85]. Consequently, a reliable prediction in the presence of NP is difficult.

Fortunately, a theoretically much cleaner observable is provided by the $B \rightarrow K^*\gamma$ decay. While its branching ratio is plagued by the theoretical uncertainty of the $B \rightarrow K^*$ form factors, this form factor dependence largely drops out of the time-dependent CP asymmetry [59, 69, 68]

$$\frac{\Gamma(\bar{B}^0(t) \rightarrow \bar{K}^{*0}\gamma) - \Gamma(B^0(t) \rightarrow K^{*0}\gamma)}{\Gamma(\bar{B}^0(t) \rightarrow \bar{K}^{*0}\gamma) + \Gamma(B^0(t) \rightarrow K^{*0}\gamma)} = S_{K^*\gamma} \sin(\Delta M_d t) - C_{K^*\gamma} \cos(\Delta M_d t). \quad (3.4.32)$$

The coefficient $S_{K^*\gamma}$ is highly sensitive to new RS contributions. At leading order it is given by [69, 33]

$$S_{K^*\gamma} \simeq \frac{2}{|C_7|^2 + |C_7'|^2} \text{Im} \left(e^{-i\phi_d} C_7 C_7' \right), \quad (3.4.33)$$

where the Wilson coefficients are to be taken at the scale μ_b . ϕ_d is the phase of B^0 - \bar{B}^0 mixing, which has been well measured in $B^0 \rightarrow J/\psi K_S$ decays to be $\sin \phi_d = 0.67 \pm 0.02$ [55].

From (3.4.33) we see that $S_{K^*\gamma}$ is very sensitive to new physics in the chirality flipped operator C_7' and vanishes in the limit $C_7' \rightarrow 0$. Consequently the SM prediction is suppressed by the ratio m_s/m_b and is therefore very small [68],

$$S_{K^*\gamma}^{\text{SM}} = (-2.3 \pm 1.6)\%. \quad (3.4.34)$$

Measuring a sizable CP asymmetry $S_{K^*\gamma}$ would thus not only be a clear sign of physics beyond the SM, but unambiguously indicate the presence of new right handed currents. The present experimental constraint [55, 351, 61],

$$S_{K^*\gamma}^{\text{exp}} = -16\% \pm 22\%, \quad (3.4.35)$$

is still subject to large uncertainties but already puts strong constraints on NP in $b \rightarrow s$ transitions [33]. A significant improvement is expected soon from LHCb, and the next generation B factories will reduce the uncertainty even further.

3.5 Semileptonic B decays

Semileptonic B decays such as $B \rightarrow X_s \mu^+ \mu^-$ and $B \rightarrow K^* \mu^+ \mu^-$ offer an interesting opportunity to not only look for deviations from the SM, but also to identify the pattern of NP contributions and therewith distinguish various NP scenarios. These decays receive contributions from semileptonic four-fermion operators $(\bar{s}b)(\bar{\mu}\mu)$ in addition to the magnetic dipole operators discussed earlier. While the dipole operators receive RS contributions first at the one-loop level as required by gauge invariance, the four fermion operators are already affected at tree level by the exchange of the Z boson and the heavy electroweak KK gauge bosons.

In this section we discuss the effective Hamiltonian for $b \rightarrow s \mu^+ \mu^-$ transitions. Subsequently we will review a number of benchmark observables that are relevant for the study of RS contributions.

3.5.1 Effective Hamiltonian for $b \rightarrow s \mu^+ \mu^-$ transitions

The effective Hamiltonian for $b \rightarrow s \mu^+ \mu^-$ reads

$$\mathcal{H}_{\text{eff}} = \mathcal{H}_{\text{eff}}(b \rightarrow s \gamma) - \frac{G_F}{\sqrt{2}} V_{ts}^* V_{tb} \left[C_{9V}(\mu) Q_{9V}(\mu) + C'_{9V}(\mu) Q'_{9V}(\mu) + C_{10A}(\mu) Q_{10A}(\mu) + C'_{10A}(\mu) Q'_{10A}(\mu) \right] + \text{h.c.}, \quad (3.5.36)$$

where we neglect the terms proportional to $V_{us}^* V_{ub}$, and

$$Q_{9V} = 2(\bar{s} \gamma_\mu P_L b)(\bar{\mu} \gamma^\mu \mu) \quad Q'_{9V} = 2(\bar{s} \gamma_\mu P_R b)(\bar{\mu} \gamma^\mu \mu) \quad (3.5.37)$$

$$Q_{10A} = 2(\bar{s} \gamma_\mu P_L b)(\bar{\mu} \gamma^\mu \gamma_5 \mu) \quad Q'_{10A} = 2(\bar{s} \gamma_\mu P_R b)(\bar{\mu} \gamma^\mu \gamma_5 \mu). \quad (3.5.38)$$

In the SM only the unprimed Wilson coefficients are relevant. At the scale M_W they are given by

$$C_{9V}^{\text{SM}}(M_W) = \frac{\alpha}{2\pi} \left[\frac{Y_0(x_t)}{\sin^2 \theta_W} - 4Z_0(x_t) \right] \quad C_{10A}^{\text{SM}}(M_W) = -\frac{\alpha}{2\pi} \frac{Y_0(x_t)}{\sin^2 \theta_W} \quad (3.5.39)$$

where $x_t = m_t^2/M_W^2$ and the dimensionless loop functions $Y_0(x_t) \approx 0.94$ and $Z_0(x_t) \approx 0.65$ are explicitly written in (3.27) and (3.28) of [112].

While $C_7^{(\prime)}$ and $C_8^{(\prime)}$ receive the loop-level RS contributions calculated in Section 3.3, $C_{9V}^{(\prime)}$ and $C_{10A}^{(\prime)}$ are corrected at tree level from the new flavor-changing couplings to the Z boson and the exchange of neutral electroweak gauge boson KK modes. In this analysis we only keep the leading contribution to each of these operators, i.e. we consider $\Delta C_{7\gamma,8G}^{(\prime)}$ at one loop and $\Delta C_{9V,10A}^{(\prime)}$ at tree level. Strictly speaking, such an approach leads to an inconsistent perturbative expansion, but it is reasonable to expect that the one loop corrections to the latter Wilson coefficients are sub-dominant with respect to the tree level contributions, and by considering only the RS tree level contribution one should still capture the dominant NP effects.

Explicit expressions for $\Delta C_{9V}^{(\prime)}$ and $\Delta C_{10A}^{(\prime)}$ can be straightforwardly obtained from [95]. These expressions can be written in terms of RG invariants $\Delta Y^{(\prime)}$ and $\Delta Z^{(\prime)}$ and the coupling α , which itself is only very weakly scale dependent above M_W . Thus one may use these expressions to directly write the RS contributions at the scale M_W ,

$$\Delta C_{9V} = \frac{\alpha}{2\pi} \left[\frac{\Delta Y_s}{\sin^2 \theta_W} - 4\Delta Z_s \right] \quad (3.5.40)$$

$$\Delta C'_{9V} = \frac{\alpha}{2\pi} \left[\frac{\Delta Y'_s}{\sin^2 \theta_W} - 4\Delta Z'_s \right] \quad (3.5.41)$$

$$\Delta C_{10A} = -\frac{\alpha}{2\pi} \frac{\Delta Y_s}{\sin^2 \theta_W} \quad (3.5.42)$$

$$\Delta C'_{10A} = -\frac{\alpha}{2\pi} \frac{\Delta Y'_s}{\sin^2 \theta_W} \quad (3.5.43)$$

The functions $\Delta Y^{(\prime)}$ and $\Delta Z^{(\prime)}$ are given by

$$\Delta Y_s = -\frac{1}{V_{ts}^* V_{tb}} \sum_X \frac{\Delta_L^{\mu\mu}(X) - \Delta_R^{\mu\mu}(X)}{4M_X^2 g_{\text{SM}}^2} \Delta_L^{bs}(X), \quad (3.5.44)$$

$$\Delta Y'_s = -\frac{1}{V_{ts}^* V_{tb}} \sum_X \frac{\Delta_L^{\mu\mu}(X) - \Delta_R^{\mu\mu}(X)}{4M_X^2 g_{\text{SM}}^2} \Delta_R^{bs}(X), \quad (3.5.45)$$

$$\Delta Z_s = \frac{1}{V_{ts}^* V_{tb}} \sum_X \frac{\Delta_R^{\mu\mu}(X)}{8M_X^2 g_{\text{SM}}^2 \sin^2 \theta_W} \Delta_L^{bs}(X), \quad (3.5.46)$$

$$\Delta Z'_s = \frac{1}{V_{ts}^* V_{tb}} \sum_X \frac{\Delta_R^{\mu\mu}(X)}{8M_X^2 g_{\text{SM}}^2 \sin^2 \theta_W} \Delta_R^{bs}(X). \quad (3.5.47)$$

Here the summation runs over $X = Z, Z^{(1)}, A^{(1)}$ in the minimal model and over $X = Z, Z_H, Z', A^{(1)}$ in the custodial model. The 4D fermion gauge boson couplings $\Delta_{L,R}^{ij}(X)$ are defined in (3.21–3.22) of [95]. Furthermore

$$g_{\text{SM}}^2 = \frac{G_F}{\sqrt{2}} \frac{\alpha}{2\pi \sin^2 \theta_W}. \quad (3.5.48)$$

The tree level contributions to $b \rightarrow s\mu^+\mu^-$ transitions in the minimal RS model are evaluated in [73] without making the approximations of taking into account only the first KK modes or treating the Higgs vacuum expectation value as a perturbation. In this paper we are mainly interested in the effects of ~ 2.5 TeV KK modes. As these are ruled out in the minimal model by precision electroweak constraints, we focus on the phenomenological effects of the custodial RS model on these transitions.

For the study of observables related to $b \rightarrow s\mu^+\mu^-$, it is useful to introduce the effective Wilson coefficients at the scale μ_b that include the effects of operator mixing,

$$C_7^{\text{eff}} = (C_7^{\text{eff}})_{\text{SM}} + \Delta C_7(\mu_b), \quad C_7'^{\text{eff}} = (C_7'^{\text{eff}})_{\text{SM}} + \Delta C_7'(\mu_b), \quad (3.5.49)$$

$$C_{9V}^{\text{eff}}(q^2) = (C_{9V}^{\text{eff}})_{\text{SM}}(q^2) + \frac{2\pi}{\alpha} \Delta C_{9V}, \quad C_{9V}'^{\text{eff}} = \frac{2\pi}{\alpha} \Delta C_{9V}', \quad (3.5.50)$$

$$C_{10A}^{\text{eff}} = (C_{10A}^{\text{eff}})_{\text{SM}} + \frac{2\pi}{\alpha} \Delta C_{10A}, \quad C_{10A}'^{\text{eff}} = \frac{2\pi}{\alpha} \Delta C_{10A}'. \quad (3.5.51)$$

The SM values of the effective Wilson coefficients can be found in Table 2 of [32], which also gives the q^2 dependence of $(C_{9V}^{\text{eff}})_{\text{SM}}(q^2)$ in terms of a linear combination of the other Wilson coefficients. While in principle all contributions have to be taken at the scale μ_b , the NP contributions to $C_{9V,10A}^{(\prime)}$ are invariant under renormalization group evolution.

With these effective Wilson coefficients at the B scale, we are now equipped to study observables in $b \rightarrow s\mu^+\mu^-$ transitions. While this system offers a plethora of observables for study, a detailed analysis of all of them is beyond the scope of this paper, and we concentrate on studying a few benchmark observables that are particularly relevant for RS physics. A numerical analysis is presented in Section 3.6.

In passing we would like to remark on the pattern of contributions to $C_{9V,10A}^{(\prime)}$ in the custodial model, as pointed out in [95]. Due to the suppression of flavor violating $Z d_L^i \bar{d}_L^j$ couplings by the discrete P_{LR} symmetry, the main contributions arise in the primed Wilson coefficients $C'_{9V,10A}$, which are absent in the SM. Since the right-handed b quark, localized significantly further away from the IR brane than the left-handed one, is far less sensitive to flavor violating effects introduced by the RS KK modes, the RS effects in $Y_s^{(\prime)}, Z_s^{(\prime)}$ turn out to be rather small (typically below 10%). This pattern is very different from the minimal model, where the P_{LR} suppression mechanism is absent and large tree level flavor violating Z couplings to left-handed down-type quarks are present.

3.5.2 Benchmark observables

$$\text{Br}(B \rightarrow X_s \mu^+ \mu^-)$$

For very low lepton invariant mass $q^2 \rightarrow 0$, the $B \rightarrow X_s \mu^+ \mu^-$ transition is completely dominated by the photon pole and doesn't provide any new insight with respect to the $B \rightarrow X_s \gamma$ decay discussed above. Furthermore, in the intermediate region $6 \text{ GeV}^2 < q^2 < 14.4 \text{ GeV}^2$ the sensitivity to NP is very small, as the decay rate in this region is completely dominated by charm resonances. Hence one usually restricts oneself to either the low q^2 region $1 \text{ GeV}^2 < q^2 < 6 \text{ GeV}^2$, or the high q^2 region $q^2 > 14.4 \text{ GeV}^2$. In what follows we will consider only the low q^2 region. While the high q^2 region is potentially interesting since it exhibits a small tension between SM prediction [254] and experimental data [60, 264], it is far less sensitive to NP in $C_7^{(\prime)}$, which is the main focus of this study. In the custodial RS model, the tension in the high q^2 region cannot be resolved since the new contributions to $C_{9V,10A}^{(\prime)}$ are generally small [95]. In addition, the high q^2 region is subject to larger theoretical uncertainties.

In the low q^2 region, adapting the formulae of [173] to the more general case of complex NP contributions, we find

$$\text{Br}(B \rightarrow X_s \mu^+ \mu^-)^{\text{low } q^2} = \text{Br}(B \rightarrow X_s \mu^+ \mu^-)_{\text{SM}}^{\text{low } q^2} + \Delta \text{Br}(B \rightarrow X_s \mu^+ \mu^-)^{\text{low } q^2} \quad (3.5.52)$$

with the NNLL prediction [252]

$$\text{Br}(B \rightarrow X_s \mu^+ \mu^-)_{\text{SM}}^{\text{low } q^2} = (15.9 \pm 1.1) \cdot 10^{-7} \quad (3.5.53)$$

and the NP contribution [173]

$$\begin{aligned}
\Delta\text{Br}(B \rightarrow X_s \mu^+ \mu^-)^{\text{low } q^2} \simeq 10^{-7} \cdot \Big[& -0.517 \text{Re}(\Delta C_7(\mu_b)) - 0.680 \text{Re}(\Delta C_7'(\mu_b)) \\
& + 2.663 \text{Re}(\delta C_{9V}) - 4.679 \text{Re}(\delta C_{10A}) \\
& + 27.776 (|\Delta C_7(\mu_b)|^2 + |\Delta C_7'(\mu_b)|^2) \\
& + 0.534 (|\delta C_{9V}|^2 + |\delta C_{9V}'|^2) \\
& + 0.543 (|\delta C_{10A}|^2 + |\delta C_{10A}'|^2) \\
& + 4.920 \text{Re}(\Delta C_7(\mu_b) \delta C_{9V}^* + \Delta C_7'(\mu_b) \delta C_{9V}'^*) \Big] \quad (3.5.54)
\end{aligned}$$

where we defined

$$\delta C_i = \frac{2\pi}{\alpha} \Delta C_i. \quad (3.5.55)$$

Note that we dropped all interference terms between unprimed and primed contributions since they are suppressed by a factor m_s/m_b and therefore small. The only exception is the term linear in $\Delta C_7'$, which receives a large numerical enhancement factor, and is therefore non-negligible; hence we keep it in our analysis.

The measurements of BaBar [60] and Belle [264] yield the averaged value

$$\text{Br}(B \rightarrow X_s \mu^+ \mu^-)_{\text{exp}}^{\text{low } q^2} = (16.3 \pm 5.0) \cdot 10^{-7}. \quad (3.5.56)$$

As LHCb is not well suited for performing inclusive measurements, a significant reduction of uncertainties will only be feasible at the next generation B factories Belle-II and SuperB [63, 101, 316, 303].

$$B \rightarrow K^{0*}(\rightarrow \pi K) \mu^+ \mu^-$$

While the inclusive $B \rightarrow X_s \mu^+ \mu^-$ mode is theoretically very clean, such measurements are experimentally challenging, and competitive results (in particular for angular distributions) will not be available before the Belle II and SuperB era [63, 101, 316, 303]. For

this reason, exclusive decay modes have received well-deserved attention. An especially interesting decay is $B \rightarrow K^*(\rightarrow K\pi)\mu^+\mu^-$, where a plethora of angular observables can be studied thanks to the four-body final state [33, 32, 283, 191, 192, 299, 100]. These can provide detailed information on the operator and flavor structure of the underlying NP scenario.

The downside is that many $B \rightarrow K^*(\rightarrow K\pi)\mu^+\mu^-$ observables, such as the branching ratio and differential decay distribution, are plagued by large theoretical uncertainties in the determination of the $B \rightarrow K^*$ matrix elements governed by long-distance non-perturbative QCD dynamics. These matrix elements are most conveniently described by a set of seven form factors. Presently, the best predictions for these form factors at large final state meson K^* energies, i.e. small lepton invariant mass q^2 , stem from QCD sum rules at the light cone [140]. Furthermore, non-factorizable corrections are calculated using QCD factorization, which is only valid in the low q^2 regime.³ On the other hand, as mentioned above, at very low $q^2 < 1 \text{ GeV}^2$ the $b \rightarrow s\mu^+\mu^-$ transition is dominated by the $C_7^{(\prime)}$ contributions due to the infrared photon pole and therefore does not provide any insight beyond what is already obtained from $b \rightarrow s\gamma$. Consequently, we henceforth restrict our attention to the range $1 \text{ GeV}^2 \leq q^2 \leq 6 \text{ GeV}^2$.

Fortunately, it is possible to partly circumvent the theoretical uncertainties by studying angular observables that are less dependent on the form factors in question. Detailed analyses of their NP sensitivity and discovery potential have been performed by various groups, both model-independently and within specific NP scenarios [33, 32, 283, 191, 192, 299]. We leave such a detailed analysis in the context of RS models for future work. We focus instead on two benchmark observables, the forward backward asymmetry A_{FB} ,

³Significant progress has recently been made on the form factor predictions in the large q^2 region [88, 81, 235, 82]; nevertheless we will not consider this kinematic regime since it is less sensitive to NP entering $C_7^{(\prime)}$ than the low q^2 region.

which is experimentally well constrained, and the transverse asymmetry $A_T^{(2)}$, which offers unique sensitivity to NP in the primed Wilson coefficients.

We note that the recently measured CP asymmetry A_9 [6, 2], as defined in [32, 99], is also very sensitive to NP in C'_7 and therefore is in principle an interesting observable to look for RS effects. Because it is sensitive to the phase of C'_7 , it yields partly complementary information with respect to the CP conserving transverse asymmetry $A_T^{(2)}$. Although this CP asymmetry is theoretically very clean, contrary to those studied in [192], we leave a detailed study within RS for future work.

Forward backward asymmetry The forward-backward asymmetry A_{FB} in $B \rightarrow K^* \mu^+ \mu^-$ decays is defined by

$$A_{\text{FB}}(q^2) = \frac{1}{d\Gamma/dq^2} \left(\int_0^1 d(\cos \theta_\mu) \frac{d^2\Gamma}{dq^2 d(\cos \theta_\mu)} - \int_{-1}^0 d(\cos \theta_\mu) \frac{d^2\Gamma}{dq^2 d(\cos \theta_\mu)} \right), \quad (3.5.57)$$

where θ_μ is the angle between the K^* momentum and the relative momentum of μ^+ and μ^- . A_{FB} has recently received a lot of attention as data from BaBar, Belle, and the Tevatron seem to indicate a deviation from the SM, albeit with low statistical significance [62, 263, 6]. On the other hand, recent LHCb data [1] show excellent agreement with the SM prediction, and as uncertainties are presently dominated by statistics, an improved measurement should be available soon.

A precise theoretical determination of A_{FB} is appealing since it offers a sensitive probe of the helicity of NP contributions. To leading order, the forward backward asymmetry is proportional to [99]

$$A_{\text{FB}}(q^2) \propto \text{Re} \left[\left(C_{9V}(q^2) + \frac{2m_b^2}{q^2} C_7 \right) C_{10A}^* - \left(C'_{9V} + \frac{2m_b^2}{q^2} C'_7 \right) C_{10A}^{\prime*} \right], \quad (3.5.58)$$

where we dropped the superscript “eff” for the effective Wilson coefficients at the scale μ_b , (3.5.49–3.5.51). From (3.5.58) we can see explicitly that A_{FB} does not receive contribu-

tions from the interference of different chirality operators (unprimed and primed). Consequently, with the SM contribution being the dominant effect, potential non-standard effects in A_{FB} arise mainly from NP in C_7 and C_{9V} . On the other hand, A_{FB} is rather insensitive to NP in the primed Wilson coefficients $C'_{7,9V,10A}$.

A_{FB} has been studied in the context of the minimal RS model considering only tree level contributions and omitting loop level dipole contributions to $C_7^{(\prime)}$ [73], where small positive contributions to A_{FB} were found. While A_{FB} is very sensitive to NP effects in C_7 , the RS dipole contributions we calculated predict rather small contributions to this Wilson coefficient. On the other hand, A_{FB} is insensitive to C'_7 , where RS effects are expected to be more pronounced over the SM. Thus the overall prediction of small deviations of A_{FB} from the SM obtained in [73] remains consistent with our calculations. Note that the restriction to tree level RS effects is not necessarily a good approximation for observables sensitive to C'_7 , such as F_L , which was also studied in [73]. A detailed study including one-loop contributions to the dipole operators would therefore be desirable but lies beyond the scope of the present analysis.

In the custodial RS model, due to the protection of the $Z d_L^i \bar{d}_L^j$ vertex [94], the RS contributions to $C_{9V,10A}$ are highly suppressed, and only the new contributions to the primed operators are relevant. As A_{FB} is insensitive to the latter Wilson coefficients, it remains very close to the SM prediction.

We conclude that RS effects in the forward backward asymmetry A_{FB} are generally small, so the recent data from LHCb do not pose any stringent constraint on the minimal or custodial model, the latter being even more insensitive to RS contributions.

Transverse asymmetry $A_T^{(2)}$ The asymmetries $A_T^{(i)}$, which are introduced in [191, 282], offer a particularly good probe of NP in $b \rightarrow s\mu^+\mu^-$ transitions since at leading order they are free of any hadronic uncertainties and are given in terms of calculable short distance physics. In this paper we will restrict ourselves to the study of the asymmetry

$$A_T^{(2)} = \frac{|A_\perp|^2 - |A_\parallel|^2}{|A_\perp|^2 + |A_\parallel|^2}. \quad (3.5.59)$$

Here A_\perp and A_\parallel are the transversity amplitudes [282] describing the polarization of the K^* and the $\mu^+\mu^-$ pair; both are transverse with linear polarization vectors perpendicular (\perp) or parallel (\parallel) to each other. In the limit of heavy quark ($m_B \rightarrow \infty$) mass and large K^* energy (small q^2), this asymmetry takes a particularly simple form [192]

$$A_T^{(2)}(q^2) = \frac{2 [\text{Re}(C'_{10A} C_{10A}^*) + F^2 \text{Re}(C'_7 C_7^*) + F \text{Re}(C'_7 C_{9V}^*)]}{|C_{10A}|^2 + |C'_{10A}|^2 + F^2 (|C_7|^2 + |C'_7|^2) + |C_{9V}|^2 + 2F \text{Re}(C_7 C_{9V}^*)} \quad (3.5.60)$$

with $F = 2m_b m_B / q^2$, and we have again dropped the superscript “eff” from the Wilson coefficients. In this limit it is clear that $A_T^{(2)}$ is independent of form factors and is governed only by calculable short distance physics, making this observable theoretically clean. Second, we notice that since the primed Wilson coefficients are highly suppressed in the SM, $(A_T^{(2)})_{\text{SM}}$ is very small. $A_T^{(2)}$ therefore offers unique sensitivity to NP entering dominantly in the primed operators $C'_{7\gamma, 9V, 10A}$. This asymmetry is thus a benchmark observable for discovering RS physics in $B \rightarrow K^* \mu^+ \mu^-$ decays. We investigate the possible size of RS contributions to this channel in our numerical analysis in the next section.

A first measurement of $A_T^{(2)}$ recently presented by CDF [6] is still plagued by large uncertainties. LHCb has recently put more stringent constraints on this asymmetry, and more precise measurements will be possible in the near future [2].

3.6 Numerical analysis

3.6.1 Strategy

In this section we present a numerical analysis of the observables introduced in the previous sections. To this end we follow the following strategy:

1. The first goal is to understand the generic pattern of effects induced by RS penguins on flavor observables. We generate a set of parameter points that satisfy the known experimental constraints from quark masses and CKM parameters. However, we do not yet impose any additional flavor bounds so as not to be biased by their impact. With these points we evaluate the new RS contributions to the Wilson coefficients $\Delta C_7^{(\prime)}$ and $\Delta C_8^{(\prime)}$ at the KK scale for both the minimal and the custodial model. Subsequently we calculate the new contributions to the branching ratios of $B \rightarrow X_{s,d}\gamma$ and analyze the constraints.
2. The second goal is to understand the effect of the RS penguins on the existing parameter space for realistic RS models. We restrict our attention to the custodial model, which can be made consistent with electroweak precision tests for KK scales as low as $M_{\text{KK}} \simeq 2.5 \text{ TeV}$. In addition to quark masses and CKM parameters, we now also impose constraints from $\Delta F = 2$ observables which are analyzed at length in [94]. After evaluating the size of the effects in the $B \rightarrow X_{s,d}\gamma$ branching ratios and their constraint on the model, we study the benchmark observables outlined above, namely the CP asymmetry in $B \rightarrow K^*\gamma$, the branching ratio $\text{Br}(B \rightarrow X_s \mu^+ \mu^-)$, and the transverse asymmetry $A_T^{(2)}$ in $B \rightarrow K^* \mu^+ \mu^-$ decays.

Throughout our analysis we restrict ourselves to $1/R' = 1 \text{ TeV}$, so that the lowest KK gauge bosons have a mass of $M_{\text{KK}} \simeq 2.5 \text{ TeV}$. We note that in the minimal model such low KK masses are already excluded due to unacceptably large corrections to electroweak precision observables. However, we use the same mass scale for both the minimal and custodial models to enable a straightforward comparison of the two sets of results. Furthermore, we restrict the fundamental Yukawa couplings to lie in their perturbative regime, i. e. $|Y_{ij}| \leq 3$. More details on the parameter scan can be found in [94].

3.6.2 General pattern of RS contributions

This part of the numerical analysis is dedicated to determining the size of NP effects generated by the RS KK modes in the dipole operators C_7, C'_7 and C_8, C'_8 mediating the $b \rightarrow (s, d)\gamma$ and $b \rightarrow (s, d)g$ transitions respectively. We advise caution when interpreting the density of points since these distributions are influenced by the details of the parameter scan performed. The qualitative features in our plots should remain unaffected by the scanning procedures.

The first row of Fig. 3.4 shows the RS contributions to $C_7(M_{\text{KK}})$ and $C'_7(M_{\text{KK}})$ in the $b \rightarrow s$ system. Observe that the total RS contribution (red and blue histograms, corresponding to the minimal and custodial model) to the primed Wilson coefficient is typically an order of magnitude larger than the corresponding effect in the unprimed Wilson coefficient. This matches the naive expectation that the $b_L \rightarrow s_R$ transition should be enhanced relative to $b_R \rightarrow s_L$ due to the hierarchy $f_{Q_3} \gg f_{b_R}$ of fermion localizations. Furthermore the custodial contribution is somewhat enhanced relative to the minimal one, due to the additional fermion modes running in the loop. Also shown, in yellow, is the contribution to $C_7(M_{\text{KK}})$ and $C'_7(M_{\text{KK}})$ generated by only the misalignment term,

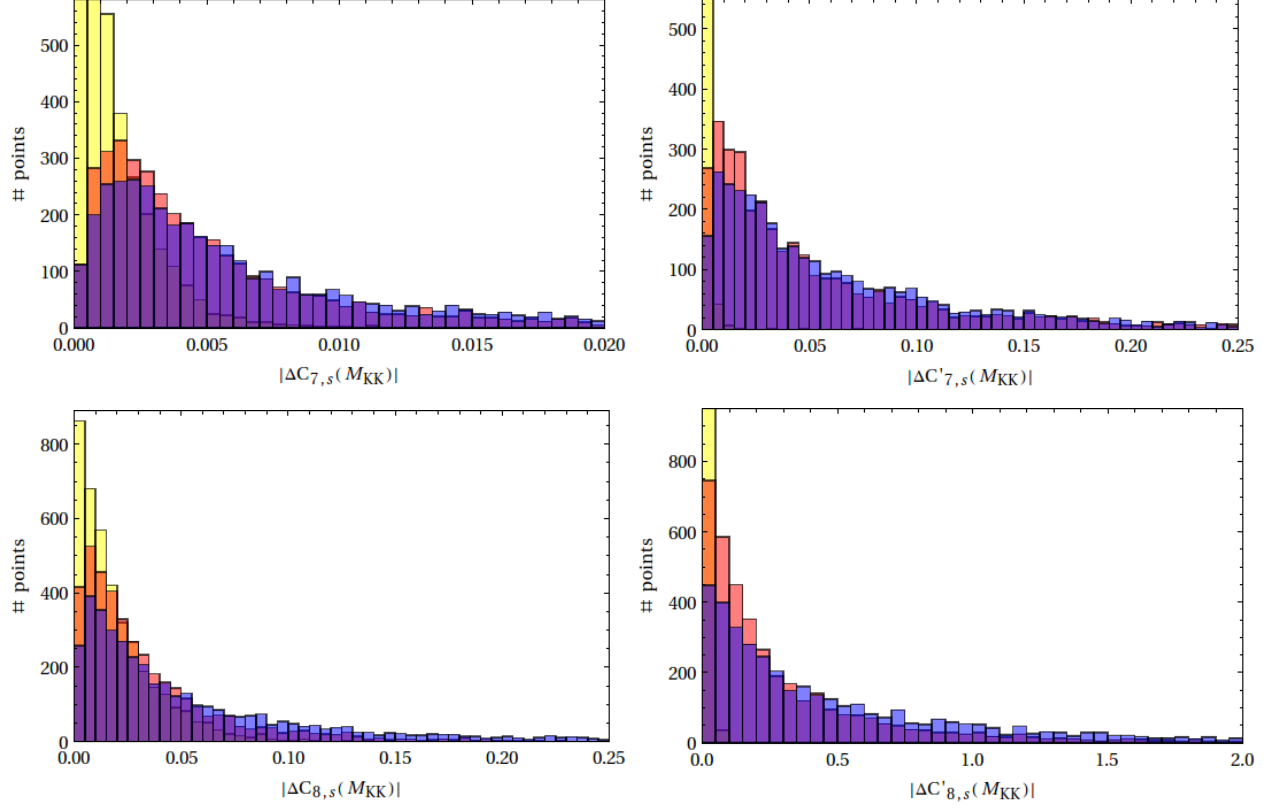


Figure 3.4: RS contributions to the $b \rightarrow s$ Wilson coefficients $C_7(M_{KK})$ (upper left), $C'_7(M_{KK})$ (upper right), $C_8(M_{KK})$ (lower left) and $C'_8(M_{KK})$ (lower right) in the minimal (red) and custodial (blue) models, and from the misalignment contribution alone (yellow).

which is equal for the minimal and the custodial models. Unlike the anarchic term, this contribution is generically comparable in both cases. This naively unexpected behavior is explained in Appendix B.2. While it is subdominant but non-negligible in the case of $C_7(M_{KK})$, it turns out to be generally irrelevant in the case of $C'_7(M_{KK})$.

The second row of Fig. 3.4 shows the results for the gluonic penguin Wilson coefficients C_8 and C'_8 . The values at the KK scale are larger than the corresponding values of C_7 and C'_7 by about an order of magnitude due to the large contribution from the diagram containing the non-Abelian $SU(3)_c$ vertex, which is absent in the $b \rightarrow s\gamma$ penguin. Other than that, the pattern of effects is qualitatively similar to that for $C_7^{(\prime)}$: the primed Wilson

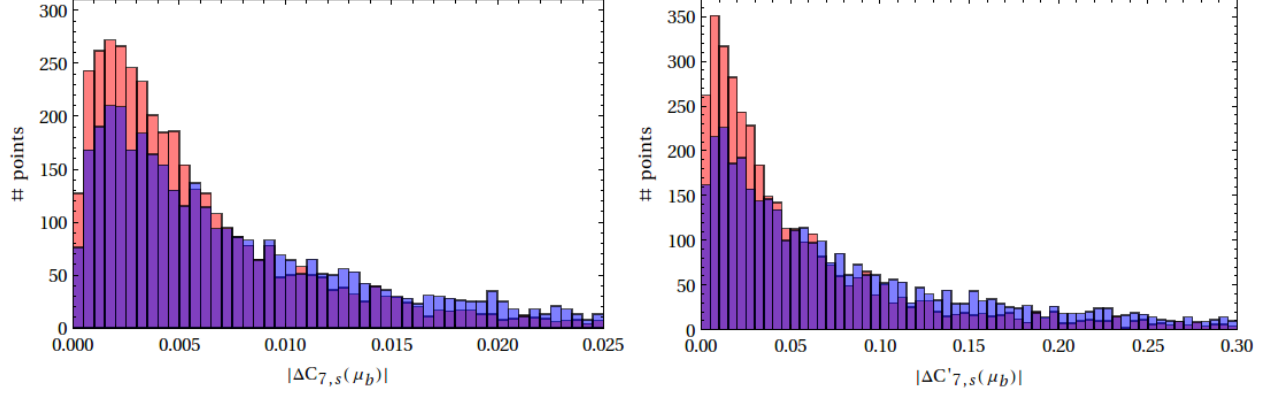


Figure 3.5: RS contributions to the $b \rightarrow s\gamma$ Wilson coefficients C_7 (left) and C'_7 (right), evaluated at the scale $\mu_b = 2.5 \text{ GeV}$. The minimal model distribution is shown in red, and the custodial one in blue.

coefficient is larger than the unprimed coefficient by about an order of magnitude, and the custodial model yields somewhat bigger effects than the minimal model. Furthermore, the misalignment contributions to the unprimed and primed Wilson coefficients are again roughly comparable; consequently, its effect is negligible in C'_8 but can be sizable in C_8 .

To facilitate comparison with other models of NP, Fig. 3.5 shows the RS contributions to the $b \rightarrow s\gamma$ Wilson coefficients C_7 (left) and C'_7 (right) evaluated at the scale $\mu_b = 2.5 \text{ GeV}$, i.e. taking into account the RG evolution and operator mixing with $C_8^{(\prime)}$. The RS contribution to C_7 turns out to be small and typically constitutes less than a few percent of the SM value $C_7^{(\prime)}(\mu_b)^{\text{SM}} = -0.353$. On the other hand, C'_7 is suppressed by m_s/m_b in the SM, so the unsuppressed contribution from RS dominates, though its value is still typically smaller than $C_7(\mu_b)^{\text{SM}}$.

Next, we examine the relative importance of the various RS contributions to the effective $b \rightarrow s\gamma$ Wilson coefficients at the scale μ_b . Fig. 3.6 shows the size of the two main anarchic contributions to $\Delta C_8^{(\prime)}(M_{\text{KK}})$ (see Fig. 3.2a for the relevant Feynman diagrams) normalized to the anarchic contribution to $\Delta C_7^{(\prime)}(M_{\text{KK}})$ (see Fig. 3.1a). For a straightforward comparison, we also include the relevant RG evolution factors from eq. (3.4.24). The

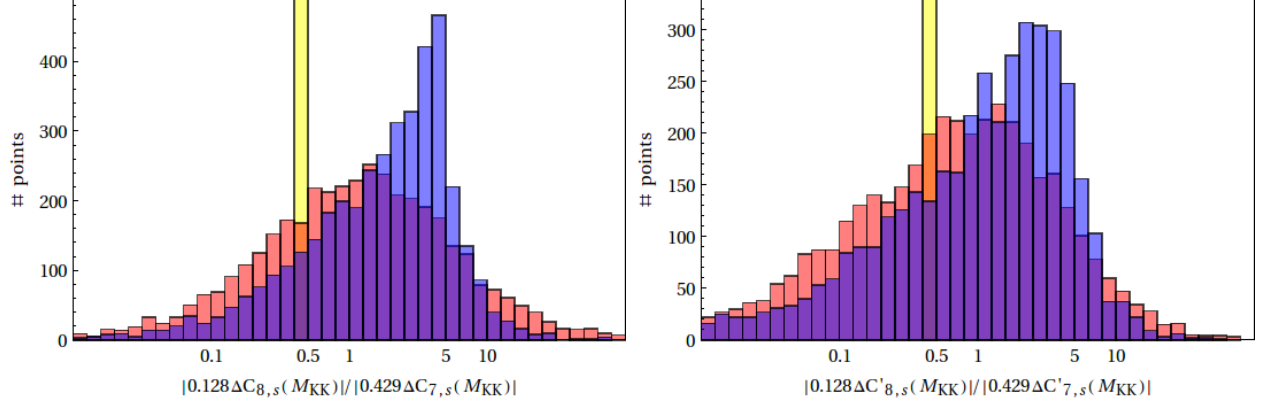


Figure 3.6: Relative sizes of anarchic contributions to the Wilson coefficients $C_7(\mu_b)$ (left) and $C'_7(\mu_b)$ (right) from the RG evolution and operator mixing of $\Delta C_8^{(\prime)}$ from M_{KK} to μ_b , normalized to the Higgs penguin contribution to $\Delta C_7^{(\prime)}(M_{\text{KK}})$, with relevant RG evolution factors included. The yellow bin shows the ratio of the Higgs penguin contribution to $\Delta C_8^{(\prime)}(M_{\text{KK}})$. The red and blue distributions show the ratio of the gluon penguin to $\Delta C_8^{(\prime)}(M_{\text{KK}})$ for the minimal and custodial model respectively.

ratio of the Higgs penguin contribution to $\Delta C_7^{(\prime)}(M_{\text{KK}})$ and $\Delta C_8^{(\prime)}(M_{\text{KK}})$, shown by the yellow band, is constant and equal for both the minimal and custodial model. As the relevant diagrams depend on the same loop integral and the same combination of Yukawa couplings, their relative size at the KK scale is simply given by the electric charge Q_u of the up-type quark coupled to the photon. After including the RG running down to the scale μ_b , the Higgs penguin contribution to $C_8^{(\prime)}$ turns out to be roughly a 50% correction to the effect of the anarchic $\Delta C_7^{(\prime)}(M_{\text{KK}})$ contribution.

The effect of the gluon penguin diagram in $\Delta C_8^{(\prime)}(M_{\text{KK}})$ depends on a different loop integral and a different combination of Yukawa couplings than the Higgs diagram in $\Delta C_7^{(\prime)}(M_{\text{KK}})$. Consequently its relative size, again including the relevant RG factors, varies considerably within the minimal (shown in red) and the custodial (shown in blue) model. Observe that the distribution for the minimal model is rather symmetric and peaked around 1, implying that the RS $b \rightarrow sg$ loop generally contributes as much as the RS $b \rightarrow s\gamma$ loop in low energy observables, even yielding the dominant RS contribution in

parts of the parameter space. This should be contrasted to the SM case, where the C_8 contribution only gives a few percent correction to the dominant C_7 contribution. In the custodial model the gluon penguin contribution becomes even more important, so that the peak of the distribution gets shifted above 1. Since, as opposed to the Higgs penguin, the additional custodial gluon penguin diagram shown in Fig. 3.3 carries the same Yukawa spurion as the minimal model diagram, they simply add constructively, further enhancing the effect of the gluonic penguin contribution. Neglecting these contributions or even the $C_8^{(\prime)}$ contribution as a whole, as sometimes done in the literature, would therefore be a rather poor approximation. Note that the relative importance of the gluon penguin diagrams depends crucially on the matching of the 5D to the 4D strong gauge coupling. Invoking one loop level matching rather than tree level matching as done here would reduce their relative size by roughly a factor of four. On the other hand the presence of brane kinetic terms could further enhance the gluonic penguin contribution.

Fig. 3.7 is analogous to Fig. 3.4 for the $b \rightarrow d$ system. The pattern of effects is very similar to the case of the $b \rightarrow s$ system discussed above.

Fig. 3.8 shows the predicted deviations from the SM in the $B \rightarrow X_{s,d}\gamma$ branching ratios in the minimal and custodial models. We observe that in both models these branching ratios typically obtain a moderate positive NP contribution well within the current experimental and theoretical uncertainties. Nevertheless, the decays in question put nontrivial constraints on parts of the RS parameter space and should be included in a complete analysis of RS flavor phenomenology. As expected from the size of the Wilson coefficients, the custodial model induces somewhat larger effects than the minimal model.

Interestingly, this pattern of effects is very different from that of the ADD model of a universal extra dimension [42], where the KK excitations affect mainly the Wilson coeffi-

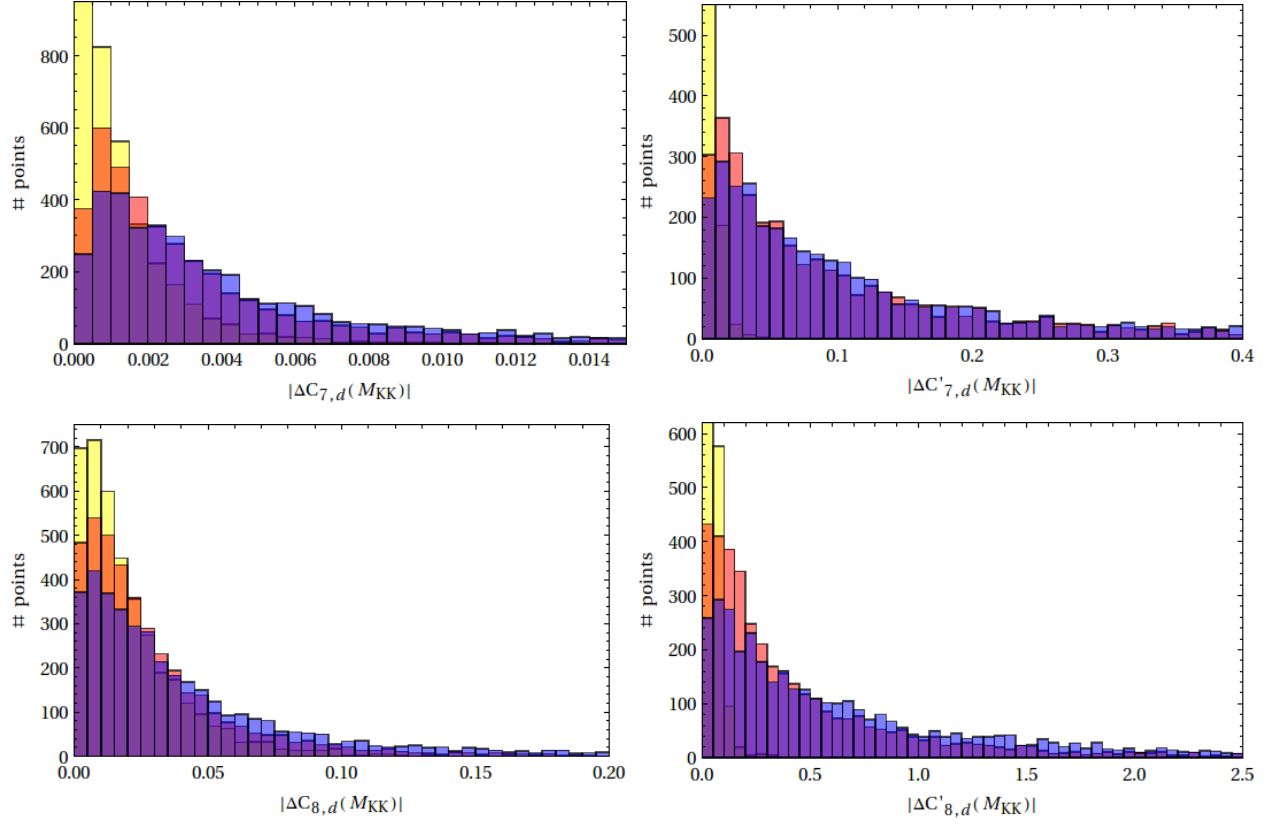


Figure 3.7: RS contributions to the $b \rightarrow d$ Wilson coefficients $C_7(M_{KK})$ (upper left), $C'_7(M_{KK})$ (upper right), $C_8(M_{KK})$ (lower left) and $C'_8(M_{KK})$ (lower right) in the minimal model (red), the custodial model (blue), and from the misalignment contribution alone (yellow).

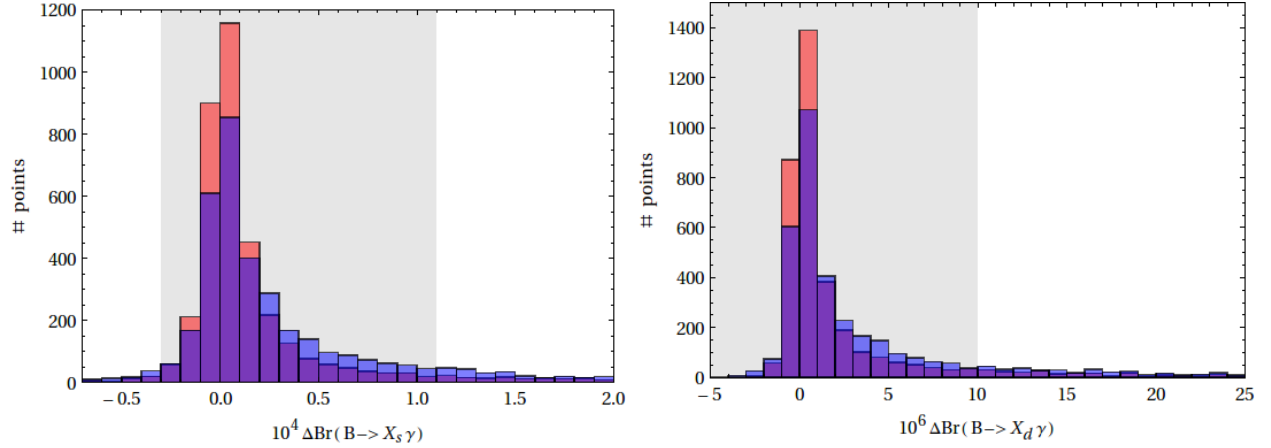


Figure 3.8: RS contribution to $\text{Br}(B \rightarrow X_s \gamma)$ (left) and $\langle \text{Br}(B \rightarrow X_d \gamma) \rangle$ in the minimal (red) and custodial (blue) model. The experimental constraints according to (3.4.21) and (3.4.22) are displayed as grey bands.

cient C_7 , while the opposite-chirality Wilson coefficient C'_7 remains very small [15, 116]. Since the ADD contribution interferes destructively with the SM contribution, a rather pronounced suppression of $\text{Br}(B \rightarrow X_s \gamma)$ is predicted, which was used in [244] to derive the bound $1/R > 600 \text{ GeV}$ on the radius R of the extra dimension.

3.6.3 Effects on benchmark observables

We now restrict our attention to the custodial model and consider only parameter points that agree with the existing constraints from $\Delta F = 2$ transitions, as analyzed in [94]. We also impose the bounds from the $B \rightarrow X_{s,d} \gamma$ decays as approximated in (3.4.21–3.4.22), so that all points displayed in the plots lie within the experimentally allowed region.

Since the dipole operators depend on a different combination of RS flavor parameters than the tree level contributions to $\Delta F = 2$ processes [94] and $\Delta F = 1$ rare decays [95], observables related to the various sectors are essentially uncorrelated; hence we do not show any numerical results here.

Fig. 3.9 shows the correlation between the time-dependent CP asymmetry $S_{K^* \gamma}$ and the branching ratio of $B \rightarrow X_s \gamma$. Observe that $S_{K^* \gamma}$ can receive large enhancements relative to its tiny SM value. While non-standard effects in $S_{K^* \gamma}$ are possible for any value of $\text{Br}(B \rightarrow X_s \gamma)$, large effects are more likely with enhanced values of the branching ratio. This is related to the fact that RS contributions dominantly affect C'_7 . While the SM prediction for $B \rightarrow X_s \gamma$ is in good agreement with data, it lies below the central value, and an enhancement of this branching ratio is preferred. One can also see that large enhancements are possible in $S_{K^* \gamma}$, and that the present experimental 2σ range excludes only a small fraction of the RS parameter space.

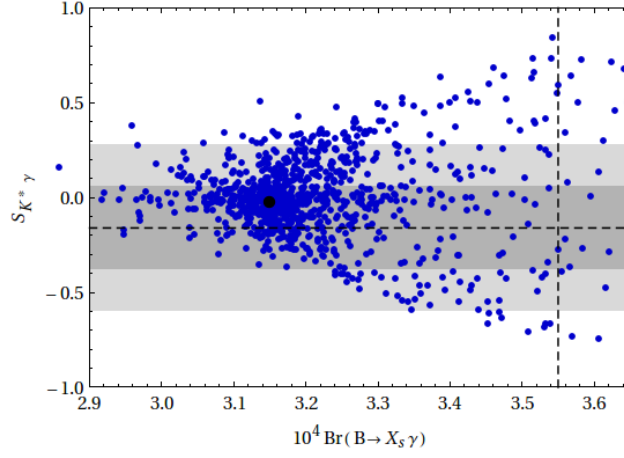


Figure 3.9: CP asymmetry $S_{K^*\gamma}$ as a function of $\text{Br}(B \rightarrow X_s \gamma)$. The black dot indicates the central SM prediction, while the dashed lines show the experimental central values. The grey bands display the experimental 1σ and 2σ ranges for $S_{K^*\gamma}$.

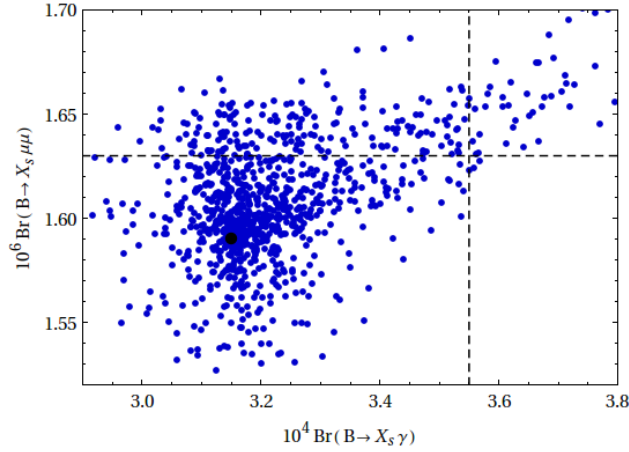


Figure 3.10: Correlation between $\text{Br}(B \rightarrow X_s \gamma)$ and $\text{Br}(B \rightarrow X_s \mu^+ \mu^-)$ for $q^2 \in [1, 6] \text{ GeV}^2$. The black dot indicates the central SM prediction, while the dashed lines show the experimental central values.

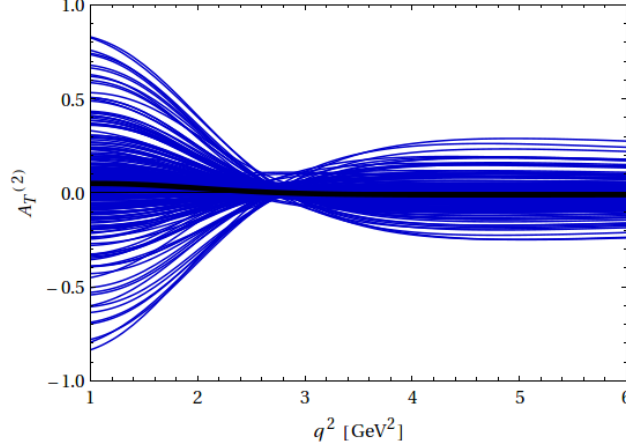


Figure 3.11: Transverse asymmetry $A_T^{(2)}$ as a function of q^2 . The SM prediction is indicated by the black line, while each blue line corresponds to an RS parameter point.

The decay $B \rightarrow X_s \mu^+ \mu^-$ poses strong constraints on various extensions of the SM, hence it is worth studying it in the custodial RS model. Fig. 3.10 shows the custodial RS branching ratio $\text{Br}(B \rightarrow X_s \mu^+ \mu^-)$ in the low q^2 region as a function of $\text{Br}(B \rightarrow X_s \gamma)$. We observe that the enhancement in the custodial RS model is rather small, typically below 10%. Due to the experimental and theoretical uncertainties involved, this channel does not put any significant constraint on the model.

Observables far more sensitive to NP in C'_7 can be constructed from the angular distribution of $B \rightarrow K^* \mu^+ \mu^-$. Of particular interest is the transverse asymmetry $A_T^{(2)}$, whose q^2 dependence is shown in Fig. 3.11. Observe that large enhancements relative to the small SM value are possible, in particular in the very small q^2 region $< 2 \text{ GeV}^2$. This pattern can be understood from (3.5.60): the C'_7 contribution is enhanced at small q^2 due to a $1/q^2$ factor, see also [192, 75]. The differential asymmetry would exhibit a very different shape if the dominant NP contribution appeared in C'_{10A} . This underlines the model-discriminating power of the $A_T^{(2)}$ asymmetry—in the custodial RS model a deviation from the SM is most likely to be observed for small q^2 , whereas other models that dominantly

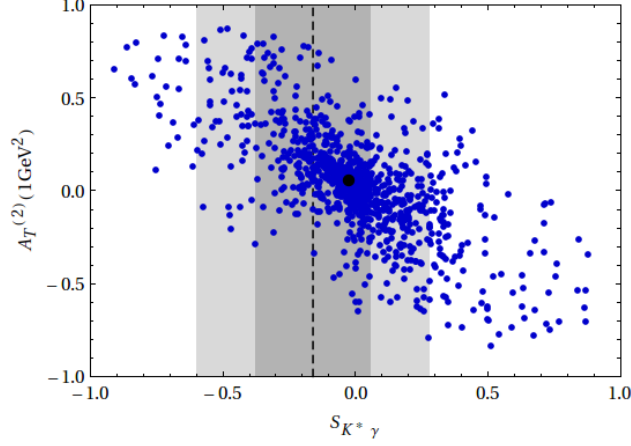


Figure 3.12: Correlation between $S_{K^*\gamma}$ and $A_T^{(2)}(q^2 = 1 \text{ GeV}^2)$. The black dot indicates the central SM prediction, while the dashed line shows the experimental central value. The grey bands display the experimental 1σ and 2σ ranges for $S_{K^*\gamma}$.

affect C'_{10A} predict large effects for larger q^2 . This pattern is particularly interesting in light of LHCb and the next generation B factories, which will soon be able to measure this asymmetry.

Finally, one may consider a possible correlation between $S_{K^*\gamma}$ and $A_T^{(2)}$. Both observables are mostly affected by a large C'_7 , hence some nontrivial correlation can be expected. On the other hand, $S_{K^*\gamma}$ is CP violating while $A_T^{(2)}$ is CP conserving, so the phase of C'_7 can wash out such correlations. Fig. 3.12 shows $A_T^{(2)}(q^2 = 1 \text{ GeV}^2)$ as a function of $S_{K^*\gamma}$, where a nontrivial linear anti-correlation is seen between the two observables in question. However, this correlation is visibly weakened by the impact of the phase of C'_7 , as expected.

3.7 Conclusions

In this paper we have performed an explicit 5D calculation of the dominant contributions to the Wilson coefficients C_7 , C'_7 , and C_8 , C'_8 that mediate the $b \rightarrow s, d\gamma$ and $b \rightarrow s, dg$ transitions respectively, in the RS setup with bulk fermions and gauge bosons and an IR-brane localized Higgs. We have evaluated the relevant diagrams for both the minimal scenario with only the SM gauge group in the bulk, and for the custodial model with the electroweak gauge group extended by $SU(2)_R$ and a discrete P_{LR} symmetry. Our main findings from this analysis can be summarized as follows:

- The RS contributions to C'_7 typically exceed those to C_7 by an order of magnitude, and the latter remain a rather small correction to the SM value. This pattern can be understood by considering the bulk profiles of the quark fields involved: the primed Wilson coefficient describes the decay of a left-handed b quark, which, being localized towards the IR brane, is more sensitive to flavor violating effects than the right-handed b quark entering C_7 . Analogous comments apply regarding the hierarchy $C_8 \ll C'_8$.
- Contrary to the SM, where $C_8 < C_7$, RS contributions to the gluonic penguins are larger than the ones to the photonic penguins. This results from the large contributions from the diagram containing the non-abelian triple gluon (KK gluon) vertex, which is absent in $C_7^{(\prime)}$ and does not change flavor in the SM. In addition, the renormalization group mixing of $C_7^{(\prime)}$ and $C_8^{(\prime)}$ is more pronounced due to the large separation of the M_{KK} and m_b scales. Consequently, gluonic penguin contributions have a significant impact on $b \rightarrow s, d\gamma$, comparable to or larger than the photonic penguin contribution. This is in contrast to the SM, where they yield only a few percent correction to the photonic Wilson coefficients at the m_b scale.

- In all cases, the dominant effect comes from the anarchic contributions, which are not aligned with the SM quark mass matrices. However, the unprimed (right to left) operators pick up appreciable contributions from misalignment diagrams, which are proportional to the SM quark mass matrices up to a dependence on the bulk spectrum. This is because, in contrast to the anarchic diagrams, the misalignment diagrams are not suppressed by the b_R wave function relative to the b_L wavefunction, as explained in Appendix B.2.
- The impact on the Wilson coefficients in question is somewhat larger in the custodial model than in the minimal model, since the extended fermion content that was introduced to reconcile the model with the $Zb\bar{b}$ constraint yields additional contributions.

For a study of the phenomenological implications of these new contributions, we restricted our attention to the custodial model since the minimal model is not consistent with electroweak precision constraints for low KK masses $M_{\text{KK}} = 2.5 \text{ TeV}$. To this end, following [94] we performed a parameter scan of the 5D bulk masses and fundamental Yukawa coupling matrices, imposing constraints from quark masses and CKM parameters and from meson-antimeson mixing. We studied the bounds provided by the branching ratios $\text{Br}(B \rightarrow X_s \gamma)$ and $\langle \text{Br}(B \rightarrow X_d \gamma) \rangle$ and the effects in a number of benchmark observables, namely the time-dependent CP asymmetry $S_{K^* \gamma}$, the inclusive branching ratio $\text{Br}(B \rightarrow X_s \mu^+ \mu^-)$ and the forward-backward asymmetry A_{FB} and the transverse asymmetry $A_T^{(2)}$ in $B \rightarrow K^* \mu^+ \mu^-$, where we found the following patterns:

- The branching ratios of the radiative inclusive $B \rightarrow X_{s,d} \gamma$ decays provide a non-negligible constraint on RS models and exclude roughly 15% of the parameter points generated for the custodial model that were in agreement with bounds from $\Delta F = 2$

observables. A complete phenomenological study should therefore take these constraints into account. However, since the major part of parameter space survives, no useful bound on the KK scale can be derived.

- Due to more precise data and SM theory prediction, $\text{Br}(B \rightarrow X_s \gamma)$ generally puts a stronger constraint on the RS parameter space than $\langle \text{Br}(B \rightarrow X_d \gamma) \rangle$. The latter observable is still useful as it yields complementary information on the allowed parameter space.
- As the RS contributions enter dominantly through the primed operators, a modest enhancement of the $B \rightarrow X_{s,d} \gamma$ branching ratios can be expected, although a slight suppression is not rigorously excluded. Such an enhancement would be welcome in $B \rightarrow X_s \gamma$, where the data lie somewhat above the SM value, albeit still in good agreement. On the other hand, for $B \rightarrow X_d \gamma$ the central values of the SM and the data are in excellent agreement and the uncertainties are sizable, and no preferred sign for the NP contribution can be deduced.
- The inclusive branching ratio $\text{Br}(B \rightarrow X_s \mu^+ \mu^-)$ and the forward backward asymmetry A_{FB} in $B \rightarrow K^* \mu^+ \mu^-$ receive very small corrections from RS physics and remain in good agreement with recent data. While we restricted our analysis to the low q^2 region, these statements also apply to the high q^2 region since the latter region is mostly sensitive to NP in the electroweak Wilson coefficients $C_{9V,10A}^{(l)}$, which remain SM-like in the custodial model.
- We identify the time-dependent CP asymmetry $S_{K^* \gamma}$ in $B \rightarrow K^* \gamma$ decays and the transverse asymmetry $A_T^{(2)}$ in the low q^2 region of $B \rightarrow K^* \mu^+ \mu^-$ as promising benchmark observables to look for large effects generated by the custodial RS model. Both observables are known to be very sensitive to the primed Wilson coefficients, in particular C_7' , which is dominantly affected by RS contributions. Furthermore, studying

the q^2 dependence of $A_T^{(2)}$ allows for a clear distinction of models such as the custodial RS model that dominantly affect C_7' from models that predict large NP effects in the electroweak Wilson coefficient C_{10A}' .

In summary, our analysis shows that radiative and semileptonic B decays offer intriguing possibilities to find deviations from the SM generated by RS KK modes and anarchic Yukawa structure. If such effects are found at the LHCb and the next generation B factories, it will be particularly interesting to study the plethora of observables provided by these decay modes in a correlated manner, which offers the ability to distinguish RS with custodial symmetry from other NP scenarios that predict a different pattern of effects.

CHAPTER 4

SPONTANEOUS R -SYMMETRY BREAKING WITH MULTIPLE PSEUDOMODULI

Based on the 2012 article “Spontaneous R -symmetry breaking with multiple pseudomoduli”, written in collaboration with David Curtin, Zohar Komargodski, David Shih and published in arXiv:1202.5331

4.1 Introduction

The O’Raifeartaigh (O’R) model [318] and its generalizations constitute the simplest theories which spontaneously break supersymmetry (SUSY). Despite their simplicity, they are interesting subjects for study, because they often arise as low-energy effective theories of models which dynamically break SUSY [261, 266, 262, 181].

Spontaneous SUSY breaking generically requires the existence of an R -symmetry [314]. An unbroken R -symmetry forbids Majorana gaugino masses, so if SUSY is relevant to nature at the TeV scale, R -symmetry must be broken somehow.¹ In this paper we will examine the possibility of spontaneous R -symmetry breaking in generalized O’Raifeartaigh models (renormalizable Wess-Zumino models with F -term SUSY-breaking).

In general one can envision either tree-level spontaneous R -breaking or radiatively induced breaking [333]. Models that break the R -symmetry at tree-level exist [123, 345, 274], but they are rather cumbersome and have not yet been found naturally in dynamical models of SUSY breaking. One is therefore led to investigate the possibility of radiatively broken R -symmetry. In fact, radiative effects in Wess-Zumino models have always played a pivotal role because any SUSY-breaking vacuum is necessarily accompanied by a flat direction [332]. (Such flat directions in Wess-Zumino models are often called pseudomoduli.) Hence, to determine the correct vacuum of the theory one is generally forced to consider radiative effects.

A special class of generalized O’R models consists of theories where all the R -charges are either 0 or 2. Several well-known dynamical models of calculable SUSY breaking lead to such theories (e.g. [262, 261, 266]); hence our interest in this class. For such theories one

¹One can also consider models with Dirac mass terms for the gauginos, see for instance the general analysis of [80] and references therein.

can prove the absence of tree-level R -breaking [274]. In addition, it was shown in [341] that in models with a *single* pseudomodulus, spontaneous R -breaking through the one-loop Coleman-Weinberg (CW) potential required the presence of fields with R -charges other than 0 or 2. This theorem has often been used to guide model building.

In this paper, we will generalize the result of [341] to O’R models with arbitrarily many pseudomoduli fields. We will show that even in this case, if all the R -charges are 0 or 2, the one-loop effective potential has a local minimum at the R -symmetric origin of field space (which could be a manifold in general). Additionally, we will also show that pseudomoduli can remain massless after one-loop corrections are taken into account only if they are in fact manifestly decoupled in the Lagrangian at the one-loop level. Such pseudomoduli can receive important two-loop corrections (see e.g. [226, 260, 36]), and it would be interesting to investigate these two-loop corrections in general.

We do not consider the general problem of Wess-Zumino models with R -charges other than 0, 2. That is left as an interesting problem for the future. For the case of a single pseudomodulus it was argued [341] that there is no obstruction to obtaining R -symmetry breaking. It would be interesting to see precisely how this works if more than one pseudomodulus is present. Another obvious generalization of our study is to introduce gauge fields. Introducing gauge fields can lead to a variety of interesting phenomena, such as spontaneous radiative breaking, and even classical destabilization of all the vacua [300].

This work was partly motivated by recent interesting papers which considered the possibility of spontaneous R -symmetry breaking with additional pseudomoduli [338, 195]. In specific models, it was found by explicit computations that loop corrections preserve the R -symmetry. In [195], it was also shown that having a *single* additional pseudomodulus did not induce spontaneous R -breaking at one-loop and at leading order in

SUSY breaking. Here we provide the general derivation for arbitrarily many pseudomoduli, and to all orders in SUSY breaking.

Our short note proceeds as follows. In Section 4.2 we define the most general O’Raifeartaigh model containing only R -charges 0 and 2 and discuss the relevant terms. In Section 4.3 we explicitly calculate the effective potential, and show that the generated mass matrix for $R = 2$ fields at the origin is positive semi-definite. For completeness, we analyze the zero modes of this mass matrix in Section 4.4 and explicitly confirm that they can only arise for fields that are completely decoupled from SUSY breaking at one-loop order. For such zero modes one would need to investigate higher-order effects in order to determine the vacuum of the theory (or its absence). An appendix summarizes some technical details pertaining to Section 4.4.

4.2 Model Definition

Consider any theory with R -charges 0, 2 only. Label the R -charged fields $X, \sigma_i, i = 1, \dots, N_2$ and the $R = 0$ fields $\rho_a, a = 1, \dots, N_0$. By a simple scaling argument of the R -charged fields, it is clear that from any field configuration one can find a path that terminates at $\sigma_i = 0$ and along which the tree-level potential strictly decreases [274]. In other words, from every point one can continuously lower the classical energy until an R -symmetric point is reached. (It can also be that the energy along this path stays constant, but by simply rescaling the R -charged fields it can never grow.) This makes tree-level breaking of the R -symmetry in such models impossible, and one has to rely on radiative corrections.

Consider now the most general O’R model containing only R -charges 0 and 2. Then

the superpotential can always be brought into the canonical form [332, 274]

$$W = fX + m_{ai}\rho_a\sigma_i + \lambda_{ab}X\rho_a\rho_b + \tilde{\lambda}_{iab}\sigma_i\rho_a\rho_b, \quad (4.2.1)$$

where $R(X) = 2$ and ρ, σ are as above. X is the canonical SUSY-breaking pseudomodulus. There can also be other pseudomoduli not associated with SUSY breaking. If these have $R = 0$, then we do not care what happens to them radiatively, since they will not break R -symmetry regardless. Therefore we are free to expand those ρ fields which are pseudomoduli around their exact vevs.² On the other hand, any additional $R = 2$ pseudomoduli are potentially important. If they get vevs radiatively then they will break R -symmetry spontaneously. So our task is to compute the Coleman-Weinberg potential in this multi-dimensional space and show that the R -symmetric origin is attractive.

There are additional $R = 2$ pseudomoduli if and only if $\text{rank } m < N_2$. Let us single out those that do not have mass terms and call them Y_n , $n = 1, \dots, N'_2$. We will continue to denote the massive $R = 2$ fields with σ_i , with an obvious reduction in their number. Then we can rewrite (4.2.1) as

$$W = fX + m_{ai}\rho_a\sigma_i + \lambda_{ab}X\rho_a\rho_b + \tilde{\lambda}_{nab}Y_n\rho_a\rho_b + \tilde{\lambda}'_{iab}\sigma_i\rho_a\rho_b, \quad (4.2.2)$$

where $m^\dagger m$ is non-singular. Note that mm^\dagger could have zero modes, but there are no tree-level tachyons at the origin. For the purposes of computing the one-loop effective potential for X and Y , the cubic couplings $\tilde{\lambda}'$ never contribute, so we will ignore them henceforth and focus on the simplified superpotential

$$W = fX + m_{ai}\rho_a\sigma_i + \lambda_{ab}X\rho_a\rho_b + \tilde{\lambda}_{nab}Y_n\rho_a\rho_b, \quad (4.2.3)$$

Finally, it is convenient to introduce a pseudomoduli-dependent matrix N_{ab} defined by

$$N_{ab} = \lambda_{ab}X + \tilde{\lambda}_{nab}Y_n. \quad (4.2.4)$$

²Radiatively-generated SUSY-breaking tadpoles in the scalar potential will shift the classical vevs for all the $R = 0$ fields away from the origin if they are not protected by additional symmetries, but as long as those corrections are small we need not worry about them.

Note that N can be taken to be symmetric (but not necessarily real) without loss of generality. In the next section, we will compute the Coleman-Weinberg one-loop effective potential for X and Y_n that follows from this superpotential.

4.3 Pseudomoduli Masses at 1-Loop

In terms of the tree-level boson and fermion mass matrices, the 1-loop effective potential [333] is given by

$$V_{eff}^{(1)} = \frac{1}{64\pi^2} \sum_{i=F,B} \text{Tr}(-1)^F \mathcal{M}_i^4 \log \frac{\mathcal{M}_i^2}{\Lambda^2}. \quad (4.3.1)$$

Following [341], we rewrite this as

$$V_{eff}^{(1)} = -\frac{1}{32\pi^2} \int_0^\Lambda dv v^5 \text{Tr} \left(\frac{1}{v^2 + M_B^2} - \frac{1}{v^2 + M_F^2} \right). \quad (4.3.2)$$

The mass matrices that follow from (4.2.2) are (in the basis $(\rho, \sigma, \rho^*, \sigma^*)$)

$$M_B^2 = \begin{pmatrix} W_{ik}^\dagger W^{kj} & W_{ijk}^\dagger W^k \\ W^{ijk} W_k^\dagger & W^{ik} W_{kj}^\dagger \end{pmatrix} = M_0^2 + M_1^2 + M_2^2 + F \quad (4.3.3)$$

$$M_0^2 = \begin{pmatrix} m^* m^T & 0 & 0 & 0 \\ 0 & m^\dagger m & 0 & 0 \\ 0 & 0 & m m^\dagger & 0 \\ 0 & 0 & 0 & m^T m^* \end{pmatrix} \quad (4.3.4)$$

$$M_1^2 = \begin{pmatrix} 0 & N^\dagger m & 0 & 0 \\ m^\dagger N & 0 & 0 & 0 \\ 0 & 0 & 0 & N^T m^* \\ 0 & 0 & m^T N^* & 0 \end{pmatrix} \quad (4.3.5)$$

$$M_2^2 = \begin{pmatrix} N^\dagger N & 0 & 0 & 0 \\ 0 & 0 & 0 & 0 \\ 0 & 0 & N^T N^* & 0 \\ 0 & 0 & 0 & 0 \end{pmatrix} \quad (4.3.6)$$

$$F = \begin{pmatrix} 0 & 0 & \lambda^\dagger f & 0 \\ 0 & 0 & 0 & 0 \\ \lambda f^* & 0 & 0 & 0 \\ 0 & 0 & 0 & 0 \end{pmatrix} \quad (4.3.7)$$

and M_F^2 is the same but with $F \rightarrow 0$. We would like to expand (4.3.2) out to second order in N . Using (4.3.3)-(4.3.7), we obtain

$$\begin{aligned} V_{eff}^{(1)} \Big|_{N^2} &= \frac{1}{32\pi^2} \int_0^\Lambda dv v^5 \text{Tr} \left((v^2 + M_0^2 + F)^{-2} (M_2^2 - M_1^2 (v^2 + M_0^2 + F)^{-1} M_1^2) - (f \rightarrow 0) \right) \\ &= \frac{1}{16\pi^2} \int_0^\infty dv v^3 \text{Tr} \left((v^2 + M_0^2 + F)^{-1} \left(M_2^2 - \frac{1}{2} M_1^2 (v^2 + M_0^2 + F)^{-1} M_1^2 \right) - (f \rightarrow 0) \right) \end{aligned} \quad (4.3.8)$$

where in the second line we have integrated by parts. This is the generalization of Eqn. (2.12) in [341].

Next we expand out $(v^2 + M_0^2 + F)^{-1}$ in powers of F , delete the terms that vanish

under the trace, and resum the series. This results in:

$$V_{eff}^{(1)}|_{N^2} = \frac{1}{16\pi^2} \int_0^\infty dv v^3 \text{Tr} \left(\frac{\hat{F}^2}{1 - \hat{F}^2} (\hat{M}_2^2 - \hat{M}_1^4) \right), \quad (4.3.9)$$

where the hatted quantities are defined by

$$\hat{F} = (v^2 + M_0^2)^{-1/2} F (v^2 + M_0^2)^{-1/2}, \quad (4.3.10)$$

$$\hat{M}_{1,2}^2 = (v^2 + M_0^2)^{-1/2} M_{1,2}^2 (v^2 + M_0^2)^{-1/2}. \quad (4.3.11)$$

(Since M_0 can be singular this may not be well-defined at $v = 0$, but this does not matter for the v -integral.) Evaluating the block-matrix multiplication and making use of the fact that $\lambda, \tilde{\lambda}_n$ are symmetric, this finally becomes

$$V_{eff}^{(1)}|_{N^2} = \frac{1}{8\pi^2} \int_0^\infty dv v^5 \text{Tr} \left(\frac{\hat{\lambda}^\dagger \hat{\lambda}}{1 - \hat{\lambda}^\dagger \hat{\lambda}} \hat{N}^\dagger \hat{N} \right), \quad (4.3.12)$$

where

$$\begin{aligned} \hat{\lambda} &\equiv (v^2 + mm^\dagger)^{-1/2} \lambda f^* (v^2 + m^* m^T)^{-1/2}, \\ \hat{N} &\equiv (v^2 + mm^\dagger)^{-1/2} N (v^2 + m^* m^T)^{-1/2}. \end{aligned} \quad (4.3.13)$$

The absence of tree-level tachyons at the origin implies that mm^\dagger is positive-semidefinite. Therefore $(1 - \hat{\lambda}^\dagger \hat{\lambda})^{-1}$ is positive-semidefinite, which makes the integrand a trace of a product of positive-semidefinite Hermitian matrices. Hence it is manifestly non-negative for all X and Y_n , making all pseudomoduli masses non-tachyonic at the origin. Generally, they will have positive mass-squareds; we will examine the case where their mass-squareds vanish in the next section.

4.4 Vanishing 1-Loop Masses

We have so far shown that the pseudomoduli mass-squareds around the origin are all non-negative, and thus there is no R -breaking at one-loop in the sense defined before. To

complete the story we need to discuss the pseudomoduli which are massless at one-loop. We will show that this is only possible if these pseudomoduli are manifestly decoupled from SUSY breaking at one-loop order. This shows that there are no possible accidental cancellations, and all the pseudomoduli that can become massive indeed do so. Pseudomoduli which are manifestly decoupled at one-loop can still communicate with SUSY breaking at two and higher loops, and there are known examples where two-loop effects trigger spontaneous R -breaking [226, 260, 36]. It would be interesting to say something general about the two-loop effective potential, but this is beyond the scope of this note.

In terms of the superpotential (4.2.2), what we would like to show is that if some pseudomodulus direction³, labelled by $N_{ab} = \lambda_{ab}X_0(t) + \sum_n Y_{n0}(t)\tilde{\lambda}_{nab}$ with $t \in \mathbb{R}$, is massless at one-loop, then ρ and σ can be split into two nearly-decoupled sets of fields $\{\rho\} \rightarrow \{\rho', \rho''\}$, $\{\sigma\} \rightarrow \{\sigma', \sigma''\}$:

$$W = \left(f\delta X + \rho'^T m' \sigma' + \delta X \rho'^T \lambda \rho' \right) + \left(\rho''^T m'' \sigma'' + \rho''^T N \rho'' \right) + \text{cubic} \quad (4.4.1)$$

These fields only talk to each other through the cubic interactions (which include terms like $\sigma\rho\rho$ and $\delta Y\rho\rho$), and so the pseudomoduli N acquire SUSY-breaking masses only at two and higher loops.

We will take a constructive approach to deriving (4.4.1). That is, we will start from the formula for the one-loop pseudomoduli mass-squareds (4.3.12), use this to derive constraints on λ , N , and m in the superpotential (4.2.2) in the event that the mass-squareds vanish, and show that these constraints necessarily lead us to the nearly-decoupled form (4.4.1).

To begin, suppose the mass of some pseudomodulus vanishes at one-loop order. Ac-

³Here we are being careful to distinguish between the pseudomodulus vevs X_0 , Y_{n0} , and their fluctuations $\delta X \equiv X - X_0$, $\delta Y_n \equiv Y - Y_{n0}$.

according to (4.3.12), this means that

$$\text{Tr}(\hat{\lambda}^\dagger \hat{\lambda} \hat{N}^\dagger \hat{N}) = 0 \quad (4.4.2)$$

for N in the background field direction of this zero mode. This in turn can only be satisfied if

$$\hat{\lambda} \hat{N}^\dagger = 0 \quad (4.4.3)$$

Note that $\hat{\lambda}$ and \hat{N}^\dagger are functions of v via (4.3.13), and (4.4.3) must be true for all v . Expanding in $\frac{1}{v^2}$ yields the following conditions that must be satisfied by the coupling matrices:

$$\lambda(m^* m^T)^k N^\dagger = 0 \quad \text{for all } k = 0, 1, 2, \dots \quad (4.4.4)$$

λ is a complex symmetric matrix, so by a unitary rotation of the ρ fields $\lambda \rightarrow U \lambda U^T$, we can always diagonalize it:

$$\lambda = \begin{pmatrix} \lambda'_{n_1 \times n_1} & 0 \\ 0 & 0 \end{pmatrix} \quad (4.4.5)$$

where λ' is non-singular. The $k = 0$ version of (4.4.4) implies $\lambda N^\dagger = 0$, so in the basis where λ takes the form (4.4.5), we can do another unitary rotation on the ρ fields not coupling to λ' so that

$$N = \begin{pmatrix} 0_{n_1 \times n_1} & & \\ & 0_{n_2 \times n_2} & \\ & & N'_{n_3 \times n_3} \end{pmatrix}, \quad (4.4.6)$$

with N' non-singular. n_2 could of course be zero.

Having used the $k = 0$ condition of (4.4.4) to fix the block-form of λ and N , the $k > 0$ conditions will restrict the form m . Writing the hermitian matrix $m^* m^T$ in 3×3 block form as in (4.4.6), the $k > 0$ conditions of (4.4.4) imply

$$((m^* m^T)^k)_{13} = 0 \quad \text{for all } k = 1, 2, \dots \quad (4.4.7)$$

(The 13 subscript refers to the upper-right block of $(m^*m^T)^k$.) In the appendix, we prove the following lemma in linear algebra: when (4.4.7) is satisfied, one can always find a 3×3 block-unitary transformation that puts m^*m^T into the form

$$m^*m^T = \begin{pmatrix} [m^*m^T]'_{n_4 \times n_4} & 0 \\ 0 & [m^*m^T]''_{n_5 \times n_5} \end{pmatrix} \quad (4.4.8)$$

with $n_4 \geq n_1$ and $n_5 \geq n_3$. Combining this with (4.4.5) and (4.4.6), we conclude that all the ρ fields can be separated into two sectors in which λ , N , and m^*m^T are block-diagonal. By a unitary transformation on the σ fields, the same can be done for m itself, and we arrive at the desired result (4.4.1).

CHAPTER 5

AVOIDING LIGHT GAUGINO MASS PROBLEM WITH AN UPLIFTED MODEL

Based on the 2011 article “Singlet-Stabilized Minimal Gauge Mediation”, written in collaboration with David Curtin and published in Phys.Rev. D83 (2011) 075005.

5.1 Introduction

Supersymmetry (SUSY) is an extremely elegant proposed solution to the hierarchy problem in the Standard Model (SM). However, the question of how SUSY is broken and how this breaking is communicated to the Supersymmetric Standard Model (SSM) is far from settled. Over the years many approaches have been proposed, and one of the most promising avenues is Gauge Mediation [292, 176, 178, 180, 285, 311, 184, 179, 185]. It automatically solves the SUSY flavor problem, since soft terms are generated by flavor-blind SM gauge interactions, and has the additional advantage of being calculable in many cases. The simplest GM models feature a single set of messengers that are charged under the SM gauge groups and couple to a SUSY-breaking hidden sector, generating the SSM soft masses through loop interactions (see [225] for a review). Many generalizations of this minimal theme exist in the literature (see, for example, [292, 176, 178, 180, 285, 311, 184, 179, 185, 256, 324, 50, 308, 291, 177, 343, 16, 265, 183, 257, 262, 302, 132]). For reasons of simplicity, models of Direct Gauge Mediation are particularly appealing since they do not require a separate messenger sector; the SUSY-breaking sector talks directly with the SSM [256, 324, 50, 308, 291, 177, 343, 16, 265]. By defining General Gauge Mediation as any SUSY-breaking model where the soft masses vanish as the SM gauge couplings are taken to zero, it is possible to parametrize the effects of Gauge Mediation in a very model-independent fashion [302].

Gauge mediation does not answer the question of how SUSY is broken, and a large variety of SUSY-breaking models can act as its hidden sector. The most desirable scenario is a hidden sector which breaks supersymmetry dynamically.

Constructing models of dynamical SUSY breaking is extremely difficult, since the absence of any supersymmetric vacua imposes strong constraints on the theory [356]. Those

requirements can be relaxed if we allow for the possibility that our universe lives in a long-lived *meta-stable* SUSY-breaking vacuum, and Intriligator, Seiberg and Shih (ISS) generated enormous interest in 2006 when they demonstrated that such scenarios are fairly generic by showing that simple SUSY QCD with light quark masses can have metastable SUSY-breaking vacua near the origin of field space [262]. While the ISS model is not a fully dynamical model in the strict sense (the small quark mass must be inserted by hand), it does break SUSY non-perturbatively from the point of view of the UV theory and is under full calculational control using the Seiberg Duality [336]. This, in addition to its sheer simplicity, makes it an extremely attractive model-building arena for exploring SUSY-breaking and Direct Gauge Mediation, and several attempts were made to incorporate it into phenomenologically realistic models [183, 272, 243, 228, 194, 12, 160].

The meta-stable ground state of the unmodified ISS model has an unbroken (approximate) R-symmetry that forbids gaugino masses. Breaking that symmetry spontaneously generates gaugino masses that are at least a factor of ~ 10 lighter than the sfermion masses. This is actually a generic feature of many Direct Gauge Mediation models, and the resulting split-SUSY-type spectrum is phenomenologically very undesirable since it exacerbates the little hierarchy problem. Explicit breaking [272, 243, 228, 194] can generate larger masses but creates new SUSY vacua and often creates a tension between reasonably large gaugino masses and stability of the ISS vacuum.

Recent work by Komargodski and Shih [274] sheds light on the issue. It was shown that the leading-order gaugino mass vanishes if the SUSY-breaking vacuum is stable within the renormalizable theory. This applies to unmodified ISS, where in the magnetic theory the SUSY-vacua only show up far out in field space through non-perturbative effects. The first example of a sufficiently destabilized ISS model was [272], and an existence-proof of an ‘uplifted’ model that is stabilized on a higher branch of the pseu-

domoduli space of massive SQCD was presented in [227], with later variations by [298, 280, 64, 72].

This brings us to the motivation for this paper. As is evident from the above discussion, there exists a large variety of ISS-based models of direct gauge mediation, uplifted or not. However, most of them share several shortcomings:

1. Landau pole in the SM gauge couplings below the GUT-scale due to (sometimes very large amount of) excess matter in the hidden sector.
2. The addition of nongeneric or seemingly contrived couplings and deformations, which often break global symmetries. Often there is also an unexplained partial breaking of the hidden sector flavor symmetry, both to stabilize the vacuum and to embed the SM gauge group.
3. Often severe fine-tuning to stabilize the vacuum.

Putting aside the fine-tuning problem for the moment, we would like to address the first two issues. We construct a Direct Gauge Mediation model with an absolutely minimal SQCD sector which has no Landau Pole, no flavor symmetry breaking and (depending on one's judgement) no contrived deformations/couplings. The price we pay for this simplicity is the addition of the singlet sector proposed by [183]. We call this model *Singlet-Stabilized Minimal Gauge Mediation*. Our UV theory will be $SU(4)_C \times SU(5)_F$ s-confining SQCD [337, 258] with a single quark mass scale. The IR theory has trivial gauge group and the standard model gauge group is identified with the $SU(5)_F$. There are two pseudomoduli spaces, the ISS branch with an $SU(4)$ flavor symmetry and a single uplifted branch with unbroken $SU(5)$. The vacuum is stabilized on the uplifted branch by the singlet sector. The spectrum of soft masses is precisely that of Minimal Gauge Mediation, the best possible solution from the point of view of the gaugino mass problem.

We also address an issue that may have not been explicitly discussed in the past: stabilizing an uplifted branch of massive SQCD requires *two* stabilization mechanisms: one each for the adjoint and singlet components of the meson. This makes it extremely hard to avoid some meson deformations.

This paper is laid out somewhat hierarchically. In Section 5.2 we outline the construction of our model and summarize all of the important results. Each summary refers to one of the later sections for details, but the essence of our work is contained in this short overview. The later chapters are organized as follows. A self-contained review of the ISS framework and related model building development is given in Section 5.3. Based on the need for two stabilization mechanisms we derive some guidelines for building uplifted ISS models in Section 5.4. We then move on to slightly more detailed discussions of the overall vacuum structure and spectrum (Section 5.5), implementation of Direct Gauge Mediation to get ISS-based model of Minimal Gauge Mediation (Section 5.6) and the mechanism of stabilizing the uplifted vacuum (Section 5.7). We conclude with Section 5.8.

5.2 Overview of the SSMGM Model

We would like to build a model of direct gauge mediation based on the ISS model [262] that avoids both light gauginos and Landau Poles. *A review of the ISS framework for metastable SUSY braking and direct gauge mediation can be found in section Section 5.3.* In this section we summarize the highlights of our model and its main physical consequences, while the details of the analysis are deferred to Sections 5.4 - 5.7.

In this paper, we construct the smallest possible ISS model stabilized on the high-

est possible pseudomoduli space to ensure that all messengers contribute to the gaugino mass (i.e. we get Minimal Gauge Mediation). This model has no Landau Pole due to minimal excess matter and no flavor breaking. The uplifted vacuum is stabilized via a separate singlet sector, so we call this setup *Singlet-Stabilized Minimal Gauge Mediation* (SSMGM).

Constructing the Magnetic Theory

We want a trivial low-energy gauge group and an $SU(N_f) = SU(5)$ flavor symmetry. This means the electric theory must be s-confining [337, 258], and strictly speaking it is inaccurate to speak of a *magnetic* theory – at low energies we use a *confined* description, where the fundamental degrees of freedom are just the baryons and mesons of the original theory. However, s-confining SQCD displays similar metastable SUSY-breaking behavior as free magnetic SQCD, so in the interest of using familiar ISS-terminology we shall refer to the confined description as ‘magnetic’ and the baryons as ‘magnetic squarks’.

For this choice of electric theory, pseudomoduli space of the magnetic theory only has two branches: the ISS vacuum corresponding to $k = 1$ (i.e. the magnetic squarks get a VEV) and an uplifted branch corresponding to $k = 0$ (i.e. no squarks get a VEV). If we could stabilize the uplifted branch we can identify the SM gauge group with the unbroken $SU(5)$ flavor group. The squarks would then act as a pair of Minimal Gauge Mediation messengers and generate gaugino masses at leading order in SUSY-breaking. The authors of [227] have shown that meson deformations alone cannot achieve this stabilizations for such a small flavor group. Therefore, the price we pay for the pleasing minimality in the SQCD sector is the addition of a singlet sector with its own $U(1)$ gauge group, which spontaneously breaks the $U(1)_R$ symmetry by the inverted hierarchy mechanism [355]

and stabilizes the uplifted vacuum.

In the magnetic description of the ISS model, the field content is

		$SU(N_f)$	$U(1)_B$	$U(1)_R$	$U(1)_S$
SQCD sector	ϕ^i	\square	1	0	0
	$\bar{\phi}_j$	$\bar{\square}$	-1	0	0
	M	Adj + 1	0	2	0
singlet sector	S	1	0	0	1
	\bar{S}	1	0	0	-1
	Z	1	0	2	1
	\bar{Z}	1	0	2	-1

(5.2.1)

where $U(1)_S$ is the gauge group of the singlet sector with coupling g . The complete superpotential is

$$W = h\bar{\phi}_i M_j^i \phi^j + (-hf^2 + dS\bar{S})\text{Tr}M + m'(Z\bar{S} + S\bar{Z}) - a\frac{\det M}{|\Lambda|^{N_f-3}} + m_{adj}\text{Tr}(M'^2), \quad (5.2.2)$$

where a, h are unknown positive $O(1)$ numbers and f, m' are mass scales (which can be complex) much smaller than Λ . The instanton term breaks the approximate $U(1)_R$ symmetry and restores SUSY for large meson VEVs. To explain the last term, decompose the meson into singlet and adjoint components $M = M_{sing} + M_{adj}$. The M' denotes the traceless part of the meson, meaning the deformation only gives a mass to M_{adj} . This is necessary because the singlet sector couples to M_{sing} and stabilizes it away from the origin, but M_{adj} is tachyonic at the origin in the uplifted pseudomoduli space. Therefore, unfortunately, we must give it a mass by hand – this is a general feature of uplifted ISS models. *For the derivation of this model-building requirement, please refer to Section 5.4.*

The Corresponding Electric Theory & Scales of the Model

The electric description is an augmented massive s-confining SQCD with gauge group $SU(N_f - 1) = SU(4)$ and superpotential

$$W = \left(\tilde{f} + \frac{\tilde{d}}{\Lambda_{UV}} S \bar{S} \right) \text{Tr} Q \bar{Q} + m' (Z \bar{S} + S \bar{Z}) + \frac{\tilde{a}}{\Lambda_{UV}} \text{Tr} (Q \bar{Q})'^2, \quad (5.2.3)$$

where \tilde{a} is assumed to be some $O(1)$ number. We make no attempt at explaining the origin of the small quark mass term (see [160] for example). $\Lambda_{UV} > \Lambda$ is the scale of some UV-physics which generates the non-renormalizable $SSQ\bar{Q}$, $Q\bar{Q}Q\bar{Q}$ terms. The natural sizes of the IR parameters are therefore

$$d \sim \frac{\Lambda}{\Lambda_{UV}}, \quad h \sim 1 \quad m_{adj} \sim \frac{\Lambda^2}{\Lambda_{UV}} \sim d\Lambda. \quad (5.2.4)$$

To protect the Seiberg Duality transition from the physics at scale Λ_{UV} , we conservatively require $\Lambda_{UV} \gtrsim 100\Lambda$. The masses f and m' are free parameters as long as they are both smaller than $\sim \Lambda/100$.

A natural choice for Λ_{UV} would be either the GUT-scale or the Planck-scale, with Λ at least two orders of magnitude below that. However, we show in Section 5.7.2 that if Λ is much smaller than $\sim \Lambda_{UV}/100$ the coupling between the singlet sector and the SQCD sector is too weak to stabilize the magnetic meson against the effect of the instanton term, which wants to push the meson towards a supersymmetric vacuum far out in field space. This effectively locks the Λ/Λ_{UV} to be $\sim 10^{-2}$. The two plausible scenarios are then

	Λ	Λ_{UV}
Scenario 1	10^{16}	10^{18}
Scenario 2	10^{14}	10^{16}

(all masses in GeV), setting $d \sim 0.01$.

The Uplifted Vacuum

Ignoring the instanton term near the origin, F_M is given by

$$-F_{M_j^i}^* = h\bar{\phi}_i\phi^j - (hf^2 - dS\bar{S})\delta_i^j. \quad (5.2.5)$$

Since the first term has maximal rank 1 and the second term has maximal rank 5, some F -terms must be nonzero, breaking SUSY by the rank condition. We want to live in the uplifted vacuum, so we set $\langle\bar{\phi}\phi\rangle = 0$. The singlets then obtain nonzero VEV whenever $r = \sqrt{N_f h d} f/m' > 1$, in which case $F_Z, F_{\bar{Z}} \neq 0$ so the singlets participate in the SUSY-breaking. Some of the $\phi, \bar{\phi}$ are tachyonic for

$$\langle|M_{sing}|\rangle < \frac{m'}{\sqrt{hd}}, \quad (5.2.6)$$

but 1-loop corrections from the messengers and the singlet sector give the meson a VEV at

$$\langle|M_{sing}|\rangle \sim \sqrt{\frac{h}{d}}f, \quad (5.2.7)$$

which is large enough to stabilize the messengers and give a viable uplifted vacuum. *A complete discussion of the vacuum structure and spectrum is given in Section 5.5.*

Implementing Direct Gauge Mediation

If we identify the $SU(5)$ flavor group with the SM GUT gauge group and live in the uplifted vacuum, we obtain a model of direct gauge mediation with a single pair of $(5 + \bar{5})$ messengers $\phi, \bar{\phi}$. Since the messengers are tachyonic for small VEVs of the meson M they generate gaugino masses at lowest order in SUSY-breaking – in fact, this is just an

uplifted-ISS implementation of standard Minimal Gauge Mediation. There is no Landau pole, and the singlet degrees of freedom are all heavier than the messengers (except for the pseudomodulus, goldstino and R-axion). *See Section 5.6 for details.*

Stabilizing the Uplifted Vacuum

The one-loop potential from the messengers tries to push the pseudomodulus (and hence the meson) towards the origin where the messengers are tachyonic, while the singlet sector contribution pushes it away from the origin. To cancel these competing contributions and create a local minimum it is necessary to adjust the ratio m'/f to a precision of roughly

$$\Delta \sim \left(\frac{\Lambda}{\Lambda_{UV}} \right)^2, \quad (5.2.8)$$

which is $\sim 10^{-4}$ in our two scenarios. The tuning could be significantly reduced if one were less conservative about the separation of the two scales Λ, Λ_{UV} .

In our scenarios the smallness of d compared to the other couplings raises the question of whether a one-loop analysis can be trusted. We show that two-loop corrections involving the larger couplings do not invalidate our analysis, because they neither influence the non-trivial part of the effective potential which generates the minimum, nor make it impossible to cancel the other smooth contributions to high enough precision so that this interesting part survives. Therefore, the meson can always be stabilized away from the origin.

Finally one must check that decays of the uplifted vacuum to both the ISS and the SUSY vacuum are suppressed enough to make the lifetime longer than the age of the universe. This is indeed the case for our model, since the bounce actions for decay to the ISS and SUSY vacua are enhanced by $(\Lambda_{UV}/\Lambda)^2$ and $\sqrt{\Lambda/f}$ respectively.

See Section 5.7 for a detailed discussion on stabilization of the uplifted vacuum, the effect of two-loop corrections and calculation of the vacuum lifetime.

5.3 Reviewing the ISS Framework

This section provides a brief summary of the ISS framework and related model building developments which form the basis of this paper. After outlining the general need for metastable SUSY-breaking in gauge mediation we review the original ISS model as well as its more recent uplifted incarnations.

5.3.1 The necessity of metastable SUSY-breaking

The reasons for pursuing theories of meta-stable SUSY-breaking go beyond the significant model-building simplifications they potentially afford.

One possible argument goes as follows: A generic theory that breaks SUSY in its ground state must have an R -symmetry (see e.g. [259] for a review). Since this forbids gaugino masses the R -symmetry must be broken. If the R -symmetry is only spontaneously broken one might think that the massless R -axion causes cosmological and astrophysical problems, necessitating explicit R -breaking. By the Nelson-Seiberg theorem [313], this causes supersymmetric vacua to come in from infinity, making the SUSY-breaking vacuum metastable. However, [66] show that supergravity effects give the R -axion a mass, provided that the cosmological constant is tuned away, even if R -symmetry is merely spontaneously broken in the global SUSY theory. Therefore, avoiding a massless R -axion is *not* a reason for metastable SUSY-breaking. (It is still possible that the

R -breaking effects of gravity do in fact destabilize the SUSY-breaking vacuum, but it is not known whether the Nelson-Seiberg theorem applies in this case.)¹

Within the framework of Direct Gauge Mediation there is, however, another very good reason for believing in meta-stable SUSY-breaking. As first noticed in [265], many models of Direct Gauge Mediation suffer from very small gaugino masses compared to the sfermions. This results in a split-SUSY-type spectrum which reintroduces fine tuning into the Higgs Sector. Komargodski and Shih [274] explored this issue in a relatively model-independent way by examining generalized O’Raifeartaigh models (renormalizable Wess-Zumino models which break supersymmetry and have canonical Kahler potentials)². These theories form the low-energy effective description for the hidden sector of many direct gauge mediation scenarios.

Any generalized O’Raifeartaigh model features tree-level flat directions called pseudomoduli emanating from the SUSY-breaking vacuum. The pseudomodulus is the superpartner of the Goldstino, and is stabilized somewhere on the pseudomoduli space by quantum corrections. One can always write the model in the form

$$W = fX + (\lambda X + m)_{ij}\psi^i\psi^j + O(\psi^3) \quad (5.3.1)$$

where the scalar part of X is the pseudomodulus. If we take the ψ ’s to come in $5 + \bar{5}$ pairs of $SU(5)$ then this is an example of Extra-Ordinary Gauge Mediation [132]. To leading order in the SUSY-breaking parameter F/X^2 , the gaugino mass is given by

$$m_\lambda \propto f \frac{\partial}{\partial X} \log \det(\lambda X + m)_{\text{messengers}}. \quad (5.3.2)$$

One can show that if there are no tachyons for any choice of X (i.e. the pseudomoduli space is locally stable everywhere), then $\det(\lambda X + m) = \det m$. Therefore, if the pseu-

¹We thank Zohar Komargodski and Jesse Thaler for pointing this out to us.

²[342] and [310] extend this discussion to semi-Direct Gauge Mediation and models with non-canonical Kahler terms, respectively.

domoduli space is stable everywhere, the gaugino masses vanish at leading order. Since sfermion masses are created at leading order, we have a split-SUSY spectrum.

This shows that in models of Direct Gauge Mediation, the problem of the anomalously small gaugino mass is related to the vacuum structure of the theory. In order to have a gaugino mass at leading order in SUSY-breaking, it is necessary to live in a metastable vacuum from which lower-lying vacua (SUSY-breaking or not) are accessible within the renormalizable theory. SUSY-vacua created by non-perturbative effects far out in field space do not generate a large gaugino mass. (Notice that Minimal Gauge Mediation corresponds to $m = 0$ and a single messenger pair, so the messengers are tachyonic for $X^2 < F$ and large gaugino masses are generated.)

Since the gaugino mass formula eq. (5.3.2) is only valid to lowest order in F/X^2 one might think that sizeable gaugino masses could be generated for large SUSY-breaking. We conducted a small study within the framework of Extra-Ordinary Gauge Mediation using both analytical and numerical techniques, and like many before us [225, 294], we conclude that the gaugino-to-sfermion mass ratio $m_\lambda/m_{\tilde{f}}$ can not be tuned to be larger than $\sim 1/10$ due to a curious numerical suppression of the subleading terms.

5.3.2 The ISS Model

The authors of [262] considered UV-free SQCD with an $SU(N_c)$ gauge group and N_f flavors of electric quarks with a small mass term

$$W = mQ^i\bar{Q}_i \tag{5.3.3}$$

where $m \ll \Lambda$, denoting Λ as the strong coupling scale of the theory. In the free magnetic phase $N_c < N_f < \frac{3}{2}N_c$, the low-energy theory can be studied using Seiberg Duality [336]

and is simply IR-free SQCD with an $SU(N_f - N_c)$ gauge group, a gauge singlet meson Φ and N_f flavors of magnetic quarks q, \bar{q} , as well as a Landau Pole at scale Λ_m .

Writing $N = N_f - N_c < \frac{1}{3}N_f$, the symmetries of the IR theory are $[SU(N)] \times SU(N_f) \times U(1)_B \times U(1)_R$ (gauged symmetries in square brackets)³. The fields have charges Φ : $(1, \text{Adj} + 1)_{0,2}$, q : $(N, \bar{N}_f)_{1,0}$ and \bar{q} : $(\bar{N}, N_f)_{-1,0}$. The Kahler terms of the low-energy effective degrees of freedom are canonical and the superpotential is

$$W = h q_i^a \Phi_j^i \bar{q}_a^j - h \mu^2 \Phi_i^i \quad (5.3.4)$$

where a, b, \dots are gauge indices and i, j, \dots are flavor indices and $\mu \sim \sqrt{\Lambda m}$.

The Φ F-terms are

$$-F_{\Phi_j^i}^* = h q_i^a \bar{q}_a^j - h \mu^2 \delta_j^i. \quad (5.3.5)$$

They cannot all be zero, since the first term has rank at most N and the second term has rank $N_f \geq 3N$, so supersymmetry is broken *by the rank condition*. Expanding around the vacuum, the fields can be written as

$$\Phi = \begin{pmatrix} V & Y \\ \bar{Y} & Z \end{pmatrix}_{\substack{NN_F-N \\ N_F-N}} \quad q = \begin{pmatrix} N & N_F-N \\ \mu + \chi_1 & \rho_1 \end{pmatrix}_N \quad \bar{q} = \begin{pmatrix} N \\ \mu + \bar{\chi}_1 \\ \bar{\rho}_1 \end{pmatrix}_{\substack{N \\ N_F-N}} \quad (5.3.6)$$

with matrix dimensions indicated. (Writing the squark fields with a subscript 1 will be useful for comparison to the uplifted ISS case.) The gauge symmetry is completely higgsed by the squark VEVs, and the surviving global symmetry is $SU(N)_{diag} \times SU(N_f - N) \times U(1)_{B'} \times U(1)_R$. The spectrum divides into distinct sectors. (We take μ to be real for simplicity, and prime denotes traceless part.)

³We emphasize that this $U(1)_R$ symmetry is anomalous under magnetic gauge interactions, which leads to the non-perturbative restoration of supersymmetry discussed below.

1. V and $(\chi_1 + \bar{\chi}_1)$ get mass $\sim |h\mu|$ whereas $(\chi_1 - \bar{\chi}_1)'$ gets eaten by the magnetic gauge supermultiplet via the superHiggs mechanism. This part of the spectrum is supersymmetric at tree-level.
2. $\text{Tr}(\chi_1 - \bar{\chi}_1)$: the fermion is massless at tree level and the real part of the scalar is a classically flat direction (a pseudomodulus) which gets stabilized at zero. Both these fields obtain a mass at loop-level. The imaginary part of the scalar is the Goldstone boson of a broken $U(1)$ symmetry (a mixture of $U(1)_B$ and a diagonal $SU(N_f)$ generator) and is massless to all orders. This part of the spectrum can be made massive by gauging the $U(1)$ symmetry.
3. Z is another pseudomodulus which gets stabilized at the origin and obtains a loop-suppressed mass.
4. $Y, \bar{Y}, \text{Im}(\rho_1 + \bar{\rho}_1), \text{Re}(\rho_1 - \bar{\rho}_1)$ get masses $\sim |h\mu|$. $\text{Re}(\rho_1 + \bar{\rho}_1), \text{Im}(\rho_1 - \bar{\rho}_1)$ are goldstone bosons of the broken flavor symmetry and massless

In the original ISS model as it is defined above, both pseudomoduli are stabilized at the origin by quantum corrections and get a loop-suppressed mass. This leaves the R -symmetry unbroken and forbids gaugino masses, so for use in realistic scenarios of direct gauge mediation the ISS model must be modified somehow to break R -symmetry.

In the magnetic theory supersymmetry is restored non-perturbatively: for large Φ the squarks get a large mass and can be integrated out, leaving a pure SYM theory which undergoes gaugino condensation and has SUSY-vacua at

$$\langle q \rangle = 0, \quad \langle \bar{q} \rangle = 0, \quad \langle \Phi \rangle_{\text{SUSY}} = \Lambda_m \left(\frac{\mu}{\Lambda_m} \right)^{2N/N_f - N} \mathbb{1}. \quad (5.3.7)$$

This makes the SUSY-breaking vacuum at the origin meta-stable, but the smallness of the ratio μ/Λ_m guarantees that the false vacuum is parametrically long-lived.

We can understand this metastability in terms of the connection between R -symmetry and SUSY-breaking. The UV theory does not have an exact R -symmetry, but it emerges as an *accidental* symmetry near the origin of the IR theory. That $U(1)_R$ is anomalous under gauge interactions and hence SUSY is restored by non-perturbative operators far out in field space. The ‘smallness’ of the explicit R -breaking near the origin guarantees that the SUSY-breaking vacuum is long-lived.

Since it will be of special interest to us later we should make a comment about the s-confining case of $N_f = N_c + 1$ [337, 258]. The magnetic gauge group is trivial, but SUSY is still restored far out in field space. This is due to the slightly modified dual superpotential, which includes what looks like an instanton term:

$$W = h \text{Tr} q \Phi \bar{q} - h \text{Tr} \mu^2 \Phi_i^i + c \frac{1}{\Lambda^{N_f-3}} \det \Phi. \quad (5.3.8)$$

Modifying the ISS model for Direct Gauge Mediation

The ISS model looks like a promising framework for models of Direct Gauge Mediation. For example, one could gauge the unbroken $SU(N_f - N)$ flavor symmetry and embed the SM gauge group, which would give gauge charges to the (anti-)fundamentals $\rho_1, \bar{\rho}_1, Y, \bar{Y}$ and make them Extra-Ordinary Gauge Mediation [132] messengers, as well as the Adjoint + Singlet Z . The main obstacle to such a construction is the unbroken R -symmetry in the original ISS model. (Many variations which break $U(1)_R$ spontaneously or explicitly have been proposed, and this discussion is not meant to be exhaustive.) Models with meson deformations [272, 243, 228, 194] add operators of the form $\sim \frac{1}{\Lambda_{UV}} Q \bar{Q} Q \bar{Q}$ in the UV theory which gives operators $\sim \Phi^2$ in the IR theory with suppressed coefficients. This explicitly breaks the R -symmetry and gives the singlet component of the meson a VEV, generating a gaugino mass. These deformations also make the (shifted) ISS-

vacuum more unstable because new SUSY-vacua are introduced. This is per se desirable, since a nonzero gaugino mass at leading order in SUSY-breaking requires the existence of lower-lying vacua within the renormalizable theory, however there is a strong tension between making the gaugino mass somewhat comparable to the sfermion mass and making the vacuum too unstable. Another possibility is adding a baryon deformation to the superpotential, which in the example of [12] involves adding a Λ_{UV}^2 -suppressed operator in the UV theory and breaking R -symmetry spontaneously, generating a very small gaugino mass. A third possibility is the addition of a singlet-sector with its own $U(1)$ gauge symmetry to break R -symmetry spontaneously [160, 183] via the Inverted Hierarchy Mechanism [355]. This again gives a small gaugino mass, and the parameters have to be fine-tuned to stabilize the vacuum.

A common problem with these embeddings is the existence of a Landau Pole, primarily due to the existence of the SM-charged adjoint meson, and some of them also feature non-generic couplings or deformations with somewhat non-trivial flavor contractions.

5.3.3 Uplifting the ISS Model

It would be desirable to obtain a large gaugino mass in a direct gauge mediation model derived from massive SQCD (mSQCD). Adding meson deformations introduces new vacua and generates a gaugino mass at leading order, but the strong tension between stability and sizeable gaugino masses motivates the search for a different kind of metastability: finding a new stable vacuum in a higher branch of the pseudomoduli space of mSQCD (‘uplifting’ the vacuum). This possibility was first realized by Giveon, Katz and Komargodski [227], and we will sketch out their results below.

We start with the same UV theory as the standard ISS model eq. (5.3.3). In the ISS vacuum, the squark VEV matrix has $\text{rank}\langle q\bar{q}\rangle = N$. However, there are higher, unstable pseudomoduli spaces with $\text{rank}\langle q\bar{q}\rangle = k$, with $k = 0, 1, 2, \dots, N-1$. If we assume the squark VEV matrix has rank $k < N$ the surviving symmetry is $[SU(N-k)] \times SU(k)_D \times SU(N_f-k) \times U(1)_{B'} \times U(1)_{B''}$. (As we will see we must assume that the meson is stabilized at a nonzero value, breaking the $U(1)_R$ symmetry.) We expand around the squark VEV and split the fields into representations of the unbroken symmetries:

$$\Phi = \begin{pmatrix} V & Y \\ \bar{Y} & Z \end{pmatrix} \begin{matrix} k \\ N_F-k \end{matrix} \quad q = \begin{pmatrix} \mu + \chi_1 & \rho_1 \\ \chi_2 & \rho_2 \end{pmatrix} \begin{matrix} k \\ N-k \end{matrix} \quad \bar{q} = \begin{pmatrix} \mu + \bar{\chi}_1 & \bar{\chi}_2 \\ \bar{\rho}_1 & \bar{\rho}_2 \end{pmatrix} \begin{matrix} k \\ N_F-k \end{matrix} \quad (5.3.9)$$

The spectrum can again be described in terms of a few separate sectors:

1. $(\chi_2 \pm \bar{\chi}_2), (\chi_1 - \bar{\chi}_1)$ get eaten by the massive gauge supermultiplets. Notice how $\text{Tr}(\chi_1 - \bar{\chi}_1)$ is no longer massless at tree-level because the broken $U(1)$ is a mixture between a gauged diagonal generator and the $U(1)_B$.
2. $V, (\chi_1 + \bar{\chi}_1)$ get F -term mass $\sim |h\mu|$
3. The Y, ρ, Z -type fields can be analyzed separately. The $(Y, \bar{Y}, \rho_1, \bar{\rho}_1)$ fields obtain Z -dependent masses and contain $2k(N_f - k)$ flavor goldstone bosons. In a scenario of Extra-Ordinary Gauge Mediation, these fields constitute messengers that are stable for all Z and hence do not contribute to the gaugino mass. The $(\rho_2, \bar{\rho}_2)$ scalars are tachyonic for $|Z| < |\mu|$, as we would expect from living on an uplifted pseudomoduli space, but if Z can be stabilized at a large-enough value they too are stable and act as messengers which *do* contribute to the gaugino mass at leading order.

The model-building quest is now to break R -symmetry and stabilize the Z at a large

enough value to ensure that all scalars are non-tachyonic. The authors of [227] show that in a renormalizable Wess-Zumino model, no stable SUSY-breaking minimum exists for VEVs much above the highest mass scale of the theory. Hence stabilizing $Z > \mu$ is not feasible in the original model. They circumvent this problem by introducing a *mass hierarchy* into the quark masses, with the first k flavors having mass μ_1 and the remaining $N_f - k$ flavors having a much smaller mass μ_2 . This means that the $\rho_2, \bar{\rho}_2$ fields are tachyonic for $Z < \mu_2 \ll \mu_1$, so stabilizing the meson VEV in the region $\mu_2 < Z < \mu_1$ is possible. They achieve this stabilization for large flavor groups and k close to N by adding finely-tuned meson deformations $\text{Tr}(Z^2), (\text{Tr}Z)^2$. This model is a very important proof-of-principle and it does achieve sizeable gaugino masses as desired, but its drawbacks (Landau pole & non-minimal hidden sector, imposed flavor-breaking mass hierarchies and meson deformations) motivated further research into stabilizing an uplifted ISS model.

Further Developments in Stabilizing Uplifted ISS

There have since been other attempts at stabilizing the uplifted ISS model. [280] examined the equivalent case for $SO(10)$ -unified Direct Gauge Mediation, [298] considered stabilization using SUGRA, and issues of cosmological vacuum selection were discussed in [64]. Stabilization of an uplifted ISS model via baryon deformations was investigated in [72], and while a stable vacuum can be achieved this way for much smaller flavor groups than the proof-of-principle case discussed above, that model also features many non-renormalizable operators with non-trivial flavor contractions and non-generic couplings, as well as an explicit breaking of the hidden sector flavor symmetry. It is in this context that we are motivated to construct an uplifted ISS model with a minimal hidden sector.

5.4 The Adjoint Instability

Before introducing our minimal uplifted ISS model in the next section we examine the general requirements for stabilizing a higher pseudomoduli space of massive SQCD (mSQCD). We emphasize a hitherto neglected point: there must actually be *two* stabilization mechanisms, one for the singlet and one for the adjoint component of the $SU(N_f - k)$ meson Z . This in turn yields to some very general requirements on model building, which suggest that single-trace meson deformations are very hard to avoid in uplifted ISS models.

5.4.1 The messenger contribution to $V_{\text{eff}}(Z)$

Let us examine an uplifted pseudomoduli space in the unmodified ISS model. (We will later add some structure to stabilize it.) The $SU(N_f - k)$ meson Z is a pseudomodulus which is flat at tree-level. The leading contribution to its potential arises from one-loop corrections to the vacuum energy and can be computed using the Coleman-Weinberg formula

$$V_{\text{CW}} = \frac{1}{64\pi^2} \text{STr} M^4 \log \frac{M^2}{\Lambda_m^2} \quad (5.4.1)$$

where Λ_m is the cutoff of the magnetic theory. Since the tree-level spectrum of the magnetic gauge vector multiplet is supersymmetric it does not contribute at one-loop level, and by inspecting the superpotential it is clear that the masses of $V, (\chi_1 + \bar{\chi}_1)$ do not depend on Z at tree-level. Therefore, we only need to consider the dependence of the ρ, Y -type spectrum on Z to determine its 1-loop potential. The relevant part of the superpotential is

$$\frac{1}{h} W_Z = -\mu_2^2 Z_i^i + \rho_{2j} Z_i^j \bar{\rho}_2^i + \rho_{1j} Z_i^j \bar{\rho}_1^i + \mu_1 (\rho_{1i} \bar{Y}^i + Y_i \bar{\rho}_1^i) \quad (5.4.2)$$

where i, j are $SU(N_f - k)$ flavor indices and we hide the trivial color contractions. We have also implemented the flavor-breaking of [227] for generality.

Since V_{CW} due to messengers is generated by single planar Z -loops, it can only depend on single-trace combinations of the form $\text{Tr}[(ZZ^\dagger)^n]$. Furthermore, even if $\langle Z \rangle$ breaks the flavor symmetry, we can use broken $SU(N_f - k)$ generators to diagonalize $\langle Z \rangle$. Therefore it is justified to diagonalize Z and treat the diagonal components separately. It is then easy to verify that $V_{\text{CW}}^{\text{mess}}$ slopes towards the region where $\rho_2, \bar{\rho}_2$ become tachyonic.

It is instructive to phrase this familiar argument in a slightly different way. Decompose the meson Z into adjoint and singlet components:

$$Z_j^i = Z_{adj}^A T_j^{A^i} + Z_{sing} T_S \quad (5.4.3)$$

where T^A are the usual $SU(N_F - k)$ -generators with a slightly modified canonical normalization due to the Z being a complex scalar: $\text{Tr} T^A T^B = \delta^{AB}$, $T_S = \frac{1}{\sqrt{N_F - k}} \mathbb{1}$. Our basic dynamical degrees of freedom are then the $(N_f - k)^2 - 1$ complex fields Z_{adj}^A and the flavor singlet complex field Z_{sing} .

We can do a flavor transformation and push all the VEV of the adjoint into one of the diagonal generators. Call this generator \tilde{T}_{adj} and the associated meson component \tilde{Z}_{adj} . Then

$$\langle Z \rangle = \langle \tilde{Z}_{adj} \rangle \tilde{T}_{adj} + \langle Z_{sing} \rangle T_S \quad (5.4.4)$$

Replacing $Z \rightarrow \tilde{Z}_{adj} \tilde{T}_{adj} + Z_{sing} T_S$ in $\text{Tr}[(ZZ^\dagger)^n]$ we can see that the expression is symmetric under exchange of \tilde{Z}_{adj} and Z_{sing} , since the generators satisfy $\text{Tr} T_S \tilde{T}_{adj} = 0$ and $\text{Tr} T^2 = 1$. *The single-trace condition is therefore equivalent to saying that the adjoint and the singlet components make identical contributions to V_{CW} .* Hence the behavior of $V_{\text{CW}}^{\text{mess}}$ is dictated by its dependence on the singlet component.

5.4.2 Model Building Requirements for Stabilizing Z

This reasoning shows that uplifted ISS models really need *two* stabilization mechanisms:

(i) Z_{sing} must be stabilized at a nonzero VEV large enough to make the messengers non-tachyonic, and (ii) Z_{adj} must be stabilized at zero VEV. If the effective potential is a single-trace object then both requirements are automatically satisfied. However, if only the singlet is stabilized (separately from the adjoint) then the vacuum will be unstable along the Z_{adj} direction and the fields roll towards the lower-lying ISS vacuum. We call this phenomenon the *Adjoint Instability*, and it has direct model building implications. Stabilizing the adjoint in an uplifted vacuum can be done in two ways.

1. Add an additional flavor adjoint. This would allow us to give Z_{adj} a mass (either at tree-level or, more indirectly, at 1-loop).
2. Alternatively, to obtain an effective Z_{adj}^2 term we can do one of the following:
 - (a) Break R-symmetry explicitly by adding meson deformations like $(\text{Tr} Z)^2, \text{Tr}(Z^2)$.
 - (b) Break R-symmetry spontaneously, e.g. by introducing a field A with R-charge -2 which somehow gets a VEV and gives a mass to the adjoint via the coupling $W \supset AMM$.

Adding a flavor adjoint would greatly exacerbate the Landau Pole Problem, and Option 2 (b) is not very attractive because the corresponding operators in the UV would be even more non-renormalizable than meson deformations. (Not to mention the additional machinery required to give A its VEV.) 2 (a) seems like the best solution.

This was also the path taken by the authors of [227]. They stabilize the vacuum by effectively adding a *single*-trace deformation $\text{Tr}(Z^2)$. This deformation treats the singlet and the adjoint equally, and therefore stabilizing the singlet also stabilizes the adjoint. To

lift the mass of Z_{adj} and avoid a Landau Pole below Λ_m without destabilizing the nonzero singlet VEV they must then add another single-trace deformation $\text{Tr}(Z_{adj}^2)$. [72] must also include a single-trace meson deformation to stabilize the meson.

This leads us to conclude that meson deformations $\sim \frac{1}{\Lambda_{UV}} Q\bar{Q}Q\bar{Q}$ are extremely hard to avoid in mSQCD models with meta-stable SUSY-breaking vacua on uplifted pseudo-moduli spaces.

5.5 Vacuum Structure & Spectrum

Near the origin of field space there are two branches of the pseudomoduli space for this model. One is the ISS vacuum, where $k = \text{rank}\langle\bar{\phi}\phi\rangle = 1$ and the flavor symmetry is broken down to $SU(N_f - 1)$. The other is the uplifted vacuum where $k = \text{rank}\langle\bar{\phi}\phi\rangle = 0$, i.e. no squark VEV. To solve the gaugino mass problem we must stabilize the uplifted vacuum. Before we can analyze that stabilization, we must understand the structure of the vacuum manifold at tree-level.

5.5.1 The Uplifted Vacuum ($k = 0$)

We want to live in this uplifted vacuum without squark VEVs to solve the gaugino mass problem. With the meson decomposed into singlet and adjoint components, the superpo-

tential is

$$\begin{aligned}
W = & h\text{Tr}\bar{\phi}M_{adj}\phi + m_{adj}\text{Tr}(M_{adj}^2) \\
& + \left[\frac{h\text{Tr}\bar{\phi}\phi}{\sqrt{N_f}} + \sqrt{N_f}(-hf^2 + dS\bar{S}) \right] M_{sing} + m'(Z\bar{S} + S\bar{Z}) \\
& - \frac{a}{N_f^{N_f/2}} \frac{M_{sing}^{N_f}}{|\Lambda|^{N_f-3}} + \dots
\end{aligned} \tag{5.5.1}$$

where we have omitted Λ -suppressed interactions of M_{adj} . For simplicity, let f , m' and Λ as well as a, h be real and positive throughout this analysis. For now we simply assume that the singlet sector stabilizes M_{sing} at large enough VEV to make the messengers non-tachyonic, and we postpone the detailed discussion of stabilizing the uplifted vacuum to Section 5.7.

Tree-level VEVs near origin of field space

Close to the origin of field space we can ignore the instanton term in determining the VEVs of the fields. For $\langle M_{ad} \rangle = 0$ and $\langle \bar{\phi}\phi \rangle = 0$ we then only need to analyze the second line of eq. (5.5.1) and the tree-level potential for the singlet scalar VEVs becomes

$$\begin{aligned}
V_{tree} \rightarrow & \frac{1}{2}g^2 (|S|^2 + |Z|^2 - |\bar{S}|^2 - |\bar{Z}|^2) \\
& + \left| d\sqrt{N_f}M_{sing}S + m'Z \right|^2 + \left| d\sqrt{N_f}M_{sing}\bar{S} + m'\bar{Z} \right|^2 \\
& + N_f \left| dS\bar{S} - hf^2 \right|^2 + |m'S|^2 + |m'\bar{S}|^2
\end{aligned} \tag{5.5.2}$$

The first line is the D -term potential for the singlet $U(1)_S$ gauge group, and can be set to zero by imposing $|S| = |\bar{S}|, |Z| = |\bar{Z}|$. The $F_{S,\bar{S}}$ -terms in the second line vanish for

$$\langle Z \rangle = -d\sqrt{N_f} \frac{\langle M_{sing}S \rangle}{m'}, \quad \langle \bar{Z} \rangle = -d\sqrt{N_f} \frac{\langle M_{sing}\bar{S} \rangle}{m'}. \tag{5.5.3}$$

This leaves the last line as the potential for S, \bar{S} , which implies

$$\langle S\bar{S} \rangle = \frac{hf^2}{d} - \frac{m'^2}{d^2N_f} \quad \text{whenever} \quad r > 1 \quad \text{where} \quad r = \sqrt{N_fhd} \frac{f}{m'}. \tag{5.5.4}$$

(Often it is convenient to parametrize f in terms of r , as we will see below.) We will assume that this condition is satisfied so that the singlets get a VEV and break the $U(1)_S$ gauge symmetry, which in turn can lead to spontaneous R -symmetry breaking via the inverted hierarchy mechanism. The only nonzero F-terms are

$$\langle F_{M_{sing}} \rangle = -\frac{m'^2}{d\sqrt{N_f}}, \quad \langle F_{Z,\bar{Z}} \rangle = \frac{m'^2}{d\sqrt{N_f}} \sqrt{\frac{hf^2 dN_f}{m'^2} - 1}, \quad (5.5.5)$$

and the total vacuum energy is

$$\langle V_0^{k=0} \rangle = 2hf^2 \frac{m'^2}{d} - \frac{m'^4}{d^2 N_f} \quad (5.5.6)$$

To be precise we decompose all the complex scalar singlets into amplitudes and phases:

$$S = \sigma_S e^{i\frac{\pi_S}{\langle \sigma_S \rangle}}, \quad Z = \sigma_Z e^{i\frac{\pi_Z}{\langle \sigma_Z \rangle}}, \quad M_{sing} = \sigma_{M_{sing}} e^{i\frac{\pi_{M_{sing}}}{\langle \sigma_{M_{sing}} \rangle}}, \quad \text{etc.} \quad (5.5.7)$$

This reveals that of the 5 phases, three are fixed at tree-level whereas the other two are the $U(1)_S$ Nambu-Goldstone boson and the R -axion

$$\pi_R = \frac{1}{F_{tot}} (|F_{M_{sing}}| \pi_{\pi_{sing}} + |F_Z| \pi_Z + |F_{\bar{Z}}| \pi_{\bar{Z}}) \propto \langle \sigma_{M_{sing}} \rangle \pi_{M_{sing}} + \langle \sigma_Z \rangle \pi_Z + \langle \sigma_{\bar{Z}} \rangle \pi_{\bar{Z}} \quad (5.5.8)$$

respectively. Of the 5 amplitudes, one combination

$$\sigma_{PM} = \frac{1}{F_{tot}} (|F_{M_{sing}}| \sigma_{M_{sing}} + |F_Z| \sigma_Z + |F_{\bar{Z}}| \sigma_{\bar{Z}}) \quad (5.5.9)$$

is undetermined at tree-level. This is the pseudomodulus, part of the scalar superpartner of the Goldstino, and since its value affects the masses of the other particles this flat direction is lifted at 1-loop, see eq. (5.4.1).

Tree-level spectrum

The M_{adj} has mass m_{adj} . The messenger fermion and scalar masses are

$$m_\phi = \frac{h}{\sqrt{N_f}} M_{sing} \quad m_\phi^2 = m_\phi^2 \pm \frac{h}{dN_f} m'^2. \quad (5.5.10)$$

Quantum corrections need to stabilize M_{sing} in a region where the messengers are not tachyonic, hence we require

$$\langle |M_{sing}| \rangle > \frac{m'}{\sqrt{hd}}. \quad (5.5.11)$$

We define the singlet sector to mean the superfields $S, \bar{S}, Z, \bar{Z}, M_{sing}$ and the vector superfield of the $U(1)_S$. The singlet spectrum is complicated and we discuss it in detail when analyzing the stabilization of the uplifted vacuum in Section 5.7. The vector multiplet eats a chiral multiplet via the superHiggs mechanism and two (one) chiral multiplets get an F -term (D -term) mass. One multiplet is massless at tree-level: it contains the Goldstino, the pseudomodulus and the R-axion.

Effect of instanton term

Turning on the instanton term creates SUSY-vacua far out in field space. The additional terms in $F_{M_{sing}}$ are easily accounted for by replacing $hf^2 \rightarrow h\tilde{f}^2$ in eq. (5.5.2), where

$$h\tilde{f}^2 = hf^2 - \frac{a}{N_f^{(N_f-1)/2}} \frac{M_{sing}^{N_f-1}}{\Lambda^{N_f-3}}. \quad (5.5.12)$$

(Some of the previously undetermined phases now also get a non-zero VEV, but this does not affect the one-loop stabilization of the pseudomodulus.) As M_{sing} increases $h\tilde{f}^2 \rightarrow 0$ and hence $S, \bar{S}, Z, \bar{Z} \rightarrow 0$. Hence

$$\langle M_{sing} \rangle_{\text{SUSY}} \sim f \left(\frac{f}{\Lambda} \right)^{(N_f-3)/(N_f-1)} \stackrel{N_f \rightarrow 5}{=} \sqrt{f\Lambda}. \quad (5.5.13)$$

The small value of f/Λ is crucial for guaranteeing long-levity of the uplifted vacuum. The effect of these R -breaking terms as well as the stabilization of the uplifted vacuum via quantum corrections is illustrated in fig. 5.1.

Near the origin of field space we care about the changed behavior of the R-axion and the pseudomodulus. The explicit breaking of the R -symmetry gives a small mass to the

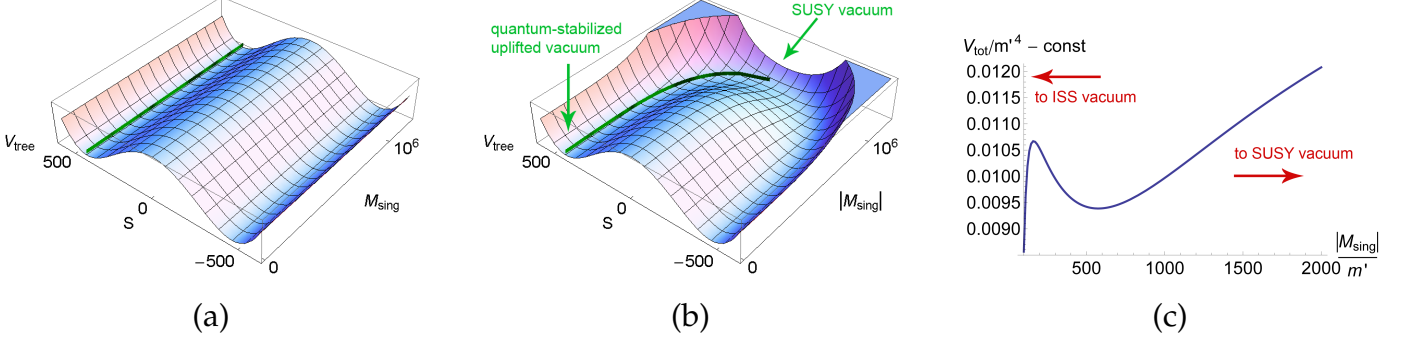


Figure 5.1: (a) The tree-level potential without the instanton term as a function of $|M_{sing}|$ and S , where we have enforced tree-level VEVs $|\bar{S}| = |S|$ and $Z = \bar{Z} = -d\sqrt{N_f}M_{sing}S/m'$. The valley marked with a green band is perfectly flat in the $|M_{sing}|$ direction and shows that the potential has a SUSY-breaking minimum for $S^2 = \frac{hf^2}{d} - \frac{m'^2}{d^2N_f}$. Note that the messengers are tachyonic for $|M_{sing}| < m'/\sqrt{dh}$. (b) The same potential with the instanton term added. The minimum along the S -direction is approximately unchanged close to the origin but is significantly shifted as we move outwards along the $|M_{sing}|$ direction. As we walk along the the valley in the $|M_{sing}|$ direction (which now tilts slightly away from the origin) we eventually reach the SUSY-minimum at $|M_{sing}| \sim \sqrt{\Lambda f}$ and $S, Z = 0$. (c) We compute quantum corrections to the potential along the pseudomodulus direction, i.e. the green band in (b), by setting all fields to their VEVs in terms of $|M_{sing}|$. The vacuum is stabilized at $|M_{sing}| \sim \sqrt{h/d} f \rightarrow Z, \bar{Z} \sim \sqrt{h/d} f^2/m'$. The parameters used for these plots in units of m' were $N_f = 5$, $\Lambda = 3.8 \times 10^9$, $f = 63$ and $(g, d, h) = (0.02513, 0.02, 1)$.

R -axion. Note that even though the large adjoint mass represents a very large explicit R -breaking, since the adjoint does not get a VEV it is not part of the axion. The pseudomodulus is no longer a flat direction at tree-level, but is slightly tilted away from the origin.

Tree-level zero modes

The fermionic component of the tree-level zero mode multiplet is the Goldstino, which is eaten by the Gravitino once SUSY is gauged and gets the familiar mass

$$m_{\tilde{G}} = \frac{F_{tot}}{\sqrt{3}M_{pl}^*} \approx 0.4 \frac{r}{d} \frac{m'^2}{M_{pl}^*} + O(r^{-1}) \quad \text{for } N_f = 5, \quad (5.5.14)$$

where $M_{pl}^* = (8\pi G_N)^{-1/2} = 2.4 \times 10^{18} \text{ GeV}$ is the reduced Planck Mass. (Since $r = \sqrt{hdN_f}f/m' > 1$ and $d \ll 1$, it is often instructive to expand for large r or large f/m' .) The scalar components are the pseudomodulus and the R-axion (eqns 5.5.8, 5.5.9). To compute the 1-loop potential for the pseudoflat direction we set all their phases to their tree-level VEV or zero and express $\langle Z \rangle, \langle \bar{Z} \rangle$ in terms of M_{sing} , which gives $V_{CW}(M_{sing})$. We emphasize that $|M_{sing}|$ is not the pure pseudomodulus, but its value parametrizes where we are along the pseudo-flat direction in field space.¹ This gives $V_{eff}(M_{sing}) = V_{tree}(M_{sing}) + V_{CW}(M_{sing})$. As per the discussion above, the first term is nonzero if we include the instanton term. Minimizing V_{eff} gives $\langle M_{sing} \rangle$ and hence $\langle Z \rangle, \langle \bar{Z} \rangle, \langle S \rangle, \langle \bar{S} \rangle$. To compute the derivative V_{eff} along the flat direction we differentiate with respect to M_{sing} and multiply by a scaling factor $F_{M_{sing}}/F_{tot}$ to account for the fact that moving by δ along the M_{sing} axis moves us by $\delta \sqrt{(F_Z/F_{M_{sing}})^2 + (F_{\bar{Z}}/F_{M_{sing}})^2 + 1}$ along the pseudo-flat direction. Hence we obtain the pseudomodulus mass as

$$m_{PM}^2 = \left(\frac{F_{M_{sing}}}{F_{tot}} \right)^2 \frac{d^2 V_{eff}}{d(M_{sing})^2}. \quad (5.5.15)$$

A similar argument holds for the R -axion mass if we restore the undetermined phases in the tree-level potential. To ensure that we move along the correct direction in field space we impose $\pi_{Z,\bar{Z}} = \frac{F_Z}{F_{M_{sing}}} \pi_{M_{sing}}$, differentiate with respect to $\pi_{M_{sing}}$ and apply the same scaling factor.

These masses can be readily estimated. As we will see in Section 5.7, M_{sing} is stabilized at $\sim \sqrt{d/h}f$. Therefore it is convenient to parametrize

$$\langle M_{sing} \rangle = b \sqrt{\frac{h}{d}} f, \quad \text{where } b \sim O(1). \quad (5.5.16)$$

To obtain the R -axion mass we differentiate the tree-level potential with all VEVs subbed

¹To avoid clutter, we omit the absolute value signs around M_{sing} from now on – they are understood when we talk about M_{sing} as parameterizing the pseudomodulus direction.

in. To lowest order in $1/r$ and $1/\Lambda$ we find that

$$\frac{F_{M_{sing}}}{F_{tot}} \approx -\frac{1}{\sqrt{2dhN_f}} \frac{m'}{f} \longrightarrow m_R \approx 0.2 b \sqrt{\frac{a}{d^3}} \frac{m'^2}{\Lambda} \quad \text{for } N_f = 5. \quad (5.5.17)$$

To estimate the mass of the pseudomodulus we pre-empt another result from Section 5.7.

The rough *scale* of the second derivative of the 1-loop potential is

$$\left| \frac{d^2 V_{CW}}{d(M_{sing})^2} \right| \sim \frac{1}{16\pi^2} \frac{m'^4}{\langle M_{sing} \rangle^2} \quad (5.5.18)$$

(where $Z, \bar{Z} \rightarrow Z(M_{sing}) = -d\sqrt{N_f} M_{sing} \langle S \rangle / m'$). To lowest order in $1/r$ this yields

$$m_{PM} \sim \frac{1}{\sqrt{32N_f} \pi b h} \frac{m'}{f} \left(\frac{m'}{f} \right)^2 \approx 0.1 \frac{d}{b} \frac{m'}{r^2} \quad \text{for } N_f = 5. \quad (5.5.19)$$

Notice the m'/f suppression, simply due to the fact that if $f \gg m'$ then $F_{M_{sing}} \ll \langle M_{sing} \rangle^2$ (similarly for Z, \bar{Z}) and SUSY-breaking is weak. (Effectively this can also be seen as a suppression for small d , since decreasing d increases the minimum size of f to ensure eq. (5.5.4) is satisfied.)

5.5.2 The ISS Vacuum ($k = 1$)

Since this is very similar to a standard $(N, N_f) = (1, 5)$ ISS vacuum we will use the notation of Section 5.3.2 (except for renaming the $SU(N_f - N)$ meson $Z \rightarrow \tilde{M}$ to avoid confusion with the singlets \bar{Z}, Z) and split up the meson according to eq. (5.4.3). The squark VEV $\langle \bar{\chi}_1 \chi_1 \rangle = f^2 - \frac{d}{h} S \bar{S}$ sets $F_V = 0$, with all other SQCD-sector VEVs zero (except \tilde{M}_{sing}). This gives the same singlet potential as eq. (5.5.2) with $N_f \rightarrow N_f - 1$. Therefore the VEVs at tree-level close to the origin are $\langle |S| \rangle = \langle |\bar{S}| \rangle, \langle |Z| \rangle = \langle |\bar{Z}| \rangle, \langle Z \rangle = -\sqrt{N_f - 1} \frac{\langle \tilde{M}_{sing} S \rangle}{m'}$, and

$$\langle S \bar{S} \rangle = \frac{hf^2}{d} - \frac{m'^2}{d^2(N_f - 1)} \quad \text{whenever} \quad hf^2 > \frac{m'^2}{(N_f - 1)d}. \quad (5.5.20)$$

If this condition is not satisfied the singlets do not get a VEV and we have a standard ISS vacuum. If we assume the condition holds (slightly stronger than eq. (5.5.4)), then $\langle \bar{\chi}_1 \chi_1 \rangle = m'^2 / (dhN_f - 1)$, meaning the scale of the squark VEV is given by m' instead of f . The total vacuum energy is

$$\langle V_0^{k=1} \rangle = 2hf^2 \frac{m'^2}{d} - \frac{m'^4}{d^2(N_f - 1)} \quad (5.5.21)$$

The SQCD spectrum is the same as ISS with mass scale $\sim m'$, and the singlet spectrum looks very similar to the uplifted case. We will not dwell on analyzing this vacuum, we only needed to know the potential difference

$$\Delta V_0 \equiv \langle V_0^{k=0} \rangle - \langle V_0^{k=1} \rangle = \frac{m'^4}{d^2} \frac{1}{N_f(N_f - 1)} \quad (5.5.22)$$

to calculate the uplifted vacuum lifetime in Section 5.7.4.

5.6 Direct Gauge Mediation

If we weakly gauge the $SU(5)$ flavor group and identify it with the SM GUT gauge group, this model realizes Minimal Gauge Mediation with a single $5 \oplus \bar{5}$ messenger pair:

$$W_{eff} = X \bar{\phi}_i \phi^i, \quad (5.6.1)$$

where the SUSY-breaking spurions $X = X + \theta^2 F$ is given by

$$X = \frac{h}{\sqrt{N_f}} M_{sing} \quad \rightarrow \quad F = \frac{h}{\sqrt{N_f}} F_{M_{sing}} = -\frac{h}{dN_f} m'^2. \quad (5.6.2)$$

Gaugino and sfermion masses are generated via the well-known 1- and 2-loop diagrams and are parametrically the same size, solving the Gaugino Mass Problem. Using equations (5.2.4), (5.5.16) and (5.5.4) we can see that SUSY-breaking is weak:

$$\left| \frac{X^2}{F} \right| = \left(\frac{f}{m'} \right)^2 h^2 b^2 > \frac{hb^2}{dN_f} \gg 1, \quad (5.6.3)$$

and therefore the soft masses are given by the usual simple expression

$$m_{soft} \sim \frac{\alpha}{4\pi} \left| \frac{F}{X} \right|. \quad (5.6.4)$$

Requiring TeV-scale soft masses sets $|F/X| \sim 100 \text{ TeV}$. This determines the scale of m' (and hence f):

$$m' \sim \left| \frac{F}{X} \right| br, \quad (5.6.5)$$

which sets the messenger mass at

$$X \sim b^2 r^2 \frac{h}{dN_f} \left| \frac{F}{X} \right| \sim r^2 \frac{0.01}{d} \times (10^7 \text{ GeV}) \quad (5.6.6)$$

in the scenarios we are considering. The pseudomodulus, and Goldstino mass scales are

$$m_{PM} \sim \frac{1}{r} \left(\frac{d}{0.01} \right) \times (10 \text{ GeV}) \quad (5.6.7)$$

$$m_{\tilde{G}} \sim b^2 r^3 \left(\frac{0.01}{d} \right) \times (\text{keV}). \quad (5.6.8)$$

The field theory contribution to the R -axion mass is

$$m_R \sim b^3 r^2 \left(\frac{0.01}{d} \right)^{3/2} \frac{\Lambda_{GUT}}{\Lambda} \times (100 \text{ keV}). \quad (5.6.9)$$

Depending on the size of r and b as well as the choice of scenario, this can be smaller or larger than the BPR contribution [66].

Again using results from the next section for convenience, the mass of the singlet vector multiplet is similar to the messenger mass whereas the other singlets (with the exception of the tree-level zero modes) obtain a smaller mass $\sim r^2 |F/X|$. Stabilizing the uplifted vacuum in scenarios 1 and 2 requires $r \lesssim 10^2$ and $r \lesssim 10^1$ respectively, but saturating the former bound gives a very heavy gravitino and reintroduces the SUSY flavor problem. Therefore $1 < r \lesssim 10^1$ is the relevant parameter range for our model.

Since the adjoint meson gets a mass that is only a few orders of magnitude below the duality transition scale Λ , which itself is either at or close to the GUT-scale, there

is no Landau Pole in our model. (Scenario 2 is also an example of *deflected unification* [13].) However, we point out that due to the minimality of this hidden sector such a heavy adjoint is not required to solve the Landau Pole Problem – if the adjoint mass was generated by some other mechanism it could be as low as $\sim 10 - 100$ TeV.

5.7 Stabilizing the Uplifted Vacuum

We now examine how the singlet sector originally proposed in [182] stabilizes the uplifted vacuum. The stabilization is possible due to the singlet sector's $U(1)_S$ gauge group [355], which can supply a negative coefficient to the logarithmic dependence of V_{CW} and push the minimum away from the origin beyond the region where the messengers are tachyonic. We perform this analysis to 1-loop order even though $d \ll h$ and 2-loop effects from h might be competitive. This will be justified in Section 5.7.3. For simplicity we set $a = 1$ throughout.

The effective potential is given by

$$V_{\text{eff}} = V_{\text{tree}} + V_{\text{CW}}, \quad (5.7.1)$$

where all tree-level VEVs and masses are expressed as functions of M_{sing} , which parametrizes the pseudomodulus VEV. V_{tree} is easily obtained by combining equations (5.5.6) and (5.5.12).

$$V_{\text{tree}} = \frac{2hf^2m'^2}{d} - \frac{m'^4}{d^2N_f} - \frac{2m'^2}{d} \frac{a}{N_f^{(N_f-1)/2}} \frac{M_{\text{sing}}^{N_f-1}}{\Lambda^{N_f-3}}. \quad (5.7.2)$$

slopes away from the origin due to the effect of the instanton term. V_{CW} is computed by obtaining the mass spectrum *without the effects of the instanton term*¹ and using eq. (5.4.1).

¹If the instanton term is so large that its backreaction significantly affects the 1-loop potential, its tree-contribution will be so large as to erase any minima created by V_{CW} anyway.

5.7.1 Organizing the Spectrum & Contributions to V_{CW}

All nonzero tree-level masses depend on the value of the pseudomodulus, parametrized by the value of M_{sing} by imposing $Z = \bar{Z} = -d\sqrt{N_f}SM_{\text{sing}}/m'$. It is helpful to express all masses in units of m' and define the following set of parameters:

$$x = d\sqrt{N_f}|M_{\text{sing}}|, \quad r = \sqrt{hdN_f}\frac{f}{m'}, \quad q = \frac{4}{N_f}\frac{g^2}{d^2}(r^2 - 1), \quad p = \frac{h}{dN_f}. \quad (5.7.3)$$

In this parametrization, h just rescales the other variables. $r > 1$ is required for singlet VEVs. This parametrization has the advantage that the masses in every split supermultiplet depend only on x and one of the r, q, p parameters. This allows us to study the different V_{CW} contributions independently as functions of just two variables each.

- The messenger masses can be written as $m_F^2 = p^2x^2$ and $m_S^2 = p^2x^2 \pm p$, and are tachyonic for $x < 1/p$. In the leading-log approximation for large x their contribution to the 1-loop potential is $V_{\text{CW}}^{\text{mess}} \approx \frac{1}{64\pi^2}8N_fp^2 \log x$. (We will ignore additive constants to the potential.)
- Two singlet chiral supermultiplets have F -term masses that depend only on r and x . For large x their masses go as $\sim x$ and $\sim 1/x$, so we denote them R_{heavy} and R_{light} respectively. The contribution $V_{\text{CW}}^{R_{\text{heavy}}}$ stands out because it is the only one that always has a local minimum, located at $x \approx 1.3r - 1$ to a very good approximation. For most values of the parameters the other contributions to the 1-loop potential wash out this minimum and the uplifted pseudomoduli space is not stabilized. However, if the other components cancel to high enough precision then the minimum survives and is located at $\langle x \rangle \sim r$. This justifies the parametrization

$$\langle M_{\text{sing}} \rangle = b\sqrt{\frac{h}{d}}f \quad \text{where} \quad b = O(1). \quad (5.7.4)$$

For large x the light multiplet does not contribute to V_{CW} , whereas $V_{\text{CW}}^{\text{Rheavy}} \approx \frac{1}{64\pi^2} 4 \log x$. Near the local minimum of the total 1-loop potential, their masses to lowest order in $1/r$ are $m_{\text{Rheavy}}^2 \approx \frac{1}{2} (4 + b^2 \pm b\sqrt{8 + b^2}) r^2$.

- One chiral and one vector multiplet get masses from the $U(1)_S$ D -term, both $\sim x$ for large x . Call them Q_{vector} and Q_{chiral} . In the leading-log approximation the contributions to the 1-loop potential are $V_{\text{CW}}^{Q_{\text{vector}}} \approx \frac{1}{64\pi^2} (-8q) \log x$ and $V_{\text{CW}}^{Q_{\text{chiral}}} \approx \frac{1}{64\pi^2} 4 \log x$. Near the local minimum of V_{CW} , their masses to lowest order in $1/r$ are $m_{Q_{\text{vector}}}^2 \approx 4b^2 g^2 r^4 / (d^2 N_f)$ and $m_{Q_{\text{chiral}}}^2 \approx b^2 r^2$.

Adding all the contributions together, we see that the total 1-loop potential in the leading log approximation valid at large x is

$$V_{\text{CW}} \approx \frac{1}{8\pi^2} (1 - t) \log x, \quad (5.7.5)$$

where it will be convenient to define

$$t = q - N_f p^2. \quad (5.7.6)$$

5.7.2 Conditions for local minimum

The leading-log approximation is excellent for $V_{\text{CW}}^{\text{mess}}$ and V_{CW}^Q , even as close to the origin as $x \sim \langle x \rangle$. Hence we can understand the tuning required for stabilizing the uplifted vacuum as follows. Imagine starting out with a choice of parameters for which there is a local minimum of V_{CW} . If we then increase t , the coefficient of the logarithm in the potential decreases until the minimum is wiped out and the potential just slopes towards the SUSY-minimum. Conversely, if we decrease t the coefficient of the logarithm increases and the minimum gets pushed towards the origin, eventually disappearing into the region where

the messengers are tachyonic. Therefore having a local minimum requires $t \in (t_{min}, t_{max})$, where $t_{min, max}$ are $O(1)$ functions of the other parameters. Expressing the singlet-sector gauge coupling in terms of t ,

$$g(t)^2 = \frac{h^2 + d^2 N_f t}{4(r^2 - 1)}, \quad (5.7.7)$$

translates this condition into a required tuning for g . However, it is more instructive to recast the stabilization requirement as a constraint on the mass ratio

$$\left(\frac{m'}{f}\right)^2 = 4g^2 N_f \frac{d}{h} \left(1 - \frac{d^2}{h^2} N_f t\right) + O(g^4) + O(d^5). \quad (5.7.8)$$

We can see immediately that even if t is allowed to take on an $O(1)$ -range of values to guarantee a local minimum, m'/f must actually be adjusted to a precision of

$$\Delta \sim \frac{d^2}{h^2} \sim \left(\frac{\Lambda}{\Lambda_{UV}}\right)^2. \quad (5.7.9)$$

This is $\sim 10^{-4}$ in the two scenarios we are considering but could be significantly larger if one were less conservative about the separation of scales for Λ, Λ_{UV} . Tuning of this order of severity is typical in uplifted models that are stabilized by 1-loop corrections, and we make no attempt to explain it here. It would be very interesting to investigate whether such a mass ratio might be generated by some kind of UV-completion, but it lies beyond the scope of this paper.

What is the actual allowed range of t ? If we switch off the instanton term then there can be no minima of V_{CW} if the coefficient of the logarithm is negative for large x . Hence $t_{max}^{approx} = 1$. To find the smallest allowed value of t we numerically investigate the behavior of V_{CW} and we find that $t_{min}^{approx} \geq 1/2$, with the inequality becoming saturated for $r \gtrsim 10$. Switching on the instanton term has the effect of reducing t_{max} from the approximate value of 1, since the V_{tree} contribution has negative slope and increasing t beyond t_{min} causes the overall potential to have negative slope before we reach $t = 1$. This effect is

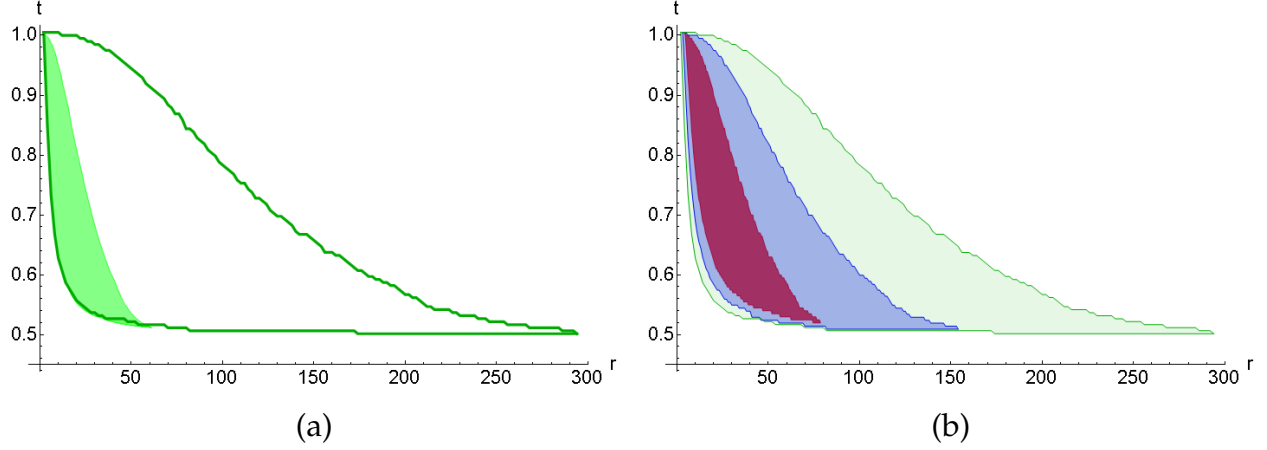


Figure 5.2: (a) For $|F/X| = 100$ TeV and $d = 0.04$ in Scenario 1, V_{eff} has a local minimum in area of the r - t plane enclosed by the green curve. For Scenario 2 this area shrinks down to the shaded region due to the increased effect of the instanton term. (b) Areas of the r - t plane where V_{eff} has a local minimum for $d = 0.04, 0.02, 0.01$ (green/light, blue/medium, red/dark) in Scenario 1. $r_{max} \propto d^{5/6}$, so decreasing d from 0.04 to 0.01 decreases the area where there is a minimum. These areas do not depend significantly on h .

more pronounced for larger r , since increasing f/Λ increases the effect of the instanton term.

To understand this in more detail we studied the complete V_{eff} numerically. By fixing $|F/X|$ in eq. (5.6.4) at 100 TeV one can find t_{min}, t_{max} as functions of r for various values of d and h in scenarios 1 and 2, see fig. 5.2. As expected the instanton term does not have a significant effect on t_{min} but decreases t_{max} from 1 with increasing severity for larger r . This effectively defines a maximum value of r for which there can still be a local minimum of V_{eff} , and r_{max} appears approximately $\propto d$ for fixed Λ, Λ_{UV} .

We can explain this behavior of r_{max} analytically. For fixed other parameters, r_{max} is approximately the value of r for which the scale of the gradient of V_{CW} near the minimum becomes smaller than the scale of the gradient of V_{tree} (eq. (5.7.2)). We can roughly estimate r_{max} by equating the gradient of the leading log approximation to V_{CW} (eq. (5.7.5))

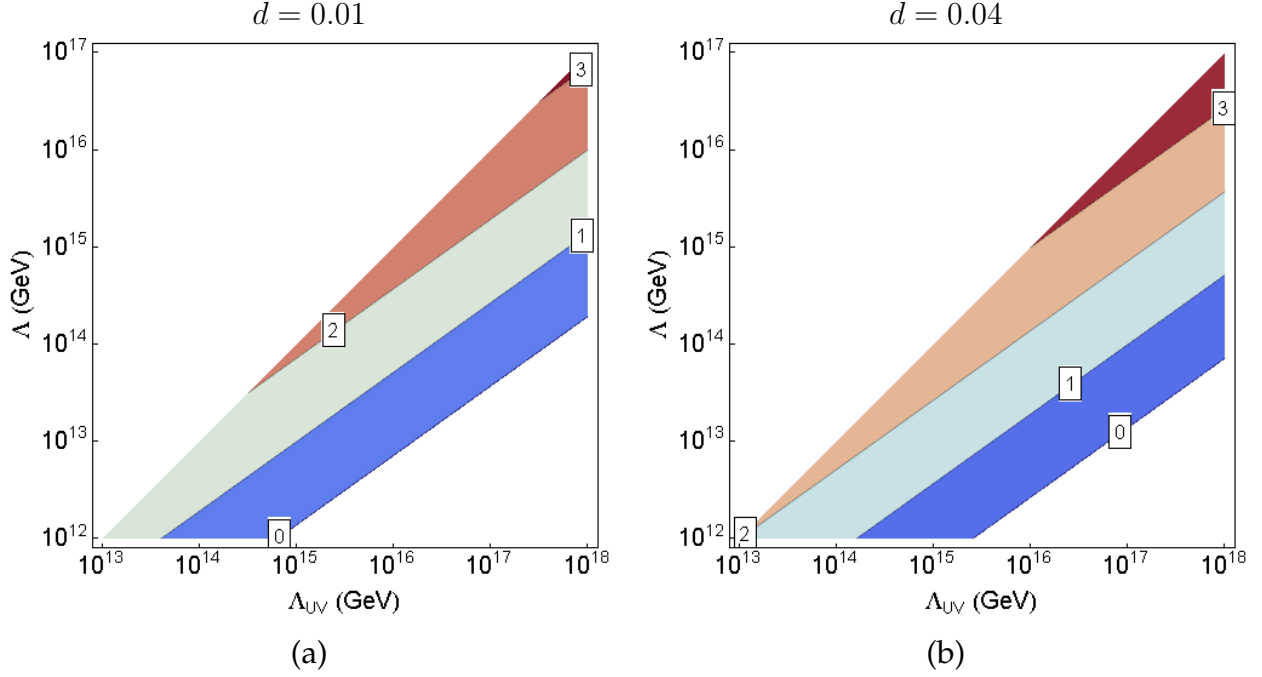


Figure 5.3: Estimate of $\log_{10} r_{max}$ for different values of $d \sim \Lambda/\Lambda_{UV}$. The upper and lower regions are excluded to satisfy $\Lambda \ll \Lambda_{UV}$ and $r > 1$.

to the gradient of V_{tree} for $M_{sing} \sim \sqrt{h/df}$ and $t \sim 0.5$. This yields

$$r_{max} \sim d^{5/6} \left(\frac{\Lambda}{|F/X|} \right)^{1/3} \quad (5.7.10)$$

and explains the approximate linear dependence of r_{max} on d observed numerically.

For Scenarios 1 and 2 this gives $r_{max} \sim 10^2$ and $\sim 10^1$, depending on the exact value of d . This agrees with our numerical results to $\sim 30\%$. Figure 5.3 shows that there are no minima for $\Lambda \ll \Lambda_{UV}/100$ since the coupling between the singlet and SQCD sectors becomes too weak for effective stabilization, which justifies considering only our two scenarios.

Finally, we can also use these ideas to get a rough estimate of the pseudomodulus mass scale. Simply differentiating eq. (5.7.5) and setting $t \sim 0.5$ yields eq. (5.5.18).

5.7.3 Validity of 1-loop calculation

The smallness of $d \sim 0.01$ compared to $h \sim 1$ and g (depending on the size of r) might cause us to suspect that all these results would be invalidated by 2-loop corrections. Fortunately, this naive expectation is not realized due to the nature of contributions to the effective potential. The leading-log approximation to the 1-loop potential eq. (5.7.5) is a very good approximation for the *complete* contributions from messengers (loops involving the h -coupling) and singlets with D -term masses (involving the g -coupling), as well as the *logarithmic* contributions from singlets with F -term masses. The only components not included are the small- x contributions from singlets with F -term masses, and those are the contributions with non-trivial features required to generate the minimum.

The tuning can be understood as canceling the smooth logarithmic contributions to the effective potential to high enough precision so that the minimum created by the contributions from singlets with F -term masses survives. Since d is so small, this local minimum is pushed out to rather large field values $M_{sing} \sim \sqrt{h/d} f$ where the leading log approximation for the ‘uninteresting’ contributions is excellent. This makes the two-loop corrections involving two h and g couplings (messengers and singlets with D -term masses, respectively) very smooth as well, meaning they do not introduce any gross new features to the effective potential. Therefore they just generate a smooth correction to eq. (5.7.5), which can be compensated for by slightly adjusting the gauge coupling g (or the ratio m'/f) and should not significantly affect the existence of local minima or the severity of tuning (though eq. (5.7.8) might have to be slightly adjusted). Therefore the important features of our analysis are valid.

5.7.4 Lifetime Constraints on Uplifted Vacuum Stabilization

We now check that the uplifted vacuum is stable enough to have not decayed in the lifetime of the universe. For each decay path across the potential landscape we estimate the Bounce Action B which exponentially suppresses the decay width [141]. We require $B \gtrsim 10^3$ [242, 98]. For rough estimates of the bounce action we approximate the potential along the decay path as a triangular barrier, which yields very simple analytical expressions for B [190].

There are two decay paths that are only forbidden by loop-sized effects. As illustrated in fig. 5.1, M_{sing} can either tunnel towards the origin, in which case the messengers become tachyonic and the fields roll towards the ISS vacuum, or it can tunnel away from the origin and roll towards the SUSY-minimum.

To estimate the bounce action for decay to the ISS vacuum along the pseudoflat direction we take limit where the height of the potential barrier and the distance from the edge of the barrier to the ISS vacuum goes to zero. This *underestimates* B and gives

$$B_{ISS} > 2\pi^2 \frac{N_f - 1}{N_f} \frac{r^4 (2r^2 - 1)^2}{(d/b^2)^2} \sim \underbrace{\frac{8\pi^2}{5}}_{\sim 15} \underbrace{\left(\frac{\Lambda_{UV}}{\Lambda}\right)^2}_{> 10^4} \underbrace{b^2 r^4 (2r^2 - 1)^2}_{> 1} \gg 10^3 \quad (5.7.11)$$

Turning to the bounce action for decay to the SUSY vacuum along the pseudoflat direction we again take the height of the potential barrier to zero and neglect several unknown or parametrically smaller contributions to the length of the decay path. Using ΔV^0 from eq. (5.5.22) as the depth of the potential well on the other side of the barrier we obtain (neglecting $O(1)$ factors)

$$B_{SUSY} > \frac{32\pi^2}{3} \sqrt{\frac{\Lambda}{f}} \frac{1}{d^{3/2}} \gg 10^3 \quad (5.7.12)$$

Both decays are sufficiently suppressed.

5.8 Conclusions

The ISS framework [262] is an extremely appealing model building arena for exploring non-perturbative meta-stable SUSY-breaking. However, previous ISS-based models of Direct Gauge Mediation are plagued by several problems, both aesthetic and phenomenological, which include small gaugino masses (exacerbating the little hierarchy problem), Landau Poles and non-renormalizable operators with somewhat contrived flavor contractions. Since the issue of small gaugino masses has been understood to be related to the vacuum structure of the theory [227], one model-building challenge is the formulation of plausible uplifted ISS models.

We first outlined some simple but general model-building guidelines for stabilizing uplifted ISS models, which lead us to conclude that meson-deformations are required (or at least heavily favored) to stabilize the adjoint component of the magnetic meson in the hidden sector. However, the singlet can be stabilized by a variety of mechanisms, which makes it possible that an uplifted hidden sector with minimal flavor group might be viable.

This lead us to propose Singlet Stabilized Minimal Gauge Mediation as a simple ISS-based model of Direct Gauge Mediation which avoids both light gauginos and Landau Poles. The hidden sector has trivial magnetic gauge group and minimal unbroken $SU(5)$ flavor group, while the uplifted vacuum is stabilized by a singlet sector with its own $U(1)$ gauge symmetry, generating a nonzero VEV for the singlet meson via the inverted hierarchy mechanism.

The stabilization mechanism used in our model necessitates adjusting parameters to a precision of $\sim (\Lambda/\Lambda_{UV})^2 \sim 10^{-4}$, a common problem with quantum-stabilized models.

While this tuning can be reduced by being less conservative about the separation of scales, one might question the advantage of this tuning compared to the tuning in the MSSM higgs-sector associated with a split-SUSY spectrum. Apart from the fact that a split-SUSY spectrum might not be experimentally observed, the key is that a split-SUSY spectrum *cannot be avoided* in most models of Direct Gauge Mediation that are in the ground state, in particular standard ISS¹. This paper shows that it is possible to stabilize an *uplifted* ISS model with *very small flavor group*, a necessary condition for avoiding Landau Poles of the SM gauge couplings, and while the current stabilization mechanism requires said tuning it seems plausible that an alternative mechanism with generically stabilized up-lifted vacua exists. That makes our stabilization-tuning preferable to the ‘unavoidable’ higgs-sector tuning from a split-SUSY spectrum.

¹One might have an independent suppression mechanism for the sfermion masses, see for example [234]

CHAPTER 6

LEPTOGENESIS IN THE COMPOSITE NEUTRINO MODEL

Based on the 2008 article “Leptogenesis with Composite Neutrinos”, written in collaboration with Yuval Grossman and published in JHEP 0812 (2008) 016.

6.1 INTRODUCTION

In recent years it has become clear that neutrinos have very small masses and that they mix. The origin of these masses is still an open question. The see-saw mechanism is probably the most elegant explanation for small neutrino masses. The idea is to add heavy Majorana right handed (RH) neutrinos to the theory. These added particles give very small Majorana masses to the active, Standard Model (SM) neutrinos. The see-saw mechanism has one more virtue: it provides an elegant mechanism to explain the observed baryon asymmetry in the universe. The idea of this mechanism, called Leptogenesis (LG) [212], is that the heavy RH neutrinos that drive the see-saw also generate lepton asymmetry when they decay. Part of this lepton asymmetry is transformed into the observed baryon asymmetry of the universe (for a review see [164]).

While the see-saw mechanism is very simple and successful, it is not the only way to explain the observed small neutrino masses. Another idea for getting light neutrinos that has not been widely discussed is that of composite RH neutrinos [48, 315]. The basic idea is that there exists a new sector with strong dynamics at a scale Λ . The confinement in this sector leaves some chiral symmetries exact and produces massless composite fermions. The only interaction between the preons of the new sector and the SM sector is via heavy messengers with large masses of order M . Then, the Yukawa coupling between the LH and RH neutrinos is suppressed by powers of the small factor Λ/M . This can give a natural explanation for small Dirac or Majorana neutrino masses.

In this article we further investigate the composite RH neutrino idea. First, we find UV completions for models that give Dirac or Majorana neutrino masses. We then study how these full models can give LG. We find that it exhibits interesting LG possibilities. In particular, it can have see-saw like LG and a low mass scale Dirac LG.

In the next section, we give a brief review of the composite RH neutrino idea of ref. [48]. We find UV complete theories in section III for both Dirac and Majorana neutrinos where the new particle content is given, and the experimental constraints are discussed. In section IV, we study LG possibilities in the model. When the temperature T is below the confinement scale, $T \ll \Lambda$, and the RH neutrinos are heavy, the composite structure of the RH neutrinos cannot be probed and standard LG become possible (IV.A). When $T \sim M \gg \Lambda$, the preons are asymptotically free and standard LG cannot work. In the case of Dirac neutrinos, the decay of heavy messengers gives a realization of a low energy Dirac LG (IV.B). In section V we conclude. A detailed calculation of the effective couplings is given in Appendix A. The experimental bounds on the masses and couplings of the new fields arising from lepton flavor violating processes are given in Appendices B and C.

6.2 COMPOSITE RIGHT-HANDED NEUTRINO

We first review the idea of composite right-handed neutrinos [48]. Consider a new strong sector such that all the new fields are SM singlets. Like QCD, where the interaction becomes strong at a scale Λ_{QCD} , the new sector becomes strong at a new scale Λ . Unlike QCD, however, we assume that the confinement in the new sector keeps some of the chiral symmetries unbroken. In that case, massless composite fermions are generated since they are required for anomaly matching of the unbroken chiral symmetries.

The view point in [48] is that of an effective field theory where the model is a low energy description of a more fundamental theory. In that case one needs to include non-normalizable operators that are suppressed by some high energy scale M . We can think about such operators as emerging from integrating out heavy fields. That is, it is assumed

that the “preons” in the new sector interact with the SM fields through “messengers.” The messengers are fields that are charged under both the SM and the preon sector, and are assumed to be very heavy, with the mass scale $M \gg \Lambda$. After confining dynamics occur, the couplings between the composite fermions and the SM fields are naturally suppressed by powers of the small ratio Λ/M . In particular, the fact that the coupling between the composite and SM fermions are suppressed makes the composite fermions candidates to be light RH neutrinos.

The work of Ref. [175] is a well known example of a model and strong dynamics with unbroken chiral symmetries. The model is based on an $SU(n+4)_C$ gauge group with a single antisymmetric tensor A and n antifundamentals ψ_f (with $f = 1..n$). Below the confinement scale the theory is described by $n(n+1)/2$ massless composite “baryons” $\hat{B}_{ff'} = \hat{B}_{f'f} = \psi_f A \psi_{f'}$. These baryons are identified with the RH neutrinos.

In this work, we focus on the $n = 2$ case, that is a model with a gauge group $SU(6)_C$. This model has three massless baryons that can give mass to the three SM neutrinos. These baryons are connected to the SM neutrinos through higher dimension operators suppressed by the high mass scale M . The lowest dimension operator of interest is

$$\lambda^{ff',i} \frac{(\psi_f^T A^* \psi_{f'}) L_i^\dagger \tilde{H}}{M^3} \equiv \lambda^{ff',i} \epsilon^3 B_{ff'} L_i^\dagger \tilde{H}, \quad (6.2.1)$$

where $i = 1, 2, 3$ runs over the three SM generations and we define

$$\epsilon \equiv \frac{\Lambda}{M}, \quad B_{ff'} \equiv \frac{\psi_f^T A^* \psi_{f'}}{\Lambda^3}, \quad \tilde{H} \equiv i\sigma^2 H^*, \quad (6.2.2)$$

such that $B_{ff'}$ are the canonically normalized baryon fields. If lepton number is a good symmetry of the model, the term in (6.2.1) generates Dirac masses to the SM neutrinos

$$m_\nu = \lambda \epsilon^3 v, \quad (6.2.3)$$

where v is the Higgs vev and flavor indices are suppressed.

We can also include lepton number violating terms in the theory. Then we have the well known see-saw term

$$y_{ij} \frac{\bar{L}_i \bar{L}_j H H}{M}. \quad (6.2.4)$$

In addition, there are new terms involving the composite fermions

$$h^{ff',gg'} \frac{(\psi_f A \psi_{f'}) (\psi_g A \psi_{g'})}{M^5} = h^{ff',gg'} M \epsilon^6 B_{ff'} B_{gg'}. \quad (6.2.5)$$

The neutrino mass matrix is now a 6×6 matrix that in the $(L_\alpha, B_{ff'})$ basis is given by

$$\begin{bmatrix} yv^2/M & \lambda\epsilon^3 v \\ \lambda\epsilon^3 v & h\epsilon^6 M \end{bmatrix}, \quad (6.2.6)$$

where flavor indices are implicit. Diagonalizing the matrix and assuming that all the dimensionless couplings are order one we get

$$m_\nu \sim \frac{v^2}{M}, \quad m_N \sim \epsilon^6 M, \quad \theta_{LR} \sim \min \left(\sqrt{\frac{m_\nu}{m_N}}, \sqrt{\frac{m_N}{m_\nu}} \right). \quad (6.2.7)$$

m_ν and m_N are, respectively, the LH and RH neutrino masses, and θ_{LR} are the mixing angles between the LH and RH neutrinos.

We learn that composite RH neutrinos can naturally give small neutrino masses. They can be Dirac masses, eq. (6.2.3), or Majorana masses, eq. (6.2.7).

6.3 THE UV COMPLETE THEORY

In [48] a low energy effective theory approach was used. In this section, we give UV completions of the models studied in [48]. In III.A, we present the particle content. In III.B, the interactions relating to the new fields are listed and the number of physical

	$SU(6)_C$	$SU(2)_L$	$U(1)_Y$	Q	spin	L	Q_{ps}	$SU(2)_\psi$
${}_i L_L^\alpha$	1	2	$-\frac{1}{2}$	$0, -1$	$\frac{1}{2}$	1	0	1
${}_i E_R$	1	1	-1	-1	$\frac{1}{2}$	-1	0	1
H^α	1	2	$\frac{1}{2}$	$1, 0$	0	0	0	1
${}_g \Omega_{ab}^\alpha$	15	2	$-\frac{1}{2}$	$0, -1$	0	0	2	1
${}_f \psi_a$	6	1	0	0	$\frac{1}{2}$	0	1	2
A_{ab}	15	1	0	0	$\frac{1}{2}$	-1	2	1
Φ_{ab}	15	1	0	0	0	0	2	1
${}_k N$	189 ; 1	1	0	0	$\frac{1}{2}$	break	0	1

Table 6.1: The fermions and scalars of the $SU(6)_C$ model. We divide the particles into four groups. From top to bottom: the SM fields, the messenger, the preons and the optional lepton number violating Majorana fermion.

parameters is discussed. In III.C, we obtain bounds on the parameters from $\mu \rightarrow e\gamma$ and muon-conversion experiments. In Appendix. A, we show how the coupling of eqs. (6.2.1) and (6.2.5) are obtained by integrating out the heavy fields of the UV complete theory.

6.3.1 Particle Content

We consider the case of an $SU(6)_C$ gauge symmetry in the preon sector. As we mention before, this gives three composite neutrinos. The generalization for models with a larger symmetry is straightforward. The minimum particle content of this model is listed in Table 6.1. In the table we identify representations by their dimension. In the SM sector, ${}_i L_L^\alpha$ and H^α are lepton and Higgs doublets carrying $SU(2)_L$ index $\alpha = 1, 2$ while ${}_i E_R$ is an $SU(2)_L$ singlet. L and E carry generation index $i = 1, 2, 3$.

There are two types of fermions in the preon sector. The first fermion, ${}_f \psi_a$, is a fundamental under $SU(6)_C$ that carries a flavor index $f = 1, 2$ and $SU(6)_C$ index, $a = 1, 2, \dots, 6$.

The other fermion, A_{ab} , is a second rank antisymmetric tensor, that is it belongs to the $(0, 1, 0, 0, 0)$ representation of $SU(6)$. Composite fermions are made of these two types of fundamental fermions.

Aside from the fermions we also need scalars that connect the fermions to the SM fields. One scalar, ${}_g\Omega_{ab}^\alpha$, is a heavy messenger, as it is charged under both the SM and preon gauge groups. It carries a generation index $g = 1, 2$ (as discuss below, this is necessary for LG) and transforms as a second rank antisymmetric tensor under $SU(6)_C$ and as a fundamental under $SU(2)_L$. The other heavy scalar, Φ_{ab} , used for connecting two ψ 's together, transforms as a second rank antisymmetric tensor under $SU(6)_C$. The mass scale of both heavy scalars is M , which is assumed to be much larger than the preon confinement scale Λ .

Lastly, in models with lepton number violation we need one more field that breaks lepton number. This field, ${}_kN$, is a SM singlet, and can be either a singlet or a 189 of $SU(6)_C$. [The 189 of $SU(6)$ is $(0, 1, 0, 1, 0)$.] Here $k = 1, 2$ is the generation index, which is needed, as discuss below, for LG.

There are three accidental symmetries for this model, $U(1)_L$, $U(1)_{ps}$, and $SU(2)_\psi$. $U(1)_L$ is the SM lepton number L . It is exact in the model without N , but broken when the Majorana field N is included. $U(1)_{ps}$, where “ps” stands for “preon sector”, corresponds to a preon sector charge, Q_{ps} . Only preons and heavy scalars carry such charge. $SU(2)_\psi$ is a symmetry due to the antisymmetry of the ψ field and correspond to flavor rotation between the two flavors of ψ . Only ψ is charged under this symmetry.

6.3.2 Interactions

We move to discuss the renormalizable interaction terms of the model. The SM Yukawa interactions

$$Y_{ij}^e \bar{L}_L^i H E_R^j + h.c., \quad i, j = 1, 2, 3, \quad (6.3.8)$$

are well known, and we do not discuss them any further. We only recall that the Yukawa couplings, Y_{ij}^e , contain 9 complex parameters.

There are mass terms for the new scalar fields

$$M_{\Omega g g'}^2 \Omega_g^\dagger \Omega_{g'} + M_\Phi^2 \Phi^\dagger \Phi. \quad (6.3.9)$$

Here M_Φ^2 is a dimensionfull coupling with 1 real parameter, and M_Ω^2 is a 2×2 hermitian matrix with 3 real and 1 imaginary parameters. We assume that all new masses are of the same order, $M_\Omega^2 \sim M_\Phi^2 \sim M^2$.

There are also interaction terms that involve the new fields. In both the L-conserving and L-violating models, the following terms are the most relevant to our study

$$Y_{gi}^L A \Omega_g^\dagger L_i + h.c., \quad (6.3.10)$$

$$\tilde{M}_g \tilde{H}^\dagger \Phi^\dagger \Omega_g + h.c., \quad (6.3.11)$$

$$Y_{ff'}^A \psi_f \Phi^\dagger \psi_{f'} + h.c.. \quad (6.3.12)$$

These couplings generate the effective Yukawa interaction of (6.2.1) via the diagram in Fig. 6.1a (see appendix A). The coupling Y_{gi}^L is a general 2×3 matrix containing 6 real and 6 imaginary parameters. \tilde{M}_g corresponds to two dimension full complex coefficients with $g = 1, 2$. We assume that each of the elements of \tilde{M}_g is of order M . The coupling $Y_{ff'}^A$ is a 2×2 antisymmetric matrix with 1 complex parameter (see appendix A).

In the L-violating case we include the N field. The relevant couplings include a Majorana mass term

$$M_{Nkk'} N_k N_{k'}, \quad (6.3.13)$$

where we assume $M_N \sim M$, and interaction terms

$$Y_k^N \Phi^\dagger A N_k + h.c. . \quad (6.3.14)$$

The mass term (6.3.13) and the interaction term (6.3.14) are included for the two possible representations of N , the singlet and the 189. These two terms generate the L-violating term of eq. (6.2.5) through the diagram in Fig. 6.1b. If N is a singlet under all the gauge symmetries, an additional coupling

$$y_{ik}^N H^\dagger L_i N_k + h.c., \quad (6.3.15)$$

exists. This term is the usual Yukawa coupling in the see-saw mechanism. Together with the mass term of (6.3.13) it generates the usual see-saw term for the light neutrinos.

Aside from the couplings relating to neutrino masses and LG, there are couplings that connect the new scalars to the SM Higgs field

$$\lambda_{gg'}^{\Omega(1)} H^\dagger \Omega_g H^\dagger \Omega_{g'} + h.c., \quad \lambda_{gg'}^{\Omega(2)} H^\dagger H \Omega_g^\dagger \Omega_{g'}, \quad \lambda^\Phi H^\dagger H \Phi^\dagger \Phi. \quad (6.3.16)$$

These couplings result in having a Higgs mass much above the weak scale unless they are fine-tuned. This is the usual fine tuning problem of the SM. In this work we do not try to solve this problem, we just assume that there is a solution. Thus, in the following we assume that the couplings in (6.3.16) vanish.

Next we count the number of physical parameters in the various models. In particular, it is important to show that there are CP violating phases in the couplings that we used for LG. We start with the L-conserving model. The parameters of the model discussed

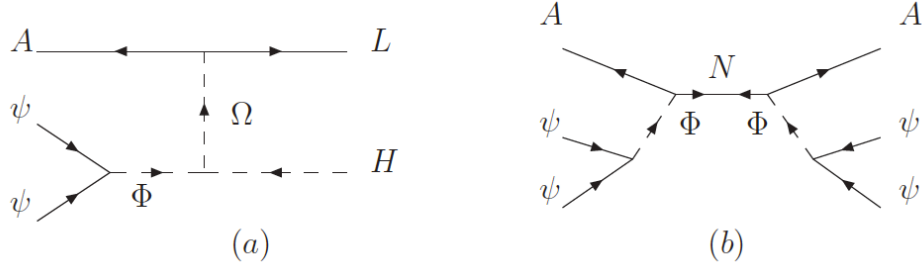


Figure 6.1: The diagrams that generate the effective couplings of the model. (a) generates the Yukawa coupling of eq. (6.2.1) and (b) the L-violating term of eq. (6.2.5).

above introduced 22 real and 19 imaginary parameters. The counting is summarized in Table 6.2. Not all of these parameters, however, are physical. In order to count the number of physics parameters we need to see how many global symmetries are broken by the new terms. The global symmetry breaking pattern is

$$U(3)_L \times U(3)_E \times U(1)_A \times U(2)_\psi \times U(2)_\Omega \times U(1)_\Phi \rightarrow U(1)_L \times U(1)_{ps} \times SU(2)_\psi.$$

Thus, we can eliminate 7 real and 16 imaginary parameters corresponding to the broken generators. This leave us with 15 real and 3 imaginary parameters. It is convenient to work in a basis where all mass parameters are real and diagonal. In that basis the three CPV phases are in Y^L . Note that if we had only one generation for Ω there would be no CPV in the model.

When including the N field there are more parameters and two more broken global symmetries, $U(2)_N$ and $U(1)_L$. The global symmetry breaking pattern becomes

$$U(3)_L \times U(3)_E \times U(1)_A \times U(2)_\psi \times U(2)_\Omega \times U(1)_\Phi \times U(2)_N \rightarrow U(1)_{ps} \times SU(2)_\psi.$$

We then eliminate 8 real and 20 imaginary parameters corresponding to the broken generators. When N is a 189, there are 19 real and 4 imaginary parameters in the theory. When N is singlet, the model has 25 real and 10 imaginary parameters.

Symbol	Number of parameters (R+I)	Number of Physical parameters (R+I)
M_Ω^2	3+1	2+0
M_Φ^2	1+0	1+0
\tilde{M}	2+2	2+0
Y^e	9+9	3+0
Y^L	6+6	6+3
Y^A	1+1	1+0
M_N	3+3	2+0
Y^N	2+2	2+1
y^N	6+6	6+6

Table 6.2: Parameter counting. We divide the couplings into three groups: For the L-conserving model, we only have the couplings in the first group. For the L-violating model, if N is a 189, we have the couplings in both the first and the second group. When N is a singlet, we have all the three groups. For each coupling we list the number of parameter as well as the number of parameter in our “physical” basis choice. We list separately the number of real and imaginary parameters.

6.3.3 Experimental Bounds

One potential issue with the full model is the contributions of the heavy particles to rare processes. The effect of new SM singlets is quite small as they do not couple to SM fields. The messenger, however, can have significant effect as it charged under the SM gauge group. Here we study the most significant bounds. They arise from $\mu \rightarrow e\gamma$, muon electron conversion in nuclei, and cosmology.

Starting with $\mu \rightarrow e\gamma$, see Fig. E.1. In the appendix we calculate the decay rate, eq. (E.2.25),

$$Br(\mu \rightarrow \gamma e) = \frac{\alpha |Y^L|^4}{3072\pi G_F^2 M^4} \quad (6.3.17)$$

Comparing it to the experimental bound [?]

$$Br(\mu \rightarrow eX) < 1.2 \times 10^{-11}, \quad (6.3.18)$$

we obtain a lower bound

$$M > 10|Y^L| \text{ TeV}. \quad (6.3.19)$$

For coherent muon electron conversion in nuclei (Fig. E.2), the theoretical expression is estimated in the appendix, eq. (E.3.32),

$$Br(\mu \rightarrow e, Ti) \equiv \frac{w_{conv}}{w_{cap}} \approx 10^8 |Y^L|^4 \left(\frac{m_\mu}{M} \right)^4. \quad (6.3.20)$$

The experimental bound on the branching ratio is [269]

$$Br(\mu \rightarrow e) < 1.7 \times 10^{-12}. \quad (6.3.21)$$

Comparing the theoretical prediction with the experimental data we get a bound on M

$$M > 10|Y^L| \text{ TeV}. \quad (6.3.22)$$

which is the same as the one we get from $\mu \rightarrow e\gamma$, (6.3.19).

Aside from the constraints coming from particle physics, constraints from big-bang nucleosynthesis (BBN) can be strong when the RH neutrinos have Dirac masses. The reason for this is that the three extra light modes can be populated before BBN. Then the energy density, which depends on the number of relativistic particles, would be different from the SM one. This difference affects the observed ratio of primordial elements.

The number of light degrees of freedom is parameterized by the number of neutrinos. The most stringent bound coming from BBN and CMB data implies $N_\nu \leq 3.3$ at 95% CL [269], that is, the effective contribution of the RH neutrinos can account for as much as 0.3 of one active neutrino.

This bound rules out any model where the RH neutrinos are populated at the same temperature as the SM ones. Yet, if the temperature of the RH sector is lower, the model is viable. The point is that the contribution to the energy density scales like T^4 (where T is the temperature). Explicitly, the energy density of the SM sector (with temperature T_{SM}) and the three light composite neutrinos (with temperature T_{CN}) is given by [273]

$$\rho = \frac{\pi^2}{30} (g_* T_{SM}^4 + \frac{7}{8} \times 3 \times 2 \times T_{CN}^4), \quad (6.3.23)$$

where $g_* \simeq 11$ is the effective number of degrees of freedom in the SM sector (including three massless LH neutrinos). Requiring that the RH neutrinos contribute less than 0.3 active neutrinos is equivalent to the condition

$$3T_{CN}^4 \lesssim 0.3T_{SM}^4 \Rightarrow T_{CN} \lesssim 0.5 T_{SM}. \quad (6.3.24)$$

We learn that we need the composite neutrino temperature to be less than about half of the SM one in order to satisfy the energy density constraint from BBN.

Next we compare the temperature of the two sectors. The preon confinement scale, Λ , is larger than the EW scale. Therefore, the light composite neutrinos decouple from the thermal bath at $T \sim \Lambda$ which is before the EW phase transitions. Thus, the temperature of the composite neutrinos is different than that of the active one. The temperatures ratio is inversely proportional to the ratio of scale factors, $T_{CN} = (a_i/a_f) \Lambda$. The temperature in the SM sector, however, is not just inversely proportional to the scale factor, but is higher than this due to the decrease in the number of degrees of freedom. The total number of degrees of freedom in SM sector is $g_* \simeq 106$ when $T = \Lambda$ but becomes $g_* \simeq 11$ when $T = T_{SM}$ just before BBN. Making the conservative assumption that the EW phase transition is of second order and thus gives no latent heat, the equality between the initial and the final entropies in SM sector gives

$$106 \times a_i^3 \times \Lambda^3 = 11 \times a_f^3 \times T_{SM}^3 \Rightarrow T_{CN} \simeq 0.47 T_{SM}, \quad (6.3.25)$$

which satisfies the BBN bound (6.3.24). When the SM is extended to include extra fields (like in the MSSM) or when the EW phase transition is first order, T_{CN}/T_{SM} is even smaller and thus also satisfies the BBN bound.

6.4 LEPTOGENESIS

As has been discussed, one phenomenological use of the composite model is the realization of leptogenesis. In this section we discuss two LG possibilities corresponding to different reheating temperatures and particle contents. First, we study a model with L-violating interactions and low reheating temperature, T , that is, $T \ll \Lambda$. In this model, standard LG from decays of the heavy composite RH neutrinos is possible. Second, we study a Lepton number conserving model with $T \gg \Lambda$. We can have a realization of Dirac type LG where the new fields can be as light as 10 TeV.

6.4.1 Standard leptogenesis

Consider the L-violating model with $T \ll \Lambda$. In this case, the preon sector is in its confining phase, and the effects of the interior structure of the RH neutrinos cannot be probed. The model looks like the standard see-saw model, and thus we should check if we can get standard LG in that case.

Using Eq. (6.2.7), assuming that all dimensionless couplings are $O(1)$, and setting the active neutrino mass to $m_\nu \sim 10^{-2}$ eV, the composite RH neutrino mass is of order

$$m_N \sim 10^{15} \epsilon^6 \text{ GeV}. \quad (6.4.26)$$

We define the standard two parameters [164]

$$\tilde{m} \equiv 8\pi \frac{v^2}{m_N^2} \Gamma_D, \quad m_* \equiv 8\pi \frac{v^2}{m_N^2} H \Big|_{T=m_N}. \quad (6.4.27)$$

They represent the particle decay and the universe expansion rate relating to LG. The baryon asymmetry is estimated [164]

$$Y_{\Delta B} \simeq \frac{135\zeta(3)}{4\pi^4 g_*} \sum_{\alpha} \varepsilon_{L\alpha\alpha} \times \eta_{\alpha} \times C \simeq 10^{-3} \times \eta \times \varepsilon_L, \quad (6.4.28)$$

where α is a flavor index, $g_* \simeq 106$ as in the SM, and η_{α} is the efficiency factor of LG under various washout effects. In the weak washout regime ($\tilde{m} \ll m_*$), we have $\eta \simeq \tilde{m}^2/m_*^2$, while in the strong washout regime ($\tilde{m} \gg m_*$) we have $\eta \simeq m_*/\tilde{m}$. We use here the SM value, $C \simeq 12/37$, to characterize the sphaleron effects that convert L-number into B-number. For the sake of simplicity, we ignore flavor effects, as they are not changing the order of magnitude of our results. (For a review of flavor effects see, for example, [164].)

Similar to standard LG, the asymmetry ε_L in this case (with Yukawa coupling $\lambda\epsilon^3$) is given by [145] (with $y_n \equiv M_{\beta}^2/M_{\alpha}^2$)

$$\begin{aligned} \varepsilon_{L\alpha\alpha} &\equiv \frac{\Gamma(N_{\alpha} \rightarrow LH) - \Gamma(N_{\alpha} \rightarrow \bar{L}H^*)}{\Gamma(N_{\alpha} \rightarrow LH) + \Gamma(N_{\alpha} \rightarrow \bar{L}H^*)} \\ &= \sum_{\alpha \neq \beta} \frac{\text{Im}[(\lambda\lambda^{\dagger})_{\alpha\beta}^2]\epsilon^6}{8\pi(\lambda\lambda^{\dagger})_{\alpha\alpha}} \sqrt{y_n} \left[1 - (1 + y_n) \ln \left(\frac{1 + y_n}{y_n} \right) \right] \sim \frac{1}{8\pi} \lambda^2 \epsilon^6. \end{aligned} \quad (6.4.29)$$

Note that we explicitly kept the $O(1)$ coupling λ in order to demonstrate where the CP violating phase arises. Using the neutrino mass condition, (6.4.26), the RH neutrino decay rate can be written as

$$\Gamma \simeq \frac{\epsilon^6}{8\pi} m_N \sim 10^{-13} \frac{m_N^2}{\text{TeV}}. \quad (6.4.30)$$

The expansion rate at the time of decay is given by [273]

$$H|_{T=m_N} \simeq 10^{-15} \frac{m_N^2}{\text{TeV}}. \quad (6.4.31)$$

Since $\Gamma \gg H$, the decay is in the strong washout regime. The baryon asymmetry is therefore

$$Y_{\Delta B} \simeq 10^{-3} \varepsilon_L \left(\frac{H|_{T=m_N}}{\Gamma} \right) \sim 10^{-5} \epsilon^6. \quad (6.4.32)$$

Comparing to the observed value, $Y_{\Delta B} \simeq 10^{-10}$, we find that the following range of parameters lead to successful leptogenesis:

$$m_N \sim 10^{10} \text{ GeV}, \quad \epsilon \sim 10^{-1}, \quad M \sim 10^{16} \text{ GeV}, \quad \Lambda \sim 10^{15} \text{ GeV}. \quad (6.4.33)$$

These parameters correspond to a high energy LG scenario which gives the observed values for m_ν and $Y_{\Delta B}$.

6.4.2 Dirac-type leptogenesis

Next we move to study the $T \gg \Lambda$ case. Then the preons are asymptotically free and we perform all the calculations at the preon level. Since we care only about rough estimates we do not include $SU(6)_C$ radiative corrections. Here we study the L-conserving model. We get L-number conservation by not including the heavy Majorana fermion N . Below we show that in that case the decay of the heavy messenger Ω gives a realization of Dirac-type LG [174, 309].

The idea is as follows. When $T \sim M$, the decay of Ω and $\bar{\Omega}$ gives different L and \bar{L} in the final state. Yet, the decays also generate exactly the same difference between the number of A and \bar{A} . Since L and A carry opposite lepton numbers, the total lepton number is zero. Yet, each sector (L and A) carry finite and opposite lepton number. Since the equilibrating rate is smaller than the expansion rate, the L-number is preserved in each sector. When the EW phase transition occurs, sphaleron processes only affects L

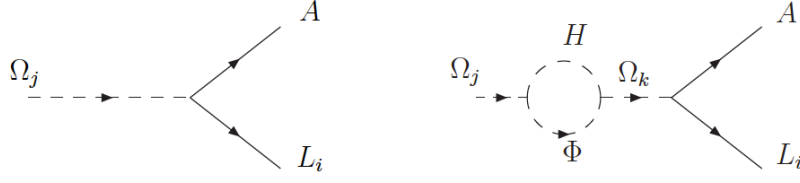


Figure 6.2: The Ω decay process that gives the L-asymmetry.

and \bar{L} , but not A and \bar{A} . Thus, the sphalerons convert part of the L-number stored in the leptons into B-number. We can end up with positive B-number and negative L-number in SM sector. Since we only observe the B-number of the universe this mechanism can be valid.

Specifically we consider the decay $\Omega \rightarrow LA$ (Fig. 6.2). The asymmetry between this decay and its conjugate process comes from the interference between the tree level and the one loop diagrams. It is given by

$$\begin{aligned} \epsilon_{\Omega_j} &\equiv \frac{\Gamma(\bar{\Omega}_j \rightarrow \bar{A}\bar{L}) - \Gamma(\Omega_j \rightarrow AL)}{\Gamma(\bar{\Omega}_j \rightarrow \bar{A}\bar{L}) + \Gamma(\Omega_j \rightarrow AL)} \\ &= \frac{1}{8\pi} \frac{M_j^2 - M_\Phi^2}{M_j^2 - M_k^2} \left(\frac{\tilde{M}_j \tilde{M}_k}{M_j^2} \right) \frac{\text{Im}((Y^{L\dagger} Y^L)_{jk})}{(Y^{L\dagger} Y^L)_{jj}} \sim \frac{r^2}{8\pi}, \quad r \equiv \frac{\tilde{M}}{M}. \end{aligned} \quad (6.4.34)$$

Here $j, k = 1, 2$ and $j \neq k$. M_j , M_k , M_Φ are the masses of Ω_i , Ω_j , Φ , and we assume $M_j \sim M_k \sim M_\Phi$ with $M_\Phi < M_j$ such that Φ can be on-shell in the loop. Following the convention in Table 6.2, we take the trilinear coupling, \tilde{M} , to be real. The CP phase that contributes to the asymmetry is in Y^L . In half of the parameter space we end up with negative L-number in the SM sector and positive L-number in the preon sector.

The natural scale of \tilde{M} is $\tilde{M} \sim M$, that is $r \sim 1$. (Yet, in the following we investigate the allowed parameter space letting the ratio r to vary.) The main result from Eq. (6.4.34) is that we can get very large lepton asymmetry. Thus, we have to check if washout effects can reduce the asymmetry to the observed level.

There are two kinds of washout processes: inverse decays and scattering that equilibrates the L-number. Here, we would like to demonstrate that we can get Dirac-LG. Thus, we only try to find some parts of the parameters space that can produce the observed value of the asymmetry. We concentrate on the part of the parameter space where the equilibrating scattering is negligible, that is, where the equilibrating rate between positive and negative L-numbers is slower than the expansion of the universe.

The parameter space where equilibrating scattering is negligible can be found as follows. First, when $T < M$ the only equilibrating process in our case is $\bar{A}\bar{L} \rightarrow H\bar{\psi}\bar{\psi}$, coming from the diagram in Fig.6.1. Its interaction rate can be estimated as

$$R_{eq}|_T \sim |Y^A|^2 |Y^L|^2 \left(\frac{\tilde{M}}{M} \right)^2 \frac{T^7}{M^6}. \quad (6.4.35)$$

Here the M^{-8} factor comes from the masses of virtual Ω and Φ . Unlike the original Dirac LG scenario [174] where $R_{eq} \propto T$, in our case R_{eq} drops much faster than H , that is, $R_{eq} \propto T^2$. Thus, if the equilibrating is slower than the expansion just when Ω begins to decay, that is,

$$R_{eq}|_{T=M} \sim |Y^L|^2 |Y^A|^2 r^2 M < H|_{T=M} \sim 10^{-15} \frac{M^2}{\text{TeV}}, \quad (6.4.36)$$

then the equilibrating rate after this is always smaller than the expansion rate. In that case scattering is very rare and can be neglected. That is, by choosing the parameter space satisfying eq. (6.4.36), we only need to include the inverse decay for washout effect.

Within this range of parameters we only need to study the effect of inverse decays. The L-asymmetry is given in eq. (6.4.34). We see that for $r > 10^{-3}$, the inverse decay must be significant in order to reduce the asymmetry into the observed value, $Y_{\Delta B} \sim 10^{-10}$. When including the efficiency factor given by the strong inverse decay, eq. (6.4.28), we

have the asymmetry

$$Y_{\Delta B, \Omega} \simeq 10^{-4} \times r^2 \times \left(\frac{H|_{T=M}}{\Gamma_{\Omega}} \right) \sim 10^{-18} \times r^2 \times |Y^L|^{-2} \frac{M}{\text{TeV}}. \quad (6.4.37)$$

If the inverse decay lowers the baryon asymmetry to the observed value, $Y_{\Delta B} \sim 10^{-10}$, the following condition should be satisfied

$$r^2 |Y^L|^{-2} \frac{M}{\text{TeV}} \sim 10^8. \quad (6.4.38)$$

We are ready to find a region of the parameter space that gives successful Dirac-LG. Besides the two constraints eqs. (6.4.36) and (6.4.38) we also have a constraint from the Dirac neutrino mass

$$m_{\nu} = \left(\frac{\tilde{M}}{M} \right) |Y^L| |Y^A| \epsilon^3 v \sim 10^{-2} \text{ eV}. \quad (6.4.39)$$

We also require $\epsilon \equiv (\Lambda/M) < 10^{-2}$, in order justify integrating out the heavy scalars. Then, eq. (6.4.39) gives

$$r |Y^L| |Y^A| > 10^{-7}. \quad (6.4.40)$$

Last, we use $|Y^L|, |Y^A| \lesssim 1$ in order for perturbation theory to work. Then, combining eqs. (6.4.36), (6.4.38) and (6.4.40) we find a representative region in the parameter space that gives a successful Dirac-type LG:

$$\begin{aligned} 10^{-3} r < |Y^L| < 1, \quad |Y^A| < 10^{-4} r^{-2}, \quad |Y^A| < 1, \quad M > 10 \text{ TeV}, \\ 10^{-7} r^{-4} \text{ TeV} < M < 10^7 r^{-2} \text{ TeV}, \quad \epsilon < 10^{-2}. \end{aligned} \quad (6.4.41)$$

As an example, when $r = 1$, the following parameters give a successful Dirac-LG with strong washout effect

$$|\tilde{M}| = M \quad M = 10 \text{ TeV} \quad |Y^L| = 10^{-3} \quad |Y^A| = 10^{-4} \quad \epsilon = 10^{-2}. \quad (6.4.42)$$

When $r = 10^{-3}$, the following parameters give a successful Dirac-LG with weak washout effect

$$|\tilde{M}| = 10^{-3}M \quad M = 10^8 \text{ TeV} \quad |Y^L| = 10^{-3} \quad |Y^A| = 10^{-1} \quad \epsilon = 10^{-2} \quad (6.4.43)$$

We note that when $r > 10^{-2}$, the Ω mass can be as low as 10 TeV, which is, much lighter than the Majorana neutrino mass in the standard LG. The reason that we can get low energy LG is that the Dirac neutrino mass is not directly related to the lepton asymmetry. That is, in the composite model the neutrino mass is suppressed by a factor $(\Lambda/M)^3$. The lepton asymmetry, however, is proportional to r , which is not a very small parameter. In standard LG, on the contrary, both the neutrino mass and the lepton asymmetry are proportional to the Yukawa couplings and thus they cannot be too small.

6.5 DISCUSSIONS AND CONCLUSIONS

We investigated models of composite RH neutrinos. First we find several UV completions of the models. These full models are not expected to be unique. They serve as an example that such models can be constructed. Then we moved on to study leptogenesis in these models. We find that such models can naturally give leptogenesis. In particular, we discussed two possibilities corresponding to different temperatures and particle contents. In the lepton number violating model we find that they can give standard LG from RH neutrino decay. In models with lepton number conservation, we find that they can provide a realization of low energy Dirac LG. We conclude that the idea of composite RH neutrino is phenomenologically interesting: it naturally gives small neutrino masses and successful leptogenesis.

CHAPTER 7

WARM DARK MATTER IN THE COMPOSITE NEUTRINO MODEL

Based on the 2012 article “KeV Warm Dark Matter and Composite Neutrinos”, written in collaboration with Dean J Robinson and published in arXiv:1205.0569.

7.1 Introduction

Sterile neutrinos with masses at the keV scale are a popular warm dark matter (WDM) candidate [317, 186, 339, 7, 187, 90, 108, 104, 54, 46, 286, 357, 215, 110, 284, 168, 167, 169, 45, 128, 304, 216]. Sterile neutrino WDM can be produced non-thermally via (non)-resonant oscillations from the active neutrinos [186, 339, 7, 106, 107, 357, 284, 110, 163, 353], or thermally with subsequent entropy dilution (see e.g. [89, 289]). Typically, the parameter space spanned by the mass (hereafter m_d) and active-sterile mixing angle (hereafter θ_d) for sterile neutrino WDM is most tightly constrained by Lyman- α [107, 89] and x-ray flux [109, 105, 106, 169, 353] bounds, along with free-streaming, Tremaine-Gunn and big-bang nucleosynthesis bounds, too (see e.g. [284, 163]). The aggregate effect of these bounds depends on the production mechanism of the sterile neutrino WDM. In particular, at present purely non-resonant production is disfavored, while windows exist for resonant production and entropy-diluted thermal freeze out [106, 107, 110, 284].

In this Note, we show that elementary keV *Dirac* sterile neutrinos can be a natural feature of the composite neutrino scenario [49, 315, 240, 301, 188], in the same way that the light fermions of the standard model (SM) can arise naturally in the extended technicolor framework [198]. Briefly, the composite neutrino scenario is a class of theories in which the right-handed neutrinos are composite bound states of a confining hidden sector (CHS).

The possibility of such keV sterile neutrinos was first mentioned briefly in Ref. [239], and some of its x-ray flux bounds were investigated in [253]. In this Note, we present a more generalized discussion of this mechanism that is independent of the precise details of the confining sector, and then proceed to investigate the possible cosmological histories for this WDM candidate. We show certain classes of CHS's

can naturally produce keV sterile neutrinos with active-sterile mixing angle in the resonant production window, and a freeze out temperature \gtrsim TeV. Provided the post-inflation reheating temperature is below the TeV scale, then these keV sterile neutrinos could be WDM produced non-thermally via the usual resonant production mechanism [186, 339, 7, 106, 107, 357, 284, 110, 163, 353].

As mentioned above, an alternative to non-thermal WDM production is ultra-relativistic thermal production followed by entropy dilution (see e.g. [89]). This has the advantage of producing colder WDM than resonant production and can better evade the Lyman- α bounds. Usually the diluting entropy is produced by the out-of-equilibrium decay of a sufficiently long-lived heavy particle. In this Note we examine another compelling possibility: The first-order phase transition induced by the confinement of the hidden sector can also produce significant entropy if there is sufficient supercooling. This results in thermal keV WDM. We will discuss the details of this mechanism.

7.2 The Composite Dirac Neutrino Model

7.2.1 Setup

The generic theory of interest is a low-energy effective field theory below a scale M . Its group structure is $G_c \otimes G_F \otimes G_{SM}$, with G_c a confining group called ν -color, G_{SM} the SM gauge groups (or a UV extension), and G_F a global (or weakly gauged) hidden flavor group. The theory consists of three sectors

$$\chi \sim G_c \otimes G_F, \quad \xi \sim G_F, \quad q \sim G_{SM} \otimes G_F, \quad (7.2.1)$$

and which interact only via M -scale irrelevant operators. We call χ ‘preons’ and say they belong to the CHS. Here q denote the SM fields extended to also carry hidden flavor G_F , and we say ξ comprise the ‘extended hidden sector’ (EHS). We assume that the χ and ξ are purely chiral fermions, but we emphasise that like the SM sector, the χ and ξ may consist of various different irreps.

The ν -color group confines at a confinement scale $\Lambda \ll M$. Necessarily $M \gg v$, the electroweak scale, so it is convenient to define two parameters

$$\epsilon \equiv \Lambda/M \ll 1, \quad \theta \equiv v/M \ll 1. \quad (7.2.2)$$

Confinement of the CHS produces preonic bound states, which we shall crudely denote as χ^p : The superscript denotes the number of preons participating in the bound state. Formation of a scalar condensate χ^m with $\langle \chi^m \rangle \neq 0$ generically induces a spontaneous breaking of the hidden flavor group $G_F \rightarrow G'_F \subset G_F$. This produces a new sub- Λ effective field theory, which consists of: preonic bound states; ξ and q decomposed into G'_F irreps; and also light ‘hidden pions’. There are three crucial ideas:

(i) If the CHS has non-trivial G'_F anomalies, then anomaly matching of the CHS to its confined phase, with ξ and q acting as chiral spectators, implies that there are *massless* bound states after confinement. The remaining bound states generically have masses $\sim \Lambda$, except for the hidden pions.

Hereafter we shall assume $G'_F = U(1)_F$, and that there are precisely three massless bound states all with the same $U(1)_F$ charge ¹. For simplicity we assume the massless bound states have the same number of preons, hereafter denoted n , necessarily an odd integer. We shall suggestively denote these bound states as n^i_R , $i = 1, 2, 3$ with $U(1)_F$

¹In this case decomposition of q under $G_F \rightarrow U(1)_F$ could result in multiple copies of SM irreps, also with the same $U(1)_F$ charges, which could be the source of flavor.

charge $F(n_R) = +1$. Explicit examples of preonic theories capable of producing such spectra are presented in Ref. [239]. The corresponding sub- Λ EFT that we shall consider in this Note is shown in Table 7.1.

	ϕ	L_L^c	E_R	Q_L^c	U_R	D_R	n_R
F	+1	0	-1	0	1	-1	+1

Table 7.1: $U(1)_F$ charges assignments to the massless bound states n_R and the SM fields $q = \{\phi, Q, U, D, L, E\}$, which also have the usual SM charges (not shown). The n_R are SM sterile by construction.

One can check $2Y - F = B - L$, so $U(1)_F$ is nonanomalous, and the electroweak symmetry breaking (EWSB) pattern is

$$SU(2)_L \otimes U(1)_Y \otimes U(1)_F \rightarrow U(1)_{EM} \otimes U(1)_{B-L} . \quad (7.2.3)$$

That is, one obtains Dirac neutrinos, with the n_R acting as right-handed neutrinos. Note $U(1)_F$ may be gauged, but we assume its gauge coupling and kinetic mixing with the photon are sufficiently small that they can be neglected.

(ii) For the sub- Λ EFT in Table 7.1, there exist irrelevant operators that couple the preons of the massless n_R – i.e. the G_c singlets χ^n – to the SM singlet $\bar{L}_L \tilde{\phi}$. Such an operator is generically of form

$$\frac{1}{M^{3(n-1)/2}} \bar{L}_L \tilde{\phi} \chi^n \rightarrow \epsilon^{3(n-1)/2} \bar{L}_L \tilde{\phi} n_R , \quad (7.2.4)$$

after confinement. That is, this operator produces a suppressed Yukawa in the sub- Λ EFT. Since n_R are massless and there is $B - L$ symmetry (7.2.3), this operator leads to light Dirac neutrino masses after EWSB, compared to the electroweak scale.

There may also be other vector-like right-handed fermionic bound states N_R and N_L^c , with $F(N_{R,L}) = +1$. We shall again assume for simplicity they contain n preons. Such bound states must form Dirac fermions with Λ scale masses, and the N_R will generically also have operators of form (7.2.4). $N_{R,L}$ are therefore Λ -scale sterile Dirac neutrinos.

(iii) Under decomposition into $U(1)_F$ irreps, the chiral EHS fields ξ may form real $U(1)_F$ representations and acquire masses. However, because the EHS couples only irrelevantly to the condensate $\langle \chi^m \rangle$ responsible for $G_F \rightarrow U(1)_F$, the mass terms must be suppressed. This is the same mechanism which suppresses the quark and lepton masses in Extended Technicolor theories [198]. Explicitly, for a Dirac fermion $\xi_{R,L}$, such mass terms arise from operators of the form

$$\frac{1}{M^{(3m-2)/2}} \xi \chi^m \xi \rightarrow \Lambda \epsilon^{(3m-2)/2} \bar{\xi}_L \xi_R, \quad (7.2.5)$$

after confinement². If also $F(\xi_{R,L}) = +1$, then there may exist irrelevant operators that couple the corresponding G_c singlet $\chi^m \xi$ to $\bar{L}_L \tilde{\phi}$. That is, we could have

$$\frac{1}{M^{3m/2}} \bar{L}_L \tilde{\phi} \chi^m \xi \rightarrow \epsilon^{3m/2} \bar{L}_L \tilde{\phi} \xi_R. \quad (7.2.6)$$

Consequently, such a $\xi_{R,L}$ forms an *elementary* sterile Dirac neutrino with naturally suppressed mass $\sim \Lambda \epsilon^{(3m-2)/2}$. In principle, there may be several species of such a Dirac neutrino, as well as other EHS fermions with $F \neq \pm 1$ that acquire Dirac or even Majorana masses of the same size.

²There may also be mass cross terms involving $\xi_L N_R$, for example. However, we assume that such cross-terms, i.e involving composite and elementary states, are suppressed by the details of the UV theory above M . An analogous assumption must also be made for the proton decay operator *uude*.

7.2.2 Spectrum

We may classify the sub- Λ EFT by a tuple (n, m) , where n (odd ≥ 3) is the number of preons in the sterile neutrino bound states, and m (even ≥ 2) is the number of preons in the symmetry breaking condensate. After EWSB, from eqs. (7.2.4)–(7.2.6) a (n, m) theory has neutrino mass term,

$$\Lambda \begin{pmatrix} \nu_L \\ \xi_L \\ N_L \end{pmatrix}^T \begin{pmatrix} \theta \epsilon^{\frac{3n-5}{2}} & \theta \epsilon^{\frac{3m-2}{2}} & \theta \epsilon^{\frac{3n-5}{2}} \\ 0 & \epsilon^{\frac{3m-2}{2}} & 0 \\ 0 & 0 & 1 \end{pmatrix} \begin{pmatrix} n_R \\ \xi_R \\ N_R \end{pmatrix}, \quad (7.2.7)$$

where ν_L is the SM active neutrino. Each entry of this mass matrix denotes the prefactor of an $\mathcal{O}(1)$ sub-block, whose dimensions depends on the number of species of each type of sterile neutrino. For example, the upper left entry must be 3×3 .

For $m \leq n - 1$, the mass spectrum can be determined by expansions in ϵ and θ . One obtains at leading order

$$m_l \sim v \epsilon^{\frac{3(n-1)}{2}}, \quad m_d \sim \Lambda \epsilon^{\frac{3m-2}{2}}, \quad m_h \sim \Lambda. \quad (7.2.8)$$

Here the superscripts l , d and h denote ‘light’, ‘dark’ and ‘heavy’. The left-handed mass basis is, at leading order in ϵ and θ ,

$$\begin{pmatrix} \nu_L^l \\ \nu_L^d \\ \nu_L^h \end{pmatrix} \sim \begin{pmatrix} 1 & \theta & \theta \epsilon^{\frac{3n-5}{2}} \\ \theta & 1 & \theta^2 \epsilon^{\frac{3n+6m-9}{2}} \\ \theta \epsilon^{\frac{3n-5}{2}} & \theta^2 \epsilon^{\frac{3n-5}{2}} & 1 \end{pmatrix} \begin{pmatrix} \nu_L \\ \xi_L \\ N_L \end{pmatrix}, \quad (7.2.9)$$

and the right-handed mass basis is

$$\begin{pmatrix} \nu_R^l \\ \nu_R^d \\ \nu_R^h \end{pmatrix} \sim \begin{pmatrix} 1 & \theta^2 \epsilon^{\frac{3(n-m-1)}{2}} & \theta^2 \epsilon^{3n-5} \\ \theta^2 \epsilon^{\frac{3(n-m-1)}{2}} & 1 & \theta^2 \epsilon^{\frac{3n+3m-7}{2}} \\ \theta^2 \epsilon^{3n-5} & \theta^2 \epsilon^{\frac{3n+3m-7}{2}} & 1 \end{pmatrix} \begin{pmatrix} n_R \\ \xi_R \\ N_R \end{pmatrix}. \quad (7.2.10)$$

We emphasise that eqs. (7.2.9) and (7.2.10) denote only sub-block prefactors; the entries of the sub-blocks themselves are generically $\mathcal{O}(1)$ numbers.

It is clear from eq. (7.2.9) that the dark-active mixing angle $\theta_d \sim \theta$. One can then rearrange eqs. (7.2.8) and (7.2.9) into

$$m_d \theta_d \sim v \left(\frac{m_l}{v} \right)^{\frac{m}{n-1}}, \quad \frac{\Lambda}{m_d} \sim \left(\frac{m_l}{v} \right)^{\frac{2-3m}{3n-3}}, \quad (7.2.11)$$

in which the right-hand sides are fully specified by (n, m) and the requirement that $m_l \sim 0.05$ eV, $v \simeq 174$ GeV. Figure 7.1 shows θ_d up to $\mathcal{O}(1)$ uncertainty as a function of m_d , with $m = n - 1$. Theories with $m < n - 1$ have much larger mixing angles, and are therefore ruled out by x-ray flux constraints, so we consider only $(n, n - 1)$ theories henceforth. For such theories $M \sim 2 \times 10^4 (m_d/5 \text{ keV}) \text{ TeV}$, and we provide the corresponding Λ and ϵ in Table 7.2.

(n, m)	$\Lambda \times (5 \text{ keV}/m_d) \text{ (TeV)}$	$\epsilon \times (5 \text{ keV}/m_d)$
(3, 2)	1	7×10^{-5}
(5, 4)	10^2	8×10^{-3}
(7, 6)	7×10^3	9×10^{-2}

Table 7.2: Confinement scale Λ and ϵ for $(n, n - 1)$ theories. Such theories with $n > 7$ have $\epsilon \not\ll 1$, and are not considered further.

It is amusing to note that for the $(n, n - 1)$ theories $m_d \sim 5 \text{ keV}$ implies $\sin^2(2\theta_d) \sim$

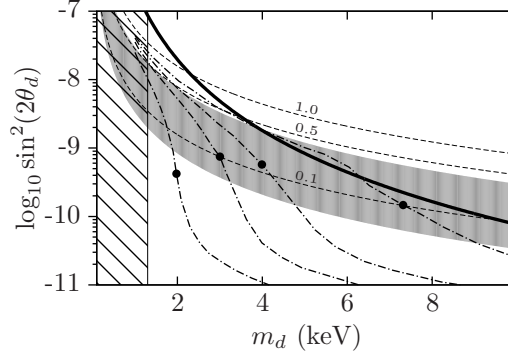


Figure 7.1: Mixing angle $\sin^2(2\theta_d)$ up to $\mathcal{O}(1)$ uncertainty (light gray) as a function of m_d , for $(n, n-1)$ theories. Also shown: The thermal production Lyman- α exclusion (hatched region, see e.g. [107]); the x-ray flux exclusion for ν^d energy fraction $\Omega_d = \Omega_{\text{DM}}$ (heavy black line, see e.g. [109, 105]); non-resonant production contours (dashed lines), labelled by the ratio of energy fractions $\Omega_d/\Omega_{\text{DM}}$ [54, 110, 284]; resonant total DM production contours (dash-dotted lines) for lepton asymmetries $Y_{\Delta L} = 8, 12, 16, 25 \times 10^{-6}$ (resp. top to bottom), and their corresponding Lyman- α lower bounds on the WDM mass (black dots) [110].

3×10^{-10} , which matches the (as yet unconfirmed) *Chandra* results in the Willman I dwarf galaxy [290].

7.2.3 Dirac vs Majorana

The keV sterile neutrinos in this Note are Dirac, in contrast with the Majorana sterile neutrinos often considered in other WDM scenarios. The WDM production mechanisms that we consider below produce dominantly symmetric DM – the resonant production mechanism requires an asymmetry in the proper number density $(n_\nu - n_{\bar{\nu}})/n_\nu < 10^{-2}$ [7, 357] – so that the DM particles and antiparticles are present in the same abundances to a very good approximation. The x-ray flux bounds due to sterile neutrinos are therefore insensitive to the mass structure, since decay modes to the active neutrino and antineutrino are present in both cases: I.e, the x-ray flux is due to either $N \rightarrow \nu\gamma$ and $N \rightarrow \nu^c\gamma$

for a Majorana neutrino N , or $\nu^d \rightarrow \nu\gamma$ and $\bar{\nu}^d \rightarrow \bar{\nu}\gamma$ for the present scenario. Similarly, (non)-resonant production by conversion from the active neutrinos will produce the same energy densities, regardless of the Dirac or Majorana nature of the masses. We therefore use existing results for these bounds and processes in Fig. 7.1 without alteration.

7.2.4 Decoupling

Our knowledge of the generic structure of the non-renormalizable operators permits us to consider the cosmological histories of the CHS and EHS, and therefore determine whether the ν^d sterile neutrinos can be a WDM candidate: satisfying the (m_d, θ_d) bounds is necessary but not sufficient for this. For the $(n, n-1)$ theories, we now enumerate various important processes and their freeze out temperatures, T_{fr} . We assume the effective degrees of freedom at the TeV scale $g_* \sim 10^2$.

(i) $\bar{X}X \leftrightarrow \bar{Y}Y$, where $X, Y \in \{q, \xi, \chi\}$. These processes couple the SM, CHS and EHS. The dimension-5 operator $\phi^\dagger \phi \bar{X}X$ is heavily suppressed, since X are all chiral. The leading operators are then the dimension-6

$$\frac{1}{M^2} \bar{X} \gamma^\mu X \bar{Y} \gamma_\mu Y ; T_{\text{fr}} \leq \left[\frac{g_*^{\frac{1}{2}} M^4}{M_{\text{pl}}} \right]^{1/3} \sim \text{TeV} , \quad (7.2.12)$$

and similarly for $\phi^\dagger \partial_\mu \phi \bar{X} \gamma^\mu X / M^2$. Note that the current collider constraint on the dark matter - quark interaction is insensitive to the coupling due to the large mediator mass, M [328, 207].

(ii) $\bar{\xi}_R \xi_L \leftrightarrow 2\Pi$, where Π denotes the hidden pions. This process is generated by the non-linear sigma operator

$$m_d \bar{\xi}_R \xi_L e^{i\Pi/\Lambda} ; T_{\text{fr}} \leq \left[\frac{g_*^{\frac{1}{2}} \Lambda^4}{(m_d)^2 M_{\text{pl}}} \right] \sim \text{TeV} , \quad (7.2.13)$$

for the (3, 2) theory, and much larger for (5, 4) and (7, 6).

(iii) $\bar{\nu}_L^d \nu_L^d \leftrightarrow \bar{q}q$. This can occur also through W and Z exchange, and must freeze out before BBN. The pertinent operators are

$$\frac{g(\theta_d)^2}{2c_W} \bar{\nu}_L^d \not{Z} \nu_L^d, \quad \frac{g\theta_d}{\sqrt{2}} \bar{\nu}_L^d W \ell_L; \quad T_{\text{fr}} \leq \left[\frac{g_*^{\frac{1}{2}} m_W^4}{(\theta_d)^4 M_{\text{pl}}} \right]^{1/3} \sim \text{TeV}.$$

(iv) $\bar{\nu}_L^l \nu_R^l \leftrightarrow 2\Pi$. This must also freeze out before the BBN epoch. The non-linear sigma coupling of $\nu_{L,R}^l$ to the hidden pions is suppressed by both the left and right mixing between active and sterile sectors. From eqs. (7.2.9) and (7.2.10) this leads to an extra prefactor of $(\theta_d)^3$ for the non-linear sigma operator in eq. (7.2.13), and therefore a decoupling much larger than the TeV scale.

7.3 Warm Dark Matter

7.3.1 Non-Thermal WDM

The moral of the above analysis is that approximately below the TeV scale, the SM, CHS and EHS are decoupled. From Table. 7.2, confinement of the CHS also occurs at latest at the TeV scale. As a result, we may imagine a scenario in which the post-inflation reheating temperature $T_{\text{rh}} < \text{TeV}$. In this case, the sterile Dirac neutrinos ν^d might never be in thermal contact with the SM plasma, and therefore be produced non-thermally through the (non)-resonant production mechanism [186, 339, 7, 357].

As can be seen in Fig. 7.1, the predicted (m_d, θ_d) values fall outside the region of significant WDM non-resonant production, which itself is ruled out by the combination

of Lyman- α and x-ray flux bounds [106, 107]. However the (m_d, θ_d) ranges still overlap an allowed window for WDM resonant production if there is a sufficiently large lepton asymmetry [7, 286, 357, 284, 110].

7.3.2 Thermal WDM

The $(3, 2)$ theory exhibits the interesting feature that the decoupling temperature of the EHS, T_d , the confinement temperature of the CHS, $T_c \sim \Lambda$, and decoupling of temperature the CHS, T_χ , all occur at the TeV scale. In contrast to the non-thermal resonant scenario, for a $(3, 2)$ theory one may plausibly consider a scenario in which all three sectors are initially in thermodynamic equilibrium, the lepton asymmetry is small, and

$$T_d > T_c > T_\chi . \quad (7.3.14)$$

In this scenario, the EHS fermions ξ freeze-out ultra-relativistically before confinement, and there is no subsequent resonant production. Defining $Y \equiv n/s$ – the ratio of the comoving number density and entropy density – then for each *Dirac* ξ species

$$Y_\xi = \frac{135\zeta(3)}{2\pi^4} \frac{1}{g_{*s}^d} , \quad (7.3.15)$$

where g_{*s}^d is entropic effective equilibrium number of degrees of freedom at freeze-out.

Even if only one species of ξ – the Dirac $\xi_{R,L}$ – obtains a mass m_d , which we assume henceforth, such a Y_ξ leads to over-closure unless $g_{*s}^d \sim 10^4$. This is unnaturally large since $g_{*s} \sim 10^2$ for the SM at this scale. However, if after freeze-out the entropy increases by a factor γ , then the frozen out species are diluted, $Y_\xi \rightarrow Y_\xi/\gamma$. The present-day energy fraction for the Dirac ν^d , which are an admixture dominantly composed of $\xi_{R,L}$, is then

$$\frac{\Omega_d}{\Omega_{\text{DM}}} \simeq \frac{Y_\xi m_d s_0}{\rho_c \Omega_{\text{DM}}} = \frac{1.1 \times 10^4}{g_{*s}^d \gamma} \left(\frac{m_d}{5 \text{ keV}} \right) , \quad (7.3.16)$$

in which we used $s_0 \simeq 2.89 \times 10^3 \text{ cm}^{-3}$, $\rho_c \simeq 10.5 h^2 \text{ cm}^{-3} \text{ keV}$, and $\Omega_{\text{DM}} = 0.105 h^{-2}$. It is clear that we need $g_{*S}^d \gamma \gtrsim 10^4$ for a DM candidate.

7.3.3 Supercooled Confinement

The ordering (7.3.14) permits us to consider the confinement of the CHS as the source of entropy that dilutes Y_ξ after freeze-out. The entropy production from a confinement-induced first-order phase transition can be significant if it occurs suddenly after supercooling [171, 161]. That is, if the confinement phase transition (CPT) begins at a cooler temperature $T_i < T_c$, and the duration of the transition $\tau_c \ll 1/H(T_i)$, the Hubble time at temperature T_i .

Before confinement – at temperature T_i – and after confinement – at temperature $T_f > T_\chi$ –, we suppose that we have equilibrium plasmas. By construction

$$\begin{aligned} g_{*S}(T_i) &\equiv g_{*S}^i = g_{*S}^{\text{SM}} + g_{*S}^c \simeq 2 \times 10^2, \\ g_{*S}(T_f) &\equiv g_{*S}^f \equiv g_{*S}^{\text{SM}} + g_{*S}^{\text{bs}} \simeq 10^2. \end{aligned} \quad (7.3.17)$$

Here g_{*S}^{SM} , g_{*S}^c and g_{*S}^{bs} denote the effective equilibrium relativistic degrees of freedom in the SM, CHS and the bound states. By construction, for three n_R we have $g_{*S}^{\text{bs}} = 2 \cdot 3 \cdot (7/8) + N_\Pi$ with N_Π the number of hidden pions. We have assumed $g_{*S}^{\text{bs}} \sim 10$ and g_{*S}^{SM} , $g_{*S}^c \simeq 10^2$. Note that since the frozen out $\xi_{L,R}$ have only four degrees of freedom, then $g_{*S}^d \simeq g_{*S}^i$.

Since $T_f > T_\chi$, then such entropy production leads to reheating of *both* the CHS and SM, before their decoupling at T_χ . This mutual reheating means the present DM temperature, T_d^0 , compared to that of the active neutrinos, T_ν^0 , is just

$$\frac{T_d^0}{T_\nu^0} = \left(\frac{g_{*S}^f}{\gamma g_{*S}^d} \frac{g_{*S}^\nu}{g_{*S}^{\text{SM}}} \right)^{1/3} \simeq \left(\frac{10.75}{1.1 \times 10^4 (m_d/5 \text{ keV})} \right)^{1/3}, \quad (7.3.18)$$

from eq. (7.3.16) and since $g_{*S}^f \simeq g_{*S}^{\text{SM}}$. The Lyman- α bounds [107, 89] require $m_d > 8(T_d^0/T_\nu^0)$ keV. Together with eq. (7.3.18) this implies such thermally produced ν^d may safely avoid the Lyman- α bound, provided $m_d > 1.3$ keV. This is the Lyman- α bound displayed in Fig. 7.1.

Note also that the n_R and hidden pion contribution to the effective number of neutrino degrees of freedom, $\delta N_\nu^{\text{eff}}$, at the big-bang nucleosynthesis (BBN) epoch is then

$$\delta N_\nu^{\text{eff}} = (8/14)g_{*S}^{\text{bs}}(g_{*S}^\nu/g_{*S}^{\text{SM}})^{4/3} \lesssim 0.26(g_{*S}^{\text{bs}}/10). \quad (7.3.19)$$

It is amusing to note that the right-handed neutrinos together with the hidden pions can supply sufficient effective degrees of freedom at the BBN epoch to significantly contribute to the observed $\delta N_\nu^{\text{eff}} \sim 1$ excess (see e.g [275, 83]). In contrast, this is difficult to achieve with seesaw models, or even ad hoc Dirac neutrino models.

7.3.4 Entropy Production Estimate

The massive bound states typically have masses $x\Lambda$, with $x \gtrsim 1$, so they are non-relativistic. Their corresponding widths are generically also $\Gamma \sim \Lambda$. This leads to $\Gamma/H(T_i) \sim M_{\text{pl}}(T_c/T_i)^2/\Lambda \gg 1$. In contrast, the longest-lived heavy bound state we could contemplate decays only via exchange of an M -scale boson, like the electroweak decay of the Λ^0 baryon of QCD. In this case, the decay rate is $\Gamma \sim \Lambda x^5 \epsilon^4$. For the $(3, 2)$ theory $\epsilon \sim 10^{-4}$, so that $\Gamma/H(T_i) \gtrsim x^5(T_c/T_i)^2 \gg 1$. This means that even for a sudden CPT, the heavy bound states all decay within τ_c and generically, predominantly produce hidden pions and n_R with energies $\sim T_c$. It seems reasonable, then, to treat the CPT as a quasiequilibrium process, in which the non-relativistic heavy bound states have exponentially suppressed number and energy densities, while pions and n_R are thermal with

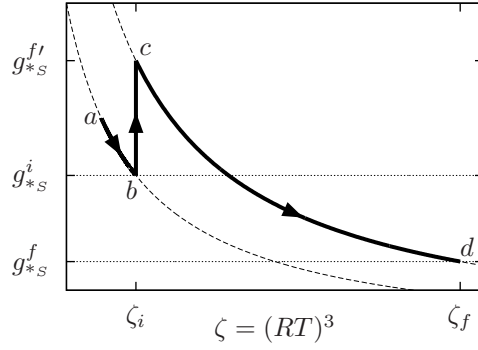


Figure 7.2: A sketch of the thermal history. Species freeze-out (a - b) along the S_i adiabat (lower dashed), is followed by the CPT (b - c), which is a first-order g_{*S} phase transition in ζ . The CPT is followed by thermalization (c - d) along the S_f adiabat (upper dashed) until $g_{*S} = g_{*S}^f$ at which $T = T_f$. Once $T = T_\chi$, the CHS and SM decouple.

temperature T_c .

With this in mind, one can estimate the amount of entropy production by treating the CPT as a first-order phase transition in g_{*S} , as a function of $\zeta \equiv (RT)^3$. Here R is the universe scale factor and T the equilibrium temperature. The picture is that confinement begins at supercooled plasma temperature T_i , and suddenly produces the relativistic pions and n_R at temperature T_c , so that g_{*S} undergoes a jump at $\zeta_i = (R_i T_i)^3$ from g_{*S}^i to

$$g_{*S}^{f'} = g_{*S}^{\text{SM}} + g_{*S}^{\text{bs}} (T_c/T_i)^3. \quad (7.3.20)$$

This expression for $g_{*S}^{f'}$ follows just from the definition $g_{*S}(T) \equiv \sum_\alpha g_{*S}^\alpha (T_\alpha/T)^3$, a sum over species at different temperatures. After the phase transition, the plasma undergoes an adiabatic thermalization until $g_{*S} = g_{*S}^f$ and $T = T_f$. SM-CHS decoupling at T_χ follows thereafter. Figure 7.2 shows this history.

Provided $(T_c/T_i)^3 \gg g_{*S}^{\text{SM}}/g_{*S}^{\text{bs}} \sim 10$, the entropy production estimate from eq. (7.3.20) is then

$$\gamma \equiv \frac{S_f}{S_i} = \frac{g_{*S}^{f'} \zeta}{g_{*S}^i \zeta} \simeq \frac{g_{*S}^{\text{bs}}}{g_{*S}^i} \left(\frac{T_c}{T_i} \right)^3. \quad (7.3.21)$$

The important feature of this naïve estimate is the $(T_c/T_i)^3$ dependence of the entropy production. A more careful treatment in Ref. [171] produces the result

$$\gamma \simeq \frac{1}{r} \left(\frac{r-1}{3} \right)^{3/4} \left(\frac{T_c}{T_i} \right)^3, \quad r \equiv \frac{g_{*S}^i}{g_{*S}^f}. \quad (7.3.22)$$

One also finds $T_f = [(r-1)/3]^{1/4} T_c$. Using this result and eq. (7.3.16), and fixing $r = 2$, it follows that for $\Omega_d \leq \Omega_{\text{DM}}$ (i.e. $\gamma g_{*S}^d \geq 1.1 \times 10^4 m^d / 5 \text{ keV}$) we require

$$\frac{T_c}{T_i} \geq 6.3 \left(\frac{2 \times 10^2}{g_{*S}^d} \right)^{1/3} \left(\frac{m_d}{5 \text{ keV}} \right)^{1/3}. \quad (7.3.23)$$

Note $T_f = 0.76 T_c$ here, so it is plausible that $T_f > T_\chi$. By comparison to eq. (7.3.23), the QCD maximal supercooling is $T_c/T_i \simeq 1.7$ [171]. However, given that this upper bound will be sensitive e.g. to the tunneling probabilities between the metastable (G_F symmetric) and stable (G'_F symmetric) vacua, the degree of supercooling required in this estimate is not implausible.

7.4 Conclusions

Within the composite neutrino framework, we have shown in this Note that keV sterile Dirac neutrinos can be naturally produced with mixing angles appropriate for non-thermal resonant production, provided the composite neutrinos are all comprised of n preons and the scalar condensate vev has $n-1$ of them. Alternatively, for a $(3, 2)$ theory, a single keV sterile Dirac neutrino species could be WDM produced by entropy-diluted ultrarelativistic freeze-out. In this latter case the entropy can be provided by a supercooled confinement-induced phase transition.

CHAPTER 8

LEP CONSTRAINTS ON DARK MATTER INTERACTIONS

Based on the 2011 article “Missing Energy Signatures of Dark Matter at the LHC”, written in collaboration with Patrick J. Fox, Roni Harnik, Joachim Kopp and published in Phys.Rev. D84 (2011) 014028.

8.1 Introduction

The search for dark matter and its interaction with standard model particles is actively pursued by experiments worldwide. Direct detection searches look for a feeble kick that a dark matter particle produces in recoiling off a nucleus. Indirect searches aim at the detection of the annihilation products of dark matter particles with each other in regions with a high density of dark matter. A signal in any experiment using either of these techniques requires the existence of a new interaction between dark matter and standard model particles. Direct and indirect searches, together with assumptions on the astrophysical dark matter density and velocity distributions, place bounds on such possible interactions.

The very same interactions may also lead to the production of dark matter at a high energy collider (with an appropriate beam of incoming particles). In this article we will explore possible couplings of dark matter to leptons and the limits on such couplings from the LEP experiments at CERN. There, the annihilation of an electron and a positron into an invisible dark matter pair may become visible if an additional hard photon is radiated during the collision, producing a distinct mono-photon signal. Since the LEP experiments did not observe an excess of mono-photon events beyond the expected background, a limit may be placed on the postulated interaction strength between dark matter and the standard model. These limits, in turn, can be reinterpreted as limits on both direct and indirect detection rates, independent of astrophysical and atomic uncertainties.

Previous work relating collider searches to direct and indirect searches for dark matter has focused on the Tevatron [67, 229] and the LHC [230]. While these hadronic machines probe the dark matter couplings to light quarks, the LEP data we are going to study is sensitive to the dark matter-electron coupling. The potential limits from ILC mono-

photons on a thermal relic that couples to leptons was studied in [92]. If dark matter were hadrophobic, as has been discussed [87, 211, 170] (but disfavored [277, 278]) as a possible explanation of the DAMA [86] and CoGeNT [3] signals, as well as various cosmic ray anomalies, the LEP mono-photon searches would provide the only sensitive, model independent, collider limits for dark matter. As we shall see, LEP searches can yield bounds on dark matter which are both competitive with, and complementary to, those placed by traditional dark matter searches.

The plan of this paper is as follows. In the next section we will introduce the effective theory formalism we will use in the first part of the paper. The list of operators we are going to consider will not be exhaustive, but will encompass the phenomenologically most relevant scenarios. We include cases where the dark matter-lepton couplings are scalar, vector and axial-vector in nature¹ which covers a broad range of phenomena, including spin independent and spin dependent scattering as well as annihilations which are either velocity suppressed or not. In section 8.3 we will set limits on the various contact operators from the mono-photon search at LEP. Then, in sections 8.4 and 8.5 we will translate our limits into bounds on dark matter nucleon scattering and dark matter self annihilation, respectively. We will compare our results to current direct and indirect searches. In section 8.6 we will consider the possibility that the effective theory described in section 8.2 is not appropriate for calculating the production rate of dark matter pairs at LEP. We will discuss several renormalizable models in which a new gauge boson or a new scalar particle is introduced to mediate the interactions of dark matter with leptons. As we shall see, the inclusion of such particles can significantly alter LEP bounds, and in certain regimes the bounds become sensitive to the details of the UV completion. We will conclude in section 8.7.

¹Throughout we consider the dark matter to be a Dirac fermion, since our bounds would not be altered significantly if dark matter is a Majorana fermion [230, 67, 229]. We also do not consider scalar or vector dark matter, though we do not expect the limits to be qualitatively different.

8.2 The Interaction of Dark matter with Leptons

In order to produce dark matter at LEP it must couple to electrons. In many models this may occur via the exchange of a heavy mediator that can be integrated out of the theory at low energies. In that case one can describe the phenomenology in an effective field theory with higher dimension operators coupling the dark matter particle χ to standard model leptons $\ell = e, \mu, \tau$. This allows us to consider a large variety of dark matter phenomena without committing to a particular high energy framework². We will be considering the operators

$$\mathcal{O}_V = \frac{(\bar{\chi}\gamma_\mu\chi)(\bar{\ell}\gamma^\mu\ell)}{\Lambda^2}, \quad (\text{vector, } s\text{-channel}) \quad (8.2.1)$$

$$\mathcal{O}_S = \frac{(\bar{\chi}\chi)(\bar{\ell}\ell)}{\Lambda^2}, \quad (\text{scalar, } s\text{-channel}) \quad (8.2.2)$$

$$\mathcal{O}_A = \frac{(\bar{\chi}\gamma_\mu\gamma_5\chi)(\bar{\ell}\gamma^\mu\gamma_5\ell)}{\Lambda^2}, \quad (\text{axial vector, } s\text{-channel}) \quad (8.2.3)$$

$$\mathcal{O}_t = \frac{(\bar{\chi}\ell)(\bar{\ell}\chi)}{\Lambda^2}, \quad (\text{scalar, } t\text{-channel}) \quad (8.2.4)$$

which capture the essential dark matter and collider phenomenology (e.g. spin dependent and spin independent scattering on nucleons as well as s - and p - wave annihilation). The classification of these operators as s -channel or t -channel refers to their possible UV-completion: (8.2.1)–(8.2.3) are most straightforwardly obtained in models in which dark matter is produced at LEP through a neutral s -channel mediator, while eq. (8.2.4) arises most naturally if the mediator is a charged scalar exchanged in the t -channel. With such a UV completion in mind, the suppression scale Λ can be interpreted as the mass of the mediator M , divided by the geometric mean of its couplings to leptons, g_ℓ , and dark matter, g_χ : $\Lambda = M/\sqrt{g_\ell g_\chi}$. Note that we assume lepton flavor to be conserved in the dark matter interaction. LEP can only constrain couplings to electrons, $\ell = e$, and in principle the

²Indeed, several recent studies have used effective theories to analyze and draw connections among dark matter experiments [245, 120, 119, 29, 197].

suppression scale Λ could be different for couplings to μ and τ leptons. In the following discussion, we will therefore consider both scenarios in which dark matter couples *only* to electrons (i.e. $\Lambda = \infty$ for $\ell = \mu, \tau$) and scenarios in which dark matter couples in a flavor-universal way to all standard model leptons. Note that the last operator, eq. (8.2.4), may be transformed into a linear combination of the first three operators, plus pseudoscalar and tensor contributions, using the Fierz identities, but we include it separately here because it is a common outcome of supersymmetric theories.

The effective theory described by equations (8.2.1)–(8.2.4) is always a valid description of processes with low momentum transfer, in particular dark matter-nucleon scattering in direct detection experiments. In high energy processes such as dark matter production at LEP or dark matter annihilation, the effective theory breaks down if the 4-momentum transfer is comparable to or larger than the mass of the particle mediating the interaction. In the first part of our analysis in sections 8.3–8.5, we assume that this is not the case, and derive bounds on the operators (8.2.1)–(8.2.4) from LEP mono-photon searches, which we will then translate into constraints on direct and indirect dark matter detection cross sections. In section 8.6 we will investigate how these bounds change if the mediator of dark matter interactions is light so that an effective theory description is no longer possible.

8.3 LEP Limits on the effective Dark Matter–electron coupling

In this section we will consider the operators (8.2.1)–(8.2.4) and derive limits on their suppression scale Λ from mono-photon searches at LEP. While all four LEP-detectors have studied single photon events [241], we will here focus on data from the DELPHI experiment [9, 10], for which we were best able to simulate the detector response. The data was

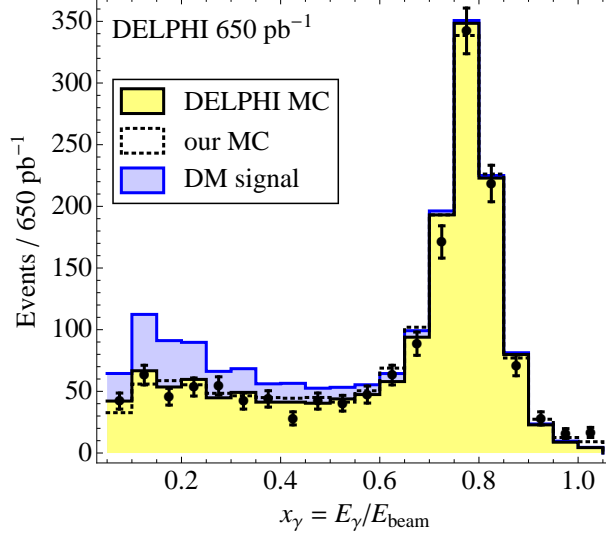


Figure 8.1: Distribution of normalized photon energy in single-photon events at DELPHI. The agreement between the data (black dots with error bars) and both the full DELPHI Monte Carlo (solid yellow/light gray shaded histogram) as well as our CompHEP simulation (dotted histogram) is excellent. The blue shaded histogram shows what a hypothetical Dark Matter signal from $e^+e^- \rightarrow \gamma\bar{\chi}\chi$ would look like. We have assumed vector-type contact interactions between electrons and dark matter, $m_\chi = 10$ GeV, and $\Lambda = 300$ GeV, see eq. (8.2.1). The peak at $x_\gamma \sim 0.8$ corresponds to the process $e^+e^- \rightarrow \gamma Z^0 \rightarrow \gamma\nu\bar{\nu}$, with an on-shell Z^0 .

taken at center of mass energies between 180 GeV and 209 GeV, but since in the analysis the events are characterized only by the relative photon energy $x_\gamma = E_\gamma/E_{\text{beam}}$, we can make the simplifying assumption that all data was taken at an energy of 100 GeV per beam. We have checked that the error introduced by this approximation is small. For our Monte Carlo simulations, we use CompHEP [102, 326], which allows us to include the effect of initial state radiation (ISR) which we find to be non-negligible. For example, we are only able to reproduce the height and width of the on-shell Z^0 peak in the x_γ distribution for the background process $e^+e^- \rightarrow \gamma\nu\bar{\nu}$ (cf. Figure 8.1) if ISR is included.

To analyze the event samples generated in CompHEP, we use a modified version of MadAnalysis [34], in which we have implemented the analysis cuts and efficiencies of the

DELPHI analysis as well as energy smearing according to the resolution of the DELPHI electromagnetic calorimeters. In doing so, we closely follow ref. [9].

In DELPHI, central photons with a polar angle θ (with respect to the beam axis) in the range $45^\circ < \theta < 135^\circ$ are detected in the High Density Projection Chamber (HPC) with a threshold of $x_\gamma > 0.06$. We assume the trigger efficiency for photons in the HPC to increase linearly from 52% at $E_\gamma = 6$ GeV to 77% at 30 GeV, and then to 84% at 100 GeV. The trigger efficiency is multiplied by the efficiency of the subsequent analysis, which we assume to increase linearly from 41% at 6 GeV to 78% at 80 GeV and above.

For photons with $12^\circ < \theta < 32^\circ$, detected in the Forward Electromagnetic Calorimeter (FEMC), the threshold is $x_\gamma > 0.1$. The trigger efficiency increases linearly from 93% at 10 GeV to 100% at 15 GeV and above, and the analysis efficiency is the product of a linear function, increasing from 57% at 10 GeV to 75% at 100 GeV, and a constant 89%, with the first factor coming from the analysis cuts, and the second one describing the loss of events due to noise and machine backgrounds. In addition, we impose an energy dependent angular cut $\theta > (28 - 80x_\gamma)^\circ$.

Very forward photons ($3.8^\circ < \theta < 8^\circ$) give a signal in the Small Angle Tile Calorimeter (STIC), whose threshold is $x_\gamma > 0.3$, and we assume the efficiency to be 48%, based on the (incomplete) information given in [9]. We again impose an energy dependent angular cut $\theta > (9.2 - 9x_\gamma)^\circ$.

The above, calorimeter specific, efficiencies are augmented by an additional 90% efficiency factor, applied to all photons. We found it necessary to introduce this overall efficiency factor to gain agreement in normalization between our simulations and the results of DELPHI.

The relative energy resolution, σ_E/E , is $0.043 \oplus 0.32/\sqrt{E}$ in the HPC, $0.03 \oplus 0.12/\sqrt{E} \oplus 0.11/E$ in the FEMC, and $0.0152 \oplus 0.135/\sqrt{E}$ in the STIC, where E is in units of GeV. Here \oplus means that the different contributions to the energy resolution function are statistically independent. For example, we simulate the effect of finite energy resolution in the HPC by shifting the energy of each HPC photon by an amount $0.043 E \cdot r_1 + 0.32 \sqrt{E} \cdot r_2$, where r_1 and r_2 are independent Gaussian random numbers. Since we find that with purely Gaussian energy smearing we are unable to reproduce the broad tails of the on-shell Z^0 peak in the x_γ distribution (Figure 8.1), we impose an additional Lorentzian energy smearing with a width of $0.052 E$. This is motivated by a fit to the calorimeter response to monoenergetic electrons, obtained from ref. [200].

We have verified our modeling of the DELPHI detector by simulating the energy distribution of single photons in the Standard Model. As demonstrated in Figure 8.1, the agreement with the data (black dots with error bars) and with the DELPHI Monte Carlo simulation (solid yellow/light gray histogram) is excellent. Only in the very last bin ($x_\gamma > 1$), the observed number of events is $\sim 4\sigma$ higher than the prediction by *both* Monte Carlo simulations, probably due to imperfect modeling of the detector resolution function. We therefore omit this bin in the following analysis. A straightforward χ^2 analysis then yields $\chi^2/\text{dof} = 21.5/19$ for our simulation, and $\chi^2/\text{dof} = 20.6/19$ for the DELPHI Monte Carlo.

When setting limits on dark matter properties, we use our own simulation only for the signal contribution, while the predicted backgrounds are taken from the DELPHI Monte Carlo. The blue shaded histogram in Figure 8.1 shows what a typical dark matter signal would look like for the case of operator \mathcal{O}_V , with a dark matter mass of 10 GeV and with $\Lambda = 300$ GeV. Since most of the signal events are in the low- x_γ region, where SM backgrounds are only moderate, and since the spectral shape of the signal is different from

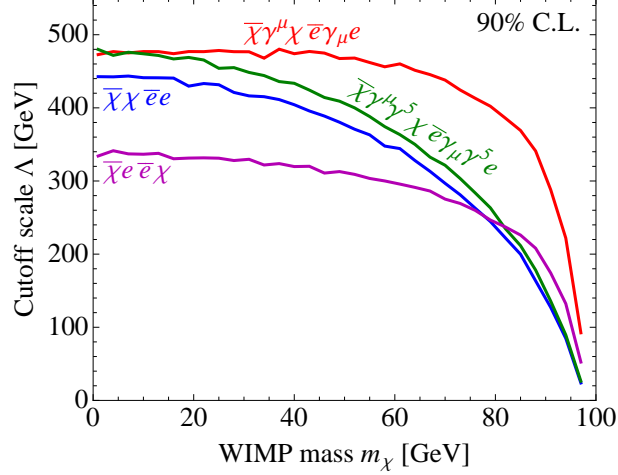


Figure 8.2: DELPHI lower limits on the cutoff scale Λ of the dark matter effective theory for the four operators eqs. (8.2.1)–(8.2.4) as a function of the dark matter mass. The wiggles in the plot are due to limited Monte Carlo statistics.

that of the background, we expect good sensitivity to the dark matter-electron coupling Λ^{-1} .

Indeed, a χ^2 analysis yields limits on the cutoff scale Λ of order 250–500 GeV for dark matter masses $m_\chi \lesssim 80$ GeV (see Figure 8.2). In this mass range, our limits on dark matter-electron coupling are slightly better than the limits on dark matter-quark couplings derived from Tevatron mono-jet events [229, 67]. The Tevatron limits, however, do not yet include spectral information, and they extend to dark matter masses of several hundred GeV, while LEP is completely insensitive to $m_\chi \gtrsim 90$ GeV for kinematic reasons. The normalized photon energy distribution is similar in shape for all the operators considered. This leads to similar limits on the operators from eqs. (8.2.1)–(8.2.3) at low dark matter mass. Only the limit on the strength of the operator $(\bar{\chi}\ell)(\bar{\ell}\chi)$, eq. (8.2.4), is somewhat weaker. Using the Fierz identities this operator may be converted to a sum of other operators involving a product of a dark matter bilinear and a lepton bilinear. There is destructive interference between these operators leading to a smaller production cross

section for mono-photon events and thus a weaker bound on the cutoff scale for this operator. When the dark matter mass m_χ exceeds ~ 30 GeV, the limits on different operators scale differently with m_χ since at this point the dark matter particles are produced closer to threshold and the detailed dependence of the cross section on the final state velocities becomes important.

8.4 Limits on the Dark Matter–nucleon scattering cross section

The next step is to translate the limits on Λ into constraints on the dark matter–nucleon scattering cross sections probed in direct detection experiments. Since LEP can only probe dark matter–electron couplings, while direct detection experiments are most sensitive to dark matter–quark couplings, this translation cannot be done in a completely model-independent way. We thus consider two extreme possibilities, one in which the dark matter couples with equal strength to quarks as it does to leptons, and another in which dark matter couples only to leptons without coupling to quarks at tree level. Limits on other models, in which the ratio of lepton and quark couplings is different (e.g. coupling proportional to $B - L$), may be easily derived from these two cases, as we shall see below.

In order to compute the dark matter scattering cross section off a nucleon, $N = p, n$, through one of the operators in (8.2.1)–(8.2.4), we need knowledge of the nucleon matrix elements $\langle N | \mathcal{O} | N \rangle$. We use the values of these matrix elements presented in [67], with the exception of $\langle N | \bar{q}q | N \rangle$ in which we follow [193] but use an updated [359] value of the pion–nucleon sigma term $\Sigma_{\pi N} = 55$ MeV.³ As mentioned earlier \mathcal{O}_t can be converted from a “ t -channel” operator to a sum of “ s -channel” operators by use of Fierz identities.

³Note however that recent lattice determinations [358, 349, 223, 41] of the strange quark content of the nucleus are considerably lower. The effect on our bounds, assuming equal coupling to all fermions, is small.

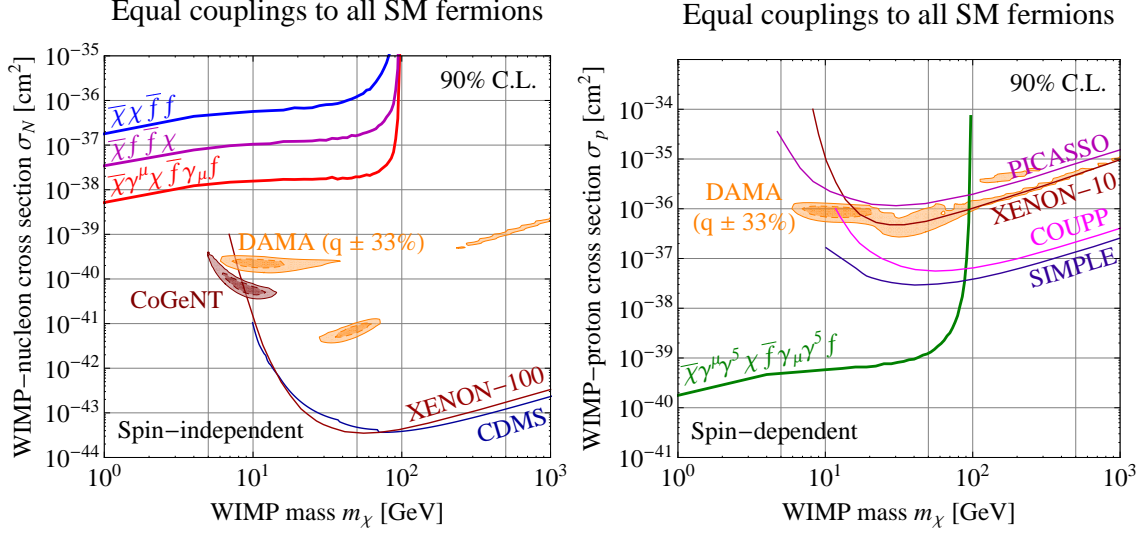


Figure 8.3: DELPHI upper limits (thick lines) on the cross section for dark matter-nucleon scattering compared to results from direct detection experiments (thin lines and shaded regions). The left-hand plot is for spin-independent scattering, as would come from operators \mathcal{O}_S , \mathcal{O}_V , \mathcal{O}_t , and the right is for spin-dependent scattering through operator \mathcal{O}_A . The spin-independent limits of CDMS and XENON-100 are taken from Refs. [30] and [43], respectively. The spin-dependent limits of DAMA, XENON-10, PICASSO, COUPP and SIMPLE are taken from Refs. [86], [38], [71], [76] and [224], respectively. The DAMA and CoGeNT-allowed regions are based on our own fit [279] to the data from Refs. [86] and [3]. Following [247], we have conservatively assumed large systematic uncertainties on the DAMA quenching factors: $q_{\text{Na}} = 0.3 \pm 0.1$ for sodium and $q_{\text{I}} = 0.09 \pm 0.03$ for iodine. All limits are computed at the 90% confidence level, while the DAMA and CoGeNT allowed regions are shown at the 90% and 3σ confidence levels.

Due to the relative size of the nucleon matrix elements it is sufficient to keep only the scalar s -channel contribution, which has a coefficient $1/4$. Thus, for equal cutoff scale Λ , the direct detection rate expected from the operator \mathcal{O}_t is the same as that expected from $\mathcal{O}_S/4$.

First we assume that the coupling of dark matter to all SM fermions, and in particular to all flavors of quarks, is identical to its couplings to electrons. In this case, the LEP bound on Λ can be immediately converted into an upper bound on the rate expected at direct detection experiments. We show these bounds in Figure 8.3 and we see that the limits on

spin-independent WIMP-nucleon scattering (left-hand plot) are competitive with direct detection results only for very light dark matter, $m_\chi \lesssim 4$ GeV. The direct detection experiments become insensitive to such light masses due to their energy threshold, whereas there is no such low mass threshold at LEP. The high mass cutoff at LEP is reflected in the rapid deterioration of the upper bound at $m_\chi \sim 90$ GeV. The LEP bound also applies directly to inelastic dark matter [350], since the splitting between the two dark matter states of ~ 100 keV is inconsequential to the kinematics at LEP. However, such models typically require considerably larger dark matter-nucleon cross sections than elastic dark matter, since the splitting allows only the high velocity fraction of the dark matter to scatter. Our bounds derived from LEP rule out the very highest scattering cross sections in the parameter space consistent with DAMA [279], but still leave the bulk of the parameter space allowed.

For spin-dependent scattering we expect the LEP bounds to be more competitive since there is little variation in the bound on Λ between the operators responsible for spin-independent scattering (\mathcal{O}_V and \mathcal{O}_S) and spin-dependent scattering (\mathcal{O}_A), whereas constraints from direct detection experiments are much weaker than in the spin-independent case. The reason for this is that, unlike spin-independent dark matter-nucleus scattering, spin-dependent scattering is not enhanced by a factor A^2 , where A is the nuclear mass number. These considerations are reflected in the right-hand plot of Figure 8.3 where the LEP limits surpass direct detection constraints for $m_\chi \lesssim 80$ GeV at which point the phase space for dark matter production at LEP again starts to shrink.

If dark matter does not couple to quarks at tree level, but only to leptons (for simplicity we assume the coupling to μ and τ is the same as that to e , our conclusions are not significantly altered even if the coupling were only to electrons), the power of the LEP limits improves dramatically. The reason is that in this case, dark matter-quark scattering to

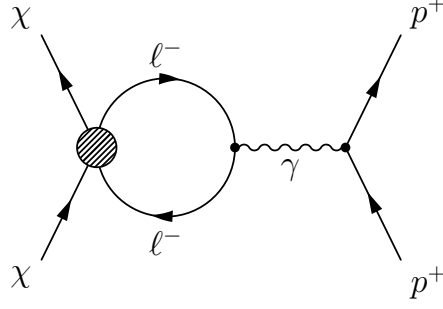


Figure 8.4: Diagram for vector-type dark matter-proton scattering at the one-loop level.

which direct detection experiments are sensitive is only induced at the loop-level [277].⁴ The cross section for loop-induced dark matter-proton scattering through the diagram shown in Figure 8.4 is

$$\sigma_{1\text{-loop}} \simeq \frac{4\alpha^2 \mu_p^2}{18^2 \pi^3 \Lambda^4} \cdot \left[\sum_{\ell=e,\mu,\tau} f(q^2, m_\ell) \right]^2, \quad (8.4.5)$$

where α is the electromagnetic fine structure constant, $\mu_p = m_p m_\chi / (m_p + m_\chi)$ is the dark matter-proton reduced mass, and the loop factor $f(q^2, m_\ell)$ is given by

$$f(q^2, m_\ell) = \frac{1}{q^2} \left[5q^2 + 12m_\ell^2 + 6(q^2 + 2m_\ell^2) \sqrt{1 - \frac{4m_\ell^2}{q^2}} \operatorname{arccoth} \left(\sqrt{1 - \frac{4m_\ell^2}{q^2}} \right) - 3q^2 \log [m_\ell^2 / \Lambda_{\text{ren}}^2] \right]. \quad (8.4.6)$$

We take the renormalization scale Λ_{ren} to be equal to Λ . Moreover, we make the approximation that all the dark matter is moving at the local escape velocity, which we take to be $v_\chi = 500$ km/sec, and that the momentum exchanged in the scattering is maximal, i.e. the scattering angle is 180° in the center-of-momentum frame. This will overestimate the rate of observed recoils at a direct detection experiment and will lead to a conservative upper bound. With these assumptions the four-momentum exchanged between the

⁴Dark matter-electron scattering is irrelevant in all direct detection experiments including DAMA [277] and CoGeNT [278]. Even though DAMA and CoGeNT would not reject bulk electron recoils as background, kinematics dictates that the recoil energy can only be above the detection threshold if the electron enters the interaction with an initial state momentum $\gtrsim 10$ MeV. The probability for this is very small due to the fast drop-off of the electron wave functions at high momentum [87, 277, 278].

dark matter and the target nucleus is $q^2 = -4\mu^2 v_\chi^2$, where μ is the invariant mass of the dark matter particle and the target nucleus.

The bounds on dark matter-nucleon cross sections quoted by direct detection experiments are derived from the actually measured dark matter-nucleus cross sections under the assumption that the dark matter couples equally to protons and neutrons and that the cross section is independent of q^2 . Here, however, it only couples to protons and there is a q^2 dependence in the loop factor $f(q^2, m_\ell)$. Thus, to enable a straight comparison, we rescale the quoted bounds on σ_p by $A^2/Z^2 \times (\sum_\ell f(q_p^2, m_\ell)/\sum_\ell f(q^2/m_\ell))^2$, with $q_p^2 = -4\mu_p^2 v_\chi^2$; and we take $\Lambda_{\text{ren}} = 500 \text{ GeV}$, the result is only very weakly sensitive to this choice. Note that (8.4.5) and (8.4.6) are only approximations in the effective theory formalism. The exact form of the loop factor depends on the embedding of the effective theory into a complete renormalizable model.

In Figure 8.5 we show the LEP bounds on dark matter in the absence of tree-level couplings to quarks. Since loop-induced dark matter-nucleon scattering is forbidden for axial-vector interactions and suppressed by two loops for s -channel scalar interactions [277], we consider only the vector-type operator \mathcal{O}_V and the scalar t -channel operator \mathcal{O}_t . As before, we apply the Fierz identity to \mathcal{O}_t to decompose the operator into a linear combination of s -channel operators, of which we keep only the vector contribution. As is apparent from Figure 8.5, an explanation of the DAMA and/or CoGeNT signal by a dominantly leptophilic dark matter candidate which couples to nuclei only through loops is ruled out by LEP.

Here we only considered two benchmark cases, where dark matter couples universally to SM fermions and when it couples only to leptons. Constraining a more general theory with a particular ratio of quark to lepton couplings, $R_{q/l}$, is straightforward. In

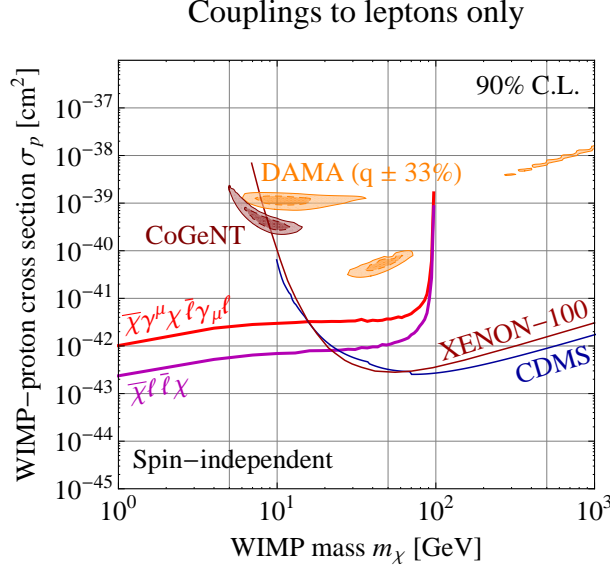


Figure 8.5: DELPHI upper limits on the cross section for spin-independent dark matter–nucleon scattering for the case of dark matter with tree level couplings only to electrons, but loop level couplings also to quarks, compared to results from the direct detection experiments DAMA [86], CoGeNT [3], CDMS [30], and XENON-100 [43]. The DAMA and CoGeNT allowed regions are based on our own fit [279] to the data from refs. [86, 3]. We conservatively assume $q_{\text{Na}} = 0.3 \pm 0.1$ and $q_l = 0.09 \pm 0.03$ for the DAMA quenching factors. All limits are computed at the 90% confidence level, while the DAMA and CoGeNT allowed regions are shown at the 90% and 3σ confidence levels.

this more general case nuclear recoil proceeds via both mechanisms, direct couplings to quarks and via a lepton loop. The limit on the former may be obtained by rescaling the bounds of Figure 8.3 by $R_{q/l}^2$, whereas the limit on the latter may be taken directly from Figure 8.5. Generically one of these limits will dominate the other over the full dark matter mass range, and the less constraining bound should be taken.

8.5 Limits on the Dark Matter annihilation cross section

The LEP constraints on the suppression scale Λ of the effective dark matter couplings can also be converted to an upper bound on the annihilation cross section of dark matter into

an electron-positron pair. They can then be compared to results from astrophysical probes of dark matter annihilation. Moreover, if dark matter is a thermal relic and if annihilation into electrons and positrons is the dominant annihilation channel, a lower bound on the dark matter abundance in the universe can be derived. If dark matter has also other annihilation modes, this bound is weakened by a factor $1/\text{BR}(\bar{\chi}\chi \rightarrow e^+e^-)$.

In order to translate the LEP constraints on the coupling strength Λ^{-1} into limits on dark matter annihilation, we need to calculate the annihilation cross sections corresponding to the operators in equations (8.2.1)–(8.2.4). For annihilation into a single lepton flavor of mass m_ℓ , they read

$$\sigma_S v_{\text{rel}} = \frac{1}{8\pi\Lambda^4} \sqrt{1 - \frac{m_\ell^2}{m_\chi^2}} (m_\chi^2 - m_\ell^2) v_{\text{rel}}^2, \quad (8.5.7)$$

$$\sigma_V v_{\text{rel}} = \frac{1}{48\pi\Lambda^4} \sqrt{1 - \frac{m_\ell^2}{m_\chi^2}} \left(24(2m_\chi^2 + m_\ell^2) + \frac{8m_\chi^4 - 4m_\chi^2 m_\ell^2 + 5m_\ell^4}{m_\chi^2 - m_\ell^2} v_{\text{rel}}^2 \right), \quad (8.5.8)$$

$$\sigma_A v_{\text{rel}} = \frac{1}{48\pi\Lambda^4} \sqrt{1 - \frac{m_\ell^2}{m_\chi^2}} \left(24m_\ell^2 + \frac{8m_\chi^4 - 22m_\chi^2 m_\ell^2 + 17m_\ell^4}{m_\chi^2 - m_\ell^2} v_{\text{rel}}^2 \right), \quad (8.5.9)$$

$$\sigma_t v_{\text{rel}} = \frac{1}{192\pi\Lambda^4} \sqrt{1 - \frac{m_\ell^2}{m_\chi^2}} \left(24(m_\chi + m_\ell)^2 + \frac{(m_\chi + m_\ell)^2 (8m_\chi^2 - 16m_\chi m_\ell + 11m_\ell^2)}{m_\chi^2 - m_\ell^2} v_{\text{rel}}^2 \right). \quad (8.5.10)$$

Here, we have made an expansion up to second order in the relative velocity v_{rel} of the annihilating particles. While $v_{\text{rel}} \ll 1$ in all relevant astrophysical and cosmological environments, its exact value ranges from $v_{\text{rel}} \sim 0.1$ at the time of dark matter decoupling in the early universe (if dark matter is a thermal relic) to values of order $v_{\text{rel}} \lesssim 10^{-4}$ (less than 100 km/s) in dwarf galaxies (see Appendix D). This large spread of relative velocities can have a large effect on annihilation rates for certain operators. Notably, annihilation through an s -channel scalar operator, (8.5.7) is suppressed by v_{rel}^2 , and annihilation through an s -channel axial vector operator, (8.5.9) is suppressed by v_{rel}^2 or by m_ℓ^2/m_χ^2 compared to the other modes. The production cross section at LEP is not suppressed in either

of these cases, giving our bounds on the suppressed modes a substantial relative advantage compared to indirect searches. However, we will see that even in cases where the annihilation rate is unsuppressed the LEP bounds are interesting and competitive for light dark matter.

In Figure 9.6, we consider both annihilation in the early universe and annihilation in the Draco dwarf galaxy⁵ and compare to the cross section required for a thermal relic ($eV\sigma v \approx 3 \times 10^{-26} \text{ cm}^3/\text{s}$) and to several astrophysical bounds. Our most model-independent bounds, those on annihilation into e^+e^- , are shown in the top left panel of Figure 9.6, where we take $eVv_{\text{rel}}^2 = 0.24$, corresponding to thermal freeze-out. We see that, if the dark matter only annihilates to electron-positron pairs, the thermal relic cross section is ruled out by LEP at 90% C.L. if $m_\chi \lesssim 20 \text{ GeV}$ for vector interactions, and if $m_\chi \lesssim 50 \text{ GeV}$ for scalar and axial vector interactions. Thus, in order for such dark matter to be a thermal relic it must have additional annihilation modes.

Even though model-independently LEP can only constrain the dark matter coupling to electrons and hence the annihilation cross section for the process $\bar{\chi}\chi \rightarrow e^+e^-$, in many models of dark matter the annihilation rate into electrons is either equal or not very far from that into μ and τ . For example, in models of supersymmetry the annihilation rate into charged leptons is set by the slepton masses, which in many cases differ by less than an order of magnitude. In other models, such as universal extra dimensions the annihilation rates to electrons, muons and taus are identical.⁶ In order to present our results we pick the simple benchmark in which the operator strengths are universal among charged leptons. Constraints on other models may be derived from this benchmark by the appropriate rescaling. Limits on this benchmark scenario are presented in the upper right,

⁵We chose the Draco dwarf galaxy because it is the dwarf galaxy for which Fermi-LAT obtains the strongest bounds on dark matter annihilation [11].

⁶In models of universal extra dimensions, dark matter is usually a vector particle, a case we are not considering in this work.

lower left, and lower right panels of Figure 9.6. Due to the strong dependence of σv on the charged lepton mass for axial vector interactions, the limit on the combined cross section for annihilation into all charged lepton species becomes significantly stronger below the τ threshold in this case. In the lower left panel of Figure 9.6, we compare the LEP limits to constraints from Fermi-LAT observations of the Draco dwarf galaxy in gamma rays [11].⁷ For $m_\chi \lesssim 80$ GeV, LEP is superior to Fermi for all annihilation operators considered here, especially for scalar interactions, for which σv is proportional to v^2 , which is extremely small in a dwarf galaxy (see Appendix D).

In the lower right panel of Figure 9.6, we have compiled several constraints on dark matter annihilation in our galaxy. Since the dark matter velocity distribution, especially at the galactic center is very uncertain, we include only the predictions for annihilation through the operators \mathcal{O}_V and \mathcal{O}_t which is v_{rel}^2 -independent and not suppressed by the small lepton masses. Limits on annihilation through the axial vector operator \mathcal{O}_A or the scalar operator \mathcal{O}_S will be between the corresponding constraints at freeze-out and those from the Draco dwarf galaxy and thus much stronger than the limits on vector interactions. Comparing the LEP constraint to limits from astrophysical observations, we find that the LEP limit is superior to Fermi results on gamma rays from dwarf galaxies [11] and on the high energy e^+e^- spectrum [233]. We also find that the excess in gamma rays at the galactic center which has recently been argued [249] to plausibly arise from dark matter annihilations into τ leptons is also strongly constrained, *if* the annihilation proceeds into electron-positron pairs at a similar rate. In fact, in [249] it was argued that an equal annihilation rate into electrons is favored because it may potentially provide an

⁷The Fermi-LAT collaboration presented their results as limits on the annihilation mode $\bar{\chi}\chi \rightarrow \mu^+\mu^-$, assuming that this is the only annihilation channel. We have reinterpreted these limits, assuming that the branching ratio for the $\mu^+\mu^-$ mode is 1/3 and that the γ -ray production is equal for all lepton flavors. In reality this will not be true, in particular there will be additional hard photon production for the τ final state. A reanalysis of Fermi-LAT data including gamma rays from annihilation channels other than $\mu^+\mu^-$ could improve the limits by an $\mathcal{O}(1)$ factor.

explanation of the WMAP Haze [202].

Constraints on dark matter properties from both indirect and direct observations are sensitive to the abundance, and velocity distribution, of dark matter both locally, at the center of the galaxy and in sub-halos. There are considerable uncertainties in all these quantities [209] that effect the exclusion curves, and preferred regions in Figure 9.6. We emphasize that the LEP constraints do not suffer from these astrophysical uncertainties.

8.6 Constraints on theories with light mediators

So far we have worked in a regime where the dark matter is the only particle of the dark sector accessible at colliders [79] and as a result all couplings of dark matter to the standard model are through higher dimension contact operators. However, since LEP is a high energy machine, there is a possibility that the particle that is mediating the interaction of dark matter with electrons is light enough to cause significant deviations from the mono-photon rates and spectra predicted by the effective theory. These deviations will be most pronounced when the mediator is produced on-shell and then decays to a dark matter pair, but as we shall see, order one deviations are possible even without on-shell production. We therefore also consider LEP bounds for several renormalizable “UV completions” of our effective theory.

Possible renormalizable theories that couple dark matter with the standard model fall into two general categories, which we will dub “ s -channel” and “ t -channel” mediators. In the first case the mediator is a neutral boson which has coupling vertices to e^+e^- and to dark matter pairs. In this case the mediator may be almost arbitrarily light if its couplings with matter are sufficiently feeble. Of the operators we consider here, s -channel

mediators give rise to operators of the form of (8.2.1)–(8.2.3) at low energies. In the second case dark matter is produced at colliders via a t -channel diagram, exchanging a charged mediator. The canonical example is supersymmetry where neutralino dark matter may be produced at LEP by exchanging a scalar selectron. At low energies this gives rise to the operator (8.2.4). Since the mediator is charged in this case, its mass should exceed about 110 GeV to evade direct LEP bounds.

In cases where the momentum flowing through the mediator in collider environments is of order the mediator mass M , the momentum-dependence of the propagator has to be taken into account. In particular, the amplitude will be proportional to

$$\mathcal{A} \propto g_e g_\chi \frac{1}{q^2 - M^2 + iM\Gamma} , \quad (8.6.11)$$

where q is the 4-momentum carried by the mediator, g_e (g_χ) is the coupling of the mediator to electrons (dark matter) and Γ is the total width of the mediator. In the case of an s -channel mediator $q^2 = s - 2\sqrt{s}E_\gamma$ is *positive*, while in the t -channel case q^2 is *negative* and depends on the relative momentum between the two dark matter particles. In the previous sections, where the massive mediator could effectively be integrated out, the higher dimension operators were suppressed by a scale Λ . For the light mediator the LEP constraints become bounds on the geometric mean of the couplings g_e and g_χ , but for ease of comparison we can still formally define

$$\Lambda \equiv \frac{M}{\sqrt{g_e g_\chi}} , \quad (8.6.12)$$

and quote the bounds in terms of that quantity.

If the mediator and the dark matter are light enough to be produced on-shell at LEP, the bounds become sensitive to the width of the mediator Γ . Γ in turn depends on g_e , g_χ (and possibly on the couplings to other particles). Here, we will treat Γ as a free parameter,

but we note that, for any given value of $\sqrt{g_e g_\chi}$ (the quantity constrained by LEP), we can derive a lower limit Γ_{\min} on Γ by noting that

$$\Gamma = \frac{g_\chi^2}{24\pi} M \sqrt{1 - \frac{4m^2}{M^2}} \left(1 + 2\frac{m^2}{M^2}\right) + \frac{g_e^2}{24\pi} M + \dots \quad (8.6.13)$$

The first term comes from decay into dark matter, the second one from decay into electrons, and ‘...’ stands for possible additional decay modes. For fixed $\sqrt{g_e g_\chi}$ the width is minimized if $g_e \approx g_\chi$, and if e^+e^- and $\bar{\chi}\chi$ are the only allowed decay modes. If the latter assumption is true we can also place an upper bound on Γ by setting $g_e = 4\pi$ and $g_\chi = M^2/(g_e \Lambda_{\text{lim}}^2)$ in (8.6.13), where Λ_{lim} is minimum value of Λ allowed by LEP. In what follows we will take the mediator’s width to be a free parameter and will consider the effects of $\Gamma_{\min} \leq \Gamma \leq 1 \text{ GeV}$. For dark matter coupling through a t -channel mediator, no resonant enhancement is possible, so the value of Γ is irrelevant in this case.

The limits on $\Lambda = M/\sqrt{g_e g_\chi}$ for various interactions are presented in Figure 8.7. From (8.6.11), we can understand the behavior of the dashed and dotted lines in this figure. Consider first the s -channel case for $m_\chi > M/2$: There is no possibility of resonant production, so the mediator width is unimportant. Comparing the cross sections for dark matter production at LEP in the contact operator and light mediator cases, we obtain

$$\left. \frac{d\sigma}{dE_\gamma} \right|_{\text{light mediator}} = \frac{M^4}{(q^2 - M^2)^2} \left. \frac{d\sigma}{dE_\gamma} \right|_{\text{contact op.}} \quad (8.6.14)$$

with $q^2 = s - 2\sqrt{s}E_\gamma$. Thus, for M slightly below \sqrt{s} , there is partial cancellation between the q^2 and M^2 terms in the denominator, leading to an enhanced cross section and an improvement in the limit on Λ compared to the contact operator case. For even smaller M , this cancellation is smaller and we expect the bound on Λ to scale with M . This is confirmed by Figure 8.7.

On the other hand, if $2m_\chi < M < \sqrt{s}$, the process $e^+e^- \rightarrow \gamma\bar{\chi}\chi$ can proceed through an on-shell mediator, which leads to a peak in the monophoton spectrum reflecting the

kinematics of a $2 \rightarrow 2$ scattering process. The absence of a strong peak in the DELPHI data, apart from standard model Z production, places a strong constraint on this scenario. The constraint depends sensitively on the width of the mediator and scales as

$$\Lambda \propto 1/\Gamma^{1/4}. \quad (8.6.15)$$

This can be understood if we note that the resonant cross section for production of the mediator together with a single photon contains a factor

$$\frac{1}{\Lambda^4} \frac{1}{(E_\gamma - E_{\text{res}})^2 + \Gamma^2/4}, \quad (8.6.16)$$

where E_{res} is the energy of the peak in the monophoton spectrum. Integrating (8.6.16) over the photon energy E_γ , we find that the total cross section for on-shell production of the mediator is proportional to $1/\Lambda^4\Gamma$ (times factors that do not depend on Λ or Γ), which explains equation (8.6.15). We have also confirmed the scaling of the bound on Λ with $\Gamma^{-1/4}$ numerically.

Going back to Figure 8.7 and comparing the limits on Λ obtained for different types of operators—scalar, vector, and axial vector—we find that they are all comparable. The t -channel case is similar to the case of the s -channel away from resonance, except that the negative q^2 causes the denominator in equation (8.6.14) to be always larger than the numerator, meaning that the bound on Λ is always weaker in the light mediator case than for the contact operator. Furthermore, in the t -channel case there is obviously no on shell production of a mediator at low dark matter mass.

Even though the effective theory is not appropriate to describe production at LEP, it is still a good description of dark matter-nucleus scattering in direct detection experiments, where the exchanged momentum is very low. The procedure of translating our bound into direct detection limits is identical to that of Section 8.4. We present these bounds in

Figure 8.8, making the assumption that dark matter has equal couplings to all standard model quarks and leptons.

For non-resonant dark matter production (s -channel with $2m_\chi > M$ or t -channel), the presence of the light mediator in general severely weakens the LEP bounds on the direct detection cross section. As discussed below equation (8.6.14), however, there is a window of mediator masses where the bounds are marginally improved compared to the contact operator case. If the mediator can be produced on-shell and is sufficiently narrow, the bounds on direct detection rates are strengthened considerably. In this case, the LEP constraints cover the (low mass) DAMA and CoGeNT-favored regions; for the vector operator a narrow resonance even impacts the DAMA region around $m_\chi \sim 50$ GeV. However, we should emphasize again that these conclusions can be evaded if the coupling of dark matter to electrons is much smaller than its coupling to quarks.

Finally, we carry out a similar analysis to Section 8.5 and compute the annihilation rate in the early universe in the case of a light mediator. We consider only the case where the mediator couples exclusively to electrons and dark matter. Figure 8.9 shows that the LEP constraints on dark matter annihilation in the early universe change significantly if the mediator is light. The sharp peaks that occur at $m_\chi(1 + \langle v^2 \rangle/2) \approx M/2$ are due to resonant annihilation of dark matter, and the dips observed just above the peaks are due to the fact that resonant annihilation and the on-set of resonant production at LEP occur at slightly different values of m_χ . As in Figures 8.7 and 8.8, the width of the mediator is of crucial importance for $m_\chi < M/2$.

8.7 Conclusions

Very little is known about the dark sector of particle physics. It is usually assumed that dark matter couples, to varying degrees, to all fermions in the standard model, and strong constraints have been placed on its coupling to quarks by direct and indirect detection experiments and by the Tevatron. However, it is possible that dark matter has no coupling to quarks or at least that couplings to leptons are dominant. In such a scenario, dark matter may be efficiently produced in collisions of electrons and positrons at LEP. Irrespective of whether dark matter is leptophilic or not, LEP is an additional probe of its properties, and in this paper we have studied what LEP can say about the dark sector. Unlike dedicated dark matter searches in direct and indirect detection experiments, our LEP bounds do not suffer from astrophysical or atomic uncertainties.

One mode in which dark matter may be searched for at LEP, with relatively little model dependence, is its pair production in association with a hard photon. The LEP experiments have searched for anomalous mono-photon events in their data sets, but have found no discrepancy from the prediction of the standard model. Unlike at hadronic machines, at LEP the kinematics of the event can be completely determined allowing the standard model backgrounds to be more easily distinguished from dark matter production. We used the mono-photon spectrum from the DELPHI experiment to place bounds upon the properties of dark matter that couples to electrons, see Figure 8.2. In the first part of the paper, we worked in an effective theory framework, in which dark matter interactions are described by four-fermion contact operators, and we derived constraints on the suppression scale, Λ , of these operators.

We applied the LEP bounds on electron-dark matter coupling to constrain both the direct detection cross section and the annihilation rate of dark matter. We considered

both the case where dark matter couples equally to all leptons and a scenario in which dark matter couples equally to all standard model fermions. Not surprisingly, for the “leptophilic” scenario, where LEP is probing tree-level interactions but direct detection proceeds through a loop process, LEP bounds are highly competitive. In fact, the bounds presented here rule out the DAMA favored region, excluding leptophilic dark matter as an explanation of the DAMA modulated events or the CoGeNT excess, see Figure 8.5.

In the case of equal couplings to quarks and charged leptons, the LEP bounds are complementary to direct detection bounds on spin-independent dark matter, see Figure 8.3. They are weaker than existing direct detection bounds for dark matter mass m_χ larger than ~ 4 GeV, but for light dark matter, $m_\chi \lesssim 4$ GeV, they are significantly stronger. For spin-dependent interactions, where direct detection constraints are relatively weak, LEP outperforms all other experiments up to its kinematic limit, $m_\chi \lesssim 80$ GeV. LEP bounds are slightly stronger than those derived in [67] from Tevatron mono-jet searches, but do not extend to as high masses, and they depend on the assumption that dark matter has universal couplings to quarks and leptons.

We have also used LEP bounds to constrain dark matter annihilation rates, both in the early universe and in present-day galaxies. Below the LEP kinematic limit the LEP constraints are highly competitive. In particular, for $m_\chi \lesssim 80$ GeV, they are stronger than those coming from Fermi-LAT observations of dwarf galaxies and of the galactic center, see Figure 9.6. They also provide a non-trivial constraint on a model invoked recently to explain a possible γ -ray excess at the galactic center [248].

In the second part of the paper, we have repeated our analysis for the case where the interaction between dark matter and electrons cannot be treated as a contact operator. We have “UV completed” the theory by introducing a particle that mediates dark

matter-standard model interactions and have investigated LEP constraints as a function of the mediator mass and width. We find that, as long as dark matter cannot be produced through an on-shell mediator at LEP, our constraints are generally weaker than in the contact operator case (except for a narrow range of mediator masses close to the kinematic threshold of on-shell production). If the mediator mass M is below the LEP center of mass energy, but larger than $2m_\chi$, dark matter can be produced resonantly. In this case, the LEP constraint depends strongly on the width Γ of the mediator—a model-dependent quantity—but if Γ is small enough, the LEP constraint on the dark matter-electron coupling can be significantly stronger than for the contact operator case, see Figures 8.7, 8.8, 8.9.

As the hunt for dark matter continues and we probe the dark sector on several fronts, both indirectly, directly and at the Tevatron and the LHC it is amusing to discover that there are non-trivial constraints still to be found in now completed experiments. It seems that dark matter requires us to be students of history as well as physics.

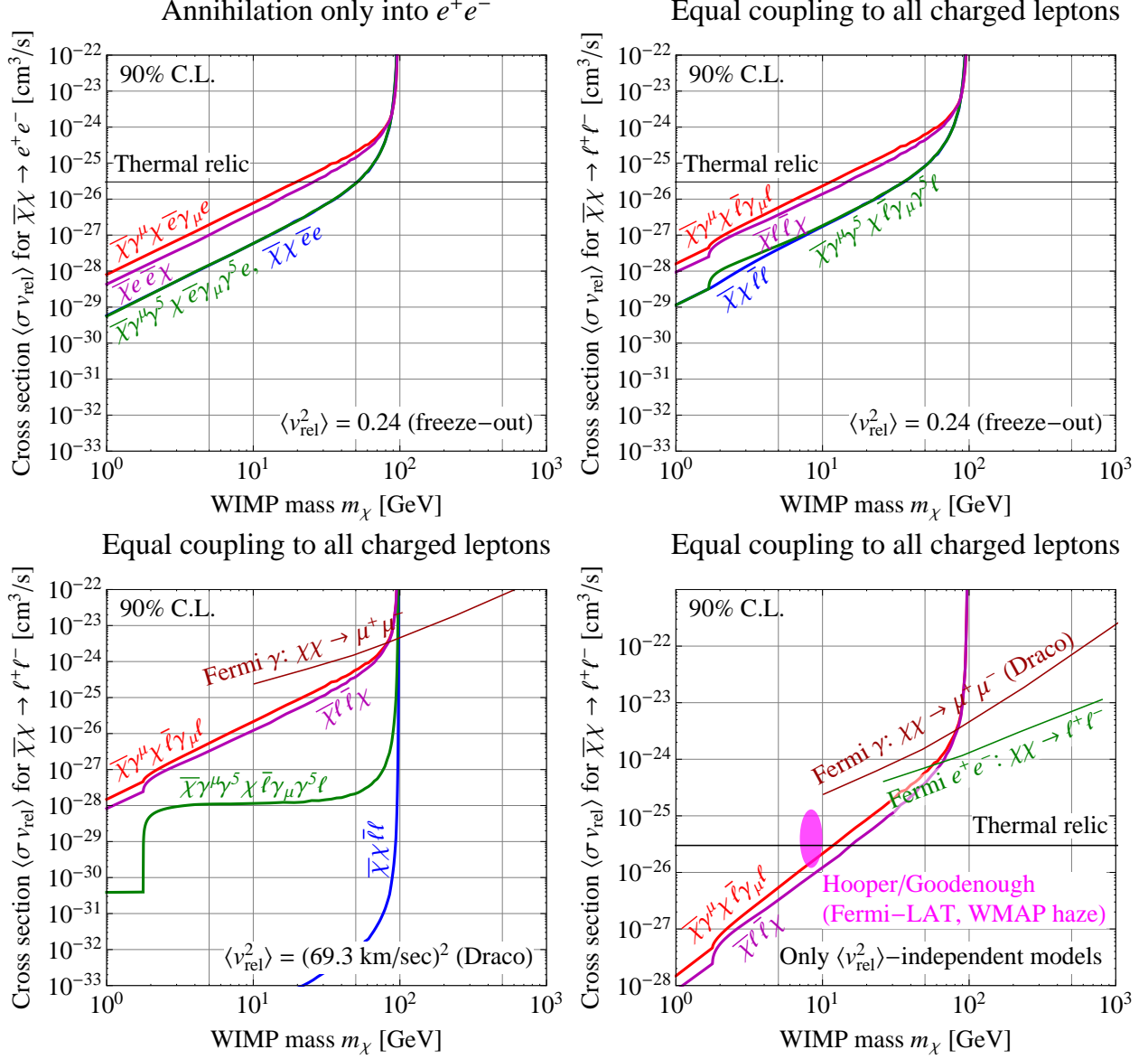


Figure 8.6: LEP upper limits on the dark matter annihilation cross section $eV\sigma v$, assuming that dark matter production at LEP and dark matter annihilation as probed by astrophysical and cosmological observations can be described by contact operators. In the upper left panel, we show limits on the process $\bar{\chi}\chi \rightarrow e^+e^-$ (the only one that can be constrained model-independently by LEP), while in the other panels we have made the assumption that dark matter couples equally to all charged leptons. For the average dark matter velocity eVv^2 we have assumed the value at freeze-out in the top panels, while the bottom left panel is for the Draco dwarf galaxy which has very small eVv^2 . In the bottom right panel we compare the LEP limit on the v -independent interactions, \mathcal{O}_V and \mathcal{O}_t , to limits from a variety of astrophysical observations [11, 233, 248].

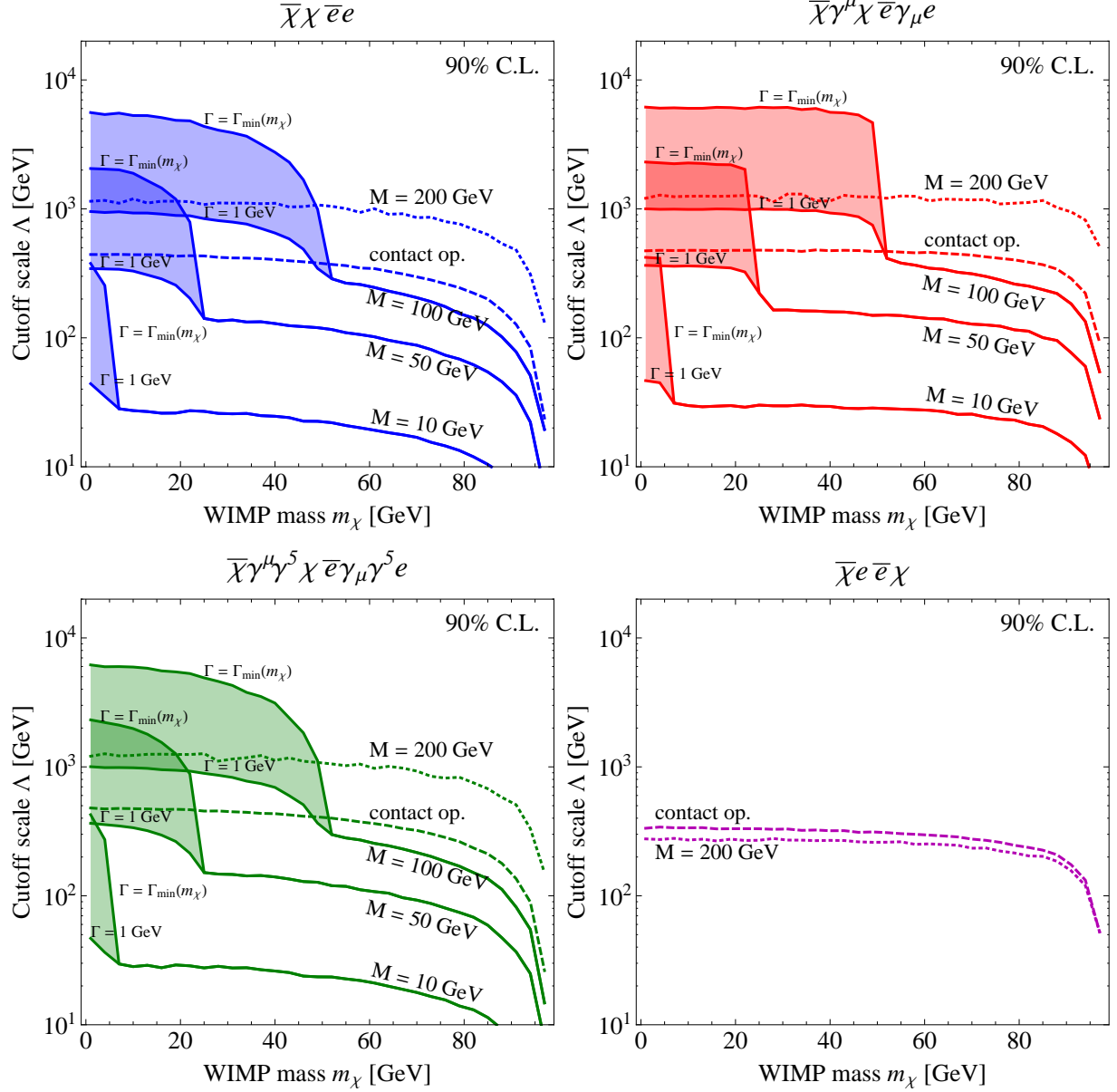


Figure 8.7: DELPHI lower limits on the cutoff scale $\Lambda = M/\sqrt{g_e g_\chi}$ of the dark matter effective theory. Dashed lines have been computed under the assumption that the effective theory is valid up to LEP energies, whereas the dotted and solid lines are for cases where the mediator mass M is so small that the effective theory breaks down. Once the mediator can be produced on-shell, its width Γ becomes relevant, as demonstrated by the shaded regions. Γ_{\min} is the minimum allowed width of the mediator, where $g_e \approx g_\chi = M/\Lambda$, and $\Gamma_{\min} \gtrsim 10^{-4}$ GeV.

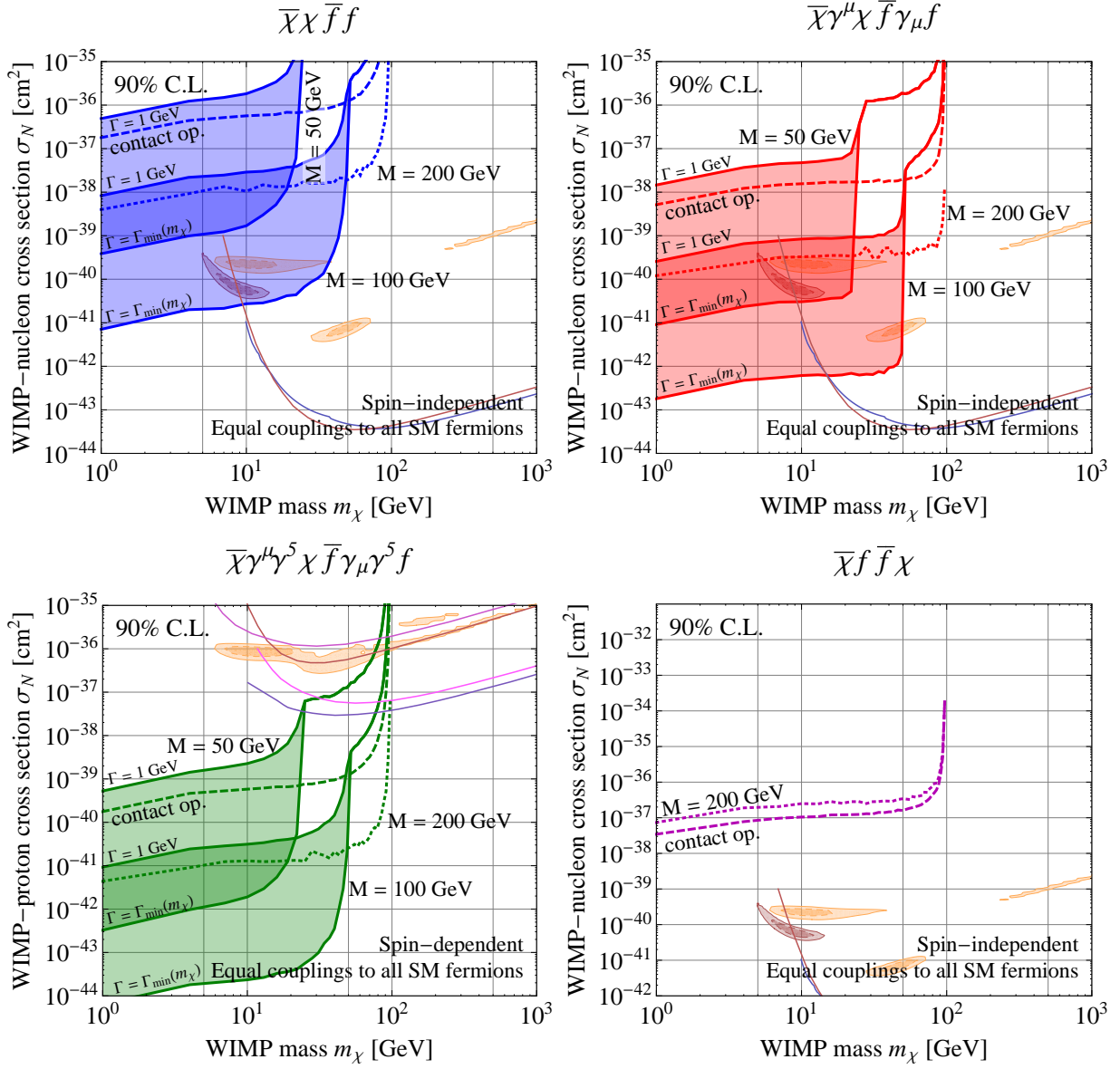


Figure 8.8: DELPHI lower limits on the cross section for dark matter-nucleon scattering for different dark matter interaction models. As in Figure 8.7, from which the limits are derived, dashed lines correspond to a contact operator interaction between dark matter and electrons at LEP, while the solid and dotted lines are for interactions mediated by light particles. In the background, we show the constraints from the direct detection experiments XENON-100, CDMS, DAMA, and CoGeNT (upper left, upper right and lower right panels) and from DAMA, PICASSO, XENON-10, COUPP and SIMPLE (lower left panel), see fig. 8.3 for details.

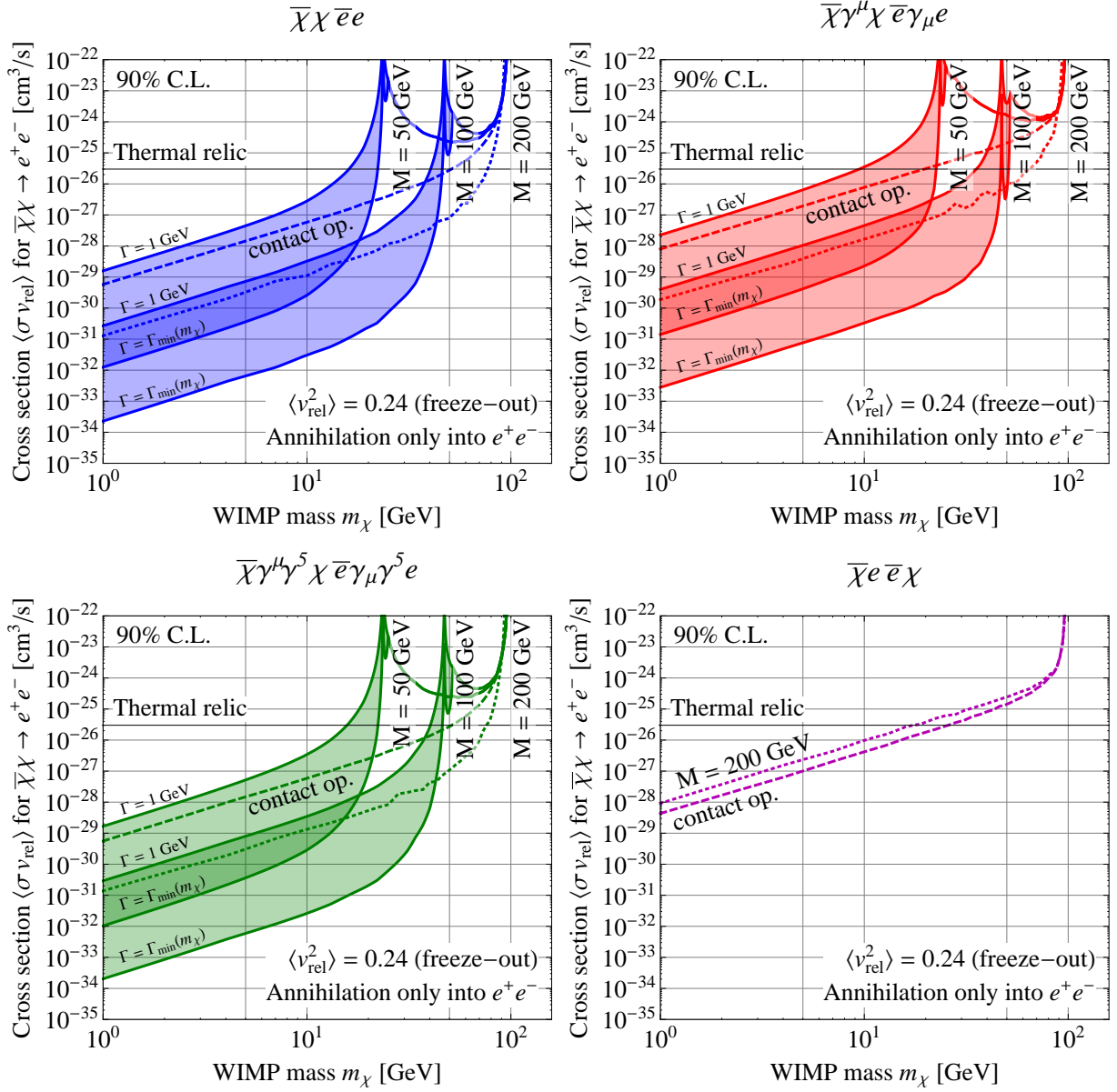


Figure 8.9: LEP upper limits on the dark matter annihilation cross section $eV\sigma v$ for different assumptions on the mass of the particle that mediates dark matter production and annihilation. We show limits only for the annihilation channel $\bar{\chi}\chi \rightarrow e^+e^-$, which is the only one that can be probed model-independently at LEP. If dark matter has several annihilation channels, these limits can be straightforwardly (but in a model-dependent way) translated into limits on the total annihilation cross section, as done in the upper right and bottom panels of Figure 9.6. As in Figure 8.7, from which the limits are derived, dashed lines correspond to a contact operator interaction between dark matter and electrons at LEP, while the solid and dotted lines are for interactions mediated by light particles.

CHAPTER 9

LHC CONSTRAINTS ON DARK MATTER INTERACTIONS

Based on the 2011 article “LEP Shines Light on Dark Matter”, written in collaboration with Patrick J. Fox, Roni Harnik, Joachim Kopp and published in Phys.Rev. D85 (2012) 056011.

9.1 Introduction

With the LHC physics program underway at full steam, the search for a dark matter (DM) candidate in high energy collisions is gaining momentum. Missing energy signatures are an integral part of many discovery channels for new physics at the LHC, and if a deviation from Standard Model (SM) predictions should be found in any of these channels, it could provide important evidence for the existence of new particles that are stable (or at least long-lived) and neutral, thus fulfilling two important requirements for being the dark matter in the universe.

In this paper, we will consider some of the more model-independent signatures of dark matter at the LHC: events with a large amount of missing energy (\cancel{E}_T) and a single jet or a single photon, as well as missing energy signals associated with invisible decays of the Higgs boson. Where available, we will use existing LHC data to set limits on the dark matter–quark and dark matter–gluon couplings in an effective field theory framework, and we will demonstrate the complementarity of these limits to those obtained from direct and indirect dark matter searches. We will also compare several mono-jet analyses that have been carried out by ATLAS and CMS, and we will outline a strategy for discovering dark matter or improving bounds in the future.

Dark matter searches using mono-jet signatures have been discussed previously in the context of both Tevatron and LHC searches [119, 29, 230, 67, 229, 276, 327], and have been shown to be very competitive with direct searches, especially at low dark matter mass and for dark matter with spin-dependent interactions. In a related work, SSC constraints on missing energy signatures due to quark and lepton compositeness have been discussed in [135]. The mono-photon channel has so far mostly been considered as a search channel at lepton colliders [92, 103, 206], but sensitivity studies exist also for the LHC [219, 352],

and they suggest that mono-photons can provide very good sensitivity to dark matter production at hadron colliders. Combined analyses of Tevatron mono-jet searches and LEP mono-photon searches have been presented in [296, 205]. The mono-photon channel suffers from different systematic uncertainties than the mono-jet channel, and probes a different set of DM–SM couplings, it can thus provide an important confirmation in case a signal is observed in mono-jets.

The outline of this paper is as follows: After introducing the effective field theory formalism of dark matter interactions in section 9.2, we will first discuss the mono-jet channel in section 9.3. We will describe our analysis procedure and then apply it to ATLAS and CMS data in order to set limits on the effective dark matter couplings to quarks and gluons. We also re-interpret these limits as bounds on the scattering and annihilation cross sections measured at direct and indirect detection experiments. We then go on, in section 9.4, to discuss how our limits are modified in models in which dark matter interactions are mediated by a light $\lesssim \mathcal{O}(\text{few TeV})$ particle, so that the effective field theory formalism is not applicable. In section 9.5, we will perform an analysis similar to that from section 9.3 in the mono-photon channel. A special example of dark matter coupling through a light mediator is DM interacting through the Standard Model Higgs boson, and we will argue in section 9.6 that in this case, invisible Higgs decay channels provide the best sensitivity. We will summarize and conclude in section 9.7.

9.2 An Effective Theory for dark matter interactions

If interactions between dark matter and Standard Model particles involve very heavy ($\gtrsim \text{few TeV}$) mediator particles—an assumption we are going to make in most of this paper—we can describe them in the framework of effective field theory. (We will investigate how

departing from the effective field theory framework changes our results in sections 9.4 as well as 9.6.) Since our goal is not to do a full survey of all possible effective operators, but rather to illustrate a wide variety of phenomenologically distinct cases, we will assume the dark matter to be a Dirac fermion χ and consider the following effective operators¹

$$\mathcal{O}_V = \frac{(\bar{\chi}\gamma_\mu\chi)(\bar{q}\gamma^\mu q)}{\Lambda^2}, \quad (\text{vector, } s\text{-channel}) \quad (9.2.1)$$

$$\mathcal{O}_A = \frac{(\bar{\chi}\gamma_\mu\gamma_5\chi)(\bar{q}\gamma^\mu\gamma_5 q)}{\Lambda^2}, \quad (\text{axial vector, } s\text{-channel}) \quad (9.2.2)$$

$$\mathcal{O}_t = \frac{(\bar{\chi}P_R q)(\bar{q}P_L\chi)}{\Lambda^2} + (L \leftrightarrow R), \quad (\text{scalar, } t\text{-channel}) \quad (9.2.3)$$

$$\mathcal{O}_g = \alpha_s \frac{(\bar{\chi}\chi)(G_{\mu\nu}^a G^{a\mu\nu})}{\Lambda^3}. \quad (\text{scalar, } s\text{-channel}) \quad (9.2.4)$$

In these expressions, χ is the dark matter field, q is a Standard Model quark field, $G_{\mu\nu}^a$ is the gluon field strength tensor, and $P_{R(L)} = (1 \pm \gamma_5)/2$. Since couplings to leptons cannot be directly probed in a hadron collider environment, we will not concern ourselves with these in this paper (see [206] for collider limits on dark matter–electron couplings).

In setting bounds we will turn on operators for up and down quarks separately. The bound for couplings to any linear combination of quark flavors can be derived from these bounds (see section 9.3). The denomination “ s -channel” or “ t -channel” in equations (9.2.1)–(9.2.4), refers to the most straightforward ultraviolet (UV) completions of the respective operators. For instance, \mathcal{O}_V arises most naturally if dark matter production in pp collisions proceeds through s -channel exchange of a new heavy gauge boson, and \mathcal{O}_t is most easily obtained if the production process is t -channel exchange of a heavy scalar. In such a UV completion, Λ would be given by $M/\sqrt{g_\chi g_q}$, where M is the mass of the mediator, g_χ is its coupling to dark matter and g_q is its coupling to Standard Model quarks. (The gluon operator \mathcal{O}_g is somewhat special in this respect since the coupling of a scalar mediator to two gluons is in itself a dimension-5 operator). In supersymmetric theories the

¹Other recent studies that have used a similar formalism to describe dark matter interactions include [245, 120, 119, 29, 230, 67, 229, 197, 231, 206, 267, 327, 134, 133].

dominant interaction of dark matter with quarks is often induced by squark exchange. For the case of degenerate left and right handed squarks an operator of the form \mathcal{O}_t is predicted (but with χ being a Majorana fermion). Here we have assumed that DM is a Dirac fermion, the case of a Majorana fermion [327] would not greatly alter our results, except in the case of the vector operator \mathcal{O}_V , which vanishes if χ is a Majorana fermion.

Ultimately we wish to compare the collider bounds to direct detection bounds, and when matching quark level operators to nucleon level operators the coupling between the SM and DM must be of the form $\mathcal{O}_{\text{SM}}\mathcal{O}_\chi$, where \mathcal{O}_{SM} involves only Standard Model fields and \mathcal{O}_χ involves only dark matter, so that the matrix element $\langle N|\mathcal{O}_{\text{SM}}|N\rangle$ can be extracted [197]. An operator like \mathcal{O}_t , which is not in this form, can be converted into it by a Fierz transformation. This leads to a sum of several operators that can all contribute to the interaction. Typically, for direct detection, one of these operators will dominate, but at colliders there can be considerable interference. For instance, we can rewrite equation (9.2.3) as

$$\frac{1}{\Lambda^2}(\bar{\chi}P_R q)(\bar{q}P_L \chi) + (L \leftrightarrow R) = \frac{1}{4\Lambda^2}[(\bar{\chi}\gamma^\mu \chi)(\bar{q}\gamma_\mu q) - (\bar{\chi}\gamma^\mu \gamma_5 \chi)(\bar{q}\gamma_\mu \gamma_5 q)] = \frac{1}{4\Lambda^2}(\mathcal{O}_V - \mathcal{O}_A). \quad (9.2.5)$$

If χ is a Dirac fermion both the \mathcal{O}_V and the \mathcal{O}_A components contribute to χ production at colliders, but in direct detection experiments, the spin-independent interaction induced by \mathcal{O}_V dominates over the spin-dependent interaction due to \mathcal{O}_A . For Majorana dark matter, of course, \mathcal{O}_V would vanish in all cases.

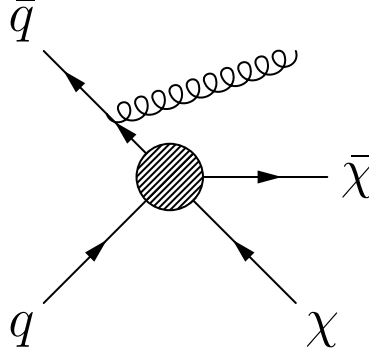


Figure 9.1: Dark matter production in association with a single jet in a hadron collider.

9.3 Mono-jets at the LHC

In this section we will derive bounds on dark matter operators with mono-jet searches. In the following subsection we will compare the reach of several mono-jet searches, a low luminosity (36 pb^{-1}) CMS search and three ATLAS searches with varying jet p_T cuts using 1 fb^{-1} of data.² For simplicity we will make this comparison only for the vector operator \mathcal{O}_V , with dark matter coupling only to up quarks. We will find that the highest jet p_T cuts are most effective in setting bounds on this dark matter interaction. In the next subsection we will proceed to use the analysis based on these highest jet- p_T cuts to set bounds on all effective operators discussed in section 9.2.

9.3.1 Comparing Various Mono-Jet Analyses

Dark matter pair production through a diagram like figure 9.1 is one of the leading channels for dark matter searches at hadron colliders [230, 67]. The signal would manifest itself as an excess of jets plus missing energy ($j + \cancel{E}_T$) events over the Standard Model

²As we were completing this manuscript, CMS has also updated its mono-jet analysis using 1.1 fb^{-1} of data [138].

background, which consists mainly of $(Z \rightarrow \nu\nu) + j$ and $(W \rightarrow \ell^{\text{inv}}\nu) + j$ final states. In the latter case the charged lepton ℓ is lost, as indicated by the superscript “inv”. Experimental studies of $j + \cancel{E}_T$ final states have been performed by CDF [5], CMS [137] and ATLAS [57, 56], mostly in the context of Extra Dimensions.

Our analysis will, for the most part, be based on the ATLAS search [56] which looked for mono-jets in 1 fb^{-1} of data, although we will also compare to the earlier CMS analysis [137], which used 36 pb^{-1} of integrated luminosity. The ATLAS search contains three separate analyses based on successively harder p_T cuts, the major selection criteria from each analysis that we apply in our analysis are given below.³

LowPT Selection requires $\cancel{E}_T > 120 \text{ GeV}$, one jet with $p_T(j_1) > 120 \text{ GeV}$, $|\eta(j_1)| < 2$, and events are vetoed if they contain a second jet with $p_T(j_2) > 30 \text{ GeV}$ and $|\eta(j_2)| < 4.5$.

HighPT Selection requires $\cancel{E}_T > 220 \text{ GeV}$, one jet with $p_T(j_1) > 250 \text{ GeV}$, $|\eta(j_1)| < 2$, and events are vetoed if there is a second jet with $|\eta(j_2)| < 4.5$ and with either $p_T(j_2) > 60 \text{ GeV}$ or $\Delta\phi(j_2, \cancel{E}_T) < 0.5$. Any further jets with $|\eta(j_2)| < 4.5$ must have $p_T(j_3) < 30 \text{ GeV}$.

veryHighPT Selection requires $\cancel{E}_T > 300 \text{ GeV}$, one jet with $p_T(j_1) > 350 \text{ GeV}$, $|\eta(j_1)| < 2$, and events are vetoed if there is a second jet with $|\eta(j_2)| < 4.5$ and with either $p_T(j_2) > 60 \text{ GeV}$ or $\Delta\phi(j_2, \cancel{E}_T) < 0.5$. Any further jets with $|\eta(j_2)| < 4.5$ must have $p_T(j_3) < 30 \text{ GeV}$.

In all cases events are vetoed if they contain any hard leptons, defined for electrons as $|\eta(e)| < 2.47$ and $p_T(e) > 20 \text{ GeV}$ and for muons as $|\eta(\mu)| < 2.4$ and $p_T(\mu) > 10 \text{ GeV}$.

³Both ATLAS and CMS impose additional isolation cuts, which we do not mimic in our analysis for simplicity and since they would not have a large impact on our results.

	ATLAS _{LowPT} 1.0 fb ⁻¹	ATLAS _{HighPT} 1.0 fb ⁻¹	ATLAS _{veryHighPT} 1.0 fb ⁻¹	CMS 36 pb ⁻¹
Expected	15100 ± 700	1010 ± 75	193 ± 25	297 ± 45
Observed	15740	965	167	275

Table 9.1: The expected and observed number of events at ATLAS and CMS, the error is a combination of a) Monte Carlo statistical uncertainties, and b) control sample statistical uncertainties and other systematic uncertainties. For the case of ATLAS we have combined a) and b) in quadrature.

The cuts used by CMS are similar to those of the _{LowPT} ATLAS analysis. Mono-jet events are selected by requiring $\cancel{E}_T > 150$ GeV and one jet with $p_T(j_1) > 110$ GeV and pseudo-rapidity $|\eta(j_1)| < 2.4$. A second jet with $p_T(j_2) > 30$ GeV is allowed if the azimuthal angle it forms with the leading jet is $\Delta\phi(j_1, j_2) < 2.0$ radians. Events with more than two jets with $p_T > 30$ GeV are vetoed, as are events containing charged leptons with $p_T > 10$ GeV. The number of expected and observed events in the various searches is shown in table 9.1.

We have simulated the dominant Standard Model backgrounds ($Z \rightarrow \nu\nu$) + j and ($W \rightarrow \ell^{\text{inv}}\nu$) + j using MadGraph [34, 35] at the matrix element level, Pythia 6 [344] for parton showering and hadronization, and PGS [144] as a fast detector simulation. We have checked that results obtained with Delphes [319] as an alternative detector simulation, would change our results by only a few per cent. In figure 9.2, we compare our simulation of the dominant backgrounds to both the data and the MC predictions of both collaborations⁴, we also show the spectrum for candidate dark matter models. In each case we rescale the normalization of the two backgrounds by a correction factor chosen to fit the number of events predicted by the collaborations. After this rescaling we find excellent agreement in shape between our predictions and theirs. When predicting the

⁴Note that the MC predictions of the collaborations are for all backgrounds. For the highest \cancel{E}_T bins the background is completely dominated by $W + j$ and $Z + j$, but in the lowest bins there can be $\sim 10\%$ contributions from $t\bar{t}$, QCD and other reducible backgrounds which we did not simulate.

dark matter signal, we rescale the rate by the correction factor found for the invisible Z background, since this background is most similar to the DM signal. The correction factors are approximately 0.9, 1.1 and 1.2 for the three ATLAS analyses (from low to very high respectively), and approximately 0.7 for the CMS analysis.

As can be seen in figure 9.2, our simulation of Standard Model backgrounds is in very good agreement with the CMS and ATLAS background predictions and with the data, so that we can have confidence in our simulations also for the signal predictions. Turning to those, we see from figure 9.2 that a dark matter signal mainly changes the slope of the distribution, leading to the most significant effects at high \cancel{E}_T [79, 67, 206]. The main reason for the difference in shape is that dark matter production in the effective theory framework is a $2 \rightarrow 3$ process proceeding through non-renormalizable operators, whereas the dominant Standard Model backgrounds have $2 \rightarrow 2$ kinematics.

Despite this clear difference in shape between the signal and the background we will nonetheless use only the total event rate to place constraints on dark matter properties since we cannot reliably model systematic uncertainties in the background shape. However, the existence of three ATLAS analyses with different p_T cuts allows a crude version of a shape analysis to be carried out. Since the DM signal spectrum is harder than the background spectrum one would expect harder selection cuts to improve the ratio of signal to background, as is reflected in figure 9.2. To quantify this we compute the expected and observed 90% exclusion limits on the dark matter–SM coupling, parameterized by the suppression scale Λ , for a given dark matter mass m_χ by requiring

$$\chi^2 \equiv \frac{[\Delta_N - N_{\text{DM}}(m_\chi, \Lambda)]^2}{N_{\text{DM}}(m_\chi, \Lambda) + N_{\text{SM}} + \sigma_{\text{SM}}^2} = 2.71. \quad (9.3.6)$$

Here σ_{SM} is the uncertainty in the predicted number of background events, see table 9.1. In computing the number of expected signal events, N_{DM} , we include the correction factor

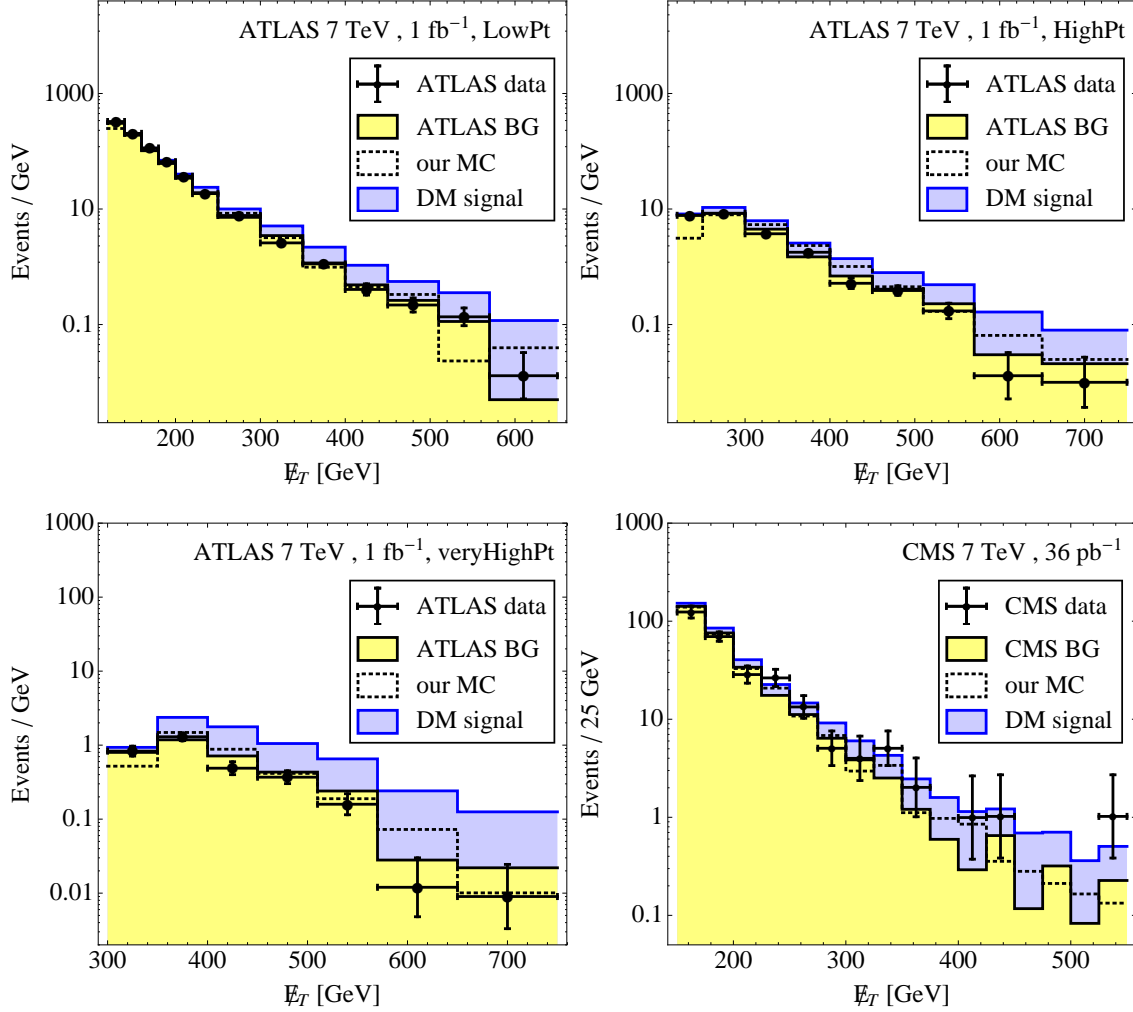


Figure 9.2: Measured missing energy spectra of $j + \cancel{E}_T$ for the three ATLAS analyses and the CMS analysis discussed in the text (black data points with error bars) compared to the collaborations' background predictions (yellow shaded histograms) and to our Monte Carlo prediction with (blue histograms) and without (black dotted lines) a dark matter signal. In all cases the DM signal comes from the vector operator, \mathcal{O}_V , and $m_\chi = 10$ GeV, $\Lambda = 400$ GeV. Our simulations are rescaled to match the overall normalization of the collaborations' background predictions.

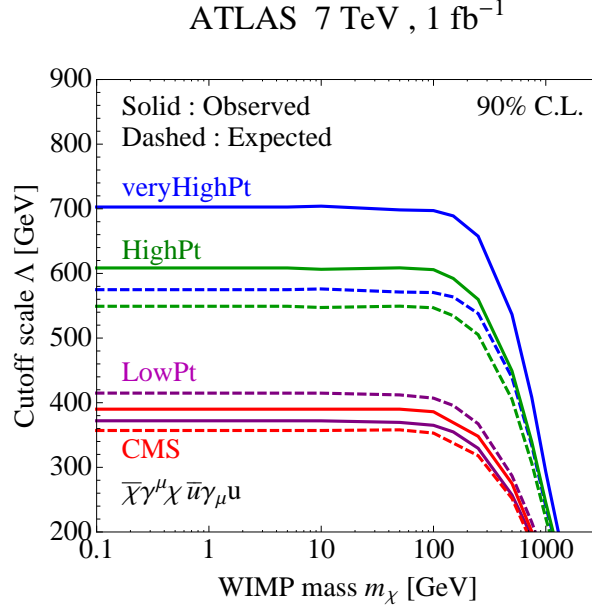


Figure 9.3: Limits on the suppression scale Λ for the vector operator, \mathcal{O}_V , where only the coupling to up quarks is considered, for the three ATLAS analyses and the analysis of CMS. In all cases the observed (expected) bound is represented by a solid (dashed) line.

discussed above to account for the inaccuracy of our detector simulation. We define a quantity

$$\Delta_N = \begin{cases} 0 & \text{expected bound} \\ N_{\text{obs}} - N_{\text{SM}} & \text{observed bound} , \end{cases} \quad (9.3.7)$$

where $N_{\text{obs(SM)}}$ is the number of observed (predicted background) events. With the exception of the `LowPt` analysis at ATLAS, all analyses experienced a downward fluctuation in the background and hence give stronger bounds on DM than expected. Since this lucky accident is unlikely to be repeated in the future we will in the following show both the observed and expected bounds. The limits on Λ for the operator \mathcal{O}_V , with coupling to up quarks only, is shown in figure 9.3. As expected the strongest bounds come from the analysis with the hardest jet p_T and \cancel{E}_T cuts, and in all cases but `LowPt` the observed bound is stronger than expected due to the downward fluctuations in the data.

It is interesting to note that the CMS and ATLAS `LowPT` bounds are comparable despite the fact that CMS used 36 pb^{-1} of data whereas ATLAS used 1 fb^{-1} . This is because both analyses are dominated by systematic uncertainties which do not decrease much with luminosity. This clearly illustrates the utility of making cuts that concentrate on the high p_T tail of the mono-jet distribution rather than simply acquiring more luminosity. The ability to harden cuts and focus on the tails of the distribution increases as the tails get populated with growing luminosity. Exactly what the best cuts for the DM search are is unclear since there is not much difference between expected bounds from the `HighPT` and `veryHighPT` analyses, despite a considerable hardening of cuts. A dedicated search, with tuned p_T and \cancel{E}_T cuts, would presumably lead to even stronger bounds than those coming from ATLAS `veryHighPT`, we strongly advocate for such a study to be carried out.

The high p_T analyses are most sensitive to the vector operator in the case in which it involves only up quarks. We have also investigated other operators and found that the advantage of the high p_T cuts persists, unless the operator involves only heavier, “sea”, quarks, such as strange or charm. For operators involving these the low p_T analysis does equally well. The reason is that for sea quarks the parton distribution functions are more rapidly falling, which leads to a softer p_T spectrum more similar to the background spectrum.

Since the expected bounds from the `HighPT` and `veryHighPT` analyses are comparable, we will concentrate from now on only the `veryHighPT` ATLAS analysis, and show both the expected and observed bounds from this analysis. It should be noted that the `veryHighPT` analysis had the largest fractional downward fluctuation and so the observed bound is considerably stronger than expected, this is unlikely to repeat with more luminosity. However, exactly how the expected bounds change with luminosity is

not straightforward because this depends on the details of systematic uncertainties at yet higher p_T with higher luminosity.

We can repeat the exercise above for each operator in turn, for both light quark flavors individually. The results for \mathcal{O}_V , \mathcal{O}_A , \mathcal{O}_t and \mathcal{O}_g are shown in figure 9.4. As for earlier Tevatron analyses [230, 67], we note that the collider bounds on the various operators are similar to one another. The collider limits are not strongly affected by the spin structure of the operator, which, as we shall soon see, will give these bounds a relative advantage over direct detection experiments for spin-dependent dark matter scattering typically mediated by axial-vector operators. The bound on the t -channel operator \mathcal{O}_t is somewhat weaker than the bound on \mathcal{O}_V and \mathcal{O}_A because of the prefactor $1/4$ and because of partial negative interference between the two terms on the right hand side of equation (9.2.5). The bound on the gluon operator \mathcal{O}_g is very strong, considering that the definition of this operator contains a factor α_s , because of the high gluon luminosity at the LHC, despite the operator being of higher dimension than the other operators we consider.

The bounds on the suppression scales of individual operators can be combined for testing models that predict contributions from multiple operators suppressed by the same scale. For instance, consider a model in which dark matter couples to up and down quarks with couplings proportional to c_u/Λ^2 and c_d/Λ^2 , where Λ is a joint suppression scale and c_u, c_d are dimensionless coefficients. The constraint on Λ can be obtained from the individual constraints on couplings only to up quarks, Λ_u , and only to down quarks, Λ_d , from figure 9.4 according to the relation

$$\Lambda^4 = c_u^2 \Lambda_u^4 + c_d^2 \Lambda_d^4. \quad (9.3.8)$$

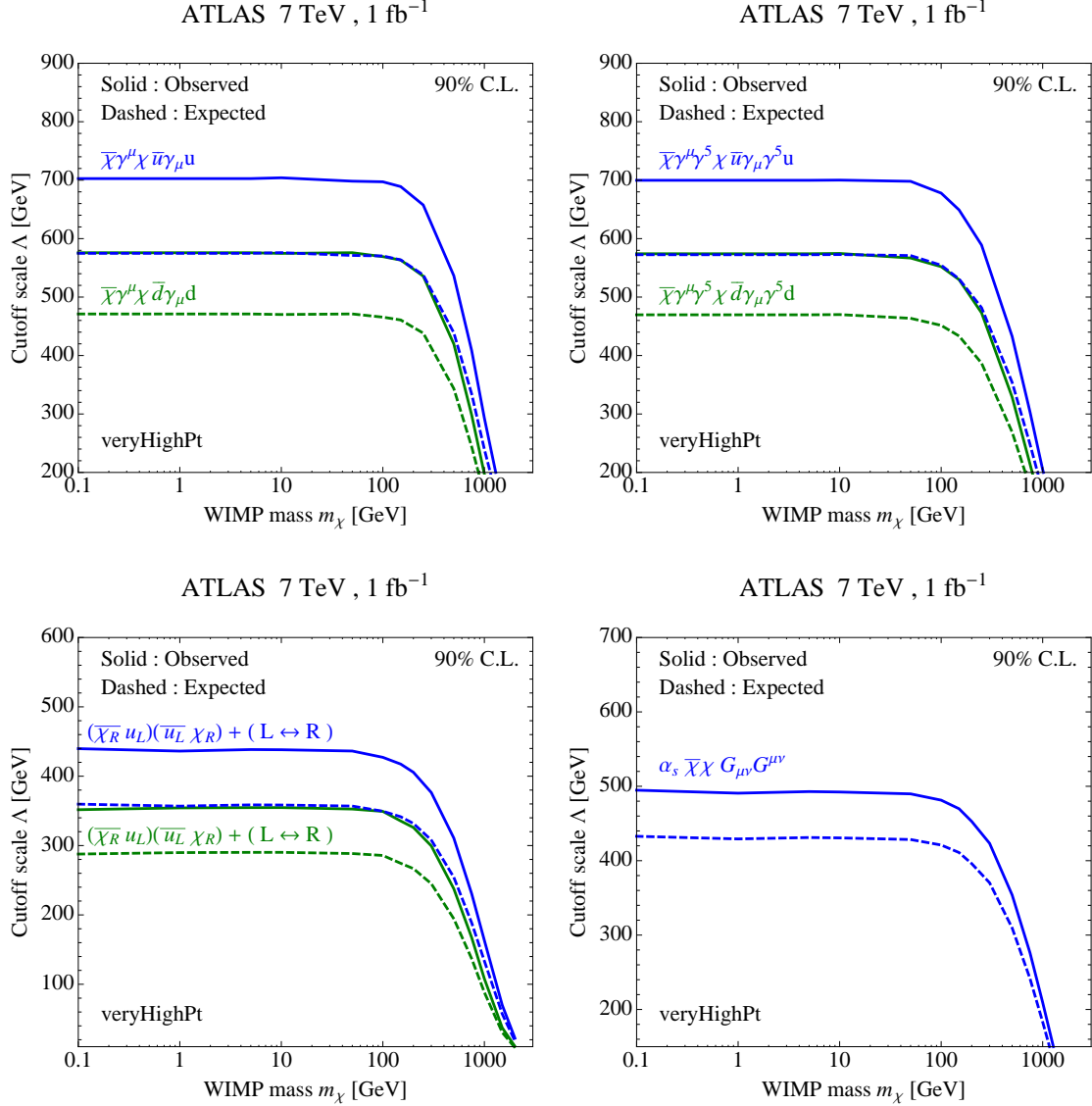


Figure 9.4: Limits on the suppression scale Λ for various operators, where only the coupling to one quark flavor at a time is considered, for the `veryHighPt` ATLAS analysis. In all cases the observed (expected) bounds are shown as solid (dashed) lines.

9.3.2 Mono-Jet Bounds Compared to Direct Dark Matter Searches

With these collider bounds in hand we can now place constraints on direct detection rates, in a similar fashion to [230, 67, 229, 206, 327]. For the coefficients required to translate the quark level matrix elements $\langle N | \bar{q} \gamma^\mu q | N \rangle$ and $\langle N | \bar{q} \gamma^\mu \gamma^5 q | N \rangle$ into nucleon level matrix

elements, we use the values from [130, 77, 70], as collected in [67]. We also need the matrix element for the gluon field strength in the nucleon [340],

$$\langle N | \alpha_s G_{\mu\nu}^a G^{a\mu\nu} | N \rangle = -\frac{8\pi}{9} \left(m_N - \sum_{q=u,d,s} \langle N | m_q \bar{q}q | N \rangle \right). \quad (9.3.9)$$

For $\langle N | m_q \bar{q}q | N \rangle$, we follow [193] but use an updated [359] value of the pion-nucleon sigma term $\Sigma_{\pi N} = 55 \text{ MeV}$.⁵

When translating collider limits on effective dark matter–Standard Model couplings into constraints on the dark matter–nucleon scattering cross section, we make the simplifying assumption that the couplings are universal in quark flavor. If flavor-ratios different from unity are desired it is straightforward to translate the collider bounds into direct detection constraints using equation (9.3.8), with $c_u \neq c_d$. In other words, the LHC limits on the dark matter–nucleon cross section shown in figure 9.5 would have to be rescaled by a factor $(\Lambda_u^4 + \Lambda_d^4)/(c_u^2 \Lambda_u^4 + c_d^2 \Lambda_d^4)$.

The bounds on the dark matter–nucleon scattering cross sections for the various operators, along with bounds (and some notable excesses) from dedicated direct detection experiments are shown in figure 9.5. A few summary comments are in order:

- For spin-independent dark matter couplings, the LHC bounds provide the most powerful constraints for m_χ below about 5 GeV for the scalar and vector operators and below 10 GeV for the gluon operator.
- The LHC bound on the vector operator is within 1–2 orders of magnitude from the parameter region suggested by DAMA, CoGeNT and CRESST. The bound on the gluon operator \mathcal{O}_g is several order of magnitude stronger and is competing with CDMS and XENON for dark matter masses up to about 500 GeV.

⁵Note however that recent lattice determinations [358, 349, 223, 348] of the strange quark content of the nucleon are considerably lower. The effect on our bounds is small.

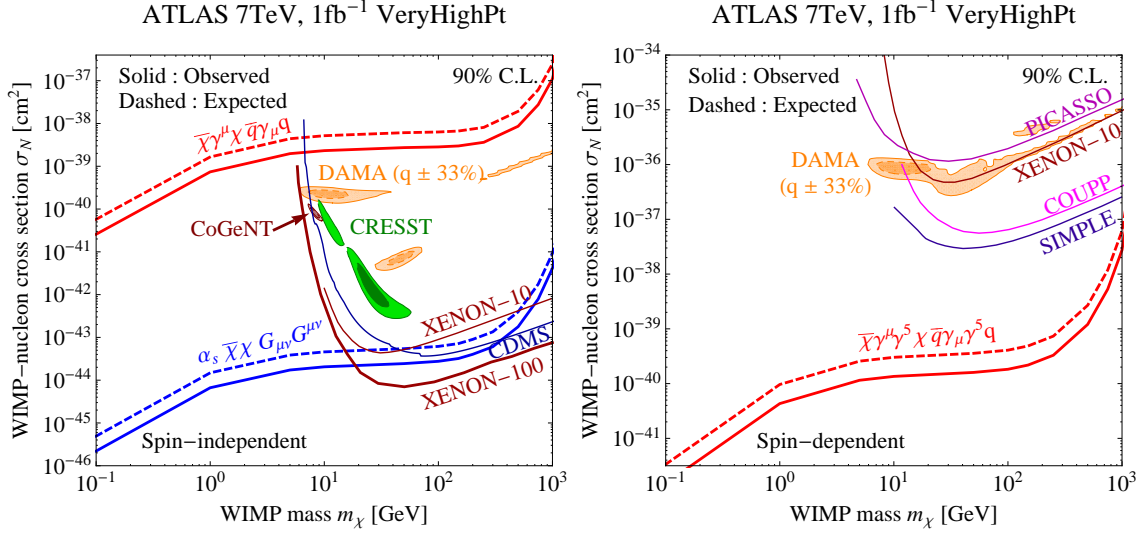


Figure 9.5: ATLAS limits on (a) spin-independent and (b) spin-dependent dark matter–nucleon scattering, compared to limits from the direct detection experiments. In particular, we show constraints on spin-independent scattering from CDMS [30], XENON-10 [39], XENON-100 [44], DAMA [86], CoGeNT [4, 208] and CRESST [40], and constraints on spin-dependent scattering from DAMA [86], PICASSO [71], XENON-10 [38], COUPP [76] and SIMPLE [224]. DAMA and CoGeNT allowed regions are based on our own fits [279, 206, 208] to the experimental data. Following [247], we have conservatively assumed large systematic uncertainties on the DAMA quenching factors: $q_{\text{Na}} = 0.3 \pm 0.1$ for sodium and $q_{\text{I}} = 0.09 \pm 0.03$ for iodine, which leads to an enlargement of the DAMA allowed regions. All limits are shown at 90% confidence level, whereas for DAMA and CoGeNT we show 90% and 3σ contours. For CRESST, the contours are 1σ and 2σ as in [40].

- The LHC provides the strongest bound on spin dependent dark matter–nucleon scattering, by a margin of about two orders of magnitude. The LHC bound becomes less powerful than current direct detection experiments for $m_\chi \gtrsim 1 - 2$ TeV.

9.3.3 Limits on Dark Matter Annihilation

In addition to limits on direct detection cross sections, we have also studied the constraints that the LHC can set on dark matter annihilation cross sections relevant to in-

direct astrophysical searches. The dark matter annihilation rate is proportional to the quantity $\langle \sigma v_{\text{rel}} \rangle$, where σ is the annihilation cross section, v_{rel} is the relative velocity of the annihilating particles, and the average $\langle \cdot \rangle$ is over the dark matter velocity distribution in the particular astrophysical environment considered. Working again in the effective field theory framework, we find for dark matter coupling to quarks through the dimension 6 vector operator, equation (9.2.1), or the axial-vector operator, equation (9.2.2), respectively [206],

$$\sigma_V v_{\text{rel}} = \frac{1}{16\pi\Lambda^4} \sum_q \sqrt{1 - \frac{m_q^2}{m_\chi^2}} \left(24(2m_\chi^2 + m_q^2) + \frac{8m_\chi^4 - 4m_\chi^2 m_q^2 + 5m_q^4}{m_\chi^2 - m_q^2} v_{\text{rel}}^2 \right), \quad (9.3.10)$$

$$\sigma_A v_{\text{rel}} = \frac{1}{16\pi\Lambda^4} \sum_q \sqrt{1 - \frac{m_q^2}{m_\chi^2}} \left(24m_q^2 + \frac{8m_\chi^4 - 22m_\chi^2 m_q^2 + 17m_q^4}{m_\chi^2 - m_q^2} v_{\text{rel}}^2 \right). \quad (9.3.11)$$

Here the sum runs over all kinematically accessible quark flavors, and m_q denotes the quark masses. We see that, for both types of interaction, the leading term in σv_{rel} is independent of v_{rel} when there is at least one annihilation channel with $m_q^2 \gtrsim m_\chi^2 v_{\text{rel}}^2$. Note that for DM couplings with different Lorentz structures (for instance scalar couplings), the annihilation cross section can exhibit a much stronger v_{rel} -dependence. For such operators, collider bounds on $\langle \sigma v_{\text{rel}} \rangle$ can be significantly *stronger* than in the cases considered here, especially in environments with low $\langle v_{\text{rel}}^2 \rangle$ such as galaxies (see, for instance, reference [206] for a more detailed discussion).

In figure 9.6, we show ATLAS constraints on $\langle \sigma v_{\text{rel}} \rangle$ as a function of the dark matter mass m_χ for a scenario in which dark matter couples equally to all quark flavors and chiralities, but not to leptons. (If dark matter can annihilate also to leptons, the bounds are weakened by a factor $1/\text{BR}(\bar{\chi}\chi \rightarrow \bar{q}q)$.) To compute these limits, we have used the bounds on Λ_u and Λ_d from figure 9.4, and have converted them into a limit on the flavor-universal cutoff scale Λ using equation (9.3.8). We have neglected the small contribution of initial states involving strange and charm quarks to the mono-jet rate at the LHC.

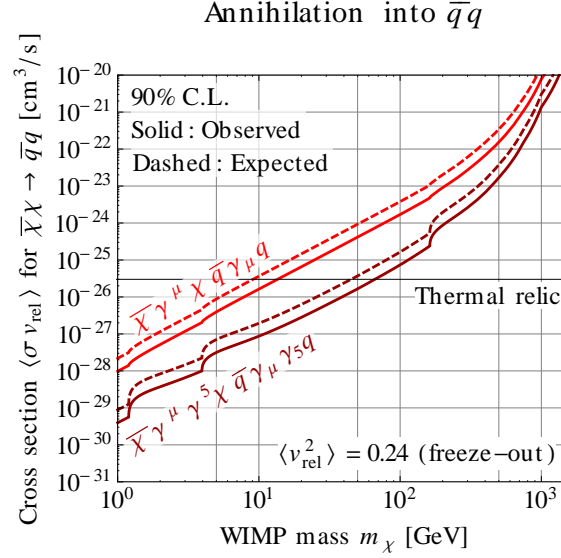


Figure 9.6: ATLAS constraints on dark matter annihilation for flavor-universal vector or axial vector couplings of dark matter to quarks. (If dark matter can annihilate also to leptons, the bounds are weakened by a factor $1/\text{BR}(\bar{\chi}\chi \rightarrow \bar{q}q)$.) We consider an environment with $\langle v_{\text{rel}}^2 \rangle = 0.24$, corresponding to the epoch at which thermal relic dark matter freezes out in the early universe. $\langle v_{\text{rel}}^2 \rangle$ is much smaller in present-day environments such as galaxies, which leads to improved collider bounds on the annihilation rate in those systems. The value of $\langle \sigma v_{\text{rel}} \rangle$ required for dark matter to be a thermal relic is indicated by the horizontal black line.

We see from figure 9.6 that, as long as the effective field theory framework provides a valid description of dark matter production at the LHC and of its annihilation in the early universe, thermal relic cross sections are ruled out at 90% confidence level for $m_\chi \lesssim 15$ GeV in the case of vector couplings and for $m_\chi \lesssim 70$ GeV in the case of axial vector couplings. As discussed above, the limits can become somewhat weaker if additional annihilation channels exist, and stronger in environments with low $\langle v_{\text{rel}}^2 \rangle$.

9.4 Light mediators

So far, we have worked entirely in the effective field theory framework, assuming the particles that mediate dark matter–Standard Model interactions to be much heavier than the typical momentum exchanged in mono-jet events, and the production at colliders to be well approximated by a contact operator. However, given that the LHC is probing record high scales, particularly for event samples with hard p_T cuts, it is worthwhile to investigate how the predictions of the effective theory are modified once a propagating particle is introduced to mediate the interaction of matter and dark matter.

As discussed in [67, 229, 206, 232, 37], the sensitivity of colliders can change dramatically in this case, either suppressing or enhancing the signal. In the case of “ s -channel” operators, resonance effects can enhance the production cross section once the mass of the s -channel mediator is within the kinematic range and can be produced on-shell. This enhancement is particularly strong when the mediator has a small decay width Γ , though it should be noted that within our assumptions Γ is bounded from below due to the open decay channels to jets and to dark matter.

On the other hand, colliders have a relative disadvantage compared to direct detection experiments in the light mediator case. The reason is that, from dimensional analysis, the cross section for the collider production process $pp \rightarrow \bar{\chi}\chi + X$ scales as,

$$\sigma(pp \rightarrow \bar{\chi}\chi + X) \sim \frac{g_q^2 g_\chi^2}{(q^2 - M^2)^2 + \Gamma^2/4} E^2, \quad (9.4.12)$$

where E is of order the partonic center-of-mass energy, M is the mass of the s -channel mediator and q is the four momentum flowing through this mediator. At the 7 TeV LHC, $\sqrt{q^2}$ has a broad distribution which is peaked at a few hundred GeV and falls slowly above. The mediator’s width is denoted by Γ , and g_q, g_χ are its couplings to quarks

and dark matter, respectively. The direct detection cross section, on the other hand, is approximately

$$\sigma(\chi N \rightarrow \chi N) \sim \frac{g_q^2 g_\chi^2}{M^4} \mu_{\chi N}^2, \quad (9.4.13)$$

with the reduced mass $\mu_{\chi N}$ of the dark matter and the target nucleus.

When $M^2 \ll q^2$, the limit that the collider sets on $g_\chi^2 g_q^2$ becomes independent of M , whereas the limit on $g_\chi^2 g_q^2$ from direct detection experiments continues to become stronger for smaller M . In other words, the collider limit on $\sigma(\chi N \rightarrow \chi N)$ becomes weaker as M becomes smaller. On the other hand, when $m_\chi < M/2$ and the condition $\sqrt{q^2} \simeq M$ can be fulfilled, collider production of $\bar{\chi}\chi + X$ experiences resonant enhancement. Improved constraints on Λ can be expected in that regime.

In figure 9.7, we investigate the dependence of the ATLAS bounds on the mediator mass M more quantitatively including both on-shell and off-shell production. Even though dark matter–quark interactions can now no longer be described by effective field theory in a collider environment, we still use $\Lambda \equiv M/\sqrt{g_\chi g_q}$ as a measure for the strength of the collider constraint, since Λ is the quantity that determines the direct detection cross section. As before, we have used the cuts from the ATLAS `veryHighPt` analysis (see section 9.3). We have assumed vector interactions with equal couplings of the intermediate vector boson to all quark flavors.

At very large M ($\gtrsim 5$ TeV), the limits on Λ in figure 9.7 asymptote to those obtained in the effective theory framework. For $2m_\chi \ll M \lesssim 5$ TeV, resonant enhancement leads to a significant improvement in the limit since the mediator can now be produced on-shell, so that the primary parton–parton collision now leads to a two-body rather than three-body final state. As expected from equation (9.4.12), the strongest enhancement occurs when the mediator is narrow. In figure 9.7, we show the effects of resonance enhancement. We

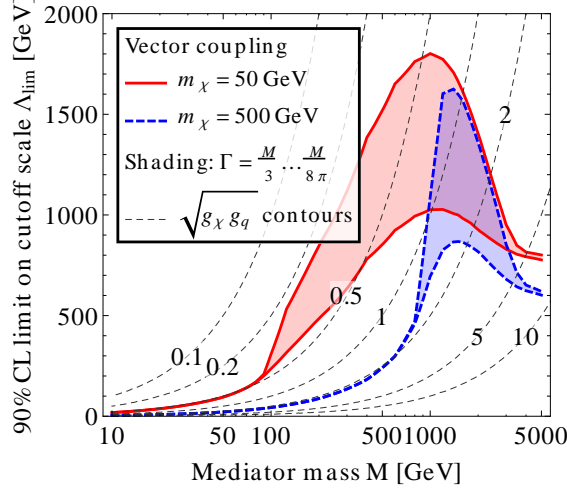


Figure 9.7: ATLAS limit on $\Lambda \equiv M/\sqrt{g_\chi g_q}$ as a function of the mass M of the particle mediating dark matter–quark interactions. We have assumed s -channel vector-type interactions, and we have considered the values $m_\chi = 50$ GeV (red) and $m_\chi = 500$ GeV (blue) for the dark matter mass. We have varied the width Γ of the mediator between the values $M/3$ (lower boundary of colored bands) and $M/8\pi$ (upper boundary of colored bands). Dashed dark gray lines show contours of constant $\sqrt{g_\chi g_q}$.

consider mediators of fixed width, ranging from $\Gamma = M/8\pi$ to $\Gamma = M/3$, the associated enhancements are illustrated by the colored bands, with the upper edge corresponding to the narrow case and the lower edge to a wide mediator.⁶ The shape of the peaks in figure 9.7 is determined by the interplay of parton distribution functions, which suppress the direct production of a heavy mediator, and the explicit proportionality of Λ to M according to its definition. Below $M \simeq 2m_\chi$, the mediator can no longer decay to $\bar{\chi}\chi$, but only to $\bar{q}q$, so in this mass range, it can only contribute to the mono-jet sample if it is produced off-shell. In that regime, the limit on Λ is rather weak (even though the limit on $g_\chi^2 g_q^2$ is independent of M there as discussed above), and the dependence on Γ disappears.

In light of this result it is important to revisit our limits from section 9.3 and check

⁶ $\Gamma = M/8\pi$ corresponds to a mediator that can annihilate into only one quark flavor and helicity and has couplings $g_\chi g_q = 1$. Since in figure 9.7, we have assumed couplings to all quark helicities and flavors (collider production is dominated by coupling to up-quarks though), and since $g_\chi g_q > 1$ in parts of the plot (see dashed contours), $\Gamma = M/8\pi$ can be regarded as an approximate lower limit on the mediator width.

that they are consistent with the effective theory in which they were derived. In other words, we have to verify that models which saturates our limits can still be described in effective field theory. Inspecting the dashed contours of constant mean coupling $\sqrt{g_q g_\chi}$ in figure 9.7, we see that for mediator masses above ~ 5 TeV, where the limits derived in the full renormalizable theory asymptote to those derived in the effective theory, our limits would correspond to $\sqrt{g_q g_\chi} \sim 5\text{--}10$, depending on m_χ . This is still below the $\sqrt{g_q g_\chi} = 4\pi$, which for small m_χ would be reached at $M \sim 10$ TeV. We thus see that there is considerable parameter space available in the renormalizable model in which effective theory provides a good low-energy approximation. Moreover, we have seen that even for lighter mediators, $M \sim \text{few} \times 100$ GeV, the limits derived from the effective theory are valid, though overly conservative. However, for very light mediators, $M \lesssim 100$ GeV, the collider bounds on direct detection cross sections are considerably weakened.

Even though we have only quantitatively demonstrated the above conclusions for dark matter with vector couplings here, the results of references [67, 206] show that they can be generalized to other types of effective operators, in particular axial vector \mathcal{O}_A and scalar t -channel \mathcal{O}_t . For the gluon operator \mathcal{O}_g , we remark that its most natural UV-completion is through a diagram in which the two gluons as well as a new scalar s -channel mediator couple to a triangular heavy quark loop. Due to the additional loop factor which need not be present in UV completions of \mathcal{O}_V and \mathcal{O}_A , the masses of the new heavy scalar and the new heavy quark propagating in the loop cannot be larger than ~ 1 TeV for a theory that saturates our limit $\Lambda \sim 500$ GeV (see figure 9.4). Therefore, as one can see from figure 9.7, effective field theory is not strictly applicable in such a model, but the limit it gives is on the conservative side.

Let us finally comment on the case of scalar dark matter–quark couplings of the form

$$\mathcal{O}_S \equiv \frac{(\overline{\chi}_L \chi_R)(\overline{q}_L q_R)}{\Lambda^2} + (L \leftrightarrow R) , \quad (9.4.14)$$

which we have not considered so far in this paper. As any UV completion of that operator has to preserve $SU(2)$ invariance, it is necessary that one of the chirality eigenstates χ is an $SU(2)$ doublet or that the UV completion of \mathcal{O}_S involves coupling to the Higgs field H . The first possibility is strongly constrained because dark matter charged under $SU(2)$ would have been detected already in direct detection experiments, unless it is very light, $m_\chi \lesssim \text{few GeV}$. The second possibility, a Higgs insertion, implies that \mathcal{O}_S should be rewritten as

$$\mathcal{O}'_S \equiv \frac{y_q(\overline{\chi}_L \chi_R)(\overline{q}_L \langle H \rangle q_R)}{\Lambda'^3} + (L \leftrightarrow R) , \quad (9.4.15)$$

where y_q is the Standard Model Yukawa coupling of q and Λ' is the cutoff scale of the effective theory (the scale Λ from equation (9.4.14) has no physical meaning in the case of a Higgs insertion). The simplest possibility to realize \mathcal{O}'_S at the renormalizable level is through mixing of the Higgs with a new scalar singlet, which in turn couples to dark matter. In this case, both dark matter production at the LHC and dark matter–nucleus scattering in direct detection experiments are dominated by sea quark contributions, due to Yukawa suppression. We have checked that, in this case, the limit the LHC could set on Λ' is below 100 GeV and thus clearly outside the regime of validity of effective field theory. We will therefore not consider operators of the form \mathcal{O}_S or \mathcal{O}'_S any further in this paper.

To conclude this section, let us emphasize that here we have only considered one possible UV completion of the effective operators introduced in section 9.2. While this helps outline some of the main effects of finite mediator masses, the exact details of these effects will be model-dependent.

9.5 Mono-photons at the LHC

While mono-jets are certainly an excellent search channel for dark matter, it is important to investigate other complementary channels with different systematic uncertainties. An interesting final state to consider is the mono-photon channel, which we will study in this section. A search in an independent channel can help determine if any excess seen in $j + \cancel{E}_T$ is due to new physics or due to mismodelling of backgrounds. Also, there are many types of new physics besides dark matter that can lead to mono-jet signatures, for instance large extra dimensions [47] and unparticles [217], so that searches in additional channels will be necessary to narrow down the origin of any observed signal. In addition, information from several channels may shed light on the nature of the DM–SM coupling. For example, the relative size of an excess in mono-photons compared to one in mono-jets is sensitive to whether the operator dominating the signal involves up or down quarks, due to their different electric charges. A gluon operator like \mathcal{O}_g from equation (9.2.4) is not expected to produce a significant mono-photon signal at all.

Studies of the mono-photon final state have been carried out by CDF [5] and DØ [8], but here we follow the recent CMS analysis, based on 1.14 fb^{-1} of luminosity [136]. Single photons can be produced in association with a dark matter pair through diagrams similar to figure 9.1, but with the outgoing gluon replaced by a photon. Thus, the cross section for mono-photon production is suppressed compared to mono-jet production by the ratio of the strong and electromagnetic fine structure constants as well as a color factor. On the other hand, the background is similarly smaller. Systematic uncertainties on the background prediction are similar, of order 10–15%, for the ATLAS `veryHighPT` mono-jet search and for the CMS mono-photon search [136]. The acceptance for mono-photons is somewhat lower than that for mono-jets because of the requirement that they fall in the

barrel part of the electromagnetic calorimeter.

In our simulations, we follow [136] and require the photon to have transverse momentum $p_T(\gamma) > 95$ GeV and pseudo-rapidity $|\eta| < 1.44$. The missing energy in the event must satisfy $\cancel{E}_T > 80$ GeV and the event is vetoed if there is a jet with $p_T(j) > 20$ GeV within $|\eta(j)| < 3$ or a lepton with $p_T(\ell) > 10$ GeV and $\Delta R(\ell, \gamma) > 0.04$. CMS applies several additional photon identification and isolation criteria which we do not attempt to mock up. Instead, we use PGS as a detector simulation and apply a correction factor of 0.71 to account for these isolation requirements. The correction factor is obtained by comparing our prediction for the dominant irreducible background $(Z \rightarrow \nu\nu) + \gamma$ to the collaboration's. We have also checked that the shape we predict for $(Z \rightarrow \nu\nu) + \gamma$ is in excellent agreement with their prediction, which provides a useful verification of our simulations. Apart from $(Z \rightarrow \nu\nu) + \gamma$, the backgrounds in the $\gamma + \cancel{E}_T$ channel are $(Z \rightarrow \nu\nu) + j$, with the jet mistaken for a photon, $W \rightarrow e\nu$, with the electron mistaken for a photon, bremsstrahlung from cosmic ray or beam halo muons and $(W \rightarrow \ell^{\text{inv}}\nu) + \gamma$, with an unidentified charged lepton ℓ . The expected number of events in the mono-photon sample, according to CMS, is 67.3 ± 8.4 (with the uncertainty dominated by statistics) and the number of observed events was 80.

To set limits on dark matter, we add our signal prediction to the number of predicted background events from [136] and compare the result to the CMS data following the same statistical procedure as in section 9.3. The resulting limits on the cutoff scale Λ for vector operators involving up and down quarks are shown in figure 9.8. The current mono-photon bounds still trail behind mono-jet limits. However, the mono-photon limits may improve more rapidly than those from mono-jets because the former are still statistics dominated as opposed to the latter which are already dominated by systematic uncertainties. Furthermore, as we saw in the previous section, applying harder p_T cuts may

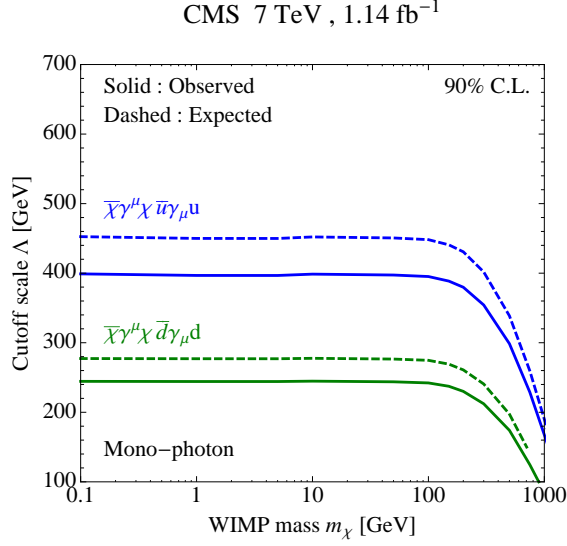


Figure 9.8: Limits from the CMS mono-photon analysis on the suppression scale Λ for the vector operator, \mathcal{O}_V , where only the coupling to one quark flavor at a time is considered. The expected bound is shown with a dashed line and the observed one with a solid line.

yield stronger bounds. The resulting limit on the direct detection cross section is shown in figure 9.9.

9.6 Dark Matter Coupling through Higgs Exchange

One of the most motivated scenarios for dark matter is the case where dark matter interacts through the exchange of a Higgs boson [117]. In this section we will consider this possibility. For concreteness we will assume a specific model, the Standard Model plus a dark matter particle that couples via the Higgs “portal”. We will place limits on the direct detection signal in this model at the LHC in two ways. First, using potential future limits on the invisible branching fraction of the Higgs, we place an future upper bound on the direct detection signal. Then we will use current Higgs limits and assume that the decay of a Higgs to dark matter is responsible for the Higgs non-discovery. This will lead to

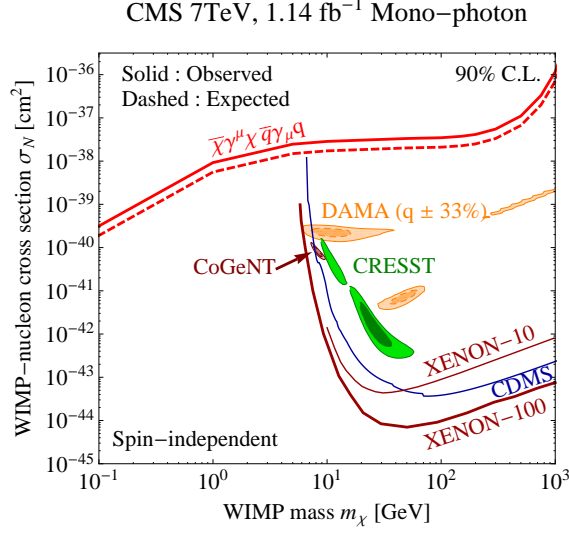


Figure 9.9: Limits from the CMS mono-photon analysis on spin-independent dark matter–nucleon scattering, compared to limits from direct detection experiments. In particular, we show constraints on spin-independent scattering from CDMS [30], XENON-10 [39], XENON-100 [44], DAMA [86], CoGeNT [4, 208] and CRESST [40]. DAMA and CoGeNT allowed regions are based on our own fits [279, 206, 208] to the experimental data. Following [247], we have conservatively assumed large systematic uncertainties on the DAMA quenching factors: $q_{\text{Na}} = 0.3 \pm 0.1$ for sodium and $q_{\text{I}} = 0.09 \pm 0.03$ for iodine, which leads to an enlargement of the DAMA allowed region. All limits are shown at 90% confidence level, whereas for DAMA and CoGeNT we show 90% and 3σ contours. For CRESST, the contours are 1σ and 2σ as in [40].

interesting *lower bounds* on dark matter–nucleon scattering rates.

9.6.1 The Invisible Higgs Analysis as a Dark Matter Search

One way to search for dark matter coupled through the Higgs is to follow the strategy of the previous sections. Namely, integrating out the Higgs induces a scalar operator $\sim (\bar{\chi}\chi)(\bar{q}q)$, which is suppressed by the Yukawa couplings, and an operator like \mathcal{O}_g that couples dark matter to gluons after a top quark loop is integrated out. One can then look for a mono-jet (or mono-photon) signal to constrain the magnitude of the operator.

However, for the light generations the Yukawa suppression will make the bound on such operators weaker (at least as compared with operators that are not Yukawa suppressed). Furthermore, a light Standard Model Higgs is a “light mediator” in the sense that its propagator may easily be dominated by the momentum transfer q^2 , rather than the mass m_h^2 , which will lead to another disadvantage of mono-jet searches (see section 9.4).

Here we will pursue a different strategy which will give stronger bounds within a model in which DM couples via a Higgs boson h , particularly when dark matter is so light that the decay $h \rightarrow \bar{\chi}\chi$ is kinematically allowed. Production of a Higgs at the LHC may proceed through the Higgs’ gauge, rather than its Yukawa, couplings. In particular, one can produce a Higgs in association with a Z or a W or through vector boson fusion (VBF). If $m_\chi < m_h/2$, the Higgs may have a sizeable branching fraction into missing energy, leading to invisible Higgs signals such as $Z + \cancel{E}_T$ (from associated production) or forward jets plus \cancel{E}_T (from VBF). For a given Higgs mass, the limits on the invisible branching fraction of the Higgs may be translated into limits on the coupling of the Higgs to dark matter and thus into a limit on the direct detection cross section mediated by a Higgs.⁷

For concreteness we consider a toy model in which a new neutral and stable dark matter fermion, χ , is added to the Standard Model, coupling to the Higgs.⁸ For example, this coupling may be written as $\bar{\chi}\chi H^\dagger H$, which below electroweak symmetry breaking leads to a coupling of the form $y_\chi h \bar{\chi}\chi$. In these expressions H denotes the SM Higgs doublet, h stands for the physical Higgs boson, and y_χ is a dimensionless coupling constant. The

⁷Some related work on the application of the invisible Higgs search to the dark matter interaction has been discussed in [268, 246]. The bounds on the invisible Higgs branching fraction from XENON-100 in the scalar dark matter case are discussed in [295]

⁸One could easily apply our methods also to the case of a minimal model of scalar dark matter [117], giving similar results, or to models with extended Higgs sectors in which Higgs production can be modified.

branching fraction of the Higgs into dark matter pairs is

$$\text{BR}(h \rightarrow \bar{\chi}\chi) = \frac{\Gamma(h \rightarrow \bar{\chi}\chi)}{\Gamma(h \rightarrow \bar{\chi}\chi) + \Gamma(\text{SM})}, \quad \Gamma(h \rightarrow \bar{\chi}\chi) = \frac{y_\chi^2}{8\pi} m_h \left[1 - \left(\frac{2m_\chi}{m_h} \right)^2 \right]^{3/2}, \quad (9.6.16)$$

where $\Gamma(\text{SM})$ is the total width of the Higgs in the Standard Model, which depends on the Higgs mass, and $\Gamma(h \rightarrow \bar{\chi}\chi)$ is the partial width for decays into dark matter. The invisible Higgs search from colliders sets an upper bound on $\text{BR}(h \rightarrow \bar{\chi}\chi)$, which in our model constrains the size of y_χ . We can then translate this bound into a bound on the direct detection cross section using the couplings of the Higgs to the nucleus at low energies. This can proceed in two ways—the Higgs can couple to the strange quark in the nucleus or it can couple to gluons via a heavy quark loop. These couplings are suppressed either by the Yukawa coupling of the strange quark or by a loop factor, which will give the collider limits a relative advantage since those involve order 1 couplings. We use the matrix element for the gluon coupling given in equation (9.3.9) and for the strange quark coupling as discussed in section 9.3.2. The resulting direct detection cross section is

$$\sigma_N = 5 \times 10^{-6} \frac{\mu^2 y_\chi^2}{\pi m_h^4}, \quad (9.6.17)$$

which sets the direct detection bounds once we extract the allowed size of y_χ from the invisible Higgs search.

There are many works discussing the future bounds on invisible Higgs decays [213, 166, 196, 320]. Here we will not conduct a study of our own, but rather take the bounds projected in an ATLAS analysis [320] where the production modes ZH and VBF are considered. The dominant SM backgrounds for these processes are $ZZ \rightarrow \ell\ell\nu\nu$ for the ZH production mode and jets from QCD, W^\pm or Z for the VBF case. The authors of [320] have simulated both signal and background with the full ATLAS detector simulation. The systematic uncertainties from Monte Carlo, experimental systematic uncertainty, and the theoretical knowledge of the production cross-sections are taken into account.

Assuming 30 fb^{-1} of data with 14 TeV center of mass energy, the projected 95% C.L. upper bounds on the invisible branching ratio are [320]

channel	ZH_{inv}	VBF
$m_h = 120 \text{ GeV}$	0.75	0.55
$m_h = 250 \text{ GeV}$	–	0.85

Using these bounds and equation (9.6.16), we can set upper limits on the direct detection cross section. These limits are shown in the left panel of figure 9.10 for various Higgs masses and production channels. These dark matter–nucleon scattering cross section bounds are more stringent than the mono-jet and mono-photon bounds of the previous sections due to the smallness of the Higgs–nucleon coupling. The bounds deteriorate when the dark matter mass approaches the kinematic limit for invisible Higgs decay at $m_\chi = m_h/2$. Comparing the results for different Higgs masses, the bound for a 250 GeV Higgs is weaker than the one for $m_h = 120 \text{ GeV}$ because at 120 GeV, the SM Higgs width $\Gamma(\text{SM})$ is small, allowing the invisible channel to compete even for moderate couplings. At 250 GeV, the SM decay rate is dominated by decays to W and Z bosons, and in order for the Higgs to have a sizeable invisible branching fraction, the coupling to dark matter must be quite large. This effect over-compensates the $1/m_h^4$ suppression in the direct detection cross section which pushes the limits in the opposite direction.

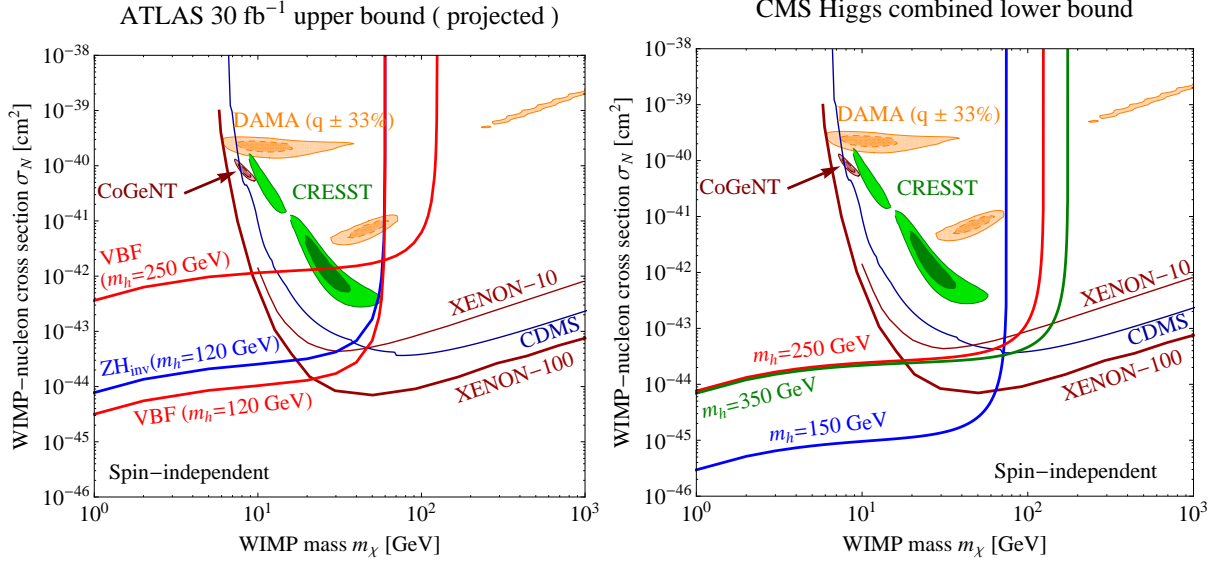


Figure 9.10: Left: Projected 95% C.L. upper bounds on dark matter–nucleon scattering mediated by a Higgs boson from future ATLAS searches for invisible Higgs decays. Limits are shown for the $Z + H$ and vector boson fusion (VBF) production modes, and for Higgs masses of 120 GeV and 250 GeV [320]. Right: *Lower* 95% C.L. bounds on dark matter–nucleon scattering mediated by a Higgs boson, derived from the CMS exclusion of a Standard Model Higgs boson in certain mass ranges [139], assuming that the Higgs was missed at the LHC due to its large invisible width. The direct detection limits we show for comparison are the same as in figures 9.5 and 9.9.

9.6.2 A Lower Bound on Dark Matter–Nucleon Scattering from Current

Higgs Limits

In the previous subsection we discussed the future reach of the LHC in discovering dark matter “directly” through invisible Higgs decay. But if dark matter indeed couples to the Standard Model through Higgs exchange, there is always an interesting connection between the Higgs search and the search for dark matter. This is true both for bounds on the Higgs, as well as for a potential Higgs discovery.

For example, the recent LHC exclusions [139, 58] of a SM Higgs between ~ 140 GeV and ~ 400 GeV have an amusing interpretation as a possible *lower* bound on the dark

matter scattering rate expected at direct detection experiments. In particular, if the Higgs has a sizeable branching fraction into dark matter, this leads to a suppression of the decay channels used in the SM Higgs searches. Thus, a Higgs mass that is inconsistent with data for SM branching ratios may be allowed if the invisible width is large enough to sufficiently suppress the SM search modes, dominantly $h \rightarrow W^+W^-$ or $h \rightarrow ZZ$ in the Higgs mass range of interest.

For concreteness we consider the combined Higgs bound from CMS [139], but results would be similar for the ATLAS bound [58]. Over the mass range $140 \text{ GeV} \lesssim m_h \lesssim 400 \text{ GeV}$ the bound on $\xi = (\sigma \times \text{BR})/(\sigma \times \text{BR})|_{SM}$ varies from ~ 0.3 – 1 , here BR is the branching ratio into the relevant search mode, in this mass range either $h \rightarrow W^+W^-$ or $h \rightarrow ZZ$. Using (9.6.16) this can be translated into a lower bound on y_χ under the assumption that the Higgs is produced with SM cross section, and one decay mode dominates the bound, but Higgs decays into SM channels are suppressed by a large invisible width (and by nothing else),

$$y_\chi^2 \geq 8\pi \frac{\Gamma_{\text{tot}}^{\text{SM}}}{m_h} \frac{1-\xi}{\xi} \left(1 - \frac{4m_\chi^2}{m_h^2}\right)^{-3/2}. \quad (9.6.18)$$

This lower bound on the Higgs–DM coupling allows us to place a *lower* bound on dark matter–nucleon scattering due to Higgs exchange, for a light Higgs that was missed at the LHC due to a large invisible width. This is shown for several candidate Higgs masses in figure 9.10. It is interesting to note that in some cases shown (e.g. Higgs masses of 250 and 350 GeV) this lower bound is already in conflict with direct detection limit for a wide range of dark matter masses. This implies that such minimal models of Higgs-coupled dark matter are already being probed by the combination of the LHC and direct detection. To evade these limits non-minimal models must be considered, either modifying Higgs production rates or modifying Higgs decay beyond the dark matter channel. It will be interesting to follow upcoming limits on the Standard Model Higgs which will cause these

lower bounds to rise and possibly come in to conflict either with dark matter searches, or with invisible Higgs searches.

Finally, we note that even if a Standard Model-like Higgs is discovered at the LHC, interesting bounds on direct detection may be extracted. The strength of these bounds as well as their nature, upper or lower, depend on the details of the discovery. For example, assume a Standard Model-like Higgs is discovered at 120 GeV, say in the $\gamma\gamma$ decay mode. If the Higgs production rate times branching fraction agrees with the Standard Model prediction, very little room will be left for decay of the Higgs into light dark matter. Because the decay channel that is competing with dark matter for this Higgs mass, $h \rightarrow b\bar{b}$, has very small branching ratio, this will set a strong upper bound on the coupling of the Higgs to χ (of order the bottom Yukawa coupling), and thus on direct or indirect detection.

On the other hand, if the Higgs is discovered with a rate that is below the Standard Model prediction, one can postulate that the decay into dark matter is responsible for the reduced rate. Within this assumption, both an upper and a lower limit on dark matter couplings may be derived. In this case the invisible Higgs search can confirm these assumption and provide a potential dark matter discovery.

9.7 Conclusions

Missing energy signatures have long been known to be among the most promising discovery channels at the LHC. They can provide sensitivity to dark matter, one of the few extensions of the Standard Model which are known to exist, even though the exact nature of dark matter, its mass(es) and coupling constants, are so far completely unknown.

In this paper, we have used new data on mono-jet ($j + \cancel{E}_T$) and mono-photon ($\gamma + \cancel{E}_T$) final states to constrain a large class of dark matter models, namely those in which dark matter–quark or dark matter–gluon interactions exist and can be described in the framework of effective field theory. (We have discussed the validity of effective field theory, and the modifications to our limits in cases where it is not valid, in sections 9.4 and 9.6, see figures 9.7 and 9.10.)

Since events in which dark matter is produced have a harder \cancel{E}_T spectrum than Standard Model background processes, it is advantageous to use rather hard cuts on the jet or photon transverse momentum and on the missing energy. We have confirmed this expectation by comparing the sensitivity of mono-jet samples with different cuts (figure 9.3) finding a clear advantage for the so called `veryHighPT` analysis. Using this ATLAS mono-jet analysis we set strong limits on a variety of different types of dark matter couplings (figure 9.4), in particular vector, axial vector, t -channel mediated scalar interaction with quarks and interactions with gluons.

These limits can be converted into constraints on the dark matter–nucleon scattering cross section measured in direct detection experiments (figure 9.5) and the dark matter annihilation cross section (figure 9.6). For small dark matter mass, $m_\chi \lesssim 5$ GeV, the LHC provides the strongest constraints for all considered operators. At higher masses, direct detection experiments still have an advantage if dark matter–nucleon scattering is spin-independent. If dark matter couples primarily to gluons (for instance through a heavy quark loop), the advantage is only marginal up to $m_\chi \sim 1$ TeV, where LHC constraints deteriorate rapidly due to the limited center of mass energy. For spin-dependent dark matter–nucleon scattering, the LHC constraints surpass direct detection bounds by several orders of magnitude for dark matter masses below the kinematic limit of the LHC. It should be noted that the collider constraints do not suffer from any astrophysical un-

certainties, such as the (unknown) abundance of DM in the Earth’s vicinity, or its velocity distribution. Finally, we emphasize that if the DM–Standard Model coupling involves a light mediator, as discussed in section 9.4, the collider bounds may become considerably weakened. If a direct detection experiment, spin-independent or spin-dependent, were to see an excess in apparent contradiction with these collider bounds, their existence would allow us to infer the presence of a light mediator—a fact we would be unaware of without these collider constraints.

As far as limits on dark matter annihilation are concerned, the LHC is able to rule out dark matter with thermal relic cross sections for $m_\chi \lesssim 15$ GeV for vector couplings to quarks, and for $m_\chi \lesssim 70$ GeV for axial vector couplings to quarks. Limits from the mono-photon channel (figures 9.8 and 9.9) are somewhat weaker than those from the mono-jet channel (figures 9.4 and 9.5), but not by much. Furthermore, since they probe a different set of operators and suffer from different systematic uncertainties they provide a useful complementary search channel giving insight into the couplings of DM should an excess be found in either channel.

In the final section of this paper, we have considered a more specific type of dark matter, interacting through a “light mediator”, namely the Standard Model Higgs boson h . If the decay channel $h \rightarrow \bar{\chi}\chi$ is kinematically allowed, we have found that the most stringent constraints on dark matter interactions can be derived from searches for invisible Higgs decays in the $Z + H$ and vector boson fusion (VBF) production channels. Amusingly, for certain Higgs mass ranges, it is possible in this framework to also set *lower* limits on dark matter–Standard Model interactions. In particular, if the Higgs boson has a mass that is already excluded within the Standard Model, the model can be reconciled with the data if the Higgs branching fraction into dark matter is sufficiently large, which limits the dark matter–Higgs couplings from *below*. This lower bound on direct detection is already

in conflict with bounds from XENON-100 for some regions of parameter space. Within the Higgs-coupled DM framework, there is an interesting interplay between dark matter searches and SM Higgs boson searches at the LHC. This interplay can be interesting and non-trivial, both in the case of new bounds on the Higgs and in the case of a SM Higgs discovery.

The analyses in this paper were carried out for the 7 TeV LHC on an integrated luminosity of at most 1.14 fb^{-1} , a tiny fraction of what we hope to accumulate in the coming years. The increased statistics, and higher center of mass energy, will improve not only the ability to harden the cuts, making the analyses more sensitive to DM, but also bring the systematic uncertainties under greater control. With dedicated analyses from both LHC collaborations, as well as searches on the final Tevatron dataset, we can expect great improvements on the bounds, or perhaps even the first observation of production of DM in the lab.

APPENDIX A

DETAILS FOR $\mu \rightarrow E\gamma$ CALCULATION

A.1 Matching 5D amplitudes to 4D EFTs

The standard procedure for comparing the loop-level effects of new physics on low-energy observables is to work with a low-energy effective field theory in which the UV physics contributes to the Wilson coefficient of an appropriate local effective operator by matching the amplitudes of full and effective theories. In this appendix we briefly remark on the matching of 5D mixed position/momentum space amplitudes to 4D effective field theories, where some subtleties arise from notions of locality in the extra dimension.

The only requirement on the 5D amplitudes that must match to the 4D effective operator is that they are local in the four Minkowski directions. There is no requirement that the operators should be local in the fifth dimension since this dimension is integrated over to obtain the 4D operator. Thus the 5D amplitude should be calculated with independent external field positions in the extra dimension. Heuristically, one can write this amplitude as a *nonlocal* 5D operator

$$\mathcal{O}_5(x, z_H, z_L, z_E, z_A) = H_5(x, z_H) \cdot \bar{L}_5(x, z_L) \sigma^{MN} E_5(x, z_E) F_{MN}(x, z_A). \quad (\text{A.1.1})$$

Note that this object has mass dimension 8. In the 5D amplitude the fields are replaced by external state wavefunctions and this is multiplied by a “nonlocal coefficient” $c_5(z_H, z_L, z_E, z_A)$ which includes integrals over internal vertices and loop momenta as well as the mixed position/momentum space propagators to the external legs. To match with the low-energy 4D operator we impose that the external states are zero modes and decompose them into 4D zero-mode fields multiplied by a 5D profile $f(z)$ of mass dimension 1/2,

$$\Phi_5(x, z) \rightarrow \Phi^{(0)}(x) f^{(0)}(z). \quad (\text{A.1.2})$$

Further, we must integrate over each external field’s z -position. Thus the 4D Wilson coef-

ficient and operator are given by

$$c_4 \mathcal{O}_4(x) = \int \left[\prod_i dz_i \right] c_5(z_H, z_E, z_L, z_A) f_H^{(0)}(z_H) f_E^{(0)}(z_E) f_L^{(0)}(z_L) f_A^{(0)}(z_A) H \cdot \bar{L} \sigma^{\mu\nu} E_{\mu\nu} \quad (\text{A.1.3})$$

where the fields on the right-hand side are all zero modes evaluated at the local 4D point x . Note that these indeed have the correct 4D mass dimensions, $[\mathcal{O}_4] = 6$ and $[c] = -2$.

Finally, let us remark that we have treated the 5D profiles completely generally. In particular, there are no ambiguities associated with whether the Higgs field propagates in the bulk or is confined to the brane. One can take the Higgs profile to be brane-localized,

$$f_H(z_H) \sim \sqrt{R'} \delta(z - R'), \quad (\text{A.1.4})$$

where the prefactor is required by the dimension of the profiles. With such a profile (or any limiting form thereof) the passage from 5D to 4D according to the procedure above gives the correct matching for brane-localized fields.

A.2 Estimating the size of each diagram

As depicted in Figs. 2.2–2.4, there are a large number of diagrams contributing to the a and b coefficients even when only considering the leading terms in a mass-insertion expansion. Fortunately, many of these diagrams are naturally suppressed and the dominant contribution to each coefficient is given by the two diagrams shown in Fig. 2.5. This can be verified explicitly by using the analytic expressions for the leading and next-to-leading diagrams are given in Appendix A.3. In this appendix we provide some heuristic guidelines for estimating the relative sizes of these diagrams.

A.2.1 Relative sizes of couplings

First note that after factoring out terms in the effective operator in (2.4.28), Yukawa couplings give order one contributions while gauge couplings give an enhancement of $g_{\text{SM}}^2 \ln R'/R$, where g_{SM} is the appropriate Standard Model coupling. This gives a factor of ~ 5 (7) enhancement in diagrams with a W over those with a Z (H).

A.2.2 Suppression mechanisms in diagrams

Next one can count estimate suppressions to each diagram coming from the following factors

- A. **Mass insertion**, $\sim 10^{-1}$ /insertion. Each fermion mass insertion on an internal line introduces a factor of $\mathcal{O}(vR')$. This comes from the combination of dimensionful factors in the Yukawa interaction and the additional fermion propagator.
- B₁. **Equation of motion**, $\sim 10^{-4}$. Higgs diagrams without an explicit chirality-flipping internal mass insertion must swap chirality using the muon equation of motion $\bar{u}(p)\not{p} = m_\mu u(p)$. This gives a factor of $\mathcal{O}(m_\mu R')$ and is equivalent to external mass insertion that picks up the zero-mode mass.
- B₂. **External mass insertion**, $\sim 10^{-1}$. Alternately, when a loop vertex is in the bulk, an external mass insertion can pick up the diagonal piece of the propagator—see (A.7.112)—representing the propagation of a zero mode into a ‘wrong-chirality’ KK mode. Unlike the off-diagonal piece which imposes the equation of motion, this is only suppressed by the $\mathcal{O}(vR')$ mentioned above¹. One can equivalently think of this as an insertion of the KK mass which mixes the physical zero and KK modes.

¹We thank Martin Beneke, Paramita Dey, and Jürgen Rohrwild for pointing this out.

C. **Higgs/Goldstone cancellation**, $\sim 10^{-3}$. The H^0 and G^0 one-mass-insertion loops cancel up to $\mathcal{O}((m_H^2 - m_Z^2)/m_{\text{KK}}^2)$ because the two Goldstone couplings appear with factors of i relative to the neutral Higgs couplings².

D. **Proportional to charged scalar mass**, $\sim 10^{-2}$. The leading loop-momentum term in the one-mass-insertion brane-localized H^\pm loop cancels due to the form of the photon coupling relative to the propagators. The gauge-invariant contribution from such a diagram is proportional to $(M_W R')^2$. This is shown explicitly in (A.2.6) below.

To demonstrate the charged scalar mass proportionality, we note that the amplitude for the one mass insertion charged Higgs diagram in Fig. 2.3 is

$$\mathcal{M}^\mu = -R^2 \left(\frac{R}{R'} \right)^6 \frac{ev}{\sqrt{2}} f_{c_{L\mu}} Y_*^3 f_{-c_{Ee}} \int \frac{d^4 k}{(2\pi)^4} \bar{u}_{p'} \Delta_k^R \Delta_k^L u_p \frac{(2k - p - p')^\mu}{[(k - p')^2 - M_W^2][(k - p)^2 - M_W^2]} \quad (\text{A.2.5})$$

Remembering that the 5D fermion propagators go like $\Delta \sim \not{k}/k$, this amplitude naïvely appears to be logarithmically divergent. However, the Ward identity forces the form of the photon coupling to the charged Higgs to be such that the leading order term in k^2 cancels. This can be made manifest by expanding the charged Higgs terms in p and p' ,

$$\frac{(2k - p - p')^\mu}{[(k - p')^2 - M_W^2][(k - p)^2 - M_W^2]} = \frac{(p + p')^\mu}{(k^2 - M_W^2)^2} \left[\frac{k^2}{k^2 - M_W^2} - 1 \right] = \frac{M_W^2 (p + p')^\mu}{(k^2 - M_W^2)^3}, \quad (\text{A.2.6})$$

where we have dropped terms of order $\mathcal{O}(m_\mu^2/M_W^2)$. Thus see that the coefficient of the gauge-invariant contribution is finite by power counting. After Wick rotation, this amplitude takes the form

$$\mathcal{M}^\mu(1\text{MI}H^\pm)|_{(p+p')} = \frac{2i}{16\pi^2} (R')^2 f_{c_{L\mu}} Y_*^3 f_{-c_{Ee}} \frac{ev}{\sqrt{2}} (R' M_W)^2 I_{1\text{MI}H^\pm} \bar{u}_{p'}(p + p') u_p, \quad (\text{A.2.7})$$

where $I_{1\text{MI}H^\pm}$ is a dimensionless integral given in (A.3). We see that the amplitude indeed carries a factor of $(M_W R')^2$.

²We thank Yuko Hori and Takemichi Okui for pointing this out.

A.2.3 Dimensionless integrals

Estimating the size of dimensionless integrals over the loop momentum and bulk field propagators (such as $I_{1\text{MH}^\pm}$) is more subtle and is best checked through explicit calculation. However, one may develop an intuition for the relative size of these integrals.

Note that the fifth component of a bulk gauge field naturally has boundary conditions opposite that of the four-vector [157] so that the fifth components of Standard Model gauge fields have Dirichlet boundary conditions. This means that diagrams with a $W^5 H^\pm A$ vertex vanish since the brane-localized Higgs and bulk W^5 do not have overlapping profiles. Further, loops with fifth components of Standard Model gauge fields and internal mass insertions tend to be suppressed since the mass insertions attach the loop to the IR brane. In the UV limit the loop shrinks towards the brane and has reduced overlap with the fifth component gauge field.

Otherwise the loop integrals are typically $\mathcal{O}(0.1)$. The particular value depends on the propagators and couplings in the integrand.

A.2.4 Robustness against equationment

As discussed in Section 2.5.2, the flavor structure of the diagrams contributing to the b coefficient is equationed with the fermion zero-mode mass matrix [28, 20, 18]. Contributions to this coefficient vanish in the zero mode mass basis in the absence of additional flavor structure from the bulk mass (c) dependence of the internal fermion propagators. The diagrams which generally give the largest contribution after passing to the zero mode mass basis are those with the strongest dependence on the fermion bulk masses. Since

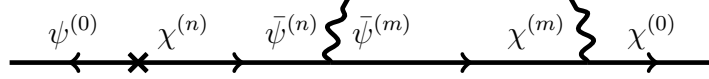


Figure A.1: equationment of the external mass insertion diagrams with Standard Model gauge bosons. χ and ψ are left- and right-chiral Weyl spinors respectively. The gauge boson vertices don't change fermion chirality so that the internal fermion must be a chirality-flipping KK mode. We have neglected the contribution where the external mass insertion connects two zero mode fermions since this is suppressed by $m_\mu R'$.

zero mode fermion profiles are exponentially dependent on the bulk mass parameter, a simple way to identify potential leading diagrams is to identify those which may have zero mode fermions propagating in the loop.

This allows us to neglect diagrams with an external mass insertion and a 4D vector boson in the loop. As shown in Fig. A.1, such diagrams do not permit intermediate zero modes to leading order. Note, however, that diagrams with an external mass insertion and the fifth component of gauge boson are allowed to have zero mode fermions in the loop. Indeed, a diagram with a W^5 and W^μ in the loop would permit zero mode fermions but is numerically small due to the size of the $W^5 A W^\mu$ coupling. The dominant diagrams for the b coefficient are the $H^\pm W^\pm$ loop and the Z loop with an internal mass insertion. In the KK reduction, the misequationment comes from diagrams with zero mode fermions and KK gauge bosons.

A.3 Analytic expressions

We present analytic expressions for the leading and next-to-leading diagrams contributing to $\mu \rightarrow e\gamma$. We label the diagrams in Figs. 2.2–2.4 according to the number of Higgs-induced mass insertions and the internal boson(s). For example, the two-mass-insertion W diagram in Fig. 2.5a is referred to as 2MIW. Estimates for the size of each contribution

are given in Appendix A.2. We shall only write the coefficient of the $\bar{u}_{p'}(p + p')^\mu u_p$ term since this completely determines the gauge-invariant contribution.

A.3.1 Dominant diagrams

As discussed in Section 2.5, the leading diagrams contributing to the a and b coefficients are

$$\mathcal{M}(2\text{MIW}) = \frac{i}{16\pi^2} (R')^2 f_{c_{L\mu}} Y_E Y_N^\dagger Y_N f_{-c_{Ee}} \frac{ev}{\sqrt{2}} \left(\frac{g^2}{2} \ln \frac{R'}{R} \right) \left(\frac{R'v}{\sqrt{2}} \right)^2 I_{2\text{MIW}} \quad (\text{A.3.8})$$

$$\mathcal{M}(0\text{MIHW}) = \frac{i}{16\pi^2} (R')^2 f_{c_L} Y_E f_{-c_E} \frac{ev}{\sqrt{2}} \left(\frac{g^2}{2} \ln \frac{R'}{R} \right) I_{0\text{MIHW}}, \quad (\text{A.3.9})$$

$$\mathcal{M}(1\text{MIZ}) = \frac{i}{16\pi^2} (R')^2 f_{c_L} Y_E f_{-c_E} \frac{ev}{\sqrt{2}} \left(g_{Z_L} g_{Z_R} \ln \frac{R'}{R} \right) I_{1\text{MIZ}}, \quad (\text{A.3.10})$$

We have explicitly labeled the 4D (dimensionless) anarchic Yukawa matrices whose elements assumed to take values of order $(Y_E)_{ij} \sim (Y_N)_{ij} \sim Y_*$, but have independent flavor structure. Note that we have suppressed the flavor indices of the Yukawas and the dimensionless integrals. Diagrams with a neutral boson and a Yukawa structure $Y_E Y_E^\dagger Y_E$ also contribute to the a coefficient, but these contributions are suppressed relative to the dominant charged boson diagrams above. These diagrams may become appreciable if one permits a hierarchy in the relative Y_E and Y_N anarchic scales, in which case one should also consider the Z boson diagrams whose analytic forms are given below. The dimen-

sionless integrals are

$$I_{2\text{MIW}} = -\frac{3}{2} \int dy dx_1 dx_2 dx_3 y^3 \left(\frac{y}{x_1}\right)^{c_L+2} \left(\frac{y}{x_2}\right)^4 \left(\frac{y}{x_3}\right) \tilde{F}_{+,y}^{L1y} \tilde{F}_{-,y}^{Ryy} \tilde{D}_- \tilde{F}_{-,y}^{Ly2} \tilde{F}_{+,y\mu}^{L2y\mu} \frac{\partial}{\partial k_E} (G_y^{13} G_y^{32}) \quad (\text{A.3.11})$$

$$I_{0\text{MIHW}} = \int dy dx \left(\frac{y}{x}\right)^{2+c_L} \left(\frac{1}{2\sqrt{2}} \frac{y^2}{y^2 + m_H^2 R'^2} \tilde{F}_{+,y}^{L1y} y \partial_{k_E} G_y^{xy}\right) \quad (\text{A.3.12})$$

$$I_{1\text{MIZ}} = - \int dy dx_1 dx_2 dx_3 \left(\frac{y}{x_1}\right)^{2+c_L} \left(\frac{y}{x_2}\right)^{2-c_E} \left(\frac{y}{x_3}\right)^4 (y \partial_{k_E} G^{12}) y^2 \times \\ \left(- \tilde{D}_+ \tilde{F}_{+,y}^{R23} \tilde{D}_- \tilde{F}_{-,y}^{R3y} \tilde{F}_{+,y}^{Ly1} + \tilde{F}_{-,y}^{R2x3} \tilde{F}_{-,y}^{R3y} \tilde{F}_{+,y}^{Ly1} \right. \\ \left. - \tilde{F}_{-,y}^{R2y} \tilde{D}_- \tilde{F}_{-,y}^{Ly3} \tilde{D}_+ \tilde{F}_{+,y}^{L31} + \tilde{F}_{-,y}^{R2y} \tilde{F}_{+,y}^{Ly3} \tilde{F}_{+,y}^{L31} \right). \quad (\text{A.3.13})$$

where $x = k_E z$, $y = k_E R'$, and $y_\mu = m_\mu R'$. The significance of these dimensionless variables is discussed below (2.6.52). The dimensionless Euclidean-space propagator functions \tilde{F} are defined in (B.1.2 – B.1.3), where the upper indices of the F functions define the propagation positions. For example, F^{R3y} represents a propagator from $z = R'$ to $z = z_3$. Similarly, G_y and \bar{G}_y are defined in (B.1.7) and (B.1.8).

A.3.2 Subdominant a coefficient diagrams

The diagrams containing a brane-localized Higgs loop are

$$\mathcal{M}(n\text{MIH}^\pm) = \frac{i}{16\pi^2} (R')^2 f_{c_L} Y_E Y_N^\dagger Y_N f_{-c_E} \frac{ev}{\sqrt{2}} I_{n\text{MIH}^\pm}, \quad (\text{A.3.14})$$

$$\mathcal{M}(n\text{MIH}^0) = \frac{i}{16\pi^2} (R')^2 f_{c_L} Y_E Y_E Y_E^\dagger f_{-c_E} \frac{ev}{\sqrt{2}} I_{0\text{MIH}^0}. \quad (\text{A.3.15})$$

Here $n = 0, 1$ counts the number of internal mass insertions in the diagram. The gauge boson loops are

$$\mathcal{M}(n\text{MIZ}^{(5)}) = \frac{i}{16\pi^2} (R')^2 f_{c_L} Y_E Y_E^\dagger Y_E f_{-c_E} \frac{ev}{\sqrt{2}} \left(g_{Z_L} g_{Z_R} \ln \frac{R'}{R} \right) \left(\frac{v}{\sqrt{2}} R' \right)^2 I_{n\text{MIZ}^{(5)}}, \quad (\text{A.3.16})$$

$$\mathcal{M}(2\text{MI}ww) = \frac{i}{16\pi^2} (R')^2 f_{c_L} Y_E Y_N^\dagger Y_N f_{-c_E} \frac{ev}{\sqrt{2}} \left(\frac{g^2}{2} \ln \frac{R'}{R} \right) \left(\frac{v}{\sqrt{2}} R' \right)^2 \times I_{2\text{MI}ww}. \quad (\text{A.3.17})$$

Where $n = 2, (1 + 2), 3$ with $(1 + 2)$ referring to a single internal mass insertion and two external mass insertions. $2\text{MI}ww$ represents $2\text{MI}W^5W^5$, $2\text{MI}WW^5$ and $2\text{MI}W^5W$. The

dimensionless integrals are

$$\begin{aligned}
I_{1\text{MIH}^0} = & \int dy dx y^2 \left(\frac{y}{x}\right)^4 \left[-2\tilde{F}_{+,y}^{Lyx} \tilde{F}_{+,y}^{Lxy} \tilde{F}_{-,y}^{Ryy} \frac{y^2}{y^2 + (M_H R')^2} \right. \\
& + \tilde{F}_{+,y}^{Lyx} \tilde{F}_{+,y}^{Lxy} \tilde{F}_{-,y}^{Ryy} \frac{y^4}{(y^2 + (m_H R')^2)^2} \\
& - \frac{1}{2} \left(y \partial_{k_E} \tilde{F}_{+,y}^{Lyx} \right) \tilde{F}_{+,y}^{Lxy} \tilde{F}_{-,y}^{Ryy} \frac{y^2}{y^2 + (M_H R')^2} \\
& - \frac{1}{2} \left(y \partial_{k_E} \tilde{D}_- \tilde{F}_{-,y}^{Lyx} \right) \tilde{D}_+ \tilde{F}_{+,y}^{Lxy} \tilde{F}_{-,y}^{Ryy} \frac{1}{y^2 + (M_H R')^2} \\
& + 2\tilde{F}_{+,y}^{Lyy} \tilde{D}_+ \tilde{F}_{+,y}^{Ryx} \tilde{D}_- \tilde{F}_{-,y}^{Rxy} \frac{1}{y^2 + (M_H R')^2} \\
& - \tilde{F}_{+,y}^{Lyy} \tilde{D}_+ \tilde{F}_{+,y}^{Ryx} \tilde{D}_- \tilde{F}_{-,y}^{Rxy} \frac{y^2}{(y^2 + (M_H R')^2)^2} \\
& + \frac{1}{2} \left(y \partial_{k_E} \tilde{F}_{+,y}^{Lyy} \right) \tilde{D}_+ \tilde{F}_{+,y}^{Ryx} \tilde{D}_- \tilde{F}_{-,y}^{Rxy} \frac{1}{y^2 + (M_H R')^2} \\
& + \tilde{F}_{+,y}^{Lyy} \tilde{F}_{-,y}^{Ryx} \tilde{F}_{-,y}^{Rxy} \frac{y^2}{y^2 + (M_H R')^2} \\
& + \frac{1}{2} \left(y \partial_{k_E} \tilde{F}_{+,y}^{Lyy} \right) \tilde{F}_{-,y}^{Ryx} \tilde{F}_{-,y}^{Rxy} \frac{y^2}{y^2 + (M_H R')^2} \\
& + \frac{1}{2} \tilde{F}_{+,y}^{Lyy} \left(y \partial_{k_E} \tilde{F}_{-,y}^{Ryy} \right) \tilde{F}_{-,y}^{Rxy} \frac{y^2}{y^2 + (M_H R')^2} \\
& \left. + \frac{1}{2} \tilde{F}_{+,y}^{Lyy} \left(y \partial_{k_E} \tilde{D}_+ \tilde{F}_{+,y}^{Ryx} \right) \tilde{D}_- \tilde{F}_{-,y}^{Rxy} \frac{1}{y^2 + (M_H R')^2} \right], \tag{A.3.18}
\end{aligned}$$

$$I_{1\text{MIH}^\pm} = \int dy \tilde{F}_{+,y}^{Lyy} \tilde{F}_{+,y}^{Ryy} \frac{2y^5}{(y^2 + (M_W R')^2)^3} \tag{A.3.19}$$

$$I_{0\text{MIH}^\pm} = \int dy \tilde{F}_{-,y}^{Ryy} \frac{y^5}{(y^2 + (M_H R')^2)^3} \tag{A.3.20}$$

$$I_{0\text{MIH}^0} = \int dy dx y^2 \left(\frac{y}{x}\right)^4 \tilde{F}_{+,y}^{Lyx} \tilde{F}_{+,y}^{Lxy} \frac{y^2}{(y^2 + (M_H R')^2)^2} \tag{A.3.21}$$

$$\begin{aligned}
I_{2\text{MIZ}} = & \int dy dx_1 dx_2 dx_3 \left(\frac{y}{x_1}\right)^{2+c_L} \left(\frac{y}{x_2}\right)^4 \left(\frac{y}{x_3}\right)^4 \times \\
& \left\{ y \partial_{k_E} G_y^{13} \tilde{D}_+ \tilde{F}_{+,y\mu}^{L3y\mu} \left[y^2 \left(\tilde{F}_{+,y}^{L12} \tilde{F}_{+,y}^{L2y} \tilde{F}_{-,y}^{Ryy} \tilde{D}_- \tilde{F}_{-,y}^{Ly3} \right. \right. \right. \\
& + \tilde{F}_{+,y}^{L1y} \tilde{F}_{-,y}^{Ry2} \tilde{F}_{-,y}^{R2y} \tilde{D}_- \tilde{F}_{-,y}^{Ly3} + \tilde{F}_{+,y}^{L1y} \tilde{F}_{-,y}^{Ryy} \tilde{D}_- \tilde{F}_{-,y}^{R2y} \tilde{F}_{-,y}^{L23} \\
& + \tilde{F}_{+,y}^{L1y} \tilde{F}_{-,y}^{Ryy} \tilde{F}_{+,y}^{Ly2} \tilde{D}_- \tilde{F}_{-,y}^{L23} \left. \right) - \left(\tilde{D}_- \tilde{F}_{-,y}^{L12} \tilde{D}_+ \tilde{F}_{+,y}^{L2y} \tilde{F}_{-,y}^{Ryy} \tilde{D}_- \tilde{F}_{-,y}^{Ly3} \right. \\
& \left. \left. + \tilde{F}_{+,y}^{L1y} \tilde{D}_+ \tilde{F}_{+,y}^{Ry2} \tilde{D}_- \tilde{F}_{-,y}^{R2y} \tilde{D}_+ \tilde{F}_{+,y}^{Ly3} \right) \right] \left. \right\}, \tag{A.3.22}
\end{aligned}$$

$$I_{2\text{MIZ}^5} = - \int dy dx_1 dx_2 dx_3 \left(\frac{y}{x_1} \right)^{2+c_L} \left(\frac{y}{x_2} \right)^4 \left(\frac{y}{x_3} \right)^4 \\ \times \frac{1}{2} \left[y \partial_{k_E} \bar{G}_y^{13} \tilde{D}_+ \tilde{F}_{+,y\mu}^{L3y\mu} \left(y^2 \tilde{F}_{-,y}^{L12} \tilde{D}_+ \tilde{F}_{+,y}^{L2y} \tilde{F}_{+,y}^{Ryy} \right) \right], \quad (\text{A.3.23})$$

$$I_{(1+2)\text{MIZ}} = - \int dy dx_1 dx_2 dx_3 \left(\frac{y}{x_1} \right)^4 \left(\frac{y}{x_2} \right)^4 \left(\frac{y}{x_3} \right)^4 \\ \times \left[\tilde{D}_+ \tilde{F}_{+,ye}^{Rye1} \tilde{D}_+ \tilde{F}_{+,y\mu}^{L2y\mu} G_y^{21} - (4 + y \partial_{k_E}) \left(\tilde{D}_- \tilde{F}_{-,y}^{R1y} \tilde{F}_{-,y}^{R3y} \tilde{D}_- \tilde{F}_{-,y}^{L32} \right. \right. \\ \left. \left. + \tilde{F}_{+,y}^{R13} \tilde{D}_- \tilde{F}_{-,y}^{R3y} \tilde{D}_- \tilde{F}_{-,y}^{L32} + \tilde{D}_- \tilde{F}_{-,y}^{R1y} \tilde{D}_- \tilde{F}_{-,y}^{Ly3} \tilde{F}_{-,y}^{L32} \right. \right. \\ \left. \left. + \tilde{D}_- \tilde{F}_{-,y}^{R1y} \tilde{F}_{+,y}^{Ly3} \tilde{D}_- \tilde{F}_{-,y}^{L32} \right) \right], \quad (\text{A.3.24})$$

$$I_{(1+2)\text{MIZ}^5} = - \int dy dx_1 dx_2 dx_3 \left(\frac{y}{x_1} \right)^4 \left(\frac{y}{x_2} \right)^4 \left(\frac{y}{x_3} \right)^4 \tilde{D}_+ \tilde{F}_{+,ye}^{Rye1} \tilde{D}_+ \tilde{F}_{+,y\mu}^{L3y\mu} \bar{G}_y^{13} \\ \times \frac{1}{2} \left[\tilde{F}_{-,y}^{R12} y \partial_{k_E} \left(\tilde{F}_{-,y}^{R2y} \tilde{F}_{+,y}^{Ly3} \right) + y \partial_{k_E} \left(\tilde{D}_+ \tilde{F}_{+,y}^{R12} \right) \tilde{D}_- \tilde{F}_{-,y}^{R2y} \tilde{F}_{+,y}^{Ly3} \right. \\ \left. + \tilde{F}_{-,y}^{R1y} \tilde{D}_- \tilde{F}_{-,y}^{Ly2} y \partial_{k_E} \left(\tilde{D}_+ \tilde{F}_{+,y}^{L23} \right) + y \partial_{k_E} \left(y^2 \tilde{F}_{-,y}^{R1y} \tilde{F}_{+,y}^{Ly2} \right) \tilde{F}_{+,y}^{L23} \right], \quad (\text{A.3.25})$$

The integral for 3MIZ and 3MIZ⁵ can be written as

$$I_{3\text{MIZ}/Z^5} = \frac{1}{2} \int dy dx_1 dx_2 dx_3 \left(\frac{y}{x_1} \right)^{2+c_L} \left(\frac{y}{x_2} \right)^{2-c_E} \left(\frac{y}{x_3} \right)^4 G_y^{13} \sum_{i=1}^8 M_i y \partial_{k_E} N_i. \quad (\text{A.3.26})$$

For 3MIZ, the (M, N) pairs are

$$(M_1, N_1) = \left(\tilde{F}_{+,y}^{L12}, y^4 \tilde{F}_{+,y}^{L2y} \tilde{F}_{-,y}^{Ryy} \tilde{F}_{+,y}^{Ly y} \tilde{F}_{-,y}^{Ry3} \right), \quad (\text{A.3.27})$$

$$(M_2, N_2) = \left(-y^2 \tilde{D}_+ \tilde{F}_{+,y}^{L2y} \tilde{F}_{-,y}^{Ryy} \tilde{F}_{+,y}^{Ly y} \tilde{F}_{-,y}^{Ry3}, \tilde{D}_- \tilde{F}_{-,y}^{L12} \right), \quad (\text{A.3.28})$$

$$(M_3, N_3) = \left(-y^2 \tilde{F}_{-,y}^{R2y} \tilde{F}_{+,y}^{Ly y} \tilde{F}_{-,y}^{Ry3}, -y^2 \tilde{F}_{+,y}^{L1y} \tilde{F}_{-,y}^{Ry2} \right), \quad (\text{A.3.29})$$

$$(M_4, N_4) = \left(\tilde{F}_{+,y}^{L1y} \tilde{D}_+ \tilde{F}_{+,y}^{Ry2}, -y^2 \tilde{D}_- \tilde{F}_{-,y}^{R2y} \tilde{F}_{+,y}^{Ly y} \tilde{F}_{-,y}^{Ry3} \right), \quad (\text{A.3.30})$$

$$(M_5, N_5) = \left(-y^2 \tilde{F}_{+,y}^{L1y} \tilde{F}_{-,y}^{Ryy} \tilde{F}_{+,y}^{Ly2}, -y^2 \tilde{F}_{+,y}^{L2y} \tilde{F}_{-,y}^{Ry3} \right), \quad (\text{A.3.31})$$

$$(M_6, N_6) = \left(\tilde{D}_+ \tilde{F}_{+,y}^{L2y} \tilde{F}_{-,y}^{Ry3}, -y^2 \tilde{F}_{+,y}^{L1y} \tilde{F}_{-,y}^{Ryy} \tilde{D}_- \tilde{F}_{-,y}^{Ly2} \right), \quad (\text{A.3.32})$$

$$(M_7, N_7) = \left(\tilde{F}_{-,y}^{R23}, y^4 \tilde{F}_{+,y}^{L1y} \tilde{F}_{-,y}^{Ryy} \tilde{F}_{+,y}^{Ly y} \tilde{F}_{-,y}^{Ry2} \right), \quad (\text{A.3.33})$$

$$(M_8, N_8) = \left(-y^2 \tilde{F}_{+,y}^{L1y} \tilde{F}_{-,y}^{Ryy} \tilde{F}_{+,y}^{Ly y} \tilde{D}_+ \tilde{F}_{+,y}^{Ry2}, \tilde{D}_- \tilde{F}_{-,y}^{R23} \right). \quad (\text{A.3.34})$$

For 3MIZ⁵, the (M, N) pairs are

$$(M_1, N_1) = (-y^2 \tilde{D}_+ \tilde{F}_{+,y}^{L1y} \tilde{F}_{-,y}^{Ryy} \tilde{F}_{+,y}^{Lyy} \tilde{F}_{-,y}^{Ry2}, \tilde{D}_+ \tilde{F}_{+,y}^{R23}), \quad (\text{A.3.35})$$

$$(M_2, N_2) = (\tilde{F}_{+,y}^{R23}, -y^2 \tilde{D}_+ \tilde{F}_{+,y}^{L1y} \tilde{F}_{-,y}^{Ryy} \tilde{F}_{+,y}^{Lyy} \tilde{D}_+ \tilde{F}_{+,y}^{Ry2}), \quad (\text{A.3.36})$$

$$(M_3, N_3) = (\tilde{D}_+ \tilde{F}_{+,y}^{L1y} \tilde{F}_{-,y}^{Ryy} \tilde{D}_- \tilde{F}_{-,y}^{Ly2}, \tilde{D}_+ \tilde{F}_{+,y}^{L2y} \tilde{D}_+ \tilde{F}_{+,y}^{Ry3}), \quad (\text{A.3.37})$$

$$(M_4, N_4) = (\tilde{F}_{+,y}^{L2y} \tilde{D}_+ \tilde{F}_{+,y}^{Ry3}, -y^2 \tilde{D}_+ \tilde{F}_{+,y}^{L1y} \tilde{F}_{-,y}^{Ryy} \tilde{F}_{+,y}^{Ly2}), \quad (\text{A.3.38})$$

$$(M_5, N_5) = (\tilde{D}_+ \tilde{F}_{+,y}^{L1y} \tilde{F}_{-,y}^{Ry2}, -y^2 \tilde{F}_{-,y}^{R2y} \tilde{F}_{+,y}^{Lyy} \tilde{D}_+ \tilde{F}_{+,y}^{Ry3}), \quad (\text{A.3.39})$$

$$(M_6, N_6) = (\tilde{D}_- \tilde{F}_{-,y}^{R2y} \tilde{F}_{+,y}^{Lyy} \tilde{D}_+ \tilde{F}_{+,y}^{Ry3}, \tilde{D}_+ \tilde{F}_{+,y}^{L1y} \tilde{D}_+ \tilde{F}_{+,y}^{Ry2}), \quad (\text{A.3.40})$$

$$(M_7, N_7) = (\tilde{F}_{-,y}^{L12}, -y^2 \tilde{D}_+ \tilde{F}_{+,y}^{L2y} \tilde{F}_{-,y}^{Ryy} \tilde{F}_{+,y}^{Lyy} \tilde{D}_+ \tilde{F}_{+,y}^{Ry3}), \quad (\text{A.3.41})$$

$$(M_8, N_8) = (-y^2 \tilde{F}_{+,y}^{L2y} \tilde{F}_{-,y}^{Ryy} \tilde{F}_{+,y}^{Lyy} \tilde{D}_+ \tilde{F}_{+,y}^{Ry3}, \tilde{D}_+ \tilde{F}_{+,y}^{L12}). \quad (\text{A.3.42})$$

The integrals for the W^5 loops are

$$\begin{aligned} I_{2\text{MIW}^5\text{W}^5} = & - \int dy dx_1 dx_2 dx_3 \left(\frac{y}{x_1} \right)^{2+c_L} \left(\frac{y}{x_2} \right)^4 \left(\frac{y}{x_3} \right) \\ & \times \left\{ \frac{1}{2} y^2 \tilde{D}_+ \tilde{F}_{+,y}^{L1y} \tilde{F}_{-,y}^{Ryy} \tilde{F}_{+,y}^{Ly2} \tilde{D}_+ \tilde{F}_{+,y\mu}^{L2y\mu} \left[4 \bar{G}_y^{13} \bar{G}_y^{23} + y \partial_{k_E} \left(\bar{G}_y^{13} \bar{G}_y^{23} \right) \right] \right\}, \end{aligned} \quad (\text{A.3.43})$$

$$\begin{aligned} I_{2\text{MIW}^5\text{W}} = & - \int dy dx_1 dx_2 dx_3 \left(\frac{y}{x_1} \right)^{2+c_L} \left(\frac{y}{x_2} \right)^4 \left(\frac{y}{x_3} \right) \\ & \times \left[\frac{1}{2} y^2 \tilde{F}_{+,y}^{L1y} \tilde{F}_{-,y}^{Ryy} \tilde{F}_{+,y}^{Ly2} \tilde{D}_+ \tilde{F}_{+,y\mu}^{L2y\mu} \left(y \partial_{k_E} G_y^{13} \partial_z \bar{G}_y^{23} - y \partial_{k_E} \partial_z G_y^{13} \bar{G}_y^{23} \right) \right], \end{aligned} \quad (\text{A.3.44})$$

$$\begin{aligned} I_{2\text{MIWW}^5} = & - \int dy dx_1 dx_2 dx_3 \left(\frac{y}{x_1} \right)^{2+c_L} \left(\frac{y}{x_2} \right)^4 \left(\frac{y}{x_3} \right) \\ & \times \left[\frac{1}{2} \tilde{D}_+ \tilde{F}_{+,y}^{L1y} \tilde{F}_{-,y}^{Ryy} \tilde{D}_- \tilde{F}_{-,y}^{Ly2} \tilde{D}_+ \tilde{F}_{+,y\mu}^{L2y\mu} \left(y \partial_{k_E} G_y^{23} \partial_z \bar{G}_y^{13} - y \partial_{k_E} \partial_z G_y^{23} \bar{G}_y^{13} \right) \right]. \end{aligned} \quad (\text{A.3.45})$$

A.3.3 Subdominant b coefficient diagrams

$$\mathcal{M}(n\text{MIZ} / Z^5) = \frac{i}{16\pi^2} (R')^2 f_{c_L} Y_E f_{-c_E} \frac{ev}{\sqrt{2}} (g_{Z_L} g_{Z_R} \ln \frac{R'}{R}) I_{n\text{MIZ} / Z^5}, \quad (\text{A.3.46})$$

$$\mathcal{M}(0\text{MIW}) = \frac{i}{16\pi^2} (R')^2 f_{c_L} Y_E f_{-c_E} \frac{ev}{\sqrt{2}} \left(\frac{q^2}{2} \ln \frac{R'}{R} \right) I_{0\text{MIW}}, \quad (\text{A.3.47})$$

$$\mathcal{M}(0\text{MIW}^5)t = \frac{i}{16\pi^2} (R')^2 f_{c_{L\mu}} Y_E f_{-c_{Ee}} \frac{ev}{\sqrt{2}} \left(\frac{q^2}{2} \ln \frac{R'}{R} \right) I_{0\text{MIW}^5} \quad (\text{A.3.48})$$

where $n = 0, 1$ counts the number of internal mass insertions.

$$\begin{aligned} I_{1\text{MIZ}^5} &= \int dy dx_1 dx_2 dx_3 \left(\frac{y}{x_1} \right)^{2+c_L} \left(\frac{y}{x_2} \right)^{2-c_E} \left(\frac{y}{x_3} \right)^4 \\ &\times \frac{1}{2} \left[\tilde{F}_{-,y}^{L13} y \partial_{k_E} \left(\tilde{D}_+ \tilde{F}_{+,y}^{L3y} \tilde{D}_+ \tilde{F}_{+,y}^{Ry2} \right) \bar{G}_y^{12} - \tilde{D}_+ \tilde{F}_{+,y}^{L13} y \partial_{k_E} \left(\tilde{F}_{+,y}^{L3y} \tilde{D}_+ \tilde{F}_{+,y}^{Ry2} \right) \bar{G}_y^{12} \right. \\ &- 4 \tilde{D}_+ \tilde{F}_{+,y}^{L13} \tilde{F}_{+,y}^{L3y} \tilde{D}_+ \tilde{F}_{+,y}^{Ry2} \bar{G}_y^{12} + \tilde{D}_+ \tilde{F}_{+,y}^{L1y} \tilde{F}_{-,y}^{Ry3} \left(y \partial_{k_E} \tilde{D}_+ \tilde{F}_{+,y}^{R32} \right) \bar{G}_y^{12} \\ &\left. - \tilde{D}_+ \tilde{F}_{+,y}^{L1y} \tilde{D}_+ \tilde{F}_{+,y}^{Ry3} y \partial_{k_E} \left(\tilde{F}_{+,y}^{R32} \bar{G}_y^{12} \right) - 4 \tilde{D}_+ \tilde{F}_{+,y}^{L1y} \tilde{D}_+ \tilde{F}_{+,y}^{Ry3} \tilde{F}_{+,y}^{R32} \bar{G}_y^{12} \right]. \end{aligned} \quad (\text{A.3.49})$$

$$\begin{aligned} I_{0\text{MIZ}} &= \int dy dx_1 dx_2 dx_3 \left(\frac{y}{x_1} \right)^{2+c_L} \left(\frac{y}{x_2} \right)^4 \left(\frac{y}{x_3} \right)^4 \\ &\times y \partial_{k_E} G_y^{13} \tilde{D}_+ \tilde{F}_{+,y\mu}^{L3y\mu} \left(\tilde{D}_- \tilde{F}_{-,y}^{L12} \tilde{F}_{-,y}^{L23} + \tilde{F}_{+,y}^{L12} \tilde{D}_- \tilde{F}_{-,y}^{L23} \right), \end{aligned} \quad (\text{A.3.50})$$

$$\begin{aligned} I_{0\text{MIZ}^5} &= - \int dy dx_1 dx_2 dx_3 \left(\frac{y}{x_1} \right)^{2+c_L} \left(\frac{y}{x_2} \right)^4 \left(\frac{y}{x_3} \right)^4 \\ &\times \left\{ \frac{1}{4} \tilde{D}_+ \tilde{F}_{+,y}^{L23} \tilde{D}_+ \tilde{F}_{+,y\mu}^{L3y\mu} \left[\tilde{F}_{-,y}^{L12} \left(4 \bar{G}_y^{13} + y \partial_{k_E} \bar{G}_y^{13} \right) + y \partial_{k_E} \tilde{F}_{-,y}^{L12} \bar{G}_y^{13} \right] \right\}, \end{aligned} \quad (\text{A.3.51})$$

$$\begin{aligned} I_{0\text{MIW}} &= - \int dy dx_1 dx_2 dx_3 \left(\frac{y}{x_1} \right)^{2+c_L} \left(\frac{y}{x_2} \right)^4 \left(\frac{y}{x_3} \right)^4 \\ &\times \frac{3}{2} y \partial_{k_E} \left(G_y^{13} G_y^{32} \right) \tilde{D}_- \tilde{F}_{-,y}^{L12} \tilde{D}_L \tilde{F}_{L,y\mu}^{+3y\mu} \end{aligned} \quad (\text{A.3.52})$$

$$\begin{aligned} I_{0\text{MIW}^5} &= \int dy dx_1 dx_2 dx_3 \left(\frac{y}{x_1} \right)^{c_L+2} \left(\frac{y}{x_2} \right)^4 \left(\frac{y}{x_3} \right)^4 \\ &\left\{ \frac{y}{2} \tilde{F}_{+,y}^{L1y} \tilde{D}_+ \tilde{F}_{+,y\mu}^{L2y\mu} \left(\frac{\partial}{\partial k_E} \frac{\partial}{\partial x_3} G_y^{13} \right) \bar{G}_y^{32} + \frac{y}{2} \tilde{F}_{+,y}^{L12} \tilde{D}_+ \tilde{F}_{+,y\mu}^{L2y\mu} \left(\frac{\partial}{\partial k_E} \frac{\partial}{\partial x_3} G_y^{32} \right) \bar{G}_y^{13} \right. \\ &\left. - \tilde{D}_+ \tilde{F}_{+,y}^{L12} \tilde{D}_+ \tilde{F}_{+,y\mu}^{L2y\mu} \left[2 \bar{G}_y^{13} \bar{G}_y^{23} + \frac{y}{2} \frac{\partial}{\partial k_E} (\bar{G}_y^{13} \bar{G}_y^{32}) \right] \right\}. \end{aligned} \quad (\text{A.3.53})$$

A.3.4 Custodial Models

For custodially protected models, one must include loops with the custodial partners of fermions and gauge bosons. See, e.g., [31] for details of the additional field content of such models. The new particles have mixed boundary conditions, $(-+)$ or $(+-)$. For the chirality flipping process $\mu \rightarrow e \gamma$, Yukawa insertions on the IR brane only allow fermions carrying either $(++)$ or $(-+)$ boundary conditions running in the loop. This limits the number of the new diagrams to be considered. The new fermion propagators can be obtained by making the replacement $\tilde{F} \rightarrow \tilde{E}$. Writing the boundary condition in terms of the Weyl components of the Dirac spinor, \tilde{E}^L corresponds to the boundary condition $(\psi_{(+ -)}, \bar{\chi}_{(- +)})$, while \tilde{E}^R corresponds to $(\psi_{(- +)}, \bar{\chi}_{(+ -)})$. For $x > x'$, the \tilde{E} -functions can be written as follows:

$$\tilde{E}_-^L = \frac{(xx')^{5/2}}{y^5} \frac{S_c(x_-, y_-) T_c(x'_-, wy_+)}{T_c(y_-, wy_+)}, \quad \tilde{E}_+^L = -\frac{(xx')^{5/2}}{y^5} \frac{T_c(x_+, y_-) S_c(x'_+, wy_+)}{T_c(y_-, wy_+)}, \quad (\text{A.3.54})$$

$$\tilde{E}_-^R = -\frac{(xx')^{5/2}}{y^5} \frac{T_c(x_-, y_+) S_c(x'_-, wy_-)}{T_c(y_+, wy_-)}, \quad \tilde{E}_+^R = \frac{(xx')^{5/2}}{y^5} \frac{S_c(x_+, y_+) T_c(x'_+, wy_-)}{T_c(y_+, wy_-)}. \quad (\text{A.3.55})$$

The $x < x'$ expressions are obtained by replacing $x \leftrightarrow x'$. Gauge bosons with $(-+)$ boundary conditions can also appear in custodial loops. The corresponding propagator for $x > x'$ is $G \rightarrow H$ with

$$H_k(x, x') = \frac{(R')^2}{R} \frac{xx'}{y} \frac{T_{10}(x, y) S_{11}(x', wy)}{T_{10}(wy, y)}. \quad (\text{A.3.56})$$

The T and S are defined in Appendix. (A.5), and the $x < x'$ case can be obtained by $x \leftrightarrow x'$.

A.4 Position, momentum, and position/momentum space

In order to elucidate the power counting in Section 2.6 and to provide some motivation for the structure of the propagators in Appendix A.6.1, we review the passage between Feynman rules in position, momentum, and mixed position/momentum space. For simplicity we shall work with massless scalar fields on a flat (Minkowski) d -dimensional background, but the generalization of the salient features to higher spins is straightforward. In position space, the two-point Green's function for a particle propagating from x' to x is

$$D(x, x') = \int d^d k \frac{i}{k^2} e^{-ik \cdot (x - x')}, \quad (\text{A.4.57})$$

a momentum-space integral over a power-law in k times a product of exponentials in $k \cdot x$ and $k \cdot x'$. Each vertex carries a $d^d x$ integral representing each spacetime point at which the interaction may occur. When some dimensions are compact, the associated integrals are reverted to discrete sums and the particular linear combination of exponentials is shifted to maintain boundary conditions. Further, when dimensions are warped the exponentials become Bessel functions. In this Appendix we will neglect these differences and focus on general features since the UV behavior of each of the aforementioned scenarios (i.e. for momenta much larger than any mass, compactification, or warping scales) reduces to the flat noncompact case presented here.

In 4D it is conventional to work in full momentum space where the Feynman rules are derived by performing the $d^d x$ integrals at each vertex over the exponential functions from each propagator attached to the vertex and amputating the external propagators. This generates a momentum-conserving δ -function at each vertex which can be used to simplify the $d^d k$ integrals in each propagator. For each diagram one such δ -function imposes overall conservation of the external momenta and hence has no dependence on

any internal momenta. For a loop diagram this means that there is a leftover $\vec{d}^d k$ which corresponds to the integration over the loop momentum. Thus the momentum space formalism involves separating the exponentials in $k \cdot x$ from the rest of the Green's function and performing the $d^d x$ integral to obtain δ -functions.

To go to the mixed position/momentum space formalism we pick one direction, z , and leave the dependence on that position in the propagator while integrating over the z -component of the momentum, k_z in (A.4.57). We shall write the Minkowski scalar product of the $(d - 1)$ momentum-space directions as k^2 so that the full d -dimensional scalar product is $k^2 - k_z^2$. The Feynman rule for each vertex now includes an explicit dz integral which must be performed *after* including each of the position/momentum space propagators, which take the form

$$\Delta(k, z, z') = \int d k_z \frac{i}{k^2 - k_z^2} e^{i k_z (z - z')}. \quad (\text{A.4.58})$$

The $(d - 1)$ other exponentials and momentum integrals are accounted in the usual momentum-space formalism. This object goes like $\Delta \sim 1/k$, which indeed has the correct dimensionality for the sum over a KK tower of scalar propagators. Similarly, the massless bulk fermion propagator is

$$\Delta(k, z, z') = \int d k_z \frac{i(\not{k} - \not{k}_z \gamma^5)}{k^2 - k_z^2} e^{i k_z (z - z')}, \quad (\text{A.4.59})$$

where we may now identify the scalar functions $F \sim d k_z e^{i k_z (z - z')} / (k^2 - k_z^2)$ in (A.6.76) and (A.6.93).

It is thus apparent that the mixed formalism contains all of the same integrals and factors as the momentum-space formalism, but that these are packaged differently between vertex and propagator Feynman rules. By identifying features between the two pictures one may glean physical intuition in one picture that is not manifest in the other. For example, the observation in the mixed formalism that each bulk vertex on a loop brings

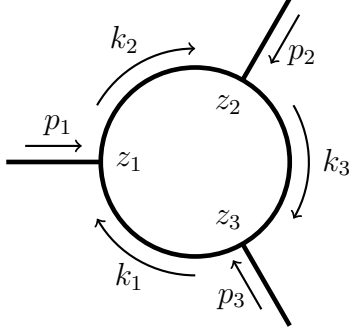


Figure A.2: A simple loop diagram to demonstrate the power counting principles presented. The lines labeled p_i represent the net external momentum flowing into each vertex so that p_i^z corresponds to the KK mass of the i^{th} external particle.

down a power of $1/k$ is straightforwardly understood to be a manifestation of momentum conservation in the momentum space picture.

On the other hand, the mixed formalism is much more intuitive for brane-localized effects. Interactions with fields on the brane at $z = L$ carry $\delta(z - L)$ factors in the vertex Feynman rules. Such interactions violate momentum conservation in the z -direction. In the KK formalism this manifests itself as the question of when it is appropriate to sum over an independent tower of KK modes. This is easily quantified in the mixed formalism since the dz integrals are not yet performed in the Feynman rules and we may directly insert $\delta(z - L)$ terms in the expression for the amplitude.

As a concrete example, consider the loop diagram with three vertices shown in Fig. A.2. It is instructive to explicitly work out loop z -momentum structure of this diagram in the case where all vertices are in the bulk and observe how this changes as vertices are localized on the brane. To simplify the structure, let us define the product of momentum-space propagators

$$f(k_1, k_2, k_3) \equiv \prod_{i=1}^3 \frac{i}{k_i^2 - (k_i^z)^2}. \quad (\text{A.4.60})$$

Using $\int dz \exp(izk) = \delta(k)$, the bulk amplitude is proportional to

$$\mathcal{M} \sim \int dz_1 dz_2 dz_3 dk_1^z dk_2^z dk_3^z f(k_1, k_2, k_3) e^{iz_1(k_1+p_1-k_2)^z} e^{iz_2(k_2+p_3-k_3)^z} e^{iz_3(k_3+p_3-k_1)^z} \quad (\text{A.4.61})$$

$$\sim \int dz_2 dz_3 dk_2^z dk_3^z f(k_2 - p_1, k_2, k_3) e^{iz_2(k_2+p_3-k_3)^z} e^{iz_3(k_3+p_3-k_2+p_1)^z} \quad (\text{A.4.62})$$

$$\sim \int dz_3 dk_3^z f(k_3 - p_2 - p_1, k_3 - p_2, k_3) e^{iz_3(p_1+p_2+p_3)^z}. \quad (\text{A.4.63})$$

We have implicitly performed the associated $d^{(d-1)}x$ integrals at each step. The final dz_3 integral gives the required δ -function of external momenta while leaving an unconstrained dk_3^z loop integral. Each $dk^z/(k^2 - k_z^2) \sim 1/k$ represents the entire KK tower associated with an internal line. The removal of two dk^z integrals by δ -functions is a manifestation of the $1/k$ suppression coming from each dz integral with the caveat that the “last” dz integral only brings down powers of external momenta and hence does not change the power of loop momenta. This explains the “overall z -momentum” contribution to the superficial degree of divergence in Section 2.6.2.

Next consider the case when the z_3 vertex is brane localized so that its Feynman rule is proportional to $\delta(z_3 - L)$. This only affects the last line of the simplification by removing the dz_3 integral. Physically this means that z -momentum (KK number) needn not be conserved for this process. Since the z_3 exponential is independent of any loop momenta, this does not affect the superficial degree of divergence.

On the other hand, if z_2 is also brane localized, then the $\delta(z_2 - L)$ from the vertex prevents the dz_2 integral in the second line from giving the $\delta(k_2 + p_2 - k_3)$ that cancels the dk_2^z integral. Thus the process has an additional dk_2^z integral which now increases the degree of divergence. In the 4D formalism this is manifested as an additional independent sum over KK states. It is now also clear that setting z_1 to be brane localized prevents the dk_1^z from being cancelled and hence adds another unit to the degree of divergence. This

counting is trivially generalized to an arbitrary number of vertices and different types of internal propagators. For a loop with V vertices, V_B of which are in the bulk, the key points are:

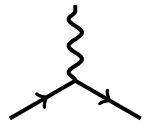
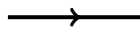




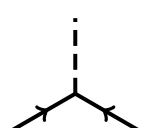

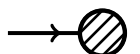
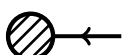
1. If $V = V_B$, then the dz integrals reduce the superficial degree of divergence by $(V_B - 1)$.
2. If, on the other hand, $V > V_B$ so that there is at least one brane-localized vertex, then the dz integrals reduce the superficial degree of divergence by V_B .

Intuitively the z -momentum nonconservation coming from brane-localized interactions can be understood as the particle picking up an arbitrary amount of momentum as it bounces off the brane (a similar picture can be drawn for the orbifold [218]). Alternately, it reflects the uniform spread in momentum associated with complete localization in z -position. While this may seem to imply sensitivity to arbitrarily high scale physics on the brane, a negative degree of divergence will prevent the loop from being sensitive to UV physics. In other words, we are free to treat brane-localized fields as having δ -function profiles independent of the physics that generates the brane.

Finally, note that we have assumed that each fermion mass insertion is brane localized. In 5D this means that higher-order diagrams in the fermion mass-insertion approximation are not suppressed by momentum since each additional brane-to-brane propagator goes like $\sim \not{k}/k$ after accounting for the dk^z integrals. Instead, these mass insertions are suppressed only by the relative sizes of the Higgs vev and compactification scale, $(vR')^2 \sim .01$. It is perhaps interesting to note that our analysis further suggests that in 6D with a Higgs localized on a 4D subspace, there are two additional momentum integrals coming from a mass insertion so that each vev-to-vev propagator goes like a positive power of the momentum $\sim \not{k}$ causing the mass-insertion approximation to break down.

A.5 Bulk Feynman Rules

Here we summarize the 5D position/momentum space Feynman rules used to derive the amplitudes in this paper. All couplings are written in terms of 5D quantities. The brane-localized Higgs field is drawn as a dashed line and the fifth component of a bulk gauge boson is drawn as a dotted line.

	$= ig_5 \left(\frac{R}{z}\right)^4 \gamma^\mu$		$= \Delta_k(z, z')$
	$= ie_5(p_+ - p_-)_\mu$		$= -i\eta^{\mu\nu} G_k(z, z')$
	$= \frac{i}{2} e_5 g_5 v \eta^{\mu\nu}$		$= i\bar{G}_k(z, z')$
	$= i \left(\frac{R}{R'}\right)^3 Y_5$		$= \epsilon^\mu(q) f_A^{(0)}$
			$= \frac{f_c}{\sqrt{R'}} \left(\frac{z}{R}\right)^2 \left(\frac{z}{R'}\right)^{-c} u(p)$
			$= \bar{u}(p') \frac{f_c}{\sqrt{R'}} \left(\frac{z}{R}\right)^2 \left(\frac{z}{R'}\right)^{-c}$

The 5D Lagrangian parameters are related to the usual Standard Model parameters by

$$g_5^2 = g_{\text{SM}}^2 R \ln R' / R \quad (\text{A.5.64})$$

$$e_5 f_A^{(0)} = e_{\text{SM}} \quad (\text{A.5.65})$$

$$Y_5 = RY, \quad (\text{A.5.66})$$

where Y represents an anarchic 4D Yukawa matrix that is related to the Standard Model Yukawa by (3.2.7). The f_c fermion flavor functions are defined in (3.2.5). The vector propagator functions $G_k(z, z')$ and $\bar{G}_k(z, z')$ are explicitly derived in [329], which also contains generic formulae for analogous functions for fields of general spin and additional gauge

boson vertices. Using the dimensionless x and y variables defined in (2.6.52) and assuming $z > z'$, the Euclidean space vector Green's functions are

$$G_k(z, z') = \frac{(R')^2}{R} G_y(x, x') = \frac{(R')^2}{R} \frac{xx'}{y} \frac{T_{10}(x, y) T_{10}(x', wy)}{S_{00}(wy, y)}, \quad (\text{A.5.67})$$

$$\bar{G}_k(z, z') = \frac{(R')^2}{R} \bar{G}_y(x, x') = \frac{(R')^2}{R} \frac{xx'}{y} \frac{S_{00}(x, y) S_{00}(x', wy)}{S_{00}(wy, y)}, \quad (\text{A.5.68})$$

where

$$T_{ij}(x, y) = I_i(x) K_j(y) + I_j(y) K_i(x) \quad (\text{A.5.69})$$

$$S_{ij}(x, y) = I_i(x) K_j(y) - I_j(y) K_i(x) \quad (\text{A.5.70})$$

and $w = R/R'$. For $z < z'$ the above formula is modified by $x \leftrightarrow x'$. The three gauge boson couplings are given by

$$\begin{array}{c} A_\mu \\ \text{wavy line} \\ \text{W}_\nu^+ \text{---} \text{---} \text{---} \text{W}_\rho^- \end{array} = ie_5 \frac{R}{z} [(k - k^+)^\rho \eta^{\mu\nu} + (k^- - k)^\nu \eta^{\mu\rho} + (k^+ - k^-)^\mu \eta^{\nu\rho}]$$

$$\begin{array}{c} A_\mu \\ \text{wavy line} \\ \text{W}_5^+ \text{---} \text{---} \text{---} \text{W}_5^- \end{array} = ie_5 \frac{R}{z} (k^- - k^+)^\mu \quad \begin{array}{c} A_\mu \\ \text{wavy line} \\ \text{W}_\nu^+ \text{---} \text{---} \text{---} \text{W}_5^- \end{array} = e_5 \frac{R}{z} \eta^{\mu\nu} (\partial_z - \partial_z^+)$$

Here we have used the convention where all momenta are labeled by the charge of the particle and are flowing into the vertex. The $A_\mu W_5^+ W_\nu^-$ vertex is given by $e_5(R/z) \eta^{\mu\nu} (\partial_z^\mu - \partial_z^\nu)$. The Euclidean space fermion propagator $\Delta_k(z, z')$ is given in (B.1.1).

A.6 Derivation of fermion propagators

General formulae for the scalar function associated with bulk propagators of arbitrary-spin fields in RS can be found in [329]. The special case of bulk fermion propagators with endpoints on the UV brane is presented in [143]. The Green's function equation for the general RS fermion propagator can be solved directly from the Sturm-Liouville equation, though this can obscure some of the intuition of the results. Here we provide a pedagogical derivation of the 5D bulk fermion propagator in a flat and warped interval extra dimension. See also the discussion in Appendix A.4 which relates this construction to the usual pure momentum space formalism.

A.6.1 Flat 5D fermion propagator

First we derive the chiral fermion propagator in a flat interval extra dimension $z \in (0, L)$ as a model calculation for the warped fermion propagator which is presented in Appendix A.6.2. A complete set of propagators for a flat 5D interval was derived in [325] using finite temperature field theory techniques.

We derive these results by directly solving the Green's function equations. The propagator from a given point x' to a another point x is given by the two-point Green's function of the 5D Dirac operator,

$$\mathcal{D} \Delta(x, x') \equiv (i\gamma^M \partial_M - m) \Delta(x, x') = i\delta^{(5)}(x - x'), \quad (\text{A.6.71})$$

where M runs over 5D indices. We shall treat the noncompact dimensions in momentum space and the finite dimension is in position space. In this formalism, the Green's function

equation is

$$(\not{p} + i\partial_5\gamma^5 - m) \Delta(p, z, z') = i\delta(z - z'), \quad (\text{A.6.72})$$

where we use $\gamma^5 = \text{diag}(i\mathbb{1}_2, -i\mathbb{1}_2)$.

This is a first-order differential equation with nontrivial Dirac structure. To solve this equation we define a pseudo-conjugate Dirac operator (which is neither a complex nor Hermitian conjugate),

$$\bar{\mathcal{D}} = i\gamma^M \partial_M + m. \quad (\text{A.6.73})$$

Using this to “square” the Dirac operator, we can swap the Dirac equation for a simpler Klein-Gordon equation that is second order and diagonal on the space of Weyl spinors,

$$\mathcal{D}\bar{\mathcal{D}} = \begin{pmatrix} \partial_5^2 - \partial^2 - m^2 & \\ & \partial_5^2 - \partial^2 - m^2 \end{pmatrix}. \quad (\text{A.6.74})$$

It is straightforward to solve for the Green’s functions $F(p, z, z')$ of the $\mathcal{D}\mathcal{D}^*$ operator in mixed position/momentum space,

$$\mathcal{D}\bar{\mathcal{D}}F(p, z, z') = \begin{pmatrix} \partial_5^2 + p^2 - m^2 & \\ & \partial_5^2 + p^2 - m^2 \end{pmatrix} \begin{pmatrix} F_- \\ F_+ \end{pmatrix} = i\delta(z - z'). \quad (\text{A.6.75})$$

From these we can trivially construct a solution for the Green’s function of (A.6.71),

$$\Delta(p, z, z') \equiv \bar{\mathcal{D}}F(p, z, z') = \begin{pmatrix} (-\partial_5 + m) F_- & \sigma^\mu p_\mu F_+ \\ \bar{\sigma}^\mu p_\mu F_- & (\partial_5 + m) F_+ \end{pmatrix}. \quad (\text{A.6.76})$$

We solve this by separating $F_\pm(z)$ into pieces

$$F_\pm(p, z, z') = \begin{cases} F_\pm^<(p, z, z') & \text{if } z < z' \\ F_\pm^>(p, z, z') & \text{if } z > z' \end{cases} \quad (\text{A.6.77})$$

and then solving the homogeneous Klein-Gordon equations for each $F^<$ and $F^>$. The general solution is

$$F_{\pm}^{<, >}(p, z, z') = A_{\pm}^{<, >} \cos(\chi_p z) + B_{\pm}^{<, >} \sin(\chi_p z), \quad (\text{A.6.78})$$

where the eight coefficients $A_{\pm}^{<, >}$ and $B_{\pm}^{<, >}$ are determined by the boundary conditions at $0, L$ and z' . The factor χ_p is the magnitude of p_5 and is defined by

$$\chi_p = \sqrt{p^2 - m^2}. \quad (\text{A.6.79})$$

We impose matching boundary conditions at $z = z'$. By integrating the Green's function equation (A.6.75) over a sliver $z \in [z' - \epsilon, z' + \epsilon]$ we obtain the conditions

$$\partial_5 F_{\pm}^>(z') - \partial_5 F_{\pm}^<(z') = i, \quad (\text{A.6.80})$$

$$F_{\pm}^>(z') - F_{\pm}^<(z') = 0. \quad (\text{A.6.81})$$

These are a total of four equations. The remaining four equations imposed at the branes impose the chirality of the fermion zero mode and are equivalent to treating the interval as an orbifold. We denote the propagator for the 5D fermion with a left-chiral (right-chiral) zero mode by Δ^L (Δ^R). We impose that the Green's function vanishes if a “wrong-chirality” state propagates to either brane,

$$P_R \Delta^L(p, z, z')|_{z=0, L} = P_R \bar{\mathcal{D}} F^L(p, z, z')|_{z=0, L} = 0, \quad (\text{A.6.82})$$

$$P_L \Delta^R(p, z, z')|_{z=0, L} = P_L \bar{\mathcal{D}} F^R(p, z, z')|_{z=0, L} = 0, \quad (\text{A.6.83})$$

where $P_{L,R} = \frac{1}{2}(1 \mp i\gamma^5)$ are the usual 4D chiral projection operators. Note from (A.6.76) that each of these equations is actually a set of two boundary conditions on each brane. For example, the left-handed boundary conditions may be written explicitly as

$$F_-^L(p, z, z')|_{z=0, L} = 0, \quad (\text{A.6.84})$$

$$(\partial_5 + m)F_+^L(p, z, z')|_{z=0, L} = 0, \quad (\text{A.6.85})$$

$A_+^{L<} = s_p(L - z')s_pL$	$A_+^{L>} = s_pz's_pL$	$A_+^{R<} = 0$	$A_+^{R>} = -c_pz's_pL$
$B_+^{L<} = 0$	$B_+^{L>} = s_pz's_pL$	$B_+^{R<} = -c_p(L - z')$	$B_+^{R>} = -c_pz's_pL$
$A_-^{L<} = 0$	$A_-^{L>} = -c_pz's_pL$	$A_-^{R<} = s_p(L - z')$	$A_-^{R>} = -s_pz's_pL$
$B_-^{L<} = c_p(L - z')$	$B_-^{L>} = -c_pz's_pL$	$B_-^{R<} = 0$	$B_-^{R>} = s_pz's_pL$

Table A.1: Flat case coefficients in (A.6.78) upon solving with the boundary conditions (A.6.80–A.6.83). We have used the notation $c_px = \cos \chi_px$ and $s_px = \sin \chi_px$.

where we have used that p_μ is arbitrary. It is well-known that only one boundary condition for a Dirac fermion needs to be imposed in order not to overconstrain the first-order Dirac equation since the bulk equations of motion convert boundary conditions for χ into boundary conditions for ψ [154]. In this case, however, we work with a *second-order* Klein-Gordon equation that does not mix χ and ψ . Thus the appearance and necessity of two boundary conditions per brane for a chiral fermion is not surprising; we are only converting the single boundary condition on $\Delta(p, z, z')$ into two boundary conditions for $F(p, z, z')$.

Solving for the coefficients $A_\pm^{<,>}(p, z)$ and $B_\pm^{<,>}(p, z)$ for each type of fermion (left- or right-chiral zero modes) one finds the results in Table A.1. Using trigonometric identities one may combine the $z < z'$ and $z > z'$ results to obtain³

$$F_\pm^X = \frac{-i \cos \chi_p (L - |z - z'|) + \gamma^5 \wp_X \cos \chi_p (L - (z + z'))}{2\chi_p \sin \chi_p L}, \quad (\text{A.6.86})$$

where $X = \{L, R\}$ with $\wp_L = +1$ and $\wp_R = -1$. The fermion Green's function can then be obtained trivially from (A.6.76).

Let us remark that the leading UV behavior of a brane-to-brane propagator (where the $k_5 \gamma^5$ term vanishes) goes like

$$\Delta \sim \frac{\not{k}}{\chi_k}. \quad (\text{A.6.87})$$

³This result differs from that of [325] by a factor of 2 since that paper treats the compactified space as an orbifold over the entire S^1 rather than just an interval $[0, \pi R]$.

A.6.2 Warped 5D fermion propagator

We now derive the chiral fermion propagator in a warped interval extra dimension following the same strategy as Appendix A.6.1. The Dirac operator is obtained from the variation of the Randall-Sundrum free fermion action,

$$S_{\text{RS}}(\text{fermion}) = \int dx \int_R^{R'} dz \left(\frac{R}{z} \right)^4 \bar{\Psi} \left(i\gamma^M \partial_M - i\frac{2}{z}\gamma^5 - \frac{c}{z} \right) \Psi, \quad (\text{A.6.88})$$

where $c = mR$ and we have integrated the left-acting derivatives by parts. The Dirac operator is a product of the $(R/z)^4$ prefactor coming from the AdS geometry and an operator \mathcal{D} given by

$$\mathcal{D} = i\gamma^M \partial_M - i\frac{2}{z}\gamma^5 - \frac{c}{z}. \quad (\text{A.6.89})$$

We would like to find the mixed position/momentum space two-point Green's function satisfying

$$(R/z)^4 \mathcal{D} \Delta(p, z, z') = i\delta(z - z'). \quad (\text{A.6.90})$$

Following (A.6.73) we define a pseudo-conjugate Dirac operator

$$\bar{\mathcal{D}} = i\gamma^M \partial_M - i\frac{2}{z}\gamma^5 + \frac{c}{z} \quad (\text{A.6.91})$$

and 'square' \mathcal{D} into a diagonal second-order operator,

$$\mathcal{D}\bar{\mathcal{D}} = \begin{pmatrix} \mathcal{D}\bar{\mathcal{D}}_- & 0 \\ 0 & \mathcal{D}\bar{\mathcal{D}}_+ \end{pmatrix} \quad \mathcal{D}\bar{\mathcal{D}}_{\pm} = \partial^2 - \partial_5^2 + \frac{4}{z}\partial_5 + \frac{c^2 \pm c - 6}{z^2}. \quad (\text{A.6.92})$$

Next we follow (A.6.75) and solve for the Green's function of this squared operator in mixed position/momentum space where $\partial^2 \rightarrow -p^2$,

$$-(R/z)^4 \mathcal{D}\bar{\mathcal{D}}F(p, z, z') = -\left(\frac{R}{z}\right)^4 \begin{pmatrix} \mathcal{D}\bar{\mathcal{D}}_- & \\ & \mathcal{D}\bar{\mathcal{D}}_+ \end{pmatrix} \begin{pmatrix} F_- \\ F_+ \end{pmatrix} = i\delta(z - z'). \quad (\text{A.6.93})$$

The solution to the Dirac Green's function equation (A.6.90) is then given by $\Delta(p, z, z') = \bar{D}F(p, z, z')$. We shall separate $F(p, z, z')$ into solutions for the cases $z > z'$ and $z < z'$ following (A.6.77). The general solution to the homogeneous equation (A.6.93) with $z \neq z'$ is

$$F_{\pm}^{<, >}(p, z, z') = A_{\pm}^{<, >} z^{\frac{5}{2}} J_{c \pm \frac{1}{2}}(pz) + B_{\pm}^{<, >} z^{\frac{5}{2}} Y_{c \pm \frac{1}{2}}(pz), \quad (\text{A.6.94})$$

where J_n and Y_n are Bessel functions of the first and second kinds, $A_{\pm}^{<, >}$ and $B_{\pm}^{<, >}$ are coefficients to be determined by boundary conditions, and p is the analog of χ_p defined by $p = \sqrt{p_\mu p^\mu}$. Note that this differs from (A.6.79) since there is no explicit bulk mass dependence. In (A.6.94) the bulk masses enter only in the order of the Bessel functions as $(c \pm \frac{1}{2})$.

The matching boundary conditions at $z = z'$ are given by (A.6.80) and (A.6.81) modified by a factor of $(R/z')^4$ from (A.6.93),

$$\partial_5 F_{\pm}^{>}(z') - \partial_5 F_{\pm}^{<}(z') = i(R/z')^{-4}, \quad (\text{A.6.95})$$

$$F_{\pm}^{>}(z') - F_{\pm}^{<}(z') = 0. \quad (\text{A.6.96})$$

The chiral boundary conditions are the same as in the flat case, (A.6.82) and (A.6.83) with the appropriate insertion of (A.6.91).

We may now solve for the A and B coefficients. It is useful to write these in terms of common factors that appear in their expressions. To this end, let us define the prefactors

$$\alpha_L = \frac{i\pi}{2R^4} \frac{1}{S_c^-(pR, pR')} \alpha_R = \frac{i\pi}{2R^4} \frac{1}{S_c^+(pR, pR')} \quad (\text{A.6.97})$$

and a set of antisymmetric functions

$$S_c^{\pm}(x, y) = J_{c \pm \frac{1}{2}}(x) Y_{c \pm \frac{1}{2}}(y) - J_{c \pm \frac{1}{2}}(y) Y_{c \pm \frac{1}{2}}(x) \quad (\text{A.6.98})$$

$$\tilde{S}_c^{\pm}(x, y) = J_{c \pm \frac{1}{2}}(x) Y_{c \mp \frac{1}{2}}(y) - J_{c \mp \frac{1}{2}}(y) Y_{c \pm \frac{1}{2}}(x) \quad (\text{A.6.99})$$

$A_+^{L<} = -\alpha_L z'^{\frac{5}{2}} Y_{c-\frac{1}{2}}(pR) \tilde{S}_c^+(pz', pR')$	$A_+^{R<} = -\alpha_R z'^{\frac{5}{2}} Y_{c+\frac{1}{2}}(pR) S_c^+(pz', pR')$
$B_+^{L<} = \alpha_L z'^{\frac{5}{2}} J_{c-\frac{1}{2}}(pR) \tilde{S}_c^+(pz', pR')$	$B_+^{R<} = \alpha_R z'^{\frac{5}{2}} J_{c+\frac{1}{2}}(pR) S_c^+(pz', pR')$
$A_-^{L<} = -\alpha_L z'^{\frac{5}{2}} Y_{c-\frac{1}{2}}(pR) S_c^-(pz', pR')$	$A_-^{R<} = -\alpha_R z'^{\frac{5}{2}} Y_{c+\frac{1}{2}}(pR) \tilde{S}_c^-(pz', pR')$
$B_-^{L<} = \alpha_L z'^{\frac{5}{2}} J_{c-\frac{1}{2}}(pR) S_c^-(pz', pR')$	$B_-^{R<} = \alpha_R z'^{\frac{5}{2}} J_{c+\frac{1}{2}}(pR) \tilde{S}_c^-(pz', pR')$

Table A.2: Left-handed RS fermion propagator coefficients: the $z > z'$ coefficients are obtained by swapping $R \leftrightarrow R'$ in the arguments of the functions, leaving the $\alpha_{L,R}$ constant.

With these definitions the coefficients for the left- and right-handed F functions are given in Table A.2. The $F_{\pm}^{L,R}$ functions may thus be written out succinctly for $z \leq z'$ as

$$F_+^{L<} = \alpha_L (zz')^{5/2} \tilde{S}_c^+(pz', pR') \tilde{S}_c^-(pR, pz) \quad (\text{A.6.100})$$

$$F_-^{L<} = \alpha_L (zz')^{5/2} S_c^-(pz', pR') S_c^-(pR, pz) \quad (\text{A.6.101})$$

$$F_+^{R<} = \alpha_R (zz')^{5/2} S_c^+(pz', pR') S_c^+(pR, pz) \quad (\text{A.6.102})$$

$$F_-^{R<} = \alpha_R (zz')^{5/2} \tilde{S}_c^-(pz', pR') \tilde{S}_c^+(pR, pz) \quad (\text{A.6.103})$$

The expressions for $z > z'$ are obtained by making the replacement $\{R \leftrightarrow R'\}$ in the arguments of the S_c functions. We now use the notation in (A.6.77) and drop the $<, >$ superscripts. From these the fermion Green's function can be obtained trivially from the analog of (A.6.76),

$$\Delta(p, z, z') \equiv \bar{D}F(p, z, z') = \begin{pmatrix} D_- F_- & \sigma^\mu p_\mu F_+ \\ \bar{\sigma}^\mu p_\mu F_- & D_+ F_+ \end{pmatrix}, \quad D_{\pm} \equiv \pm \left(\partial_5 - \frac{2}{z} \right) + \frac{2}{z} \quad (\text{A.6.104})$$

Note that in the UV limit ($\chi_p \gg 1/R$) the Bessel functions reduce to phase-shifted trigonometric functions so that we indeed recover the flat 5D propagators.

A.6.3 Euclidean warped 5D fermion propagator

Finally, it is convenient to write the Wick-rotated form of the fermion propagators since these will provide the relevant Feynman rules in loop diagrams such as $\mu \rightarrow e\gamma$. We shall write out the scalar F functions in a convenient form that we use throughout the rest of this document. The derivation is identical to that outlined above with the replacement $p^2 = -p_E^2$ (i.e. $\partial = i\partial_E$) in the Green's function equation so that we shall simply state the results. The Euclidean scalar functions are written in terms of the modified Bessel functions I and K which behave like exponentials in the UV. Let us define the auxiliary functions

$$S_c(x_\pm, x'_\pm) = I_{c\pm 1/2}(x)K_{c\pm 1/2}(x') - I_{c\pm 1/2}(x')K_{c\pm 1/2}(x) \quad (\text{A.6.105})$$

$$S_c(x_\pm, x'_\mp) = I_{c\pm 1/2}(x)K_{c\mp 1/2}(x') - I_{c\mp 1/2}(x')K_{c\pm 1/2}(x) \quad (\text{A.6.106})$$

$$T_c(x_\pm, x'_\mp) = I_{c\pm 1/2}(x)K_{c\mp 1/2}(x') + I_{c\mp 1/2}(x')K_{c\pm 1/2}(x). \quad (\text{A.6.107})$$

Since we would like to write dimensionless loop integrals, let us define the dimensionless variables $y \equiv k_E R'$ and $x = k_E z$, which are the natural quantities which appear as arguments of the Bessel functions. We write the warp factor as $w = (R/R')$. It is convenient to pull out overall factors to write the F functions as

$$F_\pm(k_E, z, z') = iw^{-4}R'\tilde{F}_{\pm,y}^{xx'}. \quad (\text{A.6.108})$$

The Euclidean scalar functions for $x > x'$ (i.e. $z > z'$) are given by

$$\tilde{F}_-^L = \frac{(xx')^{5/2}}{y^5} \frac{S_{c_L}(x_-, y_-)S_{c_L}(x'_-, wy_-)}{S_{c_L}(y_-, wy_-)}, \quad \tilde{F}_+^L = -\frac{(xx')^{5/2}}{y^5} \frac{T_{c_L}(x_+, y_-)T_{c_L}(x'_+, wy_-)}{S_{c_L}(y_-, wy_-)}, \quad (\text{A.6.109})$$

$$\tilde{F}_-^R = -\frac{(xx')^{5/2}}{y^5} \frac{T_{c_R}(x_-, y_+)T_{c_R}(x'_-, wy_+)}{S_{c_R}(y_+, wy_+)}, \quad \tilde{F}_+^R = \frac{(xx')^{5/2}}{y^5} \frac{S_{c_R}(x_+, y_+)S_{c_R}(x'_+, wy_+)}{S_{c_R}(y_+, wy_+)}. \quad (\text{A.6.110})$$

The functions for $x < x'$ are given by replacing $x \leftrightarrow x'$ in the above formulas. With these definitions the Euclidean fermion propagator given by the analog of (A.6.104),

$$\Delta(k_E, x, x') \equiv i \frac{R'}{w^4} \bar{\mathcal{D}} \tilde{F}_y^{xx'} = \begin{pmatrix} y \tilde{D}_+ \tilde{F}_- & \sigma^\mu y_\mu \tilde{F}_+ \\ \bar{\sigma}^\mu y_\mu \tilde{F}_- & y \tilde{D}_- \tilde{F}_+ \end{pmatrix}, \quad \tilde{D}_\pm \equiv \pm \left(\partial_x - \frac{2}{x} \right) + \frac{c}{x}. \quad (\text{A.6.111})$$

A.7 Finiteness of the brane-localized neutral Higgs diagram

As explained in Section 2.6.4, the finiteness of the one-loop result and logarithmic divergence at two-loop order becomes opaque to naïve 5D power counting arguments when the Higgs is brane-localized. Additional cancellations of leading-order terms in loop momentum are required to sensibly interpolate between the superficial degree of divergence of the bulk and brane-localized scenarios. For the charged Higgs this cancellation mechanism came from an M_W^2 insertion, which led to an additional $1/k^2$ factor relative to the bulk field. Here we shall elucidate the finiteness of the single-mass-insertion brane-localized neutral scalar loop.

At one-loop order this finiteness can be seen explicitly by the cancellation between the neutral Higgs and the neutral Goldstone. However, there is an additional chiral cancellation that occurs between the two diagrams associated a single intermediate neutral boson. Indeed, because the Higgs and neutral Goldstone do not appear to completely cancel at two-loop order, this additional cancellation is necessary for the power-counting arguments given in Section 2.6.7.

We highlight this cancellation in two ways. The pure momentum space calculation highlights the role of the chiral boundary conditions, while the mixed posi-

tion/momentum space calculation shows an explicit cancellation while including the full scalar structure the amplitude.

A.7.1 Momentum space

Here we shall see that 4D Lorentz invariance combined with the chiral boundary conditions forces the UV divergence of the two diagrams in Fig. 2.7 to cancel.

We first note that the propagators to the photon vertex each have an endpoint in the bulk. This implies that the leading-order contributions to these propagators in the UV limit are proportional to the uncompactified flat-space 5D propagators,

$$\Delta = \begin{pmatrix} \Delta_{\psi\chi} & \Delta_{\psi\psi} \\ \Delta_{\chi\chi} & \Delta_{\chi\psi} \end{pmatrix} \sim \frac{1}{k^2 - k_5^2} \begin{pmatrix} ik_5 & k_\mu \sigma^\mu \\ k_\mu \bar{\sigma}^\mu & -ik_5 \end{pmatrix} = \frac{k_\mu \gamma^\mu + k_5 \gamma^5}{k^2 - k_5^2}, \quad (\text{A.7.112})$$

where we have written $\Delta_{\psi\chi}$ to mean the propagation of a left-handed Weyl spinor χ into a right-handed spinor ψ . The terms along the diagonal come from $k_5 \gamma^5$ and represent the chirality-flipping part of the propagator. The boundary conditions require the wrong-chirality modes, the SU(2) doublet ψ_L and SU(2) singlet χ_R , to vanish on the IR brane. Thus, the fermion may propagate to the wrong-chirality spinor in the bulk only if it propagates back to the correct-chirality spinor when it returns to the brane. For an internal left-handed Weyl fermion χ_L , the portion of the amplitude coming from the photon emission takes the form

$$\Delta_{\chi\chi} \sigma^\mu \Delta_{\chi\chi} + \Delta_{\chi\psi} \bar{\sigma}^\mu \Delta_{\psi\chi} \sim (k_\alpha \bar{\sigma}^\alpha) \sigma^\mu (k_\beta \bar{\sigma}^\beta) + (k_5)^2 \bar{\sigma}^\mu. \quad (\text{A.7.113})$$

Combining with the analogous expression for a right-handed Weyl fermion in the loop,

the relevant part of the photon emission amplitude can be written as

$$\frac{\not{k}\gamma^\mu\not{k} + (k_5)^2\gamma^\mu}{(k^2 - k_5^2)^2}, \quad (\text{A.7.114})$$

where these terms correspond to a fermion of the correct and incorrect chirality propagating into the brane. The second term can be simplified using

$$\int dk_5 \frac{(k_5)^2}{(k^2 - k_5^2)^2} = \int dk_5 \frac{-k^2}{(k^2 - k_5^2)^2}, \quad (\text{A.7.115})$$

which can be confirmed by Wick rotating both sides, $k^2 \rightarrow -k_E^2$, and performing the dk_5 integral explicitly. Now it is easy to see that the divergent contributions from the diagrams in Fig. 2.7 cancel. The boundary conditions force brane-to-brane propagators to go like \not{k} with no γ^5 part. Thus we may write the internal fermion structure of the amplitudes as

$$\mathcal{M}_{(a)} + \mathcal{M}_{(b)} \sim \not{k} (\not{k}\gamma^\mu\not{k} - k^2\gamma^\mu) + (\not{k}\gamma^\mu\not{k} - k^2\gamma^\mu) \not{k} = 0. \quad (\text{A.7.116})$$

The key minus sign between the two terms in the photon emission comes from the chiral boundary conditions that force the second term to pick up the relative sign between the two diagonal blocks of γ^5 .

Let us remark that it is crucial that the denominator in (A.7.115) contains exactly two propagators or else the equality would not hold. One might be concerned that the brane-to-brane propagator should also contribute an additional factor of $(k^2 - k_5^2)$ to the denominator (the $k_5\gamma^5$ term vanishes in the numerator from boundary conditions). Such a factor is indeed present in the full calculation, but because 5D Lorentz invariance is broken on the brane, k_5 is not conserved there and this factor actually includes a *different*, uncorrelated fifth momentum component, \tilde{k}_5 , which can be taken to be independent of the dk_5 integral. This is a manifestation of the principles in Appendix A.1. As a check, one can perform the $d\tilde{k}_5$ integral for this brane-to-brane propagator and obtain the same $\not{k}/|k|$ UV behavior found in the careful derivation performed in Appendix A.6.1.

A.7.2 Position/momentum space

In Appendix A.6.1 we derived the flat-space bulk fermion propagator,

$$\Delta(p, x_5, x'_5) = (\not{p} - i\gamma^5 \partial_5 + m) \frac{-i \cos \chi_p (L - |x_5 - x'_5|) + \gamma^5 \wp(X) \cos \chi_p (L - (x_5 + x'_5))}{2\chi_p \sin \chi_p L}, \quad (\text{A.7.117})$$

where the zero mode chirality is given by $X = \{L, R\}$ with $\wp(L) = +1$ and $\wp(R) = -1$. We then argued at the end of Appendix A.6.2 that the propagators in a warped extra dimension reduce to this case up to overall phases. Thus we expect the amplitudes to have the same UV behavior up to finite factors. The relevant flat-space one-loop diagrams contributing to the operator (2.4.27) are shown in Fig. 2.7. We start with Fig. 2.7a and assume that the decay is from μ_L to e_R . The loop propagators with $(x_5, x'_5) = (L, z)$, (z, L) and (L, L) can be written as

$$\Delta(k', L, z) = -i \frac{\not{k}' \cos \chi_{k'} z - i\gamma^5 \chi_{k'} \sin \chi_{k'} z}{\chi_{k'} \sin \chi_{k'} L} P_R \quad (\text{A.7.118})$$

$$\Delta(k, z, L) = -i \frac{\not{k} \cos \chi_k z + i\gamma^5 \chi_k \sin \chi_k z}{\chi_k \sin \chi_k L} P_R \quad (\text{A.7.119})$$

$$\Delta(k, L, L) = -i \frac{\not{k} \cos \chi_k L}{\chi_k \sin \chi_k L} P_R, \quad (\text{A.7.120})$$

where $k' = k + q$. We have used the chiral boundary conditions to simplify $\Delta(k, L, L)$. Since we are interested in the UV behavior we have dropped the terms proportional to the bulk mass m from the internal propagators because these are finite. Combining the propagators together and doing the same calculation for Fig. 2.7b, the amplitudes become

$$\mathcal{M}_{(a)}^\mu = \int \frac{d^4 k}{(2\pi)^4} dz \bar{u}(p') \left\{ \frac{\not{k}' \gamma^\mu \not{k} f(k, z) + \chi_k \chi_{k'} \gamma^\mu g(k, z)}{\chi_k \chi_{k'} [(p+k)^2 - m_H^2]} \right\} \frac{\not{k} \cot \chi_k L}{\chi_k} u(p) \quad (\text{A.7.121})$$

$$\mathcal{M}_{(b)}^\mu = \int \frac{d^4 k}{(2\pi)^4} dz \bar{u}(p') \frac{\not{k}' \cot \chi_{k'} L}{\chi_{k'}} \left\{ \frac{\not{k}' \gamma^\mu \not{k} f(k, z) + \chi_k \chi_{k'} \gamma^\mu g(k, z)}{\chi_k \chi_{k'} [(p+k)^2 - m_H^2]} \right\} u(p) \quad (\text{A.7.122})$$

where we have written

$$f(k, z) = -\frac{\cos(\chi_{k+q}z) \cos(\chi_k z)}{\sin \chi_{k+q}L \sin \chi_k L} \quad (\text{A.7.123})$$

$$g(k, z) = -\frac{\sin(\chi_{k+q}z) \sin(\chi_k z)}{\sin \chi_{k+q}L \sin \chi_k L}. \quad (\text{A.7.124})$$

Note that all of the z dependence is manifestly contained in sines and cosines. Further we have neglected the flavor-dependence of the χ_k factors since these also come from the bulk masses via (A.6.79) and are negligible in the UV.

Upon Wick rotation the trigonometric functions become hyperbolic functions which are exponentials in the Euclidean momentum,

$$\cos \chi_k z \rightarrow \cosh(\chi_{k_E} z) = \frac{1}{2} (e^{\chi_{k_E} z} + e^{-\chi_{k_E} z}) \quad (\text{A.7.125})$$

$$\sin \chi_k z \rightarrow i \sinh(\chi_{k_E} z) = \frac{i}{2} (e^{\chi_{k_E} z} - e^{-\chi_{k_E} z}). \quad (\text{A.7.126})$$

We may now replace the trigonometric functions with the appropriate Euclidean exponentials. Since we are concerned with the UV behavior, we may drop terms which are exponentially suppressed for large k over the entire range of z . The remaining terms are simple exponentials and can be integrated over the interval. One finds that the trigonometric terms in (A.7.121) and (A.7.122) yield the expression

$$\frac{i}{\chi_{k_E+q} + \chi_{k_E}} \rightarrow \frac{-1}{\chi_{k+q} + \chi_k}, \quad (\text{A.7.127})$$

where on the right we have reversed our Wick rotation to obtain a Minkowski space expression for the terms which are not exponentially suppressed in Euclidean momentum. After doing this, the leading order term in $\cot \chi L$ in (A.7.121) and (A.7.122) equals i^{-1} and the terms in the braces become

$$\left\{ \frac{(\not{k} + \not{q}) \gamma^\mu \not{k} - \chi_{k+q} \chi_k \gamma^\mu}{\chi_k \chi_{k+q} (\chi_k + \chi_{k+q}) [(p+k)^2 - m_H^2]} \right\}, \quad (\text{A.7.128})$$

which gives the numerator of (A.7.116).

In terms of these quantities the potentially divergent amplitudes can be written as

$$\mathcal{M}_{(a)}^\mu = \int \frac{d^4 k}{(2\pi)^4} \frac{1}{(\chi_{k+q} + \chi_k)[(p+k)^2 - m_H^2]} \bar{u}(p) \left\{ \frac{(\not{k} + \not{q})}{\chi_{k+q}} \gamma^\mu - \gamma^\mu \frac{\not{k}}{\chi_k} \right\} u(p+q), \quad (\text{A.7.129})$$

$$\mathcal{M}_{(b)}^\mu = \int \frac{d^4 k}{(2\pi)^4} \frac{1}{(\chi_{k+q} + \chi_k)[(p+k)^2 - m_H^2]} \bar{u}(p) \left\{ \gamma^\mu \frac{\not{k}}{\chi_k} - \frac{(\not{k} + \not{q})}{\chi_{k+q}} \gamma^\mu \right\} u(p+q), \quad (\text{A.7.130})$$

therefore these two terms cancel each other in the UV and the operator (2.4.27) is finite.

Higher mass insertions do not spoil this cancellation since these are associated with internal brane-to-brane propagators whose UV limit goes like $\Delta(k) \sim \not{k}/\chi_k$. The chiral structure of the effective operator (2.4.27) requires that only diagrams with an odd number of mass insertions contribute. Using the UV limit $\Delta(k)^2 \rightarrow 1$ one notes that the divergence structure reduces to the case above.

APPENDIX B

DETAILS FOR $B \rightarrow S\gamma$ CALCULATION

B.1 Dimensionless Integrals for Leading Diagrams

This appendix defines the dimensionless integrals associated with the leading contributions to the a and b terms of the dipole Wilson coefficients $C_{7,8}$ in Section 3.3. Details of the derivation of these integrals are found in the appendix of [156]. In the mass insertion approximation the Standard Model contribution appears as an infrared pole, which we subtract.

B.1.1 Propagator functions

We use dimensionless integration variables $x \equiv k_E z \in [wy, y]$ and $y \equiv k_E R' \in [0, \infty]$, where k_E is the Euclidean loop momentum and $w = (R/R')$ is the warp factor. The integrals are expressed with respect to the functions that appear in the mixed position–Euclidean momentum space fermion propagator,

$$\Delta(k_E, x, x') \equiv i \frac{R'}{w^4} \bar{\mathcal{D}} \tilde{F}_y^{xx'} = \begin{pmatrix} y \tilde{D}_- \tilde{F}_- & \sigma^\mu y_\mu \tilde{F}_+ \\ \bar{\sigma}^\mu y_\mu \tilde{F}_- & y \tilde{D}_+ \tilde{F}_+ \end{pmatrix}, \quad \tilde{D}_\pm \equiv \pm \left(\partial_x - \frac{2}{x} \right) + \frac{c}{x}. \quad (\text{B.1.1})$$

where the \tilde{F} functions are defined for $x > x'$ (i.e. $z > z'$) by

$$\tilde{F}_-^L = \frac{(xx')^{5/2}}{y^5} \frac{S_{c_L}(x_-, y_-) S_{c_L}(x'_-, wy_-)}{S_{c_L}(y_-, wy_-)} \quad \tilde{F}_+^L = - \frac{(xx')^{5/2}}{y^5} \frac{T_{c_L}(x_+, y_-) T_{c_L}(x'_+, wy_-)}{S_{c_L}(y_-, wy_-)} \quad (\text{B.1.2})$$

$$\tilde{F}_-^R = - \frac{(xx')^{5/2}}{y^5} \frac{T_{c_R}(x_-, y_+) T_{c_R}(x'_-, wy_+)}{S_{c_R}(y_+, wy_+)} \quad \tilde{F}_+^R = \frac{(xx')^{5/2}}{y^5} \frac{S_{c_R}(x_+, y_+) S_{c_R}(x'_+, wy_+)}{S_{c_R}(y_+, wy_+)}. \quad (\text{B.1.3})$$

The analogous functions for $x < x'$ are given by replacing $x \leftrightarrow x'$ in the above formulas. S and T function are products of Bessel functions,

$$S_c(x_{\pm}, x'_{\pm}) = I_{c\pm 1/2}(x)K_{c\pm 1/2}(x') - I_{c\pm 1/2}(x')K_{c\pm 1/2}(x) \quad (\text{B.1.4})$$

$$S_c(x_{\pm}, x'_{\mp}) = I_{c\pm 1/2}(x)K_{c\mp 1/2}(x') - I_{c\mp 1/2}(x')K_{c\pm 1/2}(x) \quad (\text{B.1.5})$$

$$T_c(x_{\pm}, x'_{\mp}) = I_{c\pm 1/2}(x)K_{c\mp 1/2}(x') + I_{c\mp 1/2}(x')K_{c\pm 1/2}(x). \quad (\text{B.1.6})$$

Similarly, the mixed position–Euclidean momentum space vector propagators are $-i\eta^{\mu\nu}G$ and $i\bar{G}$ for the 4-vector and scalar parts respectively. For $x < x'$, the G functions are,

$$G_k(z, z') = \frac{(R')^2}{R} G_y(x, x') = \frac{(R')^2}{R} \frac{xx'}{y} \frac{T_{10}(x, y)T_{10}(x', wy)}{S_{00}(wy, y)}, \quad (\text{B.1.7})$$

$$G_{5k}(z, z') = \frac{(R')^2}{R} \bar{G}_y(x, x') = \frac{(R')^2}{R} \frac{xx'}{y} \frac{S_{00}(x, y)S_{00}(x', wy)}{S_{00}(wy, y)}, \quad (\text{B.1.8})$$

where

$$T_{ij}(x, y) = I_i(x)K_j(y) + I_j(y)K_i(x) \quad (\text{B.1.9})$$

$$S_{ij}(x, y) = I_i(x)K_j(y) - I_j(y)K_i(x). \quad (\text{B.1.10})$$

For $z < z'$ the above formula is modified by $x \leftrightarrow x'$.

B.1.2 C_7 integrals

We label vertices such that the external fermion legs attach to vertices 1 and 3, and the photon or gluon is emitted at vertex 2. Propagators attached to the brane $x = y$ signify Yukawa couplings or mass insertions, which may change the fermion flavor as labeled by its bulk mass, c . We have left this c dependence implicit in the following expressions.

$$\begin{aligned}
I_{C_{7a}} = & \int dy dx y^2 \left(\frac{y}{x}\right)^4 \left[-2\tilde{F}_{+,y}^{Lyx} \tilde{F}_{+,y}^{Lxy} \tilde{F}_{-,y}^{Ryy} \frac{y^2}{y^2 + (M_W R')^2} \right. \\
& + \tilde{F}_{+,y}^{Lyx} \tilde{F}_{+,y}^{Lxy} \tilde{F}_{-,y}^{Ryy} \frac{y^4}{(y^2 + (M_W R')^2)^2} - \frac{1}{2} \left(y \partial_{k_E} \tilde{F}_{+,y}^{Lyx} \right) \tilde{F}_{+,y}^{Lxy} \tilde{F}_{-,y}^{Ryy} \frac{y^2}{y^2 + (M_W R')^2} \\
& - \frac{1}{2} \left(y \partial_{k_E} \tilde{D}_- \tilde{F}_{-,y}^{Lyx} \right) \tilde{D}_+ \tilde{F}_{+,y}^{Lxy} \tilde{F}_{-,y}^{Ryy} \frac{1}{y^2 + (M_W R')^2} + 2\tilde{F}_{+,y}^{Lyx} \tilde{D}_+ \tilde{F}_{+,y}^{Ryx} \tilde{D}_- \tilde{F}_{-,y}^{Rxy} \frac{1}{y^2 + (M_W R')^2} \\
& - \tilde{F}_{+,y}^{Lyx} \tilde{D}_+ \tilde{F}_{+,y}^{Ryx} \tilde{D}_- \tilde{F}_{-,y}^{Rxy} \frac{y^2}{(y^2 + (M_W R')^2)^2} + \frac{1}{2} \left(y \partial_{k_E} \tilde{F}_{+,y}^{Lyx} \right) \tilde{D}_+ \tilde{F}_{+,y}^{Ryx} \tilde{D}_- \tilde{F}_{-,y}^{Rxy} \frac{1}{y^2 + (M_W R')^2} \\
& + \tilde{F}_{+,y}^{Lyx} \tilde{F}_{-,y}^{Ryx} \tilde{F}_{-,y}^{Rxy} \frac{y^2}{y^2 + (M_W R')^2} + \frac{1}{2} \left(y \partial_{k_E} \tilde{F}_{+,y}^{Lyx} \right) \tilde{F}_{-,y}^{Ryx} \tilde{F}_{-,y}^{Rxy} \frac{y^2}{y^2 + (M_W R')^2} \\
& + \frac{1}{2} \tilde{F}_{+,y}^{Lyx} \left(y \partial_{k_E} \tilde{F}_{-,y}^{Ryx} \right) \tilde{F}_{-,y}^{Rxy} \frac{y^2}{y^2 + (M_W R')^2} \\
& \left. + \frac{1}{2} \tilde{F}_{+,y}^{Lyx} \left(y \partial_{k_E} \tilde{D}_+ \tilde{F}_{+,y}^{Ryx} \right) \tilde{D}_- \tilde{F}_{-,y}^{Rxy} \frac{1}{y^2 + (M_W R')^2} \right]. \tag{B.1.11}
\end{aligned}$$

The C_{7b} integral is the sum of two parts corresponding to diagrams with an internal gluon (G) or scalar gluon (G_5) in the loop,

$$I_{C_{7b}} = I_{C_{7b}}^{(G)} + I_{C_{7b}}^{(G_5)}. \tag{B.1.12}$$

Each of these terms include diagrams with a single mass insertion, either on the incoming, internal, or outgoing fermion line.

$$\begin{aligned}
I_{C_{7b}} = & \int dy dx_1 dx_2 dx_3 y \left(\frac{y}{x_2}\right)^4 \partial_{k_E} G^{31} \\
& \left\{ \frac{1}{2} \left(\frac{y}{x_1}\right)^{2+c_L} \left(\frac{y}{x_3}\right)^4 \tilde{D}_+ \tilde{F}_{+, (m_b R')}^{L(x_3 m_b R'/y)(m_b R')} \left(\tilde{D}_- \tilde{F}_{-,y}^{L12} \tilde{F}_{-,y}^{L23} + \tilde{F}_{+,y}^{L12} \tilde{D}_- \tilde{F}_{-,y}^{L23} \right) \right. \\
& + \frac{1}{2} \left(\frac{y}{x_1}\right)^4 \left(\frac{y}{x_3}\right)^{2-c_R} \tilde{D}_+ \tilde{F}_{+, (m_b R')}^{R(m_b R')(x_1 m_b R'/y)} \left(\tilde{D}_- \tilde{F}_{-,y}^{R12} \tilde{F}_{-,y}^{R23} + \tilde{F}_{+,y}^{R12} \tilde{D}_- \tilde{F}_{-,y}^{R23} \right) \\
& + \left(\frac{y}{x_1}\right)^{2+c_L} \left(\frac{y}{x_3}\right)^{2-c_R} \left(-\tilde{D}_+ \tilde{F}_{+,y}^{R32} \tilde{D}_- \tilde{F}_{-,y}^{R2y} \tilde{F}_{+,y}^{Ly1} + y^2 \tilde{F}_{-,y}^{R32} \tilde{F}_{-,y}^{R2y} \tilde{F}_{+,y}^{Ly1} \right. \\
& \left. \left. - \tilde{D}_- \tilde{F}_{-,y}^{Ly2} \tilde{D}_+ \tilde{F}_{+,y}^{L21} \tilde{F}_{-,y}^{R3y} + y^2 \tilde{F}_{-,y}^{R3y} \tilde{F}_{+,y}^{Ly2} \tilde{F}_{+,y}^{L21} \right) \right\} \tag{B.1.13}
\end{aligned}$$

$$\begin{aligned}
I'_{C_{7b}} = & \int dy dx_1 dx_2 dx_3 \frac{1}{2} \left(\frac{y}{x_2} \right)^4 \\
& \left\{ \left(\frac{y}{x_1} \right)^{2+c_L} \left(\frac{y}{x_3} \right)^4 \tilde{D}_+ \tilde{F}_{+, (m_b R')}^{L(x_3 m_b R' / y)(m_b R')} \times \right. \\
& \left(\tilde{F}_{-, y}^{L12} \tilde{D}_+ \tilde{F}_{+, y}^{L23} (y \partial_{k_E} G_5^{31} + 4 G_5^{31}) + y G_5^{31} (\tilde{D}_+ \tilde{F}_{+, y}^{L23} \partial_{k_E} \tilde{F}_{-, y}^{L12} - \tilde{F}_{+, y}^{L23} \partial_{k_E} \tilde{D}_+ \tilde{F}_{+, y}^{L12}) \right) \\
& + \left(\frac{y}{x_1} \right)^4 \left(\frac{y}{x_3} \right)^{2-c_R} \tilde{D}_+ \tilde{F}_{+, (m_b R')}^{R(m_b R')(x_1 m_b R' / y)} \times \\
& \left(\tilde{F}_{-, y}^{R12} \tilde{D}_+ \tilde{F}_{+, y}^{R23} (y \partial_{k_E} G_5^{31} + 4 G_5^{31}) + y G_5^{31} (\tilde{D}_+ \tilde{F}_{+, y}^{R23} \partial_{k_E} \tilde{F}_{-, y}^{R12} - \tilde{F}_{+, y}^{R23} \partial_{k_E} \tilde{D}_+ \tilde{F}_{+, y}^{R12}) \right) \\
& + \left(\frac{y}{x_1} \right)^{2+c_L} \left(\frac{y}{x_3} \right)^{2-c_R} \times \\
& \left(\tilde{D}_+ \tilde{F}_{+, y}^{L12} (4 + y \partial_{k_E}) (\tilde{F}_{+, y}^{L2y} \tilde{D}_+ \tilde{F}_{+, y}^{Ry3} G_5^{13}) - y \tilde{F}_{-, y}^{L12} \partial_{k_E} (\tilde{D}_+ \tilde{F}_{+, y}^{L2y} \tilde{D}_+ \tilde{F}_{+, y}^{Ry3}) G_5^{13} \right. \\
& \left. + \tilde{D}_+ \tilde{F}_{+, y}^{L1y} \tilde{D}_+ \tilde{F}_{+, y}^{Ry2} (4 + y \partial_{k_E}) (\tilde{F}_{+, y}^{R23} G_5^{13}) - y \tilde{D}_+ \tilde{F}_{+, y}^{L1y} \tilde{F}_{-, y}^{Ry2} G_5^{13} \partial_{k_E} \tilde{D}_+ \tilde{F}_{+, y}^{R23} \right) \Big\} \\
\end{aligned} \tag{B.1.14}$$

B.1.3 C_8 integrals

The C_{8a} integral contains a piece identical to the C_{7a} integral associated with the charged Higgs loop as well as gluon loop diagrams with three mass insertions,

$$I_{C_{8a}} = I_{C_{8a}}^{(1)} + 2I_{C_{8a}}^{(2)} + I_{C_{8a}}^{(3)}. \tag{B.1.15}$$

The gluon loops are labeled by the number of internal mass insertions, so that $I_{C_{8a}}^{(1)}$ is associated with the diagram with an external mass insertion on each leg, and the factor

of two on $I_{C_{8a}}^{(2)}$ accounts for the two possible placements of the external mass insertion¹.

$$I_{C_{8a}}^{(1)} = \int dy dx_1 dx_2 dx_3 \left(\frac{y}{x_1} \right)^4 \left(\frac{y}{x_2} \right) \left(\frac{y}{x_3} \right)^4 \times \\ \tilde{D}_+ \tilde{F}_{+,y_s}^{Ry1} \tilde{D}_- \tilde{F}_{-,y}^{R10} \tilde{D}_- \tilde{F}_{-,y}^{Ly3} \tilde{D}_+ \tilde{F}_{+,y_b}^{L3y} \left\{ -\frac{5}{2} y \partial_{k_E} (G_y^{12} G_y^{23}) + 10 G_y^{12} G_y^{23} \right\}, \quad (\text{B.1.16})$$

$$I_{C_{8a}}^{(2)} = \int dy dx_1 dx_2 dx_3 \left(\frac{y}{x_1} \right)^{2+c_L} \left(\frac{y}{x_2} \right) \left(\frac{y}{x_3} \right)^4 y^3 \times \\ \tilde{F}_{+,y}^{L1y} \tilde{F}_{-,y}^{Ryy} \tilde{D}_- \tilde{F}_{-,y}^{Ly3} \tilde{D}_+ \tilde{F}_{+, (m_b R')}^{L(x_3 m_b R' / y)(m_b R')} \partial_{k_E} (G_y^{12} G_y^{23}) \quad (\text{B.1.17})$$

$$I_{C_{8a}}^{(3)} = \int dy dx_1 dx_2 dx_3 \left(\frac{y}{x_1} \right)^{2+c_L} \left(\frac{y}{x_2} \right) \left(\frac{y}{x_3} \right)^{2-c_R} y^2 \times \\ \tilde{F}_{+,y}^{L1y} \tilde{F}_{-,y}^{Ry3} \tilde{F}_{+,y}^{Lyy} \tilde{F}_{-,y}^{Ryy} \left\{ -\frac{5}{2} y \partial_{k_E} (G_y^{12} G_y^{23}) + 10 G_y^{12} G_y^{23} \right\}. \quad (\text{B.1.18})$$

For C_{8b} , the only dominant diagram is the gluon loop with an internal mass insertion. All other analogous diagrams (e.g. mass insertion on an external leg, or loops with G^5) contain no zero modes and hence give negligible contributions after alignment.

$$I_{C_{8b}} = \int dy dx_1 dx_2 dx_3 \left(\frac{y}{x_1} \right)^{2+c_L} \left(\frac{y}{x_2} \right) \left(\frac{y}{x_3} \right)^{2-c_R} y^2 \times \\ \tilde{F}_{+,y}^{L1y} \tilde{F}_{-,y}^{Ry3} \left\{ -\frac{5}{2} y \partial_{k_E} (G_y^{12} G_y^{23}) + 10 G_y^{12} G_y^{23} \right\}. \quad (\text{B.1.19})$$

B.2 Estimating the size of the misalignment contribution

In this appendix we clarify a subtlety in the size of the anarchic contributions ($\Delta C_{7,8a}^{(\prime)}$) versus the misalignment contributions ($\Delta C_{7,8b}^{(\prime)}$) to the Wilson coefficients, as defined in Section 3.3.2. For the anarchic contributions the relative sizes of the right-to-left (unprimed) coefficients to the left-to-right (primed) coefficients are given by the relative size of the f_{b_L} and f_{b_R} wavefunctions on the IR brane. On the other hand, the misalignment contributions for the two chiral transitions do not follow this pattern and are, in fact, of the same

¹ These integrands differ by $L \leftrightarrow R$, but the integrals are approximately the same.

order of magnitude. We show here that this apparent inconsistency can be understood by accounting for cancelations coming from the rotation to the SM fermion mass basis.

For simplicity, consider the 2×2 matrix of misalignment diagrams $q_j^R \rightarrow q_i^L$ where we only consider the second and third generations. This transition is given by the b_{ij} term in (3.3.13), which we may parameterize as

$$(\text{misalignment term})_{ij} \sim \begin{pmatrix} (b - c - d) y_{11} & (b - c + d) y_{12} \\ (b + c - d) y_{21} & (b + c + d) y_{22} \end{pmatrix}. \quad (\text{B.2.20})$$

Here we have written b as an average scale for the b_{ij} matrix, and $y_{ij} = f_{Q_i} Y_{d_{ij}}^\dagger f_{D_j}$. The $c \sim 10^{-1}$ and $d \sim 10^{-2}$ terms represent deviations from the average. In particular, the c deviations account for the effect of an internal b_L (whose zero mode profile is very different from that of the light quarks) while the d deviations account for the smaller effect of an internal b_R .

In order to pass to the physical basis, one must apply to this matrix the same rotation that diagonalizes the SM mass matrix, which is proportional to y . The off-diagonal terms of the rotated misalignment matrix give the C_7 and C_7' coefficients (the argument for C_8 is identical),

$$\begin{pmatrix} 1 & \delta \\ \delta' & 1 \end{pmatrix} (\text{misalignment term}) \begin{pmatrix} 1 & \gamma \\ \gamma' & 1 \end{pmatrix} \sim \begin{pmatrix} & C_{7b} \\ C_{7b}^\dagger & \end{pmatrix}. \quad (\text{B.2.21})$$

The parameters δ and γ are ratios of the left- and right-handed zero mode wavefunctions on the brane; the primed and unprimed parameters are related by a minus sign.

We focus on order of magnitude estimates, so we introduce a numerical parameter $\epsilon \sim 10^{-1}$. Normalizing the Yukawa to $y_{22} = 1$, our parameters are approximately

$$c \sim \epsilon \quad d \sim \epsilon^2 \quad y_{11} \sim \epsilon^3 \quad y_{12} \sim \epsilon^2 \quad y_{21} \sim \epsilon \quad \delta^{(\prime)} \sim \epsilon^2 \quad \gamma^{(\prime)} \sim \epsilon. \quad (\text{B.2.22})$$

Note that ϵ is merely a fiducial quantity, not an expansion parameter of the model. We now apply the rotation (B.2.21) and study the order of magnitude of the off-diagonal terms. By construction the terms proportional to b are completely diagonalized. We consider the terms proportional to c (f_{b_L}) and d (f_{b_R}) separately.

B.2.1 Misalignment from f_{b_L}

First consider the terms proportional to c , which are split by the relative size of f_{b_L} versus f_{s_L} from internal zero mode propagators. The part of the C'_{7b} term proportional to c goes like

$$C'_{7b} \Big|_c \sim (y_{21} + \gamma' y_{22}) - \delta' (\gamma' y_{12} + y_{11}) . \quad (\text{B.2.23})$$

Naively the first term is of $\mathcal{O}(\epsilon)$ and appears to dominate the expression. This, however, does not account for relations coming from alignment. Observe that the minus sign here comes from the choice of parameterization in (B.2.20). Further, observe that changing the relative sign in (B.2.23) is equivalent to changing the sign of c in the top row of (B.2.20). In this case, however, the c matrix would be completely aligned with the SM mass matrix and the off diagonal term (B.2.23) would vanish. Thus the first and second terms in (B.2.23) must be of the same order of magnitude in order for them to cancel when the relative sign is swapped—in other words, $(y_{21} + \gamma' y_{22}) \sim \epsilon^5$ in order to match the naive order of magnitude of the second term. We thus have

$$c C'_{7b} \Big|_c \sim \epsilon^6 . \quad (\text{B.2.24})$$

This observation reflects the key cancelation that causes the relative size of the primed and unprimed misalignment terms to differ from that of the anarchic terms of the amplitude.

The contribution to the C_{7b} term proportional to c is

$$C_{7b}|_c \sim \delta (\gamma y_{21} + y_{22}) - (\gamma y_{11} + y_{12}) . \quad (\text{B.2.25})$$

Unlike C'_{7b} , both terms in the above expression are dominated by their $\mathcal{O}(\epsilon^2)$ components and we find

$$c C_{7b}|_c \sim \epsilon \epsilon^2 = \epsilon^3, \quad (\text{B.2.26})$$

as expected from a naive estimate.

B.2.2 Misalignment from f_{b_R}

We perform the same analysis on the terms proportional to d , which implicitly encode the split between terms that carry factors of f_{b_R} versus f_{s_R} from internal propagators. For C_{7b} we have

$$C_{7b}|_d \sim (y_{12} + \delta y_{22}) - \gamma (y_{11} + \delta y_{21}) . \quad (\text{B.2.27})$$

Following the argument that the terms should cancel when the sign is swapped and using this to estimate the size of each bracketed term, one finds $d C_{7b}|_d \sim \epsilon^6$, so that the net contribution of the d term is subdominant to (B.2.26).

On the other hand, the f_{b_R} misalignment in the C'_{7b} term cannot be neglected,

$$C'_{7b}|_d \sim \gamma' (\delta' y_{12} + y_{22}) - (\delta' y_{11} + y_{21}) . \quad (\text{B.2.28})$$

Here both terms are $\mathcal{O}(\epsilon)$ so that the total contribution is

$$d C'_{7b}|_d \sim \epsilon^3, \quad (\text{B.2.29})$$

which dominates over the term proportional to c in (B.2.24).

B.2.3 Size of misalignment coefficients

Thus the final order of magnitude estimate for the C_{7b} and C'_{7b} coefficients are

$$C_{7b} \sim c \, C_{7b}|_c \sim \epsilon^3 \quad (\text{B.2.30})$$

$$C'_{7b} \sim d \, C'_{7b}|_d \sim \epsilon^3, \quad (\text{B.2.31})$$

so that unlike the anarchic contribution, the right-to-left (unprimed) and left-to-right (primed) Wilson coefficients are of the same order of magnitude.

B.3 Comments on 5D dipole theory uncertainties

Finite 5D loop effects carry subtleties associated with cutoffs and UV sensitivity². While the one loop contribution discussed in this paper is manifestly finite, higher loops are potentially divergent and require explicit calculations. Here we focus on the sensitivity of the finite loop-level result to UV physics at, for example, the strong coupling scale where the 5D theory is expected to break down. In [20] it was pointed out that the naive dimensional analysis (NDA) for a brane and a bulk Higgs differ due to the dimension of the Yukawa coupling—the NDA two-loop contribution for the former gives an $\mathcal{O}(1)$ correction relative to the one loop result, whereas this is not expected for the latter. In this appendix we comment on subtleties coming from 5D Lorentz invariance that may plausibly avoid this ‘worst case’ NDA estimate. Indeed, the NDA for the one-loop contribution to these dipole operators is logarithmically divergent; one may understand the correct one-loop finiteness as coming from 5D Lorentz symmetry.

These comments are meant to demonstrate non-trivial points in these calculations that

²We thank K. Agashe, J. Hubisz, and G. Perez for discussions on these subtleties.

require particular care when drawing conclusions about UV sensitivity in these processes; a more careful investigation with explicit calculations of these effects is beyond the scope of this work.

Note that the general features of the phenomenological picture presented in Section 3.6 are unchanged even if there are $\mathcal{O}(1)$ corrections to the Wilson coefficients.

B.3.1 KK decomposition

5D Lorentz invariance imposes that in the KK reduced theory, the 4D loop momentum cutoff should be matched to the number of KK modes in the effective theory. This was mentioned in [156] to motivate a manifestly 5D calculation by pointing out that naively taking the finite 4D loop cutoff to infinity drops terms of the form $(nM_{\text{KK}}/\Lambda)^2$, where nM_{KK} is approximately the mass of the n^{th} KK mode. Indeed, from the 4D perspective this may appear to suggest a non-decoupling effect where the dominant contribution comes from heavy KK states so that the calculation seems to be sensitive to UV physics.

However, as demonstrated in Fig. B.1, imposing 5D Lorentz invariance requires that each KK mode carries a different 4D momentum cutoff. In particular, the n^{th} KK mode carries a smaller 4D cutoff Λ_n than that of the first KK mode, Λ_1 since the momentum integral must fall within the circle of radius Λ , the 5D momentum space cutoff. Thus in 4D the high KK modes are not sensitive to the same cutoff as lower KK modes. This gives a sense in which 4D decoupling can manifest itself while preserving 5D Lorentz invariance. In this sense it is difficult to use this matching to diagnose UV sensitivity.

As a qualitative and demonstrative estimate, one can use the expression in Section 6.6 of [156] for a neutral Higgs diagram and impose a KK number dependent cutoff for each

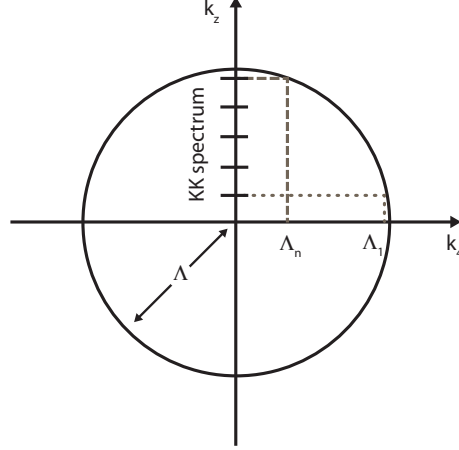


Figure B.1: A sketch of the 5D momentum space where the circle of radius Λ represents the boundary of a 5D Lorentz invariant loop momentum integration region. Marks on the k_z axis show the masses of KK states. Dashed lines demonstrate that the 4D loop cutoff which respects 5D Lorentz invariance depends on the particular KK mode.

state in the loop so that 5D Lorentz invariance is imposed as in Fig. B.1. One finds that, for example, in a sum of 200 KK modes, the highest 20 modes only contribute $\sim 20\%$ to the total result.

B.3.2 5D cutoff

Another way to diagnose UV sensitivity is to consider the effect of a cutoff in the 5D picture, for example, by setting a cutoff at $\Lambda = 5$ TeV representing the strong coupling scale at which the 5D theory breaks down. Fig. B.2 shows the dimensionless integral associated with the charged Higgs loop, where $y = R'k_E$ is the dimensionless variable representing the loop momentum. Observe that the dominant contribution to the effect does not come from arbitrarily large y but rather in the peak at low values of y . Cutting off the integral at $\Lambda = 5$ TeV (dashed line) gives an error of approximately 15%, which is comparable to the subleading diagrams that were not included in this analysis.

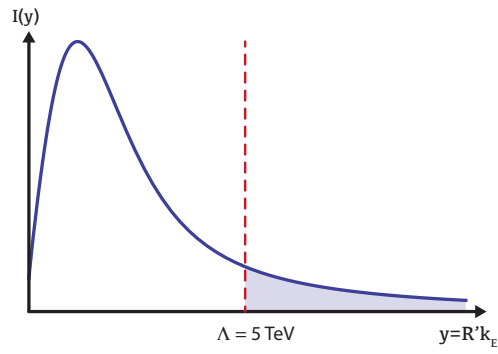


Figure B.2: Plot of the charged Higgs integrand as a function of the dimensionless loop momentum in the position/momentum space picture. The dashed line is a heuristic 5D cutoff Λ representing the strong coupling scale. The shaded region represents the error from taking the loop momentum to infinity rather than Λ ; the contribution of this shaded region is approximately 15% of the total integral.

APPENDIX C

USEFUL LEMMA FOR R -SYMMETRY BREAKING

In this appendix, we will prove the following lemma described above in section 4.

Lemma: Consider a square hermitian matrix M , divided into blocks

$$M = \begin{pmatrix} M_{11} & M_{12} & M_{13} \\ M_{12}^\dagger & M_{22} & M_{23} \\ M_{13}^\dagger & M_{23}^\dagger & M_{33} \end{pmatrix} \quad (\text{C.0.1})$$

with M_{ij} being $m_i \times m_j$. Suppose that M satisfies:

$$(M^k)_{13} = 0 \quad \text{for all } k = 1, 2, \dots \quad (\text{C.0.2})$$

Then there exists a block unitary transformation $M \rightarrow U M U^\dagger$ with

$$U = \begin{pmatrix} U_1 & & \\ & U_2 & \\ & & U_3 \end{pmatrix} \quad (\text{C.0.3})$$

such that M takes the block-diagonal form

$$M = \begin{pmatrix} \tilde{M}_{11} & 0 \\ 0 & \tilde{M}_{22} \end{pmatrix} \quad (\text{C.0.4})$$

with the 12 block that is zero in eq. (C.0.4) containing the 13 block in the original basis.

Proof: We will prove this by induction, by starting with general m_1, m_2, m_3 and then reducing this to the same claim but with smaller m_i . The $k = 1$ version of eq. (C.0.2) implies that $M_{13} = 0$. The $k = 2$ condition implies that $M_{12}M_{23} = 0$. Combining this with

a choice of U_1 , U_2 and U_3 , we can always simultaneously block-diagonalize M_{12} and M_{23} :

$$M_{12} = \begin{pmatrix} (A)_{m'_1 \times m'_1} & 0 & 0 \\ 0 & 0 & 0 \end{pmatrix} \quad M_{23} = \begin{pmatrix} 0 & 0 \\ 0 & 0 \\ 0 & (B)_{m'_3 \times m'_3} \end{pmatrix} \quad (\text{C.0.5})$$

with A and B nonsingular, and $m'_1 \leq m_1, m_2$, $m'_3 \leq m_2, m_3$, and $m'_1 + m'_3 \leq m_2$. Dividing M_{22} into 3×3 blocks like eq. (C.0.1) with $m_i \rightarrow m'_i$, the $k \geq 3$ versions of eq. (C.0.2) imply

$$((M_{22})^\ell)_{1'3'} = 0 \quad \text{for all } \ell = 1, 2, \dots \quad (\text{C.0.6})$$

So we see that eq. (C.0.2) maps on to an identical condition for the smaller matrix M_{22} .

Moreover, examining the form of eq. (C.0.1), after substituting eq. (C.0.5), we find:

$$M = \begin{pmatrix} M_{11} & \begin{pmatrix} A & 0 & 0 \\ 0 & 0 & 0 \end{pmatrix} & 0 \\ \begin{pmatrix} A^\dagger & 0 \\ 0 & 0 \\ 0 & 0 \end{pmatrix} & M_{22} & \begin{pmatrix} 0 & 0 \\ 0 & 0 \\ 0 & B \end{pmatrix} \\ 0 & \begin{pmatrix} 0 & 0 & 0 \\ 0 & 0 & B^\dagger \end{pmatrix} & M_{33} \end{pmatrix} \quad (\text{C.0.7})$$

So we see that the desired 2×2 block form eq. (C.0.4) can be achieved, provided M_{22} can be put into an analogous 2×2 block form, also with a block-unitary transformation. This completes the inductive recursion. Proceeding in this way, we can reduce the lemma to a trivial statement about 3×3 matrices, which completes the proof by induction.

APPENDIX D

**DERIVATION OF THE AVERAGE DARK MATTER VELOCITY IN A DWARF
GALAXY**

In this appendix, we discuss the derivation of the average dark matter velocity in the Draco dwarf galaxy. We assume the radial distribution of dark matter in Draco to follow a Navarro-Frenk-White (NFW) profile [312],

$$\rho(r) = \rho_s \frac{r_s}{r} \frac{r_s^2}{(r + r_s)^2}, \quad (\text{D.0.1})$$

with scale radius $r_s = 2.09$ kpc and scale density $\rho_s = 0.98 \text{ GeV/cm}^3$ [11].

We then use the Eddington formula [91]

$$f(r, v) = \frac{1}{\sqrt{8\pi^2}} \frac{d}{d\mathcal{E}} \int_0^{\mathcal{E}} \frac{d\rho}{d\Psi} \frac{d\Psi}{\sqrt{\mathcal{E} - \Psi}} \quad (\text{D.0.2})$$

$$= \frac{1}{\sqrt{8\pi^2}} \int_0^{\mathcal{E}} d\Psi \frac{1}{\sqrt{\mathcal{E} - \Psi}} \frac{d^2\rho}{d\Psi^2} + \frac{1}{\sqrt{\mathcal{E}}} \frac{d\rho}{d\Psi} \Big|_{\Psi=0} \quad (\text{D.0.3})$$

to translate $\rho(r)$ into the velocity distribution $f(r, v)$ at radius r . Here, $\Psi(r) = -G \int_R^\infty dr M(r)/r^2$ is (minus) the gravitational potential at radius r , which is determined by the enclosed mass $M(r) = \int_0^r dr 4\pi r^2 \rho(r)$, and $\mathcal{E}(r, v) = \Psi(r) - \frac{1}{2}v^2$ is (minus) the dark matter energy per unit mass. The dark matter density ρ is treated as a function of Ψ rather than r here, which is well-defined if $\Psi(r)$ is a monotonic function of r ; the NFW profile has this property. The resulting velocity distribution $f(r, v)$ satisfies the normalization condition

$$\rho(r) = 4\pi \int dv v^2 f(r, v). \quad (\text{D.0.4})$$

The annihilation rate of dark matter is proportional to $\rho^2 \sigma v$, thus to obtain $\text{eV}v^2$, the average dark matter velocity in the Draco dwarf galaxy quoted in Section 8.5, we compute

$$\text{eV}v^2 = \frac{1}{N} \int_0^\infty dr 4\pi r^2 \rho^2(r) \int_0^1 dv 4\pi v^4 f(r, v) \quad (\text{D.0.5})$$

with the normalization constant $N = \int_0^\infty dr 4\pi r^2 \rho^2(r)$. We find $\text{eV}v^2 \approx (34.7 \text{ km/s})^2$, which corresponds to $\text{eV}v_{\text{rel}}^2 \approx (69.3 \text{ km/s})^2$.

APPENDIX E

SOME REMARKS FOR LEPTOGENESIS WITH COMPOSITE NEUTRINOS

E.1 Matching the UV theory to the effective theory

In this appendix, we obtain the effective Yukawa and L-violating couplings in eqs. (6.2.1) and (6.2.5) by integrating out the heavy fields in eqs. (6.3.10)-(6.3.15). This gives the relations between the effective couplings λ , h and those of the full theory.

We start from rewriting eqs. (6.3.10)-(6.3.15) keeping all the indices explicitly

$$Y_{gi}^L A_{abm} \sigma_{mn}^2 \Omega_g^{ba\alpha} L_{i\alpha n} + h.c., \quad (E.1.1)$$

$$\tilde{M}_g \tilde{H}^\alpha \Phi^{ab} \Omega_{gba\alpha} + h.c., \quad (E.1.2)$$

$$Y_{ff'}^A \psi_{fam} \sigma_{mn}^2 \Phi^{ab} \psi_{f'bn} + h.c., \quad (E.1.3)$$

$$Y_k^N \epsilon_{abopqr} \epsilon^{opqrst} \epsilon^{uvwxyz} \Phi^{ab} A_{uvm} \sigma_{mn}^2 N_{stwxk, kn} + h.c., \quad (E.1.4)$$

$$y_{ik}^N H^\alpha L_{\alpha i} N_k + h.c. \quad (E.1.5)$$

where here the upper indices represent the hermitian conjugate of the fields. As we can see in eq. (E.1.3), the antisymmetry in the spinor and the $SU(6)_C$ indices require $Y_{ff'}^A$ to be antisymmetric. The indices here are quite cumbersome, and we write them only when it is necessary in the following calculation.

To obtain the effective Yukawa coupling as an $(\psi A \psi L \tilde{H})$ vertex, we need to integrate out the heavy Ω and Φ fields in Fig. 6.1a. The Ω and Φ related couplings, including their mass terms and three vertices in the diagram, is

$$-M^2 \Omega^\dagger \Omega - M^2 \Phi^\dagger \Phi + Y^A \psi \Phi^\dagger \psi + Y^{L\dagger} L^\dagger \Omega A^\dagger + \tilde{M}^\dagger \Omega^\dagger \Phi \tilde{H} + h.c.. \quad (E.1.6)$$

After integrating Ω and Φ out, and using the convention $|\tilde{M}| = rM$, we obtain

$$\frac{1}{M^3} [Y^{L\dagger} r Y^A (L^\dagger A^\dagger \tilde{H}) (\psi^T \psi) + h.c.] \quad (E.1.7)$$

Writing the indices explicitly, we can rearrange the fields into a more transparent form for

composite neutrino

$$\begin{aligned}
& \frac{Y_i^{L\dagger} r Y_{ff'}^A}{M^3} (L_{im}^{*\alpha} \sigma_{mn}^2 A_n^{*ab} \tilde{H}_\alpha) (\psi_{fas} \sigma_{st}^2 \psi_{f'bt}) + h.c. = \\
& \frac{Y_i^{L\dagger} r Y_{ff'}^A}{M^3} (\psi_{fas} \sigma_{st}^2 A_m^{*ab} \psi_{f'bt}) \sigma_{mn}^2 L_{in}^{*\alpha} \tilde{H}_\alpha + h.c. \equiv \\
& \lambda^{ff',i} \frac{(\psi_f^T A^* \psi_{f'}) L_i^\dagger \tilde{H}}{M^3} + h.c., \tag{E.1.8}
\end{aligned}$$

where

$$\lambda^{ff',i} = Y_i^{L\dagger} r Y_{ff'}^A \Rightarrow \lambda \sim r |Y^L| |Y^A|. \tag{E.1.9}$$

Note that the second equality implies that when interchanging ff' , the antisymmetry of A^{ab} and $Y_{ff'}^A$ makes the whole RH neutrino part invariant. This gives the correct form for $B_{ff'}$, the massless composite neutrinos.

For the L-violating coupling, eq. (6.2.5), we need to include the heavy Majorana fermion N . The related couplings in Fig. 6.1b are:

$$- M N N - M^2 \Phi^\dagger \Phi + Y^{N\dagger} N^\dagger A^\dagger \Phi A + Y^A \psi \Phi^\dagger \psi + h.c.. \tag{E.1.10}$$

After integrating out N and Φ , we obtain

$$\frac{(Y^A Y^{N\dagger})^2}{4M^5} (\psi^T \psi A^*) (A^\dagger \psi^T \psi) + h.c.. \tag{E.1.11}$$

Writing this in a form that is best for studying composite neutrinos, we have

$$\begin{aligned}
& \frac{(Y_{ff'}^A Y^{N\dagger})(Y_{gg'}^A Y^{N\dagger})}{4M^5} (\psi_{fm} \sigma_{mn}^2 \psi_{f'n} A_o^\dagger) \sigma_{op}^2 (A_p^* \psi_{gs} \sigma_{st}^2 \psi_{g't}) = \\
& \frac{(Y_{ff'}^A Y^{N\dagger})(Y_{gg'}^A Y^{N\dagger})}{4M^5} (\psi_{fm} \sigma_{mn}^2 A_o^\dagger \psi_{f'n})^T \sigma_{op}^2 (\psi_{gs} \sigma_{st}^2 A_p^* \psi_{g't}) \equiv \\
& h^{ff',gg'} \frac{(\psi_f^T A^\dagger \psi_{f'}) (\psi_g^T A^* \psi_{g'})}{M^5}, \tag{E.1.12}
\end{aligned}$$

where

$$h^{ff',gg'} = \frac{1}{4} (Y_{ff'}^A Y^{N\dagger})(Y_{gg'}^A Y^{N\dagger}) \Rightarrow h \sim |Y^N|^2 |Y^A|^2. \tag{E.1.13}$$

E.2 Calculation of $\mu \rightarrow e\gamma$

In this appendix, we calculate the bounds on M given by the lepton flavor violating (LFV) process $\mu \rightarrow e\gamma$. The vertices and the kinematics of the LFV process are shown in Fig. E.1.

Throughout the calculation, we neglect the mass of the out-going electron. We first evaluate the amplitude of the diagram where the photon coming from the external muon. This diagram scales as the electron mass and thus vanish in the limit of massless electron.

Explicitly the diagram gives

$$\begin{aligned} M_{\mu \rightarrow \gamma} &= \bar{u}_{e_R}(-iY_L^*) \int \frac{d^4k}{(2\pi)^4} \frac{i}{k^2 - M^2} \frac{i(\not{p}' - \not{k})}{(p' - k)^2} (iY_L) \frac{i(\not{p}' + m_\mu)}{(p'^2 - m_\mu^2)} (-ie\not{\varepsilon}) u_\mu \\ &= -e|Y^L|^2 \bar{u}_{e_R} \left[\int \frac{d^4k}{(2\pi)^4} \frac{\not{p}' - \not{k}}{(k^2 - M^2)(p' - k)^2} \right] \frac{\not{p}' + m_\mu}{p'^2 - m_\mu^2} \not{\varepsilon} u_\mu. \end{aligned} \quad (\text{E.2.14})$$

Here M , m_μ , m_e are the masses of Ω , μ , e , we use $p' \equiv (p - q)$, and ε^μ is the polarization of the outgoing photon. Integrating out the loop momentum and doing the dimensional regularization, we get the amplitude as

$$M_{\mu \rightarrow \gamma} = \frac{-ie|Y^L|^2}{32\pi^2} \bar{u}_{e_R} \left(\not{p}' \frac{\not{p}' + m_\mu}{p'^2 - m_\mu^2} \not{\varepsilon} \right) \left(\frac{2}{\epsilon} - \gamma + \ln(4\pi) + \frac{1}{2} - \ln M^2 \right) u_\mu. \quad (\text{E.2.15})$$

Here γ is the Euler-Mascheroni constant, $\epsilon \equiv 4 - d$ and we take $d \rightarrow 4$ for the finite terms. We use the condition of transverse polarization

$$\varepsilon_\mu q^\mu = 0, \quad \varepsilon_\mu p^\mu = 0, \quad \varepsilon_\mu p'^\mu = 0. \quad (\text{E.2.16})$$

Then, we see that the diagram vanishes, that is, $M_{\mu \rightarrow \gamma} = 0$.

The amplitude of the diagram where the external photon is emitted by the electron can be written as

$$\begin{aligned} M_{e \rightarrow \gamma} &= \bar{u}_{e_R}(-ie\not{\varepsilon}) \frac{i(\not{p})}{(p^2)} (-iY_L^*) \int \frac{d^4k}{(2\pi)^4} \frac{i}{k^2 - M^2} \frac{i(\not{p} - \not{k})}{(p - k)^2} (iY_L) u_\mu \\ &= -e|Y^L|^2 \bar{u}_{e_R} \not{\varepsilon} \frac{\not{p}}{p^2} \left[\int \frac{d^4k}{(2\pi)^4} \frac{\not{p} - \not{k}}{(k^2 - M^2)(p - k)^2} \right] u_\mu. \end{aligned} \quad (\text{E.2.17})$$

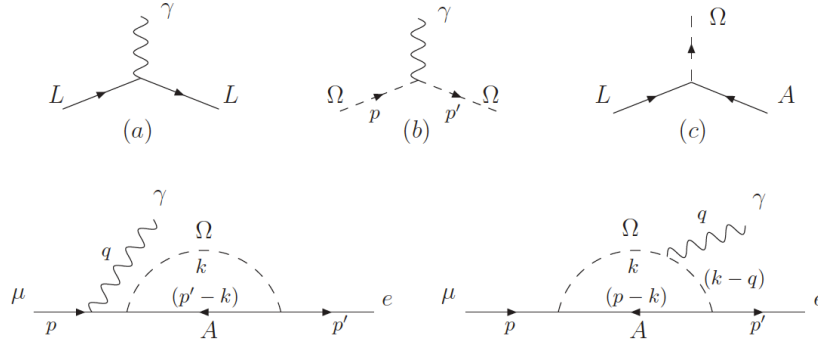


Figure E.1: In the upper part are the vertices we use in the calculation: (a) $-ie\gamma^\mu$ (b) $-ie(p+p')^\mu$ (c) iY^L . The lower part are the kinematics we use in the calculation. The case with the photon going out from e is not shown, since we can obtain the result directly from the first diagram.

Integrating out the loop momentum and doing the regularization, this gives

$$\begin{aligned}
 M_{e \rightarrow \gamma} &= \frac{-ie|Y^L|^2}{32\pi^2} \bar{u}_{e_R} \not{\epsilon} \left(\frac{\not{p}'}{m_\mu^2} \not{p} \right) \left[\frac{2}{\epsilon} - \gamma + \ln(4\pi) + \frac{1}{2} - \ln M^2 + \frac{1}{3} \left(\frac{m_\mu}{M} \right)^2 \right] u_\mu \\
 &= \frac{-ie|Y^L|^2}{32\pi^2} \left[\frac{2}{\epsilon} - \gamma + \ln(4\pi) + \frac{1}{2} - \ln M^2 + \frac{1}{3} \left(\frac{m_\mu}{M} \right)^2 \right] \varepsilon_\nu \bar{u}_{e_R} \gamma^\nu u_{\mu_R}. \quad (\text{E.2.18})
 \end{aligned}$$

when keeping terms up to order $O(m_\mu^2/M^2)$.

For the case with the photon coming out from the internal Ω (see Fig.E.1), the amplitude is

$$\begin{aligned}
 M_{\Omega \rightarrow \gamma} &= \bar{u}_{e_R} (-iY_L^*) \varepsilon_\nu \int \frac{d^4 k}{(2\pi)^4} \frac{i}{(k-q)^2 - M^2} (-ie(2k-q)^\nu) \frac{i}{(k^2 - M^2)} \frac{i(\not{p}' - \not{k})}{(p-k)^2} (iY_L) u_\mu \\
 &= -e|Y^L|^2 \varepsilon_\nu \bar{u}_{e_R} \left[\int \frac{d^4 k}{(2\pi)^4} \frac{(2k-q)^\nu (\not{p}' - \not{k})}{((k-q)^2 - M^2)(k^2 - M^2)(p-k)^2} \right] u_\mu. \quad (\text{E.2.19})
 \end{aligned}$$

Integrating out the loop momentum, taking $m_e = 0$ and using the transverse polarization condition, eq. (E.2.16), we get the amplitude when keeping the terms up to $O(\frac{m_\mu^2}{M^2})$

$$M_{\Omega \rightarrow \gamma} = \frac{ie|Y^L|^2}{32\pi^2} \left[\frac{2}{\epsilon} - \gamma + \ln(4\pi) + \frac{1}{2} - \ln M^2 + \frac{1}{6} \left(\frac{m_\mu}{M} \right)^2 \right] \varepsilon_\nu \bar{u}_{e_R} \gamma^\nu u_{\mu_R}. \quad (\text{E.2.20})$$

Combining the three diagrams, we have

$$M_{\mu \rightarrow e\gamma} = -\frac{ie|Y^L|^2}{192\pi^2} \left(\frac{m_\mu}{M} \right)^2 \bar{u}_{e_R} \not{\epsilon} u_{\mu_R}. \quad (\text{E.2.21})$$

Using $m_e = 0$ and eq. (E.2.16), we can write the result into the well known dipole operator

$$\frac{ie|Y^L|^2}{768\pi^2} \left(\frac{m_\mu}{M^2}\right) \bar{e}_R \sigma_{\mu\nu} F^{\mu\nu} \mu_L. \quad (\text{E.2.22})$$

Averaging the incoming muon spin, the amplitude square becomes

$$\langle |M|^2 \rangle_{spin} = -\frac{e^2|Y^L|^4}{2 \times 192^2 \pi^4} \left(\frac{m_\mu}{M}\right)^4 \text{Tr}[\not{p}_e \gamma^\mu (\not{p}_\mu) \gamma_\mu] = \frac{\alpha|Y^L|^4}{96^2 \pi^3} \left(\frac{m_\mu^6}{M^4}\right). \quad (\text{E.2.23})$$

This gives the decay rate

$$\Gamma(\mu \rightarrow \gamma e) = \frac{1}{32\pi^2} \langle |M|^2 \rangle_{spin} \frac{|q|}{m_\mu^2} \int d\Omega = \frac{\alpha|Y^L|^4}{768^2 \pi^4} \frac{m_\mu^5}{M^4}. \quad (\text{E.2.24})$$

Comparing to the total muon decay rate $\frac{G_F^2 m_\mu^5}{192\pi^3}$, this gives the branching ratio

$$\text{Br}(\mu \rightarrow \gamma e) = \frac{\alpha|Y^L|^4}{3072\pi G_F^2 M^4}. \quad (\text{E.2.25})$$

Comparing to the LFV bound today $\text{Br}(\mu \rightarrow eX) < 10^{-11}$ [?], we have

$$M > 10|Y^L| \text{ TeV}. \quad (\text{E.2.26})$$

E.3 Coherent muon-electron conversion

In this appendix we estimate the bounds from the LFV process of coherent muon-electron conversion (Fig. E.2). For a review of the coherent conversion and how it can be used to put bounds on new physics, see [162, 271] for example.

Our goal is to find the bound on M by comparing the theoretical expression with experimental data. Here we use the general result derived in [162] for the theoretical branching ratio. The low energy effective Hamiltonian is [162]

$$\begin{aligned} H &= -\bar{e}\tilde{O}\mu + h.c. \\ \tilde{O} &= -\sqrt{4\pi\alpha} \left[\gamma_\alpha (f_{E0} - f_{M0}\gamma_5) \frac{q^2}{m_\mu^2} + i\sigma_{\alpha\beta} \frac{q^\beta}{m_\mu} (f_{M1} + f_{E1}\gamma_5) \right] A^\alpha(q) + \frac{G_F}{\sqrt{2}} \gamma_\alpha (a - b\gamma_5) J^\alpha \\ J^\alpha &= \bar{u}\gamma^\alpha u + c_d \bar{d}\gamma^\alpha d \end{aligned} \quad (\text{E.3.27})$$

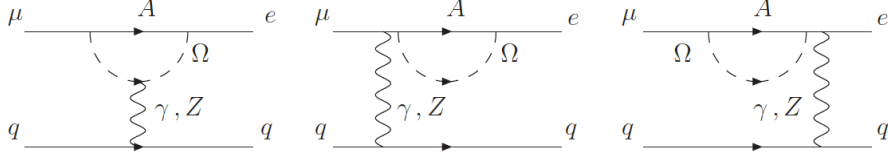


Figure E.2: $\mu - e$ conversion in nuclei emitted by photon and Z .

and the final result of the conversion rate is

$$\begin{aligned}
 w_{conv} &= 3 \times 10^{23} (w_{conv}^{(1)} + w_{conv}^{(2)}) \text{ sec}^{-1}, \\
 w_{conv}^{(1)} &= \left| f_{E0} I_p - \frac{G_F}{\sqrt{2}} \frac{m_\mu^2}{4\pi Z \alpha} a (Z(2 + c_d) I_p + N(1 + 2c_d) I_n) + f_{M1} I_{34} \right|^2, \\
 w_{conv}^{(2)} &= \left| f_{M0} I_p - \frac{G_F}{\sqrt{2}} \frac{m_\mu^2}{4\pi Z \alpha} b (Z(2 + c_d) I_p + N(1 + 2c_d) I_n) + f_{E1} I_{34} \right|^2, \quad (\text{E.3.28})
 \end{aligned}$$

where

$$I_p = -(I_1^p + I_2^p), \quad I_n = -(I_1^n + I_2^n), \quad I_{34} = I_3 + I_4. \quad (\text{E.3.29})$$

Here q represents the photon momentum, and the terms containing A^α in the Hamiltonian describe the transition that is mediated by a photon. The I 's in the last part are coefficients for various elements including the proton-neutron distribution function and the EM field inside the nucleus. They have been calculated in [271] for various materials.

We are ready to use these results in the composite model. The rate of $\mu N \rightarrow e N$ arising from the preon sector is given by the six diagrams in Fig. E.2. Doing the same calculation as in appendix B but allowing the out-going photon to be off-shell, the coefficients in eq. (E.3.27) are of order

$$f_{E0} \sim -f_{M0} \sim f_{M1} \sim -f_{E1} \sim a \sim b \sim \frac{|Y^L|^2}{768\pi^2} \frac{m_\mu^2}{M^2}, \quad c_d \sim 1. \quad (\text{E.3.30})$$

Given these coefficients and the I 's calculated in [162, 271] (which are of order $10^{-1} \text{ GeV}^{-\frac{1}{2}}$), the conversion rate with target ${}^{48}_{22}\text{Ti}$ can be estimated as:

$$w_{conv} \sim 10^{14} |Y^L|^4 \left(\frac{m_\mu}{M} \right)^4 \text{ sec}^{-1}. \quad (\text{E.3.31})$$

Comparing to the experimental total muon capture rate $w(Ti)_{cap} = 2.6 \times 10^6 \text{ sec}^{-1}$ [347], this gives the branching ratio of the conversion as

$$Br(\mu \rightarrow e, Ti) \equiv \frac{w_{conv}}{w_{cap}} = 10^8 |Y^L|^4 \left(\frac{m_\mu}{M} \right)^4. \quad (\text{E.3.32})$$

Comparing to the experimental limit $Br(\mu \rightarrow e) < 1.7 \times 10^{-12}$ [269], this gives

$$M > 10 |Y^L| \text{ TeV}. \quad (\text{E.3.33})$$

BIBLIOGRAPHY

- [1] Angular analysis of $B^0 \rightarrow K^{*0} \mu^+ \mu^-$. Aug 2011. LHCb-CONF-2011-038.
- [2] Differential branching fraction and angular analysis of the $B^0 \rightarrow K^{*0} \mu^+ \mu^-$ decay. Feb 2012. LHCb-CONF-2012-008.
- [3] C. E. Aalseth et al. Results from a Search for Light-Mass Dark Matter with a P- type Point Contact Germanium Detector. 2010.
- [4] C. E. Aalseth et al. Search for an Annual Modulation in a P-Type Point Contact Germanium Dark Matter Detector. 2011.
- [5] T. Aaltonen et al. Search for Large Extra Dimensions in Final States Containing One Photon Or Jet and Large Missing Transverse Energy Produced in P Anti-P Collisions at $S^{(1/2)} = 1.96$ - TeV. *Phys. Rev. Lett.*, 101:181602, 2008.
- [6] T. Aaltonen et al. Measurements of the Angular Distributions in the Decays $B \rightarrow K^{(*)} \mu^+ \mu^-$ at CDF. *Phys.Rev.Lett.*, 108:081807, 2012.
- [7] Kevork Abazajian, George M. Fuller, and Mitesh Patel. Sterile neutrino hot, warm, and cold dark matter. *Phys. Rev. D*, 64:023501, May 2001.
- [8] V. M. Abazov et al. Search for Large Extra Dimensions via Single Photon Plus Missing Energy Final States at $S^{(1/2)} = 1.96$ -TeV. *Phys. Rev. Lett.*, 101:011601, 2008.
- [9] J. Abdallah et al. Photon events with missing energy in $e^+ e^-$ collisions at $s^{**}(1/2) = 130$ -GeV to 209-GeV. *Eur.Phys.J.*, C38:395–411, 2005.
- [10] J. Abdallah et al. Search for one large extra dimension with the DELPHI detector at LEP. *Eur.Phys.J.*, C60:17–23, 2009.
- [11] A. A. Abdo et al. Observations of Milky Way Dwarf Spheroidal galaxies with the Fermi-LAT detector and constraints on Dark Matter models. *Astrophys. J.*, 712:147–158, 2010.
- [12] Steven Abel, Callum Durnford, Joerg Jaeckel, and Valentin V. Khoze. Dynamical breaking of $u(1)_r$ and supersymmetry in a metastable vacuum. 07 2007.
- [13] Steven Abel and Valentin V. Khoze. Direct mediation, duality and unification. 09 2008.

- [14] Yuki Adachi, C. S. Lim, and Nobuhito Maru. More on the Finiteness of Anomalous Magnetic Moment in the Gauge-Higgs Unification. *Phys. Rev.*, D79:075018, 2009.
- [15] K. Agashe, N.G. Deshpande, and G.H. Wu. Universal extra dimensions and $b \rightarrow s\gamma$. *Phys.Lett.*, B514:309–314, 2001.
- [16] Kaustubh Agashe. An improved model of direct gauge mediation.
- [17] Kaustubh Agashe. Relaxing constraints from lepton flavor violation in 5d flavorful theories. 02 2009.
- [18] Kaustubh Agashe, Aleksandr Azatov, and Lijun Zhu. Flavor Violation Tests of Warped/Composite SM in the Two- Site Approach. *Phys. Rev.*, D79:056006, 2009.
- [19] Kaustubh Agashe, Aleksandr Azatov, and Lijun Zhu. Flavor Violation Tests of Warped/Composite SM in the Two-Site Approach. *Phys. Rev.*, D79:056006, 2009.
- [20] Kaustubh Agashe, Andrew E. Blechman, and Frank Petriello. Probing the Randall-Sundrum geometric origin of flavor with lepton flavor violation. *Phys. Rev.*, D74:053011, 2006.
- [21] Kaustubh Agashe and Roberto Contino. Composite Higgs-Mediated FCNC. *Phys. Rev.*, D80:075016, 2009.
- [22] Kaustubh Agashe, Roberto Contino, Leandro Da Rold, and Alex Pomarol. A custodial symmetry for $Zb\bar{b}$. *Phys. Lett.*, B641:62–66, 2006.
- [23] Kaustubh Agashe, Roberto Contino, and Alex Pomarol. The Minimal composite Higgs model. *Nucl.Phys.*, B719:165–187, 2005.
- [24] Kaustubh Agashe, Antonio Delgado, Michael J. May, and Raman Sundrum. RS1, custodial isospin and precision tests. *JHEP*, 08:050, 2003.
- [25] Kaustubh Agashe, Takemichi Okui, and Raman Sundrum. A Common Origin for Neutrino Anarchy and Charged Hierarchies. *Phys. Rev. Lett.*, 102:101801, 2009.
- [26] Kaustubh Agashe, Gilad Perez, and Amarjit Soni. B-factory signals for a warped extra dimension. *Phys. Rev. Lett.*, 93:201804, 2004.
- [27] Kaustubh Agashe, Gilad Perez, and Amarjit Soni. B-factory signals for a warped extra dimension. *Phys. Rev. Lett.*, 93:201804, 2004.

- [28] Kaustubh Agashe, Gilad Perez, and Amarjit Soni. Flavor structure of warped extra dimension models. *Phys. Rev.*, D71:016002, 2005.
- [29] Prateek Agrawal, Zackaria Chacko, Can Kilic, and Rashmish K. Mishra. A Classification of Dark Matter Candidates with Primarily Spin-Dependent Interactions with Matter. 2010.
- [30] Z. Ahmed et al. Dark Matter Search Results from the CDMS II Experiment. *Science*, 327:1619–1621, 2010.
- [31] Michaela E. Albrecht, Monika Blanke, Andrzej J. Buras, Bjorn Duling, and Katrin Gemmler. Electroweak and Flavour Structure of a Warped Extra Dimension with Custodial Protection. *JHEP*, 09:064, 2009.
- [32] Wolfgang Altmannshofer, Patricia Ball, Aoife Bharucha, Andrzej J. Buras, David M. Straub, et al. Symmetries and Asymmetries of $B \rightarrow K^* \mu^+ \mu^-$ Decays in the Standard Model and Beyond. *JHEP*, 0901:019, 2009.
- [33] Wolfgang Altmannshofer, Paride Paradisi, and David M. Straub. Model-independent constraints on new physics in $b \rightarrow s$ transitions. 2011.
- [34] Johan Alwall, Pavel Demin, Simon de Visscher, Rikkert Frederix, Michel Herquet, et al. MadGraph/MadEvent v4: The New Web Generation. *JHEP*, 0709:028, 2007. <http://madgraph.hep.uiuc.edu/>.
- [35] Johan Alwall, Michel Herquet, Fabio Maltoni, Olivier Mattelaer, and Tim Stelzer. Madgraph 5 : Going Beyond. *JHEP*, 06:128, 2011.
- [36] Antonio Amariti and Alberto Mariotti. Two Loop R-Symmetry Breaking. *JHEP*, 0907:071, 2009.
- [37] Haipeng An and Fei Gao. Fitting CoGeNT Modulation with an Inelastic, Isospin-Violating Z' Model. 2011.
- [38] J. Angle, E. Aprile, F. Arneodo, L. Baudis, A. Bernstein, et al. Limits on spin-dependent WIMP-nucleon cross-sections from the XENON10 experiment. *Phys.Rev.Lett.*, 101:091301, 2008.
- [39] J. Angle et al. First Results from the XENON10 Dark Matter Experiment at the Gran Sasso National Laboratory. *Phys. Rev. Lett.*, 100:021303, 2008.

- [40] G. Angloher et al. Results from 730 Kg Days of the Cresst-Ii Dark Matter Search. 2011.
- [41] S Aoki et al. Nucleon strange quark content from two-flavor lattice QCD with exact chiral symmetry. 2010.
- [42] Thomas Appelquist, Hsin-Chia Cheng, and Bogdan A. Dobrescu. Bounds on universal extra dimensions. *Phys.Rev.*, D64:035002, 2001.
- [43] E. Aprile et al. First Dark Matter Results from the XENON100 Experiment. *Phys.Rev.Lett.*, 105:131302, 2010.
- [44] E. Aprile et al. Dark Matter Results from 100 Live Days of Xenon100 Data. 2011.
- [45] Takeshi Araki and Y.F. Li. Q6 flavor symmetry model for the extension of the minimal standard model by three right-handed sterile neutrinos. *Phys.Rev.*, D85:065016, 2012.
- [46] D. Aristizabal Sierra, Jisuke Kubo, D. Restrepo, Daijiro Suematsu, and Oscar Zapata. Radiative seesaw: Warm dark matter, collider and lepton flavour violating signals. *Phys.Rev.*, D79:013011, 2009.
- [47] Nima Arkani-Hamed, Savas Dimopoulos, and G. R. Dvali. The Hierarchy Problem and New Dimensions at a Millimeter. *Phys. Lett.*, B429:263–272, 1998.
- [48] Nima Arkani-Hamed and Yuval Grossman. Light active and sterile neutrinos from compositeness. *Phys.Lett.*, B459:179–182, 1999.
- [49] Nima Arkani-Hamed and Yuval Grossman. Light active and sterile neutrinos from compositeness. *Phys. Lett.*, B459:179, 1999.
- [50] Nima Arkani-Hamed, John March-Russell, and Hitoshi Murayama. Building models of gauge mediated supersymmetry breaking without a messenger sector.
- [51] Nima Arkani-Hamed, Massimo Porrati, and Lisa Randall. Holography and phenomenology. *JHEP*, 08:017, 2001.
- [52] Nima Arkani-Hamed and Martin Schmaltz. Hierarchies without symmetries from extra dimensions. *Phys. Rev.*, D61:033005, 2000.

- [53] Nima Arkani-Hamed and Martin Schmaltz. Hierarchies without symmetries from extra dimensions. *Phys. Rev.*, D61:033005, 2000.
- [54] Takehiko Asaka, Mikhail Shaposhnikov, and Mikko Laine. Lightest sterile neutrino abundance within the ν msm. *Journal of High Energy Physics*, 2007(01):091, 2007.
- [55] D. Asner et al. Averages of b-hadron, c-hadron, and tau-lepton Properties. 2010. Updates available on <http://www.slac.stanford.edu/xorg/hfag/>.
- [56] ATLAS Collaboration. Search for new phenomena in monojet plus missing transverse momentum final states using 1 fb^{-1} of pp collisions at $\sqrt{s}=7 \text{ tev}$ with the atlas detector. Technical Report ATLAS-CONF-2011-096, CERN, Geneva, Jul 2011.
- [57] ATLAS Collaboration. Search for new phenomena with the monojet and missing transverse momentum signature using the ATLAS detector in $\sqrt{s} = 7 \text{ TeV}$ proton-proton collisions. 2011.
- [58] ATLAS Collaboration. Update of the combination of higgs boson searches in 1.0 to 2.3 fb^{-1} of pp collisions data taken at $\sqrt{s} = 7 \text{ tev}$ with the atlas experiment at the lhc. *ATLAS-CONF-2011-135*, 2011.
- [59] David Atwood, Michael Gronau, and Amarjit Soni. Mixing induced CP asymmetries in radiative B decays in and beyond the standard model. *Phys.Rev.Lett.*, 79:185–188, 1997.
- [60] Bernard Aubert et al. Measurement of the $B \rightarrow X_s \ell^+ \ell^-$ branching fraction with a sum over exclusive modes. *Phys.Rev.Lett.*, 93:081802, 2004.
- [61] Bernard Aubert et al. Measurement of Time-Dependent CP Asymmetry in $B^0 \rightarrow K_S^0 \pi^0 \gamma$ Decays. *Phys.Rev.*, D78:071102, 2008.
- [62] Bernard Aubert et al. Angular Distributions in the Decays $B \rightarrow K^* \ell^+ \ell^-$. *Phys. Rev.*, D79:031102, 2009.
- [63] T. Aushev, W. Bartel, A. Bondar, J. Brodzicka, T.E. Browder, et al. Physics at Super B Factory. 2010.
- [64] Roberto Auzzi, Shmuel Elitzur, and Amit Giveon. On uplifted susy-breaking vacua and direct mediation in generalized sqcd. 01 2010.

- [65] Aleksandr Azatov, Manuel Toharia, and Lijun Zhu. Higgs Mediated FCNC's in Warped Extra Dimensions. 2009.
- [66] Jonathan Bagger, Erich Poppitz, , and Lisa Randall. The r axion from dynamical supersymmetry breaking.
- [67] Yang Bai, Patrick J. Fox, and Roni Harnik. The Tevatron at the Frontier of Dark Matter Direct Detection. *JHEP*, 12:048, 2010.
- [68] Patricia Ball, Gareth W. Jones, and Roman Zwicky. $B \rightarrow V\gamma$ beyond QCD factorisation. *Phys.Rev.*, D75:054004, 2007.
- [69] Patricia Ball and Roman Zwicky. Time-dependent CP Asymmetry in $B \rightarrow K^*\gamma$ as a (Quasi) Null Test of the Standard Model. *Phys.Lett.*, B642:478–486, 2006.
- [70] Vernon Barger, Wai-Yee Keung, and Gabe Shaughnessy. Spin Dependence of Dark Matter Scattering. *Phys. Rev.*, D78:056007, 2008.
- [71] M. Barnabe-Heider et al. Improved Spin Dependent Limits from the PICASSO Dark Matter Search Experiment. *Phys. Lett.*, B624:186–194, 2005.
- [72] James Barnard. Tree level metastability and gauge mediation in baryon deformed sqcd. 10 2009.
- [73] M. Bauer, S. Casagrande, U. Haisch, and M. Neubert. Flavor Physics in the Randall-Sundrum Model: II. Tree-Level Weak-Interaction Processes. *JHEP*, 1009:017, 2010.
- [74] Martin Bauer, Raoul Malm, and Matthias Neubert. A Solution to the Flavor Problem of Warped Extra-Dimension Models. 2011.
- [75] Damir Becirevic and Elia Schneider. On transverse asymmetries in $B \rightarrow K^*l^+l^-$. *Nucl.Phys.*, B854:321–339, 2012.
- [76] E. Behnke et al. Improved Limits on Spin-Dependent WIMP-Proton Interactions from a Two Liter CF_3I Bubble Chamber. 2010.
- [77] G. Belanger, F. Boudjema, A. Pukhov, and A. Semenov. Dark Matter Direct Detection Rate in a Generic Model with MicrOmegaS^2 .1. *Comput. Phys. Commun.*, 180:747–767, 2009.
- [78] U. Bellgardt et al. Search for the Decay $\mu^+ \rightarrow e^+e^+e^-$. *Nucl. Phys.*, B299:1, 1988.

- [79] Maria Beltran, Dan Hooper, Edward W. Kolb, Zosia A. C. Krusberg, and Tim M. P. Tait. Maverick dark matter at colliders. *JHEP*, 09:037, 2010.
- [80] K. Benakli and M.D. Goodsell. Dirac Gauginos in General Gauge Mediation. *Nucl.Phys.*, B816:185–203, 2009.
- [81] M. Beneke, T. Feldmann, and D. Seidel. Systematic approach to exclusive $B \rightarrow V l^+ l^-$, V gamma decays. *Nucl. Phys.*, B612:25–58, 2001.
- [82] M. Beneke, Th. Feldmann, and D. Seidel. Exclusive radiative and electroweak $b \rightarrow d$ and $b \rightarrow s$ penguin decays at NLO. *Eur.Phys.J.*, C41:173–188, 2005.
- [83] B.A. Benson, T. de Haan, J.P. Dudley, C.L. Reichardt, K.A. Aird, et al. Cosmological Constraints from Sunyaev-Zel’dovich-Selected Clusters with X-ray Observations in the First 178 Square Degrees of the South Pole Telescope Survey. 2011.
- [84] Michael Benzke, Seung J. Lee, Matthias Neubert, and Gil Paz. Factorization at Sub-leading Power and Irreducible Uncertainties in $\bar{B} \rightarrow X_s \gamma$ Decay. *JHEP*, 08:099, 2010.
- [85] Michael Benzke, Seung J. Lee, Matthias Neubert, and Gil Paz. Long-Distance Dominance of the CP Asymmetry in $B \rightarrow X_{s,d} \gamma$ Decays. *Phys.Rev.Lett.*, 106:141801, 2011.
- [86] R. Bernabei et al. First results from DAMA/LIBRA and the combined results with DAMA/NaI. *Eur. Phys. J.*, C56:333–355, 2008.
- [87] R. Bernabei et al. Investigating electron interacting dark matter. *Phys. Rev.*, D77:023506, 2008.
- [88] M. Beylich, G. Buchalla, and T. Feldmann. Theory of $B \rightarrow K^{(*)} l^+ l^-$ decays at high q^2 : OPE and quark-hadron duality. *Eur.Phys.J.*, C71:1635, 2011.
- [89] F. Bezrukov, H. Hettmansperger, and M. Lindner. keV sterile neutrino dark matter in gauge extensions of the standard model. *Phys. Rev. D*, 81:085032, Apr 2010.
- [90] Peter L. Biermann and Alexander Kusenko. Relic keV sterile neutrinos and reionization. *Phys.Rev.Lett.*, 96:091301, 2006.
- [91] J. Binney and S. Tremaine. *Galactic Dynamics*. Princeton Series in Astrophysics. Princeton University Press, first edition, 1987.

- [92] Andreas Birkedal, Konstantin Matchev, and Maxim Perelstein. Dark matter at colliders: A Model independent approach. *Phys.Rev.*, D70:077701, 2004.
- [93] Monika Blanke, Andrzej J. Buras, Bjoern Duling, Stefania Gori, and Andreas Weiler. $\Delta F=2$ Observables and Fine-Tuning in a Warped Extra Dimension with Custodial Protection. *JHEP*, 03:001, 2009.
- [94] Monika Blanke, Andrzej J. Buras, Bjoern Duling, Stefania Gori, and Andreas Weiler. $\Delta F = 2$ Observables and Fine-Tuning in a Warped Extra Dimension with Custodial Protection. *JHEP*, 0903:001, 2009.
- [95] Monika Blanke, Andrzej J. Buras, Bjorn Duling, Katrin Gemmler, and Stefania Gori. Rare K and B Decays in a Warped Extra Dimension with Custodial Protection. *JHEP*, 03:108, 2009.
- [96] Monika Blanke, Andrzej J. Buras, Katrin Gemmler, and Tillmann Heidsieck. $\Delta F = 2$ observables and $B \rightarrow X_q \gamma$ decays in the Left-Right Model: Higgs particles striking back. *JHEP*, 1203:024, 2012.
- [97] Monika Blanke, Bibhushan Shakya, Philip Tanedo, and Yuhsin Tsai. The birds and the Bs in RS: the b to s gamma penguin in a warped extra dimension. 2012.
- [98] Kfir Blum, Cédric Delaunay, and Yonit Hochberg. Vacuum (meta)stability beyond the mssm. 05 2009.
- [99] Christoph Bobeth, Gudrun Hiller, and Giorgi Piranishvili. CP Asymmetries in $\bar{B} \rightarrow \bar{K}^*(\rightarrow \bar{K}\pi)\bar{\ell}\ell$ and Untagged $\bar{B}_s, B_s \rightarrow \phi(\rightarrow K^+K^-)\bar{\ell}\ell$ Decays at NLO. *JHEP*, 0807:106, 2008.
- [100] Christoph Bobeth, Gudrun Hiller, and Danny van Dyk. The Benefits of $B \rightarrow K^*l^+l^-$ Decays at Low Recoil. *JHEP*, 07:098, 2010. Christoph Bobeth, Gudrun Hiller, and Danny van Dyk. More Benefits of Semileptonic Rare B Decays at Low Recoil: CP Violation. *JHEP*, 07:067, 2011.
- [101] M. Bona et al. SuperB: A High-Luminosity Asymmetric e^+e^- Super Flavor Factory. Conceptual Design Report. 2007.
- [102] E. Boos et al. CompHEP 4.4: Automatic computations from Lagrangians to events. *Nucl.Instrum.Meth.*, A534:250–259, 2004.

- [103] Natalia Borodatchenkova, Debajyoti Choudhury, and Manuel Drees. Probing MeV dark matter at low-energy e+e- colliders. *Phys.Rev.Lett.*, 96:141802, 2006.
- [104] D. Boyanovsky and C.M. Ho. Sterile neutrino production via active-sterile oscillations: The Quantum Zeno effect. *JHEP*, 0707:030, 2007.
- [105] A. Boyarsky, A. Neronov, O. Ruchayskiy, and M. Shaposhnikov. Restrictions on parameters of sterile neutrino dark matter from observations of galaxy clusters. *Phys. Rev. D*, 74:103506, Nov 2006.
- [106] Alexey Boyarsky, Dmytro Iakubovskiy, Oleg Ruchayskiy, and Vladimir Savchenko. Constraints on decaying Dark Matter from XMM-Newton observations of M31. *Mon.Not.Roy.Astron.Soc.*, 387:1361, 2008.
- [107] Alexey Boyarsky, Julien Lesgourgues, Oleg Ruchayskiy, and Matteo Viel. Lyman-alpha constraints on warm and on warm-plus-cold dark matter models. *JCAP*, 0905:012, 2009.
- [108] Alexey Boyarsky, A. Neronov, O. Ruchayskiy, M. Shaposhnikov, and I. Tkachev. Where to find a dark matter sterile neutrino? *Phys.Rev.Lett.*, 97:261302, 2006.
- [109] Alexey Boyarsky, Jukka Nevalainen, and Oleg Ruchayskiy. Constraints on the parameters of radiatively decaying dark matter from the dark matter halo of the Milky Way and Ursa Minor. *Astron.Astrophys.*, 471:51–57, 2007.
- [110] Alexey Boyarsky, Oleg Ruchayskiy, and Mikhail Shaposhnikov. The Role of sterile neutrinos in cosmology and astrophysics. *Ann.Rev.Nucl.Part.Sci.*, 59:191–214, 2009.
- [111] Gerhard Buchalla, Andrzej J. Buras, and Markus E. Lautenbacher. Weak decays beyond leading logarithms. *Rev. Mod. Phys.*, 68:1125–1144, 1996.
- [112] Andrzej J. Buras. Weak Hamiltonian, CP violation and rare decays. 1998.
- [113] Andrzej J. Buras, Bjoern Duling, and Stefania Gori. The Impact of Kaluza-Klein Fermions on Standard Model Fermion Couplings in a RS Model with Custodial Protection. *JHEP*, 09:076, 2009.
- [114] Andrzej J. Buras et al. Patterns of Flavour Violation in the Presence of a Fourth Generation of Quarks and Leptons. *JHEP*, 09:106, 2010.

- [115] Andrzej J. Buras, Luca Merlo, and Emmanuel Stamou. The Impact of Flavour Changing Neutral Gauge Bosons on $\bar{B} \rightarrow X_s \gamma$. *JHEP*, 1108:124, 2011.
- [116] Andrzej J. Buras, Anton Poschenrieder, Michael Spranger, and Andreas Weiler. The Impact of universal extra dimensions on $B \rightarrow X_s \gamma$, $B \rightarrow X_s \text{gluon}$, $B \rightarrow X_s \mu^+ \mu^-$, $K_L \rightarrow \pi^0 e^+ e^-$ and ϵ'/ϵ . *Nucl.Phys.*, B678:455–490, 2004.
- [117] C.P. Burgess, Maxim Pospelov, and Tonnies ter Veldhuis. The Minimal model of nonbaryonic dark matter: A Singlet scalar. *Nucl.Phys.*, B619:709–728, 2001.
- [118] Giacomo Cacciapaglia, Csaba Csaki, Guido Marandella, and John Terning. A New custodian for a realistic Higgsless model. *Phys.Rev.*, D75:015003, 2007.
- [119] Qing-Hong Cao, Chuan-Ren Chen, Chong Sheng Li, and Hao Zhang. Effective Dark Matter Model: Relic density, CDMS II, Fermi LAT and LHC. 2009.
- [120] Qing-Hong Cao, Ian Low, and Gabe Shaughnessy. From Pamela to CDMS and Back. *Phys.Lett.*, B691:73–76, 2010.
- [121] Marcela S. Carena, Antonio Delgado, Eduardo Ponton, Timothy M. P. Tait, and C. E. M. Wagner. Warped fermions and precision tests. *Phys. Rev.*, D71:015010, 2005.
- [122] Marcela S. Carena, Eduardo Ponton, Jose Santiago, and Carlos E.M. Wagner. Light Kaluza Klein States in Randall-Sundrum Models with Custodial SU(2). *Nucl.Phys.*, B759:202–227, 2006.
- [123] Linda M. Carpenter, Michael Dine, Guido Festuccia, and John D. Mason. Implementing general gauge mediation. 05 2008.
- [124] S. Casagrande, F. Goertz, U. Haisch, M. Neubert, and T. Pfoh. Flavor physics in the randall-sundrum model: I. theoretical setup and electroweak precision tests. 07 2008.
- [125] S. Casagrande, F. Goertz, U. Haisch, M. Neubert, and T. Pfoh. Flavor Physics in the Randall-Sundrum Model: I. Theoretical Setup and Electroweak Precision Tests. *JHEP*, 0810:094, 2008.
- [126] Sanghyeon Chang, Junji Hisano, Hiroaki Nakano, Nobuchika Okada, and Masahiro Yamaguchi. Bulk standard model in the Randall-Sundrum background. *Phys. Rev.*, D62:084025, 2000.

- [127] We-Fu Chang and John N. Ng. Lepton flavor violation in extra dimension models. *Phys. Rev.*, D71:053003, 2005.
- [128] Chian-Shu Chen and Ryo Takahashi. Hierarchically Acting Sterile Neutrinos. 2011.
- [129] Mu-Chun Chen and Hai-Bo Yu. Minimal Flavor Violation in the Lepton Sector of the Randall-Sundrum Model. *Phys. Lett.*, B672:253–256, 2009.
- [130] Hai-Yang Cheng. Low-Energy Interactions of Scalar and Pseudoscalar Higgs Bosons with Baryons. *Phys. Lett.*, B219:347, 1989.
- [131] T.̃. Cheng and L.̃. Li. Nonconservation of Separate μ - Lepton and e - Lepton Numbers in Gauge Theories with $v + a$ Currents. *Phys. Rev. Lett.*, 38:381, 1977.
- [132] Clifford Cheung, A. Liam Fitzpatrick, and David Shih. (extra)ordinary gauge mediation. 10 2007.
- [133] Kingman Cheung, Kentarou Mawatari, Eibun Senaha, Po-Yan Tseng, and Tzu-Chiang Yuan. The top window for dark matter. 09 2010.
- [134] Kingman Cheung, Po-Yan Tseng, and Tzu-Chiang Yuan. Cosmic antiproton constraints on effective interactions of the dark matter. 11 2010. Kingman Cheung, Po-Yan Tseng, and Tzu-Chiang Yuan. Gamma-ray constraints on effective interactions of the dark matter. 04 2011.
- [135] R.Sekhar Chivukula. PROBING NEUTRINO STRUCTURE AT THE SSC. *Phys.Lett.*, B202:436, 1988.
- [136] CMS Collaboration. Search for extra dimensions using the monophoton final state. Technical Report CMS-PAS-EXO-11-058, CERN, Geneva, Aug 2011.
- [137] CMS Collaboration. Search for New Physics with a Mono-Jet and Missing Transverse Energy in pp Collisions at $\sqrt{s} = 7$ TeV. 2011.
- [138] CMS Collaboration. Search for new physics with a monojet and missing transverse energy in pp collisions at $\sqrt{s} = 7$ tev with 1.1 fb^{-1} . Technical Report CMS-PAS-EXO-11-059, CERN, Geneva, Aug 2011.
- [139] CMS Collaboration. Search for standard model higgs boson in pp collisions at $\sqrt{s} = 7$ tev and integrated luminosity up to 1.7 fb^{-1} . *CMS-PAS-HIG-11-022*, 2011.

- [140] Pietro Colangelo and Alexander Khodjamirian. QCD sum rules, a modern perspective. 2000.
- [141] S. R. Coleman. *Phys. Rev.*, D(15):2929, 1977.
- [142] Roberto Contino, Leandro Da Rold, and Alex Pomarol. Light custodians in natural composite Higgs models. *Phys.Rev.*, D75:055014, 2007.
- [143] Roberto Contino and Alex Pomarol. Holography for fermions. *JHEP*, 11:058, 2004.
- [144] John Conway et al. PGS—Pretty Good Simulation, 2009. <http://physics.ucdavis.edu/~conway/research/software/pgs/pgs4-general.htm>.
- [145] Laura Covi, Esteban Roulet, and Francesco Vissani. CP violating decays in leptogenesis scenarios. *Phys.Lett.*, B384:169–174, 1996.
- [146] Andreas Crivellin and Lorenzo Mercolli. $B \rightarrow X_d \gamma$ and constraints on new physics. *Phys. Rev.*, D84:114005, 2011.
- [147] Csaba Csaki. TASI lectures on extra dimensions and branes. 2004.
- [148] Csaba Csaki, Cedric Delaunay, Christophe Grojean, and Yuval Grossman. A Model of Lepton Masses from a Warped Extra Dimension. *JHEP*, 10:055, 2008.
- [149] Csaba Csaki, Joshua Erlich, and John Terning. The effective Lagrangian in the Randall-Sundrum model and electroweak physics. *Phys. Rev.*, D66:064021, 2002.
- [150] Csaba Csaki, Adam Falkowski, and Andreas Weiler. The Flavor of the Composite Pseudo-Goldstone Higgs. *JHEP*, 09:008, 2008.
- [151] Csaba Csaki, Adam Falkowski, and Andreas Weiler. The Flavor of the Composite Pseudo-Goldstone Higgs. *JHEP*, 09:008, 2008.
- [152] Csaba Csaki, Adam Falkowski, and Andreas Weiler. A Simple Flavor Protection for RS. *Phys. Rev.*, D80:016001, 2009.
- [153] Csaba Csaki, Adam Falkowski, and Andreas Weiler. A Simple Flavor Protection for RS. *Phys. Rev.*, D80:016001, 2009.

- [154] Csaba Csaki, Christophe Grojean, Jay Hubisz, Yuri Shirman, and John Terning. Fermions on an interval: Quark and lepton masses without a Higgs. *Phys. Rev.*, D70:015012, 2004.
- [155] Csaba Csaki, Christophe Grojean, Luigi Pilo, and John Terning. Towards a realistic model of Higgsless electroweak symmetry breaking. *Phys. Rev. Lett.*, 92:101802, 2004.
- [156] Csaba Csaki, Yuval Grossman, Philip Tanedo, and Yuhsin Tsai. Warped Penguins. 2010.
- [157] Csaba Csaki, Jay Hubisz, and Patrick Meade. Electroweak symmetry breaking from extra dimensions. 2005.
- [158] Csaba Csaki, Gilad Perez, Ze'ev Surujon, and Andreas Weiler. Flavor Alignment via Shining in RS. 2009.
- [159] Csaba Csaki, Gilad Perez, Ze'ev Surujon, and Andreas Weiler. Flavor Alignment via Shining in RS. 2009.
- [160] Csaba Csáki, Yuri Shirman, and John Terning. A simple model of low-scale direct gauge mediation.
- [161] T. Csorgo and L.P. Csernai. Quark - gluon plasma freezeout from a supercooled state? *Phys.Lett.*, B333:494–499, 1994.
- [162] Andrzej Czarnecki, William J. Marciano, and Kirill Melnikov. Coherent muon electron conversion in muonic atoms. *AIP Conf.Proc.*, 435:409–418, 1998.
- [163] Subinoy Das and Kris Sigurdson. Cosmological Limits on Hidden Sector Dark Matter. *Phys.Rev.*, D85:063510, 2012.
- [164] Sacha Davidson, Enrico Nardi, and Yosef Nir. Leptogenesis. *Phys.Rept.*, 466:105, 2008.
- [165] H. Davoudiasl, J. L. Hewett, and T. G. Rizzo. Bulk gauge fields in the Randall-Sundrum model. *Phys. Lett.*, B473:43–49, 2000.
- [166] Hooman Davoudiasl, Tao Han, and Heather E. Logan. Discovering an Invisibly Decaying Higgs at Hadron Colliders. *Phys. Rev.*, D71:115007, 2005.

- [167] H.J. de Vega, P. Salucci, and N.G. Sanchez. The mass of the dark matter particle from theory and observations. *New Astron.*, 17:653–666, 2012.
- [168] H.J. de Vega and N.G. Sanchez. Model independent analysis of dark matter points to a particle mass at the keV scale. *Mon.Not.Roy.Astron.Soc.*, 404:885, 2010.
- [169] H.J. de Vega and N.G. Sanchez. Warm dark matter in the galaxies: theoretical and observational progresses. Highlights and conclusions of the chalonge meudon workshop 2011. 2011.
- [170] A. Dedes, I. Giomataris, K. Suxho, and J. D. Vergados. Searching for Secluded Dark Matter via Direct Detection of Recoiling Nuclei as well as Low Energy Electrons. 2009.
- [171] T. DeGrand and K. Kajantie. Supercooling, entropy production, and bubble kinetics in the quark-hadron phase transition in the early universe. *Phys. Lett. B*, 147(4):273 – 278, 1984.
- [172] Francisco del Aguila, Adrian Carmona, and Jose Santiago. Neutrino Masses from an A4 Symmetry in Holographic Composite Higgs Models. 2010.
- [173] Sebastien Descotes-Genon, Diptimoy Ghosh, Joaquim Matias, and Marc Ramon. Exploring New Physics in the $C_7 - C_{7'}$ plane. *JHEP*, 1106:099, 2011.
- [174] Karin Dick, Manfred Lindner, Michael Ratz, and David Wright. Leptogenesis with Dirac neutrinos. *Phys.Rev.Lett.*, 84:4039–4042, 2000.
- [175] S. Dimopoulos, S. Raby, and Leonard Susskind. Light Composite Fermions. *Nucl.Phys.*, B173:208–228, 1980.
- [176] S. Dimopoulos S. Dimopoulos S. Dimopoulos and S. Raby. *Nucl. Phys.*, B(192):353, 1981.
- [177] Savas Dimopoulos, Gia Dvali, and Riccardo Rattazzi. A simple complete model of gauge-mediated susy-breaking and dynamical relaxation mechanism for solving the mu-problem.
- [178] M. Dine and W. Fischler. *Phys. Lett.*, B(110):227, 1982.
- [179] M. Dine, A.E. Nelson, and Y. Shirman. Dynamical supersymmetry breaking simplified.

- [180] M. Dine and M. Srednicki. *Nucl. Phys.*, B(202):238, 1982.
- [181] Michael Dine, Jonathan L. Feng, and Eva Silverstein. Retrofitting o’raifeartaigh models with dynamical scales.
- [182] Michael Dine and John Mason. Gauge mediation in metastable vacua.
- [183] Michael Dine and John Mason. Dynamical supersymmetry breaking and low energy gauge mediation. 12 2007.
- [184] Michael Dine and Ann E. Nelson. Dynamical supersymmetry breaking at low energies.
- [185] Michael Dine, Ann E. Nelson, Yosef Nir, and Yuri Shirman. New tools for low energy dynamical supersymmetry breaking.
- [186] Scott Dodelson and Lawrence M. Widrow. Sterile neutrinos as dark matter. *Phys. Rev. Lett.*, 72:17–20, Jan 1994.
- [187] A.D. Dolgov and S.H. Hansen. Massive sterile neutrinos as warm dark matter. *Astropart.Phys.*, 16:339–344, 2002.
- [188] Michael Duerr, Damien P. George, and Kristian L. McDonald. Neutrino Mass and $\mu \rightarrow e + \gamma$ from a Mini-Seesaw. *JHEP*, 1107:103, 2011.
- [189] Bjoern Duling. A Comparative Study of Contributions to ϵ_K in the RS Model. *JHEP*, 1005:109, 2010.
- [190] M. J. Duncan and L. G. Jensen. *Phys. Lett.*, B(291):109, 1992.
- [191] U. Egede, T. Hurth, J. Matias, M. Ramon, and W. Reece. New observables in the decay mode $\bar{B}_d \rightarrow \bar{K}^{*0} l^+ l^-$. *JHEP*, 0811:032, 2008.
- [192] Ulrik Egede, Tobias Hurth, Joaquim Matias, Marc Ramon, and Will Reece. New physics reach of the decay mode $\bar{B} \rightarrow \bar{K}^{*0} \ell^+ \ell^-$. *JHEP*, 1010:056, 2010.
- [193] John R. Ellis, Keith A. Olive, and Christopher Savage. Hadronic Uncertainties in the Elastic Scattering of Supersymmetric Dark Matter. *Phys. Rev.*, D77:065026, 2008.

- [194] Rouven Essig, Jean-Francois Fortin, Kuver Sinha, Gonzalo Torroba, and Matthew J. Strassler. Metastable supersymmetry breaking and multitrace deformations of sqcd. 12 2008.
- [195] Jason L. Evans, Masahiro Ibe, Matthew Sudano, and Tsutomu T. Yanagida. Simplified R-Symmetry Breaking and Low-Scale Gauge Mediation. *JHEP*, 1203:004, 2012.
- [196] F. Meisel et al. Study of the discovery potential for an invisibly decaying higgs boson via the associated zh production in the atlas experiment. *ATL-PHYS-PUB-2006-009*, 2006.
- [197] JiJi Fan, Matthew Reece, and Lian-Tao Wang. Non-relativistic effective theory of dark matter direct detection. *JCAP*, 1011:042, 2010.
- [198] Edward Farhi and Leonard Susskind. Technicolour. *Phys. Rept.*, 74(3):277, 1981.
- [199] G. Feinberg, P. Kabir, and Steven Weinberg. Transformation of muons into electrons. *Phys. Rev. Lett.*, 3:527–530, 1959.
- [200] Michael Feindt, 2010. private communication, see DELPHI ELEPHANT home page <http://delphiwww.cern.ch/tasks/elephant/>.
- [201] Tai-Fu Feng, Jian-Bin Chen, Tie-Jun Gao, and Ke-Sheng Sun. Residue theorem and summing over Kaluza-Klein excitations. *Phys. Rev.*, D84:096012, 2011.
- [202] Douglas P. Finkbeiner. Microwave ISM Emission Observed by WMAP. *Astrophys. J.*, 614:186–193, 2004. Douglas P. Finkbeiner. WMAP microwave emission interpreted as dark matter annihilation in the inner Galaxy. 2004.
- [203] A. Liam Fitzpatrick, Lisa Randall, and Gilad Perez. Flavor anarchy in a Randall-Sundrum model with 5D minimal flavor violation and a low Kaluza-Klein scale. *Phys. Rev. Lett.*, 100:171604, 2008.
- [204] A. Liam Fitzpatrick, Lisa Randall, and Gilad Perez. Flavor anarchy in a Randall-Sundrum model with 5D minimal flavor violation and a low Kaluza-Klein scale. *Phys. Rev. Lett.*, 100:171604, 2008.
- [205] Jean-Francois Fortin and Tim M.P. Tait. Collider Constraints on Dipole-Interacting Dark Matter. 2011.

- [206] Patrick J. Fox, Roni Harnik, Joachim Kopp, and Yuhsin Tsai. Lep Shines Light on Dark Matter. *Phys. Rev.*, D84:014028, 2011.
- [207] Patrick J. Fox, Roni Harnik, Joachim Kopp, and Yuhsin Tsai. Missing energy signatures of dark matter at the lhc. 09 2011.
- [208] Patrick J. Fox, Joachim Kopp, Mariangela Lisanti, and Neal Weiner. A Cogent Modulation Analysis. 2011.
- [209] Patrick J. Fox, Graham D. Kribs, and Tim M. P. Tait. Interpreting Dark Matter Direct Detection Independently of the Local Velocity and Density Distribution. *Phys. Rev.*, D83:034007, 2011.
- [210] Patrick J. Fox, Ann E. Nelson, and Neal Weiner. Dirac gaugino masses and supersoft supersymmetry breaking.
- [211] Patrick J. Fox and Erich Poppitz. Leptophilic Dark Matter. *Phys. Rev.*, D79:083528, 2009.
- [212] M. Fukugita and T. Yanagida. Baryogenesis Without Grand Unification. *Phys.Lett.*, B174:45, 1986.
- [213] P. Gagnon. Invisible higgs boson decays in the $z0h0$ and $w\pm h0$ channels. *ATL-COM-PHYS-2003-011*, 2005.
- [214] Oram Gedalia, Gino Isidori, and Gilad Perez. Combining Direct & Indirect Kaon CP Violation to Constrain the Warped KK Scale. 2009.
- [215] Graciela B. Gelmini, Efunwande Osoba, and Sergio Palomares-Ruiz. Inert-Sterile Neutrino: Cold or Warm Dark Matter Candidate. *Phys.Rev.*, D81:063529, 2010.
- [216] Chao-Qiang Geng and Ryo Takahashi. Magnetic dipole moment and keV neutrino dark matter. *Phys.Lett.*, B710:324–327, 2012.
- [217] Howard Georgi. Unparticle Physics. *Phys. Rev. Lett.*, 98:221601, 2007.
- [218] Howard Georgi, Aaron K. Grant, and Girma Hailu. Brane couplings from bulk loops. *Phys. Lett.*, B506:207–214, 2001.

- [219] Yuri Gershtein, Frank Petriello, Seth Quackenbush, and Kathryn M. Zurek. Discovering hidden sectors with mono-photon Z-primeo searches. *Phys. Rev.*, D78:095002, 2008.
- [220] Tony Gherghetta. TASI Lectures on a Holographic View of Beyond the Standard Model Physics. 2010.
- [221] Tony Gherghetta and Alex Pomarol. Bulk fields and supersymmetry in a slice of AdS. *Nucl. Phys.*, B586:141–162, 2000.
- [222] Tony Gherghetta and Alex Pomarol. Bulk fields and supersymmetry in a slice of AdS. *Nucl. Phys.*, B586:141–162, 2000.
- [223] Joel Giedt, Anthony W. Thomas, and Ross D. Young. Dark matter, the CMSSM and lattice QCD. *Phys. Rev. Lett.*, 103:201802, 2009.
- [224] TA Girard et al. New limits on WIMP interactions from the SIMPLE dark matter search. 2011.
- [225] G.F. Giudice and R. Rattazzi. Theories with gauge-mediated supersymmetry breaking.
- [226] Amit Giveon, Andrey Katz, and Zohar Komargodski. On sqcd with massive and massless flavors. 04 2008.
- [227] Amit Giveon, Andrey Katz, and Zohar Komargodski. Uplifted metastable vacua and gauge mediation in sqcd. 05 2009.
- [228] Amit Giveon and David Kutasov. Stable and metastable vacua in brane constructions of sqcd. 10 2007.
- [229] Jessica Goodman et al. Constraints on Dark Matter from Colliders. *Phys. Rev.*, D82:116010, 2010.
- [230] Jessica Goodman et al. Constraints on Light Majorana Dark Matter from Colliders. *Phys. Lett.*, B695:185–188, 2011.
- [231] Jessica Goodman, Masahiro Ibe, Arvind Rajaraman, William Shepherd, Tim M.P. Tait, et al. Gamma Ray Line Constraints on Effective Theories of Dark Matter. *Nucl.Phys.*, B844:55–68, 2011.

- [232] Michael L. Graesser, Ian M. Shoemaker, and Luca Vecchi. A dark force for baryons. 2011.
- [233] D. Grasso et al. On possible interpretations of the high energy electron-positron spectrum measured by the Fermi Large Area Telescope. *Astropart.Phys.*, 32:140–151, 2009.
- [234] Daniel Green, Andrey Katz, and Zohar Komargodski. Direct gaugino mediation. 08 2010.
- [235] Benjamin Grinstein and Dan Pirjol. Precise $|V_{ub}|$ determination from exclusive B decays: Controlling the long-distance effects. *Phys. Rev.*, D70:114005, 2004.
- [236] Yuval Grossman and Matthias Neubert. Neutrino masses and mixings in non-factorizable geometry. *Phys. Lett.*, B474:361–371, 2000.
- [237] Yuval Grossman and Matthias Neubert. Neutrino masses and mixings in non-factorizable geometry. *Phys. Lett.*, B474:361–371, 2000.
- [238] Yuval Grossman and Gilad Perez. Realistic construction of split fermion models. *Phys. Rev.*, D67:015011, 2003.
- [239] Yuval Grossman and Dean J. Robinson. Composite Dirac Neutrinos. *JHEP*, 1101:132, 2011.
- [240] Yuval Grossman and Yuhsin Tsai. Leptogenesis with composite neutrinos. *JHEP*, 12:016, 2008.
- [241] LEP Exotica Working Group. http://lepexotica.web.cern.ch/LEPEXOTICA/notes/2004-03/ed_note_final.ps.gz.
- [242] A. H. Guth and E. J. Weinberg. *Phys. Rev.*, D(23):876, 1981.
- [243] Naoyuki Haba and Nobuhito Maru. A simple model of direct gauge mediation of metastable supersymmetry breaking. 09 2007.
- [244] Ulrich Haisch and Andreas Weiler. Bound on minimal universal extra dimensions from $\bar{B} \rightarrow X_s \gamma$. *Phys.Rev.*, D76:034014, 2007.
- [245] Roni Harnik and Graham D. Kribs. An Effective Theory of Dirac Dark Matter. *Phys.Rev.*, D79:095007, 2009.

- [246] Xiao-Gang He and Jusak Tandean. Hidden higgs boson at the lhc and light dark matter searches. 09 2011.
- [247] Dan Hooper, J. I. Collar, Jeter Hall, and Dan McKinsey. A Consistent Dark Matter Interpretation For CoGeNT and DAMA/LIBRA. *Phys. Rev.*, D82:123509, 2010.
- [248] Dan Hooper and Lisa Goodenough. Dark Matter Annihilation in The Galactic Center As Seen by the Fermi Gamma Ray Space Telescope. 2010.
- [249] Dan Hooper and Tim Linden. Gamma Rays From The Galactic Center and the WMAP Haze. 2010.
- [250] Stephan J. Huber. Flavor violation and warped geometry. *Nucl. Phys.*, B666:269–288, 2003.
- [251] Stephan J. Huber. Flavor violation and warped geometry. *Nucl. Phys.*, B666:269–288, 2003.
- [252] Tobias Huber, Enrico Lunghi, Mikolaj Misiak, and Daniel Wyler. Electromagnetic logarithms in $\bar{B} \rightarrow X_s l^+ l^-$. *Nucl.Phys.*, B740:105–137, 2006.
- [253] R.S. Hundi and Sourov Roy. Constraints on composite Dirac neutrinos from observations of galaxy clusters. *Phys.Lett.*, B702:228–234, 2011.
- [254] Tobias Hurth, Gino Isidori, Jernej F. Kamenik, and Federico Mescia. Constraints on New Physics in MFV models: A Model-independent analysis of $\Delta F = 1$ processes. *Nucl.Phys.*, B808:326–346, 2009.
- [255] Tobias Hurth, Enrico Lunghi, and Werner Porod. Untagged $\bar{B} \rightarrow X_{s+d} \gamma$ CP asymmetry as a probe for new physics. *Nucl.Phys.*, B704:56–74, 2005.
- [256] M. Dine I. Aeck and N. Seiberg. *Nucl. Phys. B*, B(256):557, 1985.
- [257] M. Ibe, Y. Nakayama, and T.T. Yanagida. Conformal gauge mediation.
- [258] K. Intriligator and N. Seiberg. Lectures on supersymmetric gauge theories and electric-magnetic duality.
- [259] Kenneth Intriligator and Nathan Seiberg. Lectures on supersymmetry breaking.

- [260] Kenneth Intriligator, David Shih, and Matthew Sudano. Surveying pseudomoduli: the good, the bad and the incalculable. 09 2008.
- [261] Kenneth Intriligator and Scott Thomas. Dynamical supersymmetry breaking on quantum moduli spaces.
- [262] Kenneth A. Intriligator, Nathan Seiberg, and David Shih. Dynamical SUSY breaking in meta-stable vacua. *JHEP*, 0604:021, 2006.
- [263] A. Ishikawa et al. Measurement of forward-backward asymmetry and Wilson coefficients in $B \rightarrow K^* l^+ l^-$. *Phys. Rev. Lett.*, 96:251801, 2006.
- [264] M. Iwasaki et al. Improved measurement of the electroweak penguin process $B \rightarrow X_s l^+ l^-$. *Phys.Rev.*, D72:092005, 2005.
- [265] K.-I. Izawa, Y. Nomura, K. Tobe, and T. Yanagida. Direct-transmission models of dynamical supersymmetry breaking.
- [266] K.-I. Izawa and T. Yanagida. Dynamical supersymmetry breaking in vector-like gauge theories.
- [267] Jernej F. Kamenik and Jure Zupan. Discovering Dark Matter Through Flavor Violation at the LHC. 2011.
- [268] Shinya Kanemura, Shigeki Matsumoto, Takehiro Nabeshima, and Nobuchika Okada. Can WIMP Dark Matter Overcome the Nightmare Scenario? *Phys. Rev.*, D82:055026, 2010. Shinya Kanemura, Shigeki Matsumoto, Takehiro Nabeshima, and Hiroyuki Taniguchi. Testing Higgs Portal Dark Matter via Z Fusion at a Linear Collider. *Phys. Lett.*, B701:591–596, 2011.
- [269] J. Kaulard et al. Improved limit on the branching ratio of $\mu^- \rightarrow e^+ \nu_\mu \nu_e$ conversion on titanium. *Phys.Lett.*, B422:334–338, 1998.
- [270] Ryuichiro Kitano. Lepton flavor violation in the Randall-Sundrum model with bulk neutrinos.
- [271] Ryuichiro Kitano, Masafumi Koike, and Yasuhiro Okada. Detailed calculation of lepton flavor violating muon electron conversion rate for various nuclei. *Phys.Rev.*, D66:096002, 2002.

- [272] Ryuichiro Kitano, Hiroshi Ooguri, and Yutaka Ookouchi. Direct mediation of meta-stable supersymmetry breaking.
- [273] Edward W. Kolb and Michael S. Turner. The Early universe. *Front.Phys.*, 69:1–547, 1990.
- [274] Zohar Komargodski and David Shih. Notes on SUSY and R-Symmetry Breaking in Wess-Zumino Models. *JHEP*, 0904:093, 2009.
- [275] E. Komatsu et al. Seven-Year Wilkinson Microwave Anisotropy Probe (WMAP) Observations: Cosmological Interpretation. *Astrophys.J.Suppl.*, 192:18, 2011.
- [276] Joachim Kopp. Collider limits on dark matter. 2011.
- [277] Joachim Kopp, Viviana Niro, Thomas Schwetz, and Jure Zupan. DAMA/LIBRA and leptonically interacting Dark Matter. *Phys. Rev.*, D80:083502, 2009.
- [278] Joachim Kopp, Viviana Niro, Thomas Schwetz, and Jure Zupan. Leptophilic Dark Matter in Direct Detection Experiments and in the Sun. 2010.
- [279] Joachim Kopp, Thomas Schwetz, and Jure Zupan. Global interpretation of direct Dark Matter searches after CDMS-II results. *JCAP*, 1002:014, 2010.
- [280] Daniel Koschade, Moritz McGarrie, and Steven Thomas. Direct mediation and metastable supersymmetry breaking for $so(10)$. 09 2009.
- [281] Graham D. Kribs, Erich Poppitz, and Neal Weiner. Flavor in supersymmetry with an extended r-symmetry. 12 2007.
- [282] Frank Kruger and Joaquim Matias. Probing new physics via the transverse amplitudes of $B^0 \rightarrow K^{*0}(\rightarrow K^-\pi^+)l^+l^-$ at large recoil. *Phys.Rev.*, D71:094009, 2005.
- [283] Frank Kruger, Lalit M. Sehgal, Nita Sinha, and Rahul Sinha. Angular distribution and CP asymmetries in the decays $\bar{B} \rightarrow K^-\pi^+e^-e^+$ and $\bar{B} \rightarrow \pi^-\pi^+e^-e^+$. *Phys.Rev.*, D61:114028, 2000.
- [284] Alexander Kusenko. Sterile neutrinos: The Dark side of the light fermions. *Phys.Rept.*, 481:1–28, 2009.
- [285] M. Claudson L. Alvarez-Gaume and M. B. Wise. *Nucl. Phys.*, B(207):96, 1982.

- [286] M. Laine and M. Shaposhnikov. Sterile neutrino dark matter as a consequence of nuMSM-induced lepton asymmetry. *JCAP*, 0806:031, 2008.
- [287] L. Lavoura. General formulae for $f_1 \rightarrow f_2 \gamma$. *Eur. Phys. J.*, C29:191–195, 2003.
- [288] Benjamin W. Lee and Robert E. Shrock. Natural Suppression of Symmetry Violation in Gauge Theories: Muon - Lepton and Electron Lepton Number Nonconservation. *Phys. Rev.*, D16:1444, 1977.
- [289] Wei Liao. keV scale ν_R dark matter and its detection in β decay experiment. *Phys.Rev.*, D82:073001, 2010.
- [290] Michael Loewenstein and Alexander Kusenko. Dark Matter Search Using Chandra Observations of Willman 1, and a Spectral Feature Consistent with a Decay Line of a 5 keV Sterile Neutrino. *Astrophys. J.*, 714:652, 2010.
- [291] Markus A. Luty. Simple gauge-mediated models with local minima.
- [292] W. Fischler M. Dine and M. Srednicki. *Nucl. Phys.*, B(189):575, 1981.
- [293] Juan Martin Maldacena. The large N limit of superconformal field theories and supergravity. *Adv. Theor. Math. Phys.*, 2:231–252, 1998.
- [294] D. Malyshev. *Ph.D. Thesis*, 2008.
- [295] Y. Mambrini. Higgs Searches and Singlet Scalar Dark Matter: When Xenon100 Meets the Lhc. 2011.
- [296] Yann Mambrini and Bryan Zaldivar. When LEP and Tevatron combined with WMAP and XENON100 shed light on the nature of Dark Matter. 2011.
- [297] W. J. Marciano and A. I. Sanda. Exotic Decays of the Muon and Heavy Leptons in Gauge Theories. *Phys. Lett.*, B67:303, 1977.
- [298] Nobuhito Maru. Direct gauge mediation of uplifted metastable supersymmetry breaking in supergravity. 08 2010.
- [299] Joaquim Matias, Federico Mescia, Marc Ramon, and Javier Virto. Complete Anatomy of $B \rightarrow K^* l l$ and its angular distribution. 2012.
- [300] Luis Filipe Matos. Some examples of F and D-term SUSY breaking models. 2009.

- [301] Kristian L. McDonald. Light Neutrinos from a Mini-Seesaw Mechanism in Warped Space. *Phys.Lett.*, B696:266–272, 2011.
- [302] Patrick Meade, Nathan Seiberg, and David Shih. General gauge mediation. 01 2008.
- [303] B. Meadows, M. Blanke, A. Stocchi, A. Drutskey, A. Cervelli, et al. The impact of SuperB on flavour physics. 2011.
- [304] Alexander Merle and Viviana Niro. Deriving Models for keV sterile Neutrino Dark Matter with the Froggatt-Nielsen mechanism. *JCAP*, 1107:023, 2011.
- [305] M. Misiak et al. The first estimate of $B(\bar{B} \rightarrow X_s \gamma)$ at $O(\alpha_s^2)$. *Phys. Rev. Lett.*, 98:022002, 2007.
- [306] Mikolaj Misiak and Matthias Steinhauser. NNLO QCD corrections to the $B \rightarrow X_s \gamma$ matrix elements using interpolation in m_c . *Nucl. Phys.*, B764:62–82, 2007.
- [307] G. Moreau and J. I. Silva-Marcos. Flavour physics of the RS model with KK masses reachable at LHC.
- [308] Hitoshi Murayama. A model of direct gauge mediation.
- [309] Hitoshi Murayama and Aaron Pierce. Realistic Dirac leptogenesis. *Phys.Rev.Lett.*, 89:271601, 2002.
- [310] Yuichiro Nakai and Yutaka Ookouchi. Comments on gaugino mass and landscape of vacua. 10 2010.
- [311] C. R. Nappi, C. R. Nappi, and B. A. Ovrut. *Phys. Lett.*, B(113):175, 1982.
- [312] Julio F. Navarro, Carlos S. Frenk, and Simon D. M. White. The Structure of Cold Dark Matter Halos. *Astrophys. J.*, 462:563–575, 1996.
- [313] Ann E. Nelson and Nathan Seiberg. R symmetry breaking versus supersymmetry breaking.
- [314] Ann E. Nelson and Nathan Seiberg. R symmetry breaking versus supersymmetry breaking.
- [315] Takemichi Okui. Searching for composite neutrinos in the cosmic microwave background. *JHEP*, 09:017, 2005.

- [316] B. O’Leary et al. SuperB Progress Reports – Physics. 2010.
- [317] Keith A. Olive and Michael S. Turner. Cosmological bounds on the masses of stable, right-handed neutrinos. *Phys. Rev. D*, 25:213–216, Jan 1982.
- [318] L. O’Raifeartaigh. Spontaneous symmetry breaking for chiral scalar superfields. *Nucl. Phys. B*, 96(331), 1975.
- [319] S. Oryn, X. Rouby, and V. Lemaitre. Delphes, a Framework for Fast Simulation of a Generic Collider Experiment. 2009.
- [320] P. Gagnon et al. Sensitivity to an invisibly decaying higgs boson with atlas data. *ATLAS CSC NOTE 10*, (<http://pauline.web.cern.ch/pauline/presentations/InvisibleHiggs-CSCnote.pdf>), 2008.
- [321] Gilad Perez and Lisa Randall. Natural Neutrino Masses and Mixings from Warped Geometry. *JHEP*, 01:077, 2009.
- [322] S. T. Petcov. The Processes $\mu \rightarrow e\gamma$, $\mu \rightarrow ee\bar{e}$, $\nu' \rightarrow \nu\gamma$ in the Weinberg-Salam Model with Neutrino Mixing. *Sov. J. Nucl. Phys.*, 25:340, 1977.
- [323] Alex Pomarol. Gauge bosons in a five-dimensional theory with localized gravity. *Phys. Lett.*, B486:153–157, 2000.
- [324] E. Poppitz and S.P. Trivedi. New models of gauge and gravity mediated supersymmetry breaking.
- [325] Martin Puchwein and Zoltan Kunszt. Radiative corrections with 5D mixed position- / momentum- space propagators. *Annals Phys.*, 311:288–313, 2004.
- [326] A. Pukhov, E. Boos, M. Dubinin, V. Edneral, V. Ilyin, et al. CompHEP: A Package for evaluation of Feynman diagrams and integration over multiparticle phase space. 1999. CompHEP user’s manual for version 33; <http://comphep.sinp.msu.ru>.
- [327] Arvind Rajaraman, William Shepherd, Tim M. P. Tait, and Alexander M. Wijangco. Lhc Bounds on Interactions of Dark Matter. 2011.
- [328] Arvind Rajaraman, William Shepherd, Tim M.P. Tait, and Alexander M. Wijangco. Lhc bounds on interactions of dark matter. 08 2011.

- [329] Lisa Randall and Matthew D. Schwartz. Quantum field theory and unification in AdS5. *JHEP*, 11:003, 2001.
- [330] Lisa Randall and Raman Sundrum. A large mass hierarchy from a small extra dimension. *Phys. Rev. Lett.*, 83:3370–3373, 1999.
- [331] R. Rattazzi and A. Zaffaroni. Comments on the holographic picture of the Randall-Sundrum model. *JHEP*, 04:021, 2001.
- [332] Sébastien Ray. Some properties of meta-stable supersymmetry-breaking vacua in wess-zumino models.
- [333] E. J. Weinberg S. R. Coleman. Radiative corrections as the origin of spontaneous symmetry breaking. *Phys. Rev.*, D(7):1888–1910, 1973.
- [334] Jose Santiago. Minimal Flavor Protection: A New Flavor Paradigm in Warped Models. *JHEP*, 12:046, 2008.
- [335] Jose Santiago. Minimal Flavor Protection: A New Flavor Paradigm in Warped Models. *JHEP*, 12:046, 2008.
- [336] N. Seiberg. Electric-magnetic duality in supersymmetric non-abelian gauge theories.
- [337] Nathan Seiberg. Exact results on the space of vacua of four dimensional susy gauge theories.
- [338] Yael Shadmi. Metastable Rank-Condition Supersymmetry Breaking in a Chiral Example. *JHEP*, 1108:149, 2011.
- [339] Xiang-Dong Shi and George M. Fuller. A New dark matter candidate: Nonthermal sterile neutrinos. *Phys.Rev.Lett.*, 82:2832–2835, 1999.
- [340] Mikhail A. Shifman, A. I. Vainshtein, and Valentin I. Zakharov. Remarks on Higgs Boson Interactions with Nucleons. *Phys. Lett.*, B78:443, 1978.
- [341] David Shih. Spontaneous r-symmetry breaking in o’raifeartaigh models.
- [342] Satoshi Shirai, Masahito Yamazaki, and Kazuya Yonekura. Aspects of non-minimal gauge mediation. 03 2010.

- [343] Yuri Shirman. New models of gauge mediated dynamical supersymmetry breaking.
- [344] Torbjorn Sjostrand, Stephen Mrenna, and Peter Z. Skands. Pythia 6.4 Physics and Manual. *JHEP*, 05:026, 2006.
- [345] Zheng Sun. Tree level spontaneous r-symmetry breaking in o’raifeartaigh models. 10 2008.
- [346] Raman Sundrum. From Fixed Points to the Fifth Dimension. 2011.
- [347] T. Suzuki, David F. Measday, and J.P. Roalsvig. Total Nuclear Capture Rates for Negative Muons. *Phys.Rev.*, C35:2212, 1987.
- [348] K. Takeda et al. Nucleon strange quark content from two-flavor lattice QCD with exact chiral symmetry. *Phys.Rev.*, D83:114506, 2011.
- [349] D. Toussaint and W. Freeman. The strange quark condensate in the nucleon in 2+1 flavor QCD. *Phys. Rev. Lett.*, 103:122002, 2009.
- [350] David Tucker-Smith and Neal Weiner. Inelastic dark matter. *Phys.Rev.*, D64:043502, 2001.
- [351] Y. Ushiroda et al. Time-Dependent CP Asymmetries in $B^0 \rightarrow K_S^0 \pi^0 \gamma$ transitions. *Phys.Rev.*, D74:111104, 2006.
- [352] Jian Wang, Chong Sheng Li, Ding Yu Shao, and Hao Zhang. Next-to-leading order QCD predictions for the signal of Dark Matter and photon associated production at the LHC. 2011.
- [353] Casey R. Watson, Zhiyuan Li, and Nicholas K. Polley. Constraining Sterile Neutrino Warm Dark Matter with Chandra Observations of the Andromeda Galaxy. 2011.
- [354] P. Wintz et al. Test of LFC in $\mu \rightarrow e$ conversion on titanium.
- [355] E. Witten. *Phys. Rev. Lett.*, B(105):267, 1981.
- [356] E. Witten. *Nucl. Phys.*, B(202):253, 1982.

- [357] Jun Wu, Chiu-Man Ho, and Daniel Boyanovsky. Sterile neutrinos produced near the EW scale. I. Mixing angles, MSW resonances and production rates. *Phys.Rev.*, D80:103511, 2009.
- [358] R. D. Young and A. W. Thomas. Octet baryon masses and sigma terms from an SU(3) chiral extrapolation. *Phys. Rev.*, D81:014503, 2010.
- [359] Ross D. Young and Anthony W. Thomas. Recent results on nucleon sigma terms in lattice QCD. *Nucl. Phys.*, A844:266c–271c, 2010.